Filling flows induced by a convector in a room

A. A. Przydróżna

Murray Edwards College

University of Cambridge

A thesis submitted for the degree of
Doctor of Philosophy

February 2018

To my family,
Your love inspires me everyday, gives me hope in the darkest hour and carries through any obstacles. I feel truly blessed to have you all. Thank you for believing in me and for your endless support of my life pursuits.

To my father Edward,
You have taught me everything there is to know about engineering and reignited my passion towards research and innovation.

To my mother Anna,
Your words of encouragement and wisdom give me strength and confidence to dream and to believe that impossible is nothing.

To Joanna,
You have saved me more than I can even remember and I will always look up to you.

To Magda and Darek,
I can always feel your support and love.

To Jan,
Continue pursuing your interests and believe because only then you will achieve!

Declaration

The research described in this dissertation was undertaken in the Fluid Mechanics Laboratory of the Department of Engineering at the University of Cambridge between October 2012 and December 2015. I hereby declare that no part of this thesis has been submitted for any other degree or qualification. This dissertation is the result of my own work. I herewith certify that all material in this dissertation which is not my own work has been properly acknowledged. This dissertation contains no more than 65,000 words and 150 figures.

Aleksandra Przydróżna
February 2018

Abstract

Over the last two centuries, there has been a continual evolution of how occupied rooms are heated, with inventors competing to design new heating devices. In particular, there is a wide range of convector types, which vary in shape, size, design, material, operating medium and application. With approximately 190 million convectors installed in the UK alone, the question arises regarding the dependencies on the efficiency of heat distribution through convector-induced filling flows. A standard approach to evaluate convector performance is based on the convector strength only, the implication being the stronger the convector the better the performance. This work has gone beyond the limits of a stereotypical assessment in pursuit of answers regarding the physics of convector-induced filling and a new objective method to evaluate the efficiency of this transient process. The ultimate goal has been to provide a deep understanding of filling and stratification induced by a convector, in order to heat rooms rapidly and effectively.

An experimental facility has been designed that approximates dynamic similarity between the experimental set-up and a real-life room with a convector. In the experiments, a rectangular sectioned water tank represents a room and a saline source rectangular sectioned panel with sintered side walls provides a convector representation. Experiments have been performed in water with a saline solution to ensure high Rayleigh numbers. Diagnostic techniques involve a combination of a shadowgraph method, a dye-attenuation method, direct salinity measurements and a new application of Particle Image Velocimetry (PIV).

Interesting insight into convector-induced buoyancy-driven flows has been gained. As a result, new guidelines aimed at heating rooms more rapidly and effectively have been proposed. The key outcome that can be immediately applied is that, for a given convector strength, heat distribution with height can be improved by adjusting the convector position. For instance, faster filling leading to more uniform heat distribution occurs in rooms with convectors detached from side walls, due to large-scale mixing flows in the early period of filling. Also shorter convectors relative to the room height, positioned close to the floor level, promote faster and more uniform filling. An attempt to describe the transient filling has been made and to do so statistical methods, application specific, have been developed. As a result, the empirical equations describing both the filling rates in different stages of filling and the development of stratification have been derived, which rank the governing parameters, based on their importance, as either dominant or subordinate. Two dominant parameters governing filling flows are the non-dimensional accumulation parameter $\mathcal{B}$ and the Rayleigh number ΔRa, which are related to the

convector strength. The impact of these two parameters is constant throughout the process. The parameters accounting for the system geometry and filling time (**T**) are subordinate parameters. Their impact, visible in the early period, decreases as filling continues.

Acknowledgements

In a process of going through my PhD journey I have encountered, worked with and shared experiences with many people who not only made an impact on my research but also provided me with invaluable life lessons that I will carry with me forever.

First I would like to make special acknowledgement of my supervisor, Professor Gary Hunt for inviting me to the research team, for all the opportunities he provided me with, and for the constructive criticism and technical advice.

I would also like to extend particular words of gratitude to Peter Holland, John Gould and Rod Weston from ServoRad for funding my maintenance costs and my new experimental facility in Cambridge University Engineering Department Hydraulics Laboratory. Without their financial support, I would have never been able to conduct my research and for that I will be forever grateful. Additionally, I would like to thank Peter Holland for his technical support, help with the experimental set-up and time he spent with me in the CUED laboratory.

I would also like to acknowledge Professor Gary Hunt and Peter Holland for designing and constructing the convector model used in my project.

I would like to express my gratitude to Jonathan Fall and Peter Holland for designing and constructing the new Salinity Analyser (conductivity meter). Our work on calibration and error reduction helped me in becoming a better experimentalist.

Once again, I would like to recognise the contribution of Professor Gary Hunt for defining performance indicators and rosette, which I developed and used throughout my research.

I would like to acknowledge Professor Babinsky for his invaluable help and support both technical and personal in the final stages of my PhD. I would also like to thank Professor Babinsky for granting the access to very expensive PIV equipment that I have used to investigate flows induced in the environment.

Dr Robbie Stevens and Dr Richard Stephens are thanked for providing their technical expertise in the field of PIV. Their help with challenging experimental set-up, data acquisition and post-processing is greatly appreciated.

Further I would like to acknowledge Mr. Mick Underwood, Mr. Rob Leroy, Mr. John Harvey, Mr. Ken Griggs and Mr. Kevin in the Cambridge University Engineering Department Hydraulics Laboratory Workshop for rig and electronics support.

I also wish to acknowledge the Engineering and Physical Sciences Research Council (EPSRC) for funding the work.

I would like to acknowledge Murray Edwards College for creating an inspiring environment and community that I am very proud to be a part of for the rest of my life. Special thanks are extended to Mrs Nichola Cavaleri for everything.

Anthony Haynes is thanked for his mentorship and his help with my technical writing.

Particular thanks are extended to Phil Armitage, Mike Baldwin and Andy Johnson from Max Fordham for their full support.

Last but not least, to all my research colleagues - thank you all for the inspiring conversations, walks and moments that will make us smile in the years to come.

Contents

List of Figures

List of Tables

Nomenclature

Roman letters

a	Convector distance from side wall (cm)
$\mathcal{A}$	Absorbance
$\mathcal{AR}$	Room aspect ratio, for defining equation see (4.6)
B	Buoyancy flux ($\mathrm{cm}^{4}\mathrm{s}^{-3}$)
$\mathcal{B}$	Non-dimensional accumulation parameter
c	Function of entrainment coefficient
c_P	Specific heat capacity at constant pressure ($\mathrm{Jg}^{-1}\mathrm{K}^{-1}$)
$\mathscr{C}$	Conductance (µS)
$\mathcal{C}$	Speed of light in fluid (cms^{-1})
CoD	Coefficient of determination
d	Convector width (cm)
dt	Frame rate (s)
D	Thermal diffusion ($\mathrm{cm}^{-2}\mathrm{s}^{-1}$)
$\mathcal{D}$	Cross-sectional area of electrode (cm^{2})
e	Distance between electrodes (cm)
E	Global measure of ventilation efficiency
$[E(\delta t)]_{h_1}^{h_2}$	Local measure of ventilation efficiency
$\mathscr{E}$	Error (PIV)
f	Function
F	F-distribution
FOV_x	Field of View width (m)
g	Gravitational acceleration ($\mathrm{cm\,s}^{-2}$)
g'	Buoyancy ($\mathrm{cm\,s}^{-2}$)
G	Conductivity ($\mu\mathrm{Scm}^{-1}$)
$\mathcal{G}$	Non-dimensional geometric parameter
h	Interface position (cm)
H	Room height (cm)
I	Performance indicator
$\mathcal{I}$	Current (A)
$\mathscr{I}$	Light intensity (W sr)
$\mathfrak{I}$	Non-dimensional stratification parameter
k	Number of variables
$\Bbbk$	Best fit slope

K	K - factor, $=\frac{\mathfrak{D}}{e}$
l	Length (cm)
l_y	Mean confidence limits of regression
l_{β_i}	Confidence limits of coefficient of regression
L	Convector length (cm)
$\mathcal{L}$	Convector height (cm)
m	Velocity vector field parameter, for defining equation see (4.18)
n	Number of observations
$\mathscr{N}$	Number of runs
NoR	Norm of residuals
pix_x	Field of View width (px)
pix_{shift_x}	Pixel shift (px)
$\wp$	Path length of light ray (cm)
Q	Volume flux, (cm ^{2}s $^{-1}$, cms $^{-1}$)
$\dot{Q}$	Volume flow rate (LPM, cm ^{3}s^{-1})
R	Room radius (cm)
R	Coefficient of multiple correlation
$\mathcal{R}$	Ratio
$\mathfrak{R}$	Non-dimensional flow parameter
Res	Residual
s	Standard deviation of regression
s_{β_i}	Standard deviation of coefficient of regression
s^2	Mean squared error
S	Cross-sectional area of the room (cm ^{2})
$\mathcal{S}$	Salinity/ Salt concentration (%, PPM)
t	Time (s)
t_{Stu}	Value of t-Student statistic
$t_{\infty,\gamma}$	Critical value of t-Student distribution for ∞ degrees of freedom and level of significance γ
$\mathcal{T}$	Timescale (s)
T	Temperature (K)
$\mathbf{T}$	Non-dimensional time parameter
Tr	Transmittance
$\overrightarrow{u}$	Velocity vector
u, v, w	Velocity components (cms $^{-1}$)
$\|\overline{u}\|, \|\overline{v}\|, \|\overline{w}\|$	Mean velocity magnitudes (cms $^{-1}$)
$\Delta u, \Delta v, \Delta w$	Rates of displacement (cms $^{-1}$)
$\mathcal{U}$	Potential difference (V)
$\mathscr{U}$	Velocity (cms $^{-1}$)
V	Buoyant layer volume (cm ^{3})
Var	Variance
W	Room width (cm)
Y	Room length (cm)
(x, y, z)	Cartesian coordinates (cm)
Δx	Horizontal displacement of horizontal current during observation (cm)
$\Delta x'$	Horizontal displacement of horizontal flow reflecting during observation (cm)
y_l	Dependent variable in the l-th observation

$\overline{y}$	Arithmetic mean of dependent variable
$\hat{y}_l$	Regression of the dependent variable in the l-th observation
z^*	Source virtual origin (cm)
Δz	Vertical displacement of starting plume during observation (cm)
$\Delta z'$	Vertical displacement of vertical intrusion during observation (cm)
$\Delta z''$	Vertical displacement of front ascending during observation (cm)
$\mho$	Particle diameter (cm)

Greek letters

α	Entrainment coefficient
β	Coefficient of regression
γ	Level of significance
δt	Time interval (s)
Δ	Difference
ϵ	Coefficient of molar absorption (ppm m)
ζ	Non-dimensional interface position
κ	Thermal conductivity (Wm $^{-1}$K $^{-1}$)
λ	Maximal penetration depth of side wall intrusion (cm)
ν	Kinematic viscosity (cm ^{2}s $^{-1}$)
ξ	Vertical distance from trailing edge (cm)
Ξ	Coefficient of transition to turbulence
ρ	Density (gcm $^{-3}$)
$\overline{\rho}$	Density ratio
τ	Non-dimensional time
ϕ	Refractive index
φ	Angle of deflection
χ	Correction factor
ω	Vorticity (s $^{-1}$)
ω^*	Non-dimensional vorticity
Ω	Resistance (Ω)
$\Delta\zeta/\Delta\tau$	Non-dimensional rate of interface ascent

Subscripts

$_*$	benchmark, baseline, see Table 4.1 for reference
$_a$	area
$_{AOZ}$	above occupied zone
$_{av}$	average
$_{bias}$	systematic
$_{cr}$	critical
$_{cum}$	cumulative
$_d$	design

dr	drain
ent	entrained
ep	early period
exp	experiment
f	full scale
F	feet
FF	far field
H	head
i	instantaneous
lp	late period
L	line
m	small scale
max	maximum
min	minimum
NF	near field
OZ	occupied zone
p	particle
pr	probe
P	point
rms	residual
R	room-averaged
s	saline solution
sv	settling velocity
sup	supply
tank	tank
tot	total
V	volume
Z	zone
0	initial, source

Acronyms

FOV	Field of View
LE	Leading Edge
OHP	Overhead Projector
PIV	Particle Image Velocimetry
TE	Trailing Edge
VDS	Vertically Distributed Source

Non-dimensional parameters

Fr	Froude number: ratio of source inertia to buoyancy
Ra	Rayleigh number: ratio of buoyancy effects to viscous effects

Re	Reynolds number: ratio of inertial forces to viscous forces

Chapter 1

Introduction

In prehistoric times, in pursuit of thermal comfort, humans have settled in cave dwellings and brought fire to reduce temperature variations. This objective to maintain thermal conditions within a suitable range for comfort within occupied spaces still remains a primary reason for installing heating elements in rooms today. However, a lot has changed since fire has been first brought inside, new heating technologies have been developed and the standard of living has improved. Simultaneously, a continual technological evolution resulted in significant amounts of energy required for heating. The great energy crisis of the 1970s has forced restrictions on, previously unlimited, energy consumption across all the energy sectors, including the building sector which accounts for approximately 31% of Global Energy Demand (Ürge-Vorsatz, 2012). Figure 1.1 outlines energy consumption by sector in the UK (a) and trends of total energy consumption in households between 1990 and 2010 (b).

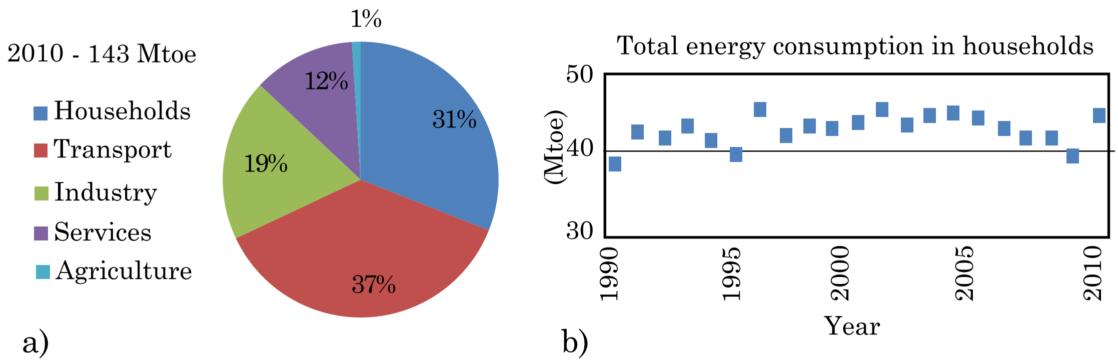

Figure 1.1: Total energy consumption in the UK (adapted from Energy Efficiency Trends and Policies in the UK, 2012).

In the UK, in 2010, similarly to the global trend, energy consumption in households comprised 31% of total energy consumption, corresponding to over 44 Mtoe[1]. Also, despite the policies introduced to use less energy, there has been an increase of 15.1% in total energy consumption in households between 1990 and 2010, primarily caused by exceptionally cold weather and longer heating periods. In an average household, two thirds of the total energy is

[1]million tonnes of oil equivalent, 1 toe $\approx$ 42 GJ

used for heating. Improving the efficiency of heating might, thus, make a considerable impact both locally, by making end-users aware of how to achieve the equivalent thermal conditions using less energy, and globally, by reducing the total energy consumption in the building sector.

The research presented in this thesis investigates the effects of filling flows on the efficiency of room heating. Figure 1.2 is a visual representation of the investigated phenomenon. The term 'filling flows' refers to the bulk flows of warm air, induced by heaters emitting the majority of their thermal energy by convection. The term 'convector' is used here to describe the class of heaters under consideration. A typical convector, as shown in Figure 1.3, consists of two vertical surfaces through which heat is transferred to the surrounding environment. The efficiency of convector-induced heating through the filling flows is evaluated by the rate of filling and the temperature gradient, referred to as stratification, that develops in a room as a result of heat accumulation.

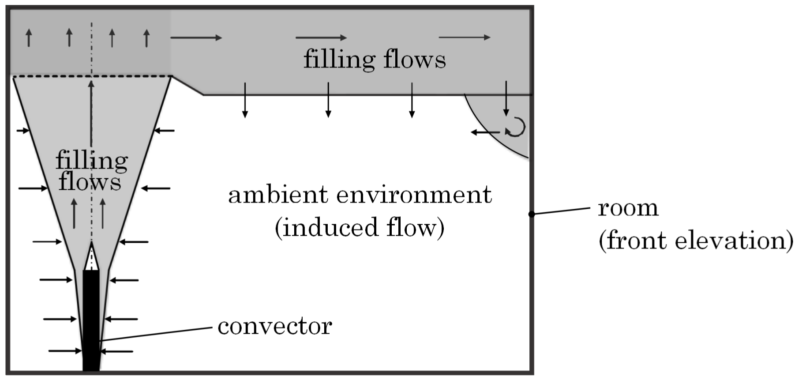

Figure 1.2: Schematic summarising the research problem (effects of filling flows on the efficiency of convector-induced heating). System considered consists of a room and a convector. Buoyant filling flows under investigation are induced by a convector. Arrows indicate flow direction.

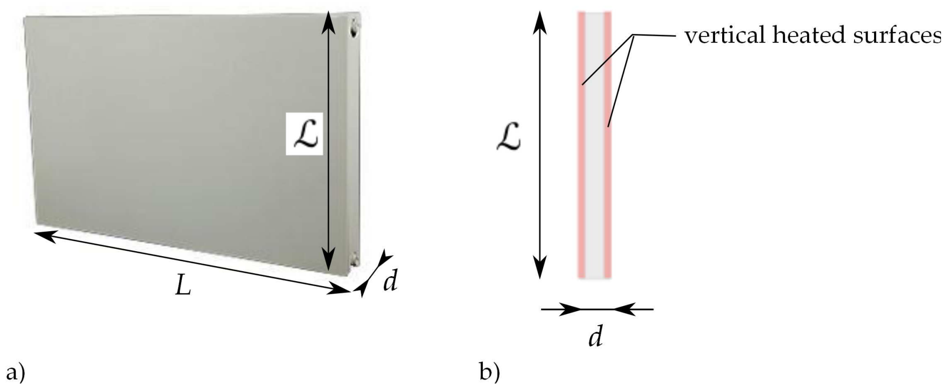

Figure 1.3: Convector: a) side view in elevation with characteristic lengths b) front view in elevation.

From the perspective of the thermal performance of a device, a stronger convector is generally judged by users to be more efficient. Typically manufacturers differentiate between convectors based on heat output alone (BS EN 442). This research identifies that a convector of a given strength but in different places within a room, results in different rates of filling and stratification that correspond to distinct *'performances'* of this convector. *'High performance'* refers to an *'efficient convector'* that accumulates heat in a designated location relatively quickly, as opposed to a *'low performance, inefficient convector'*. This research extends the interpretation of performance and efficiency to include both the rate at which room heats and stratification, and the interplay between the two, which fills the gap in the literature identified in **Chapter 2**.

The two main aspects of this research are: the in-depth investigation of the fundamental physics governing convector-induced filling and the development of objective means to evaluate the efficiency of these flows.

Over the last fifty years, the natural convection in occupied spaces has received considerable attention because of its relevance to heating (cooling) and ventilation. Baines & Turner (1969) were the first to investigate the filling induced in an isolated room by a continuous supply of heat from a point source located centrally on the floor. Their filling box model, based on the plume theory by Morton, Taylor & Turner (1956), was developed to determine the rate of filling and the evolution of stratification. In order to validate their model, Baines & Turner (1969) performed small-scale experiments in water with saline solution which was used to create density differences. Over the years this fundamental work was extended theoretically and experimentally to investigate aspects of filling not covered by the 'classic' model. Of particular significance are studies on the influence of source geometry (Cooper & Hunt 2010, Gladstone & Woods 2014, McConnochie & Kerr 2016) and the room aspect ratio (Kaye & Hunt 2007, Giannakopoulos et al. 2013). The solutions of the governing equations of Cooper & Hunt (2010) for a vertically distributed source are of particular relevance to the convector-induced filling problem as these are expected to predict the filling at the convector level. Cooper & Hunt (2010) extended the source of heat over the entire room height and described a complex stratification developing in a room with a heated wall. The question still remains, however, as to how the development of time-dependent stratification differs if a vertical extent of a convector is a fraction of the room height. This is particularly vital because the majority of convectors fall into this category and the impact of convector height relative to the room height on the efficiency of heating has yet to be evaluated.

The main motivation for this work is to determine how a room fills with bulk flows of warm air induced by a convector and which parameters are governing these filling flows. The research question is: *'what are the dependencies on the efficiency of heat distribution through filling flows?'*. The results of the research can be readily used to improve the efficiency of buoyancy-driven convector-induced heating by addressing aspects of the design that are normally overlooked and trivialised, such as the convector relative height and its relative position to the room boundaries. This research can be equally used by the end-users, to achieve equal thermal conditions using less energy, as well as designers of the heating systems, who search for the opportunities to reduce the energy demand, while still ensuring the occupants thermal comfort.

Chapter 2

Literature survey on filling flows in a heated room

Convection is a flow driven by buoyancy forces caused by density variations in a fluid. Filling flows are examples of fluid motion induced by a density (temperature) difference. Filling flows were first described by Baines & Turner (1969) in the filling box model in the context of the evolution of stratification through a continuous heat supply from a point source. The theoretical and experimental approaches developed by Baines & Turner (1969) have been applied since to describe a variety of problems in the built environment, the atmosphere and the ocean. In buildings these applications included heating (Baines & Turner 1969, Cooper & Hunt 2010, Gladstone & Woods 2014) and cooling (Cardoso & Woods 1993). These applications required modifications of the source conditions, such as location, geometry whether planar or axisymmetric and source strength described in terms of fluxes of volume, momentum and buoyancy, and the properties of the box, such as room aspect ratio. Whilst these modifications had a particular influence on the initial filling, the stratification often tended towards the classic filling box with a point source (Wong & Griffiths 1999, Cooper & Hunt 2010). Despite the success of the filling box in building applications, some fundamental questions, as identified in the previous chapter, remain unanswered. This chapter provides a review of previous research which is of particular relevance to convector-induced flows and background for the current work.

2.1 Heat source

Gladstone & Woods (2014) and Wells & Worster (2008) stated that convectors can be modelled as vertically distributed heat sources. A typical convector, as shown in Figure 1.3, consists of two vertical surfaces through which heat is transferred to the surrounding environment. The mechanisms of convective heat transfer along the vertical surfaces have been investigated in previous studies and the resulting flow structure described. Consider one of the heated vertical surfaces of a convector, which is immersed in an ambient fluid of uniform temperature T_0 (°C). If the surface temperature T_a (°C) is greater than the ambient temperature T_0, heat is conducted from the convector's surface to the fluid in contact with the heated surface (Jaluria 2003). Consequently, there is an increase in temperature and a decrease in the density of the fluid adjacent to the heated surface. In close proximity to the surface, a thermal boundary layer is established within which warm fluid rises (Prandtl 1949). Near the leading edge[1] of the vertical surface, the flow is laminar, in other words smooth, regular and well-layered, where fluid particles are sheared and distorted in an orderly way (Schlichting 1979). As the flow ascends, shear stresses between the rising buoyant fluid and the initially stationary ambient environment on one side and the vertical surface on the other side, destabilise the initially laminar thermal boundary layer, which gradually becomes more disturbed to finally transform into a turbulent boundary layer flow (Jaluria 2003). Figure 2.1 shows an example of growth of the thermal boundary layer from laminar to turbulent, adapted from Jaluria & Gebhart (1974). A spread of the turbulent flow along a heated vertical surface appears larger than of the laminar flow. This indicates that the turbulent flow develops faster with height. Jaluria & Gebhart (1974) investigated the mechanisms of transition to turbulence and derived the relationships between the flow properties (e.g. viscosity, diffusivity) and the location at which flow transitions. Mahajan & Gebhart (1979) performed experimental studies on the transition limits between laminar and turbulent regimes in a flow from a heated vertical surface. Based on their experimental results, a parameter has been established to characterise the completion of transition to turbulence:

$$\Xi_e = 5^{0.8}\left(\frac{B_a \rho_0 c_p z^4}{\kappa \nu D}\right)^{0.2}\left(\frac{g z^3}{\nu^2}\right)^{-0.167} \tag{2.1}$$

where B_a is the buoyancy flux per unit area, c_p is the thermal capacity of the fluid, ν is the kinematic viscosity, g is the gravitational acceleration, ρ_0 is the reference density, D is the thermal diffusion, κ is thermal conductivity and z is the vertical coordinate. Mahajan & Gebhart (1979) showed that the end of transition is marked by a fixed value of the parameter $\Xi_e = 11.4$. The position of transition could be subject to influences, such as surface roughness, which may change the critical value of Ξ_e. Lynch (2012) applied the approach of Jaluria & Gebhart (1974) and showed that the thermal boundary layer along the vertical surface of a heated convector is mainly turbulent in practical scenarios (> 90% in the case with a convector of height 1 m, heat output 3 kWm $^{-2}$ in a room at T_0 = 280 K).

The turbulent thermal boundary layer from a vertical surface has been the subject of theoretical and experimental investigations (e.g. Eckert & Jackson 1950, Cheesewright 1968, Warner & Arpaci 1968, George & Capp 1979, Tsuji & Nagano 1988). These have aimed at finding the velocity and temperature distributions, investigating the structure of the thermal boundary layer and developing an understanding of heat transfer from the surface to the surroundings. Also, both theoretical analysis and experimental data provided arguments as to which dimensionless groups govern the flow along the wall. The empirical equations have been established and the experimental data used to find the power-law relationship between the dimensionless groups (e.g. Nusselt 1915, Schlichting 1954). However, when the primary concern driving the research is not with the details of the flow within a thermal boundary layer but with the filling rate and development of stratification, the flow can be successfully modelled as a turbulent plume instead of the thermal boundary layer (Cooper & Hunt 2010, Caudwell, Flór & Negretti 2016). The assumptions of the plume approach are that the viscous effects along the heated surface are negligible and the flow along the entire heated surface is fully turbulent. This implies that there is no velocity-induced boundary layer. The first assumption comes at the cost of

[1]The leading edge is defined as the bottom edge in a heat-in-air case and the trailing edge is the top edge.

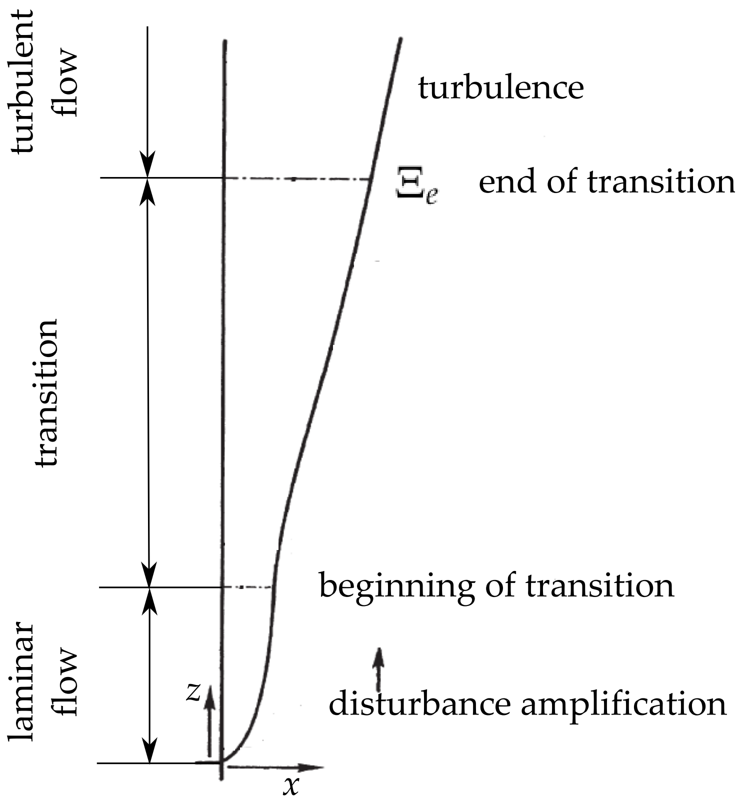

Figure 2.1: Growth of the thermal boundary layer in buoyancy-driven convection flow over a heated vertical surface in water adapted from Jaluria & Gebhart (1974).

losing accuracy in flow prediction in the region adjacent to the surface, which constitutes less than 0.25% of the total volumetric flow in the thermal boundary layer, where the velocity is significantly lower due to viscous effects (Vliet & Liu 1969, Cooper & Hunt 2010). Based on the earlier example of transition to turbulence, the second assumption of fully turbulent flow is reasonable, especially that the convector-induced filling flows are characterised by a very large Rayleigh number ($> 10^9$), which is a ratio of driving forces, induced by small density differences (Boussinesq approximation), to stabilising viscous effects (Turner 1973).

2.1.1 Fundamentals

A turbulent plume, which is a vertical column of buoyant fluid (Turner 1973), develops when a heat source supplies buoyancy steadily and continuously. Figure 2.2 shows the time-averaged outline of plumes originating from sources of different geometries. The plume development occurs through the process of entrainment of the surrounding fluid into the plume (Morton et al. 1956, van den Bremer & Hunt 2010, 2014, Ezzamel, Salizzoni & Hunt 2015). The entrainment is the transport of fluid across the plume boundary, which separates the turbulent plume flow from the surroundings. The mixing process occurs through entrainment of fluid by large-scale eddies at the boundary and a rapid small-scale mixing across the central core (Turner 1973). The plume development, is influenced by the heat source conditions (location, geometry and strength) and the enclosure boundaries, as outlined in Figure 2.3.

The classic plume theory, its subsequent modifications and applications are based on the entrainment assumption relating, at any height, the rate of entrainment to the mean upward plume velocity by a constant of proportionality, referred to as the entrainment coefficient α (Taylor 1945, Batchelor 1954). The value of the entrainment coefficient has to be obtained experimentally and for different source geometries still remains a subject of an ongoing debate. For instance, Linden (2000) and Carazzo, Kaminski & Tait (2006) reviewed thoroughly values of entrainment coefficient extracted by previous authors. Figure 2.4 shows examples of values of entrainment coefficient for different source geometries. Horizontal sources (point, line) appear to induce plumes that have higher values of α than the vertical sources. The lower rate of entrainment for plumes induced by vertical sources can be caused by the deficit of the momentum flux (Hunt & Kaye, 2005) and the vertical source blocking the meandering plume motion that increases mixing in the free-developing plumes (Caudwell et al. 2016). For a given source geometry there is an obvious variability in values of α extracted from different experimental studies. These may be caused by differences between nozzle geometry, source conditions, experimental methods, analysis techniques and their accuracy.

2.1.2 Plume development from vertical sources

Plumes from vertical sources have recently gained attention due to their relevance to space heating and cooling. Hunt & Kaye (2005) modified the equations of Morton et al. (1956) to describe plumes from vertical line sources with a linear increase in the buoyancy flux with height. Their steady-state solutions implied that the plume growth results in a quadratic increase in the volume and momentum fluxes with height, thus indicating that the plume velocity is independent of height. These characteristics of plume growth are confirmed by Gladstone & Woods

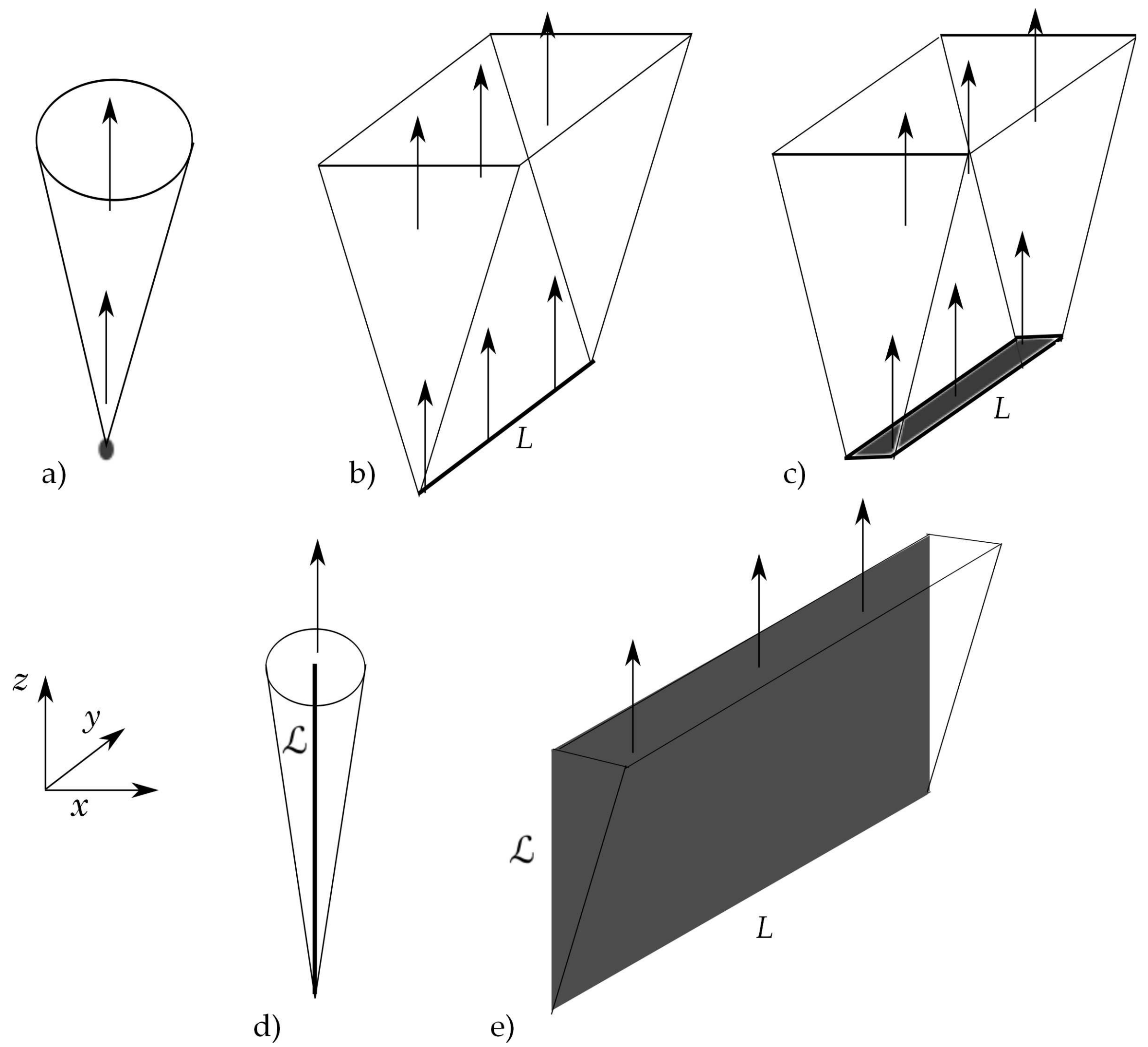

Figure 2.2: Schematics of the time-averaged outline of plumes (not to scale) originating from: a) a point source (Morton et al. 1956, Baines & Turner 1969, Baines 1975, Turner 1986, Cardoso & Woods 1993), b) a horizontal line source (Rouse et al. 1952, Baines & Turner 1969, Lee & Emmons 1961, Manins 1979, Yuana & Cox 1996), c) a horizontally-distributed source (Kaye & Hunt 2007, 2010), d) a vertical line source (Gladstone & Woods 2014), e) a vertically-distributed planar source (Cooper & Hunt 2010, Caudwell et al. 2016, McConnochie & Kerr 2016).

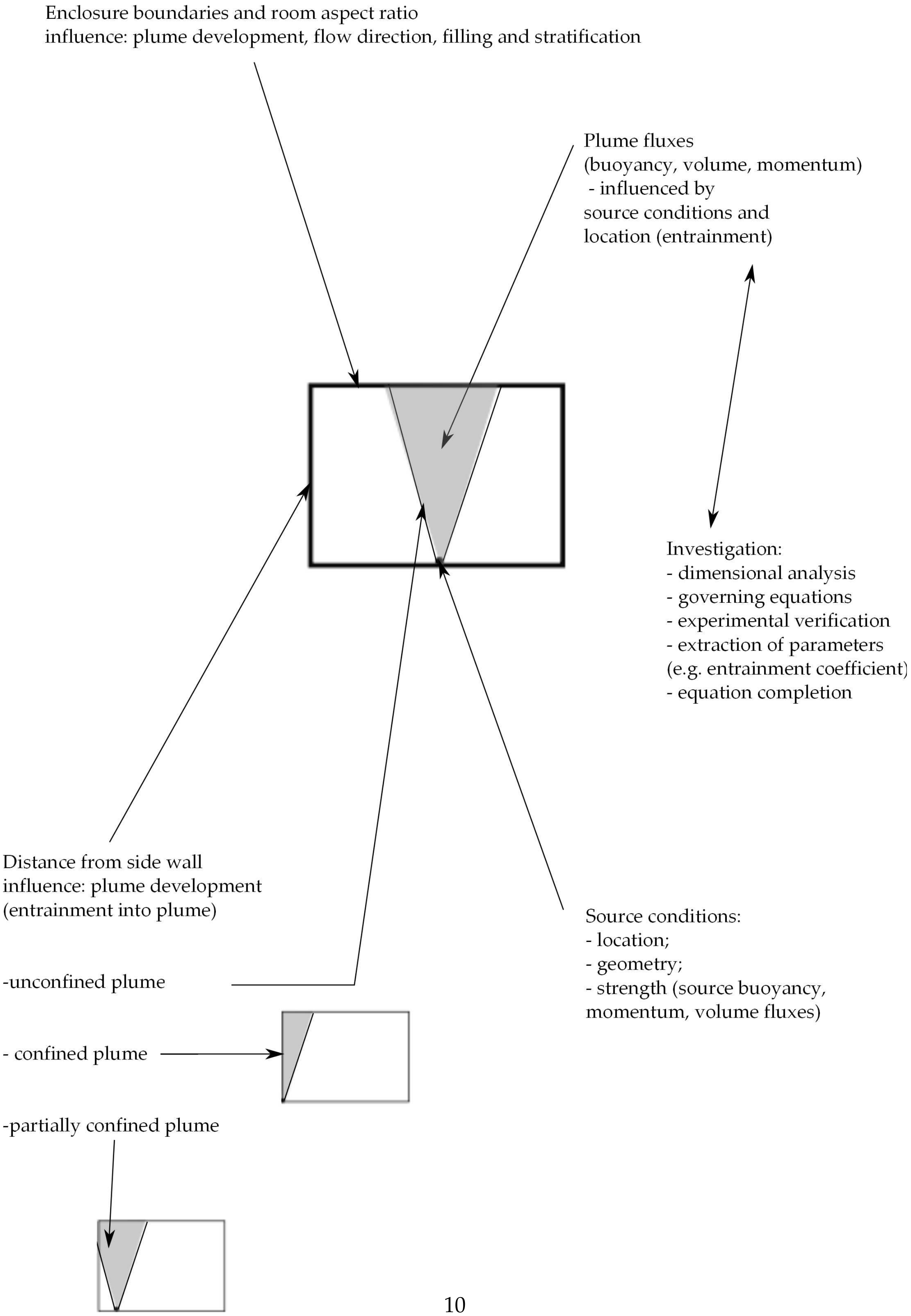

Figure 2.3: Factors considered during plume investigation and a basic outline of standard approach to investigate plumes.

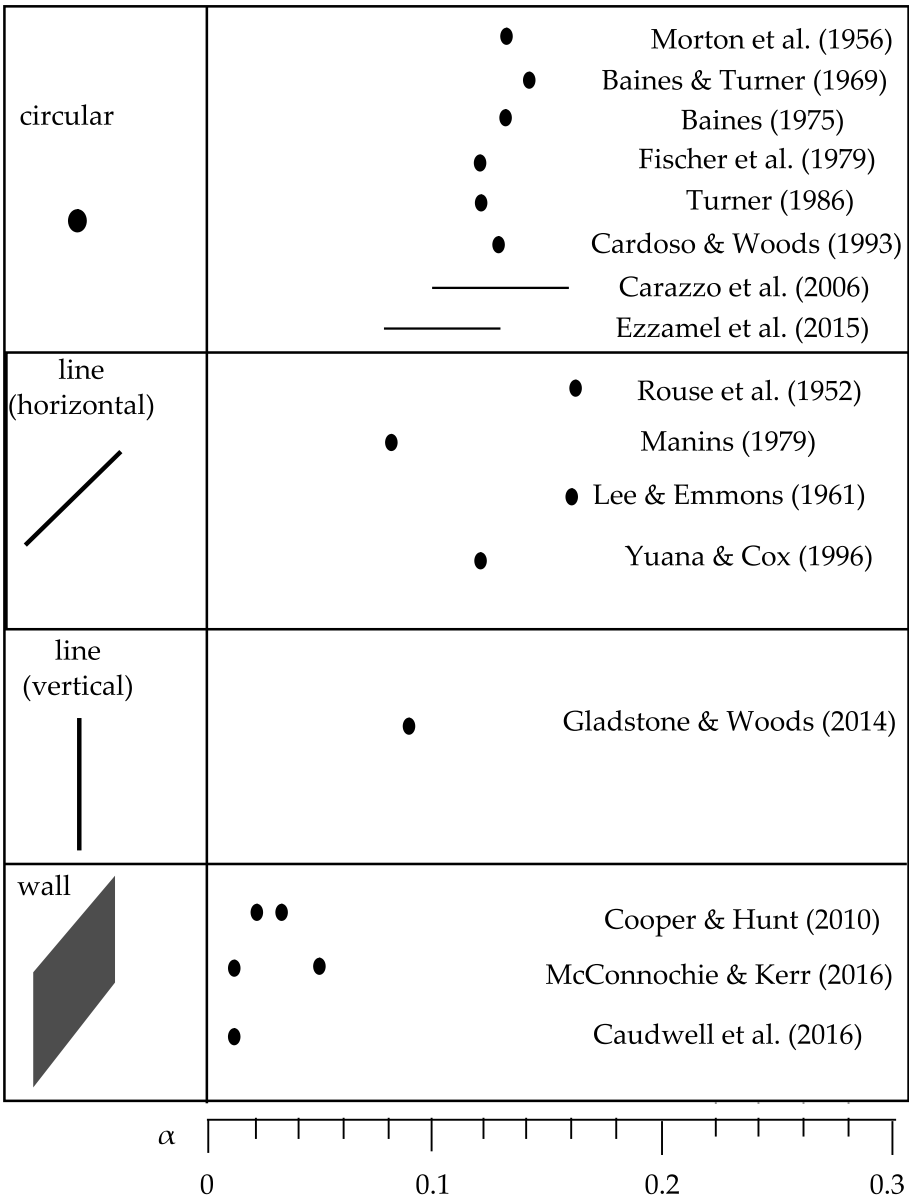

Figure 2.4: Examples of entrainment coefficient (top-hat values) for different source geometries.

(2014) theoretical model and validated by their experimental measurements. Cooper & Hunt (2010) and Caudwell et al. (2016) also modified the plume governing equations to represent the development of planar vertically-distributed sources in an unbounded environment (with no enclosure boundaries). Cooper & Hunt (2010) developed the model with a planar vertically-distributed source of constant buoyancy flux per unit area, whereas Caudwell, Flór & Negretti (2016) modified their model to investigate an isothermal wall, equivalent to a source of variable buoyancy flux per unit area. Their steady-state solutions indicated that the fluxes of volume and momentum of the planar vertically-distributed source have a weaker dependency on the height z than a vertical line source. The differences in the plume power-law behaviour appear to be justified by the differences in the plume growth, where the plume perimeter increases with height for a vertical line source and remains constant for a planar vertically-distributed source.

Experiments to obtain entrainment coefficients have been conducted. The set-ups included a heated wall in a tank of freshwater (Caudwell et al. 2016), a vertical ice wall dissolving into a homogeneous salty water (Kerr & McConnochie 2015, McConnochie & Kerr 2016) and a sintered plate producing an aerial vertically-distributed source of saline along one side wall of a tank of freshwater (Cooper & Hunt 2010). Cooper & Hunt (2010) estimated the entrainment coefficient $\alpha = 0.02$ from the position of the first front, which is a density step which separates the layer of dense saline from the ambient water. Cooper & Hunt (2010) suggested that the estimation of α from the position of the first front may be inaccurate due to discrepancies between the source conditions in the theoretical model and the experiments. In their theoretical model, the fully turbulent plume was induced by a uniform source of buoyancy flux and zero fluxes of volume and momentum. In their experiment, the plume transitioned from laminar to turbulent and the source effect was represented by adding saline to the system, thus producing non-zero volume flux. Additionally, in experiments of Cooper & Hunt (2010) the flow rate through the sintered plate was not uniform. To investigate the impact of these discrepancies, Cooper & Hunt (2010) used Germeles (1975) code to extract a value of α numerically with the laminar initial portion of the plume and the source conditions reflecting the experimental source conditions. The entrainment coefficient $\alpha = 0.03$ extracted numerically was comparable to the α-value from experiments. McConnochie & Kerr (2016) performed experiments to validate values of various coefficients of proportionality in solutions of Cooper & Hunt (2010). Initially, they estimated the entrainment coefficient of $\alpha = 0.014-0.017$ from the position of the first front. The smaller α by comparison in the results of McConnochie & Kerr (2016) can be attributed to the differences in buoyancy release, diffusive in the case of the ice wall and advective in the case of the sintered plate. McConnochie & Kerr (2016) measured the maximum plume velocity which followed the scaling of Cooper & Hunt (2010) and yielded $\alpha = 0.048$. Caudwell et al. (2016) also used velocity measurements to estimate values of α. They used Particle Image Velocimetry (PIV) to estimate the α-value for each time step and showed that the entrainment coefficient decreased, from 0.08 to 0.001, as the filling progressed. Caudwell et al. (2016) concluded that the reduction of the entrainment coefficient was caused by the development of the stratified layer in which the entrainment is smaller than in the ambient homogeneous region below the first front. Completing their theoretical solutions with variable α did not result in a significant improvement in agreement between the theoretical predictions and measurements.

Cooper & Hunt (2010) and Caudwell et al. (2016) also considered a time-dependent plume development in a sealed room. Figure 2.5 shows predictions of plume fluxes of volume and buoyancy as functions of height and time based on the solutions of Cooper & Hunt (2010) and Caudwell et al. (2016). Despite differences in source conditions, somewhat surprisingly, solutions of Cooper & Hunt (2010) and Caudwell et al. (2016) were similar. Both theoretical models predicted that at any time the plume development was also characterised by an increase in fluxes of volume and momentum with height but with a weaker dependency on the elevation than for a vertical line source. The plume buoyancy flux increased linearly in the unstratified region but decreased in the stratified region with a pronounced step change at first front. The time dependency was an important factor in the filling box modelling efforts as the plume was constantly modified in time by progressing stratification. The time-dependency was reflected at any given height with a decrease in time of all three plume fluxes, as well as plume width and velocity. Caudwell et al. (2016) were the first to use PIV and the temperature laser induced fluorescence method to evaluate plume development in filling-box-type experiments. Their experiments confirmed qualitative predictions of trends in the plume development. Quantitatively, however, there was a significant difference between theoretical predictions and experimental results. These discrepancies were not unexpected, as the filling box modelling approach was not designed to represent the plume development closely but to approximate plume development in a room. Caudwell et al. (2016) attempted to improve the agreement by modifying models to include laminar-turbulent plume transition and the variation of the entrainment coefficient. These modifications improved the description of stratification in lower regions corresponding to the laminar plume development. The results of McConnochie & Kerr (2016) also follow scalings of fluxes used for plumes induced by vertically-distributed planar sources. However, the velocities they measured were lower than Cooper & Hunt's (2010) predictions. McConnochie & Kerr (2016) attributed these discrepancies to the significant wall effect (viscous drag) that was assumed to be negligible by Cooper & Hunt (2010).

2.1.3 Plume development from horizontally-distributed sources

Unconfined plumes from long planar horizontally-distributed sources were first studied by Rouse, Yih & Humphreys (1952). They derived functional relationships to describe the mean flow development with height based on similarity considerations. Rouse et al. (1952) used their experimental measurements of velocity and temperature to complete and verify these relationships. Their results indicated that the plume expansion is linear with height, the plume velocity is independent of height and the plume temperature is inversely proportional to height. These conclusions allowed Rouse et al. (1952) to describe the plume bulk flow, whereby the plume expansion was characterised by a continuous increase with height of the fluxes of volume and momentum and a constant buoyancy flux with height. The work of Rouse et al. (1952) was followed by the work of Lee & Emmons (1961) which comprised the theoretical and experimental studies of a planar plume above a line fire. Lee & Emmons (1961) undertook the analogous modelling method to that developed by Morton et al. (1956) for axisymmetric plumes. Lee & Emmons (1961) adopted the entrainment model (Taylor 1945) and derived plume conservation equations describing the behaviour of plume fluxes. Lee & Emmons (1961) classified plume development into three categories based on the source Froude number Fr, a ratio of source inertia to buoyancy. Their results for $Fr = 1$ were in agreement with relationships derived by Rouse et al. (1952). Experimental results of Lee & Emmons (1961) matched their theoretical

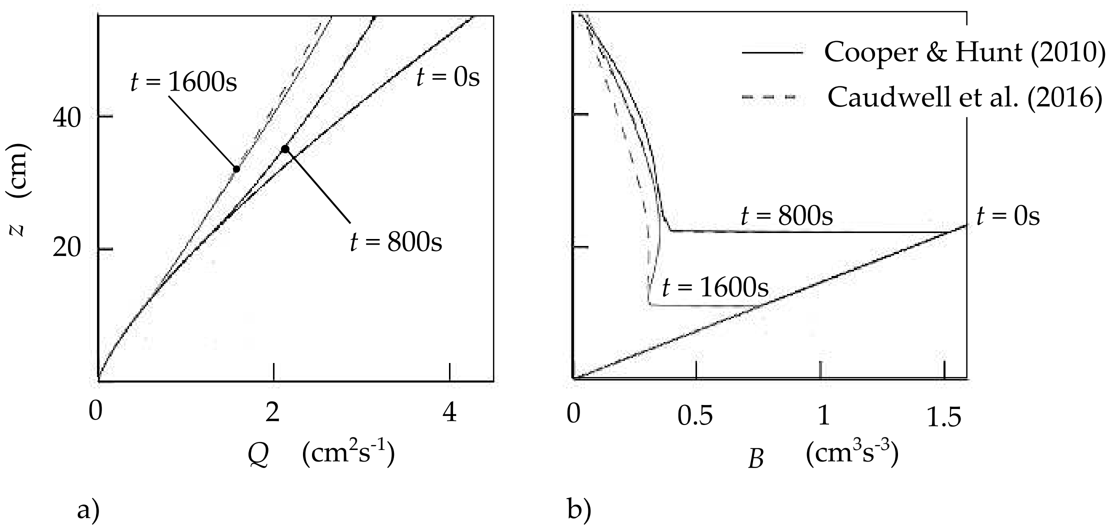

Figure 2.5: Predictions of plume development: a) plume volume flux, b) plume buoyancy flux. Comparison between the model with uniform source buoyancy flux of Cooper & Hunt (2010) and the model with isothermal wall of Caudwell et al. (2016). Figure adapted from Caudwell et al. (2016).

predictions. Both the velocity and temperature measurements were in agreement with the measurements of Rouse et al. (1952). Lee & Emmons (1961) also showed that a plume characterised by $Fr = 1$ corresponds to a balanced development of a bulk flow that plumes characterised by both ($Fr > 1$) and ($Fr < 1$) tend to with height. For $Fr > 1$, the self-regulation corresponds to a rapid plume development leading to a rapid velocity decrease, whereas for $Fr < 1$ a plume grows slowly, even contracts (Colomer et al. 1999, Friedl et al. 1999, and Epstein & Burelbach 2001), to increase a velocity. Van den Bremer & Hunt (2014) conducted another theoretical investigation of the two-dimensional planar plumes. They confirmed the predictions of Lee & Emmons (1961) and gained additional insights into the development of plumes tending to the balanced development. For $Fr < 1$, they indicated that a rapid entrainment occurs as the plume contracts, whereas for $Fr > 1$ they indicated a very slow transition to the balanced plume development.

2.1.4 Rate of filling

The initial room filling was traditionally described in terms of the descent of the first front (Baines & Turner 1969, Cooper & Hunt 2010). Figure 2.6 shows a classic schematic of the descent of the first front as assumed in the filling box model.

The filling box model consists of two interdependent filling flows, namely the rising plume and the descending first front leading to a growth of the warm layer. The term ‘first front’ refers to the interface between ambient air and heated region. Any additional, initial filling flows were neglected by assuming that upon impinging on the ceiling the plume created a horizontal intrusion where turbulent motions were suppressed instantly and the plume outflow created

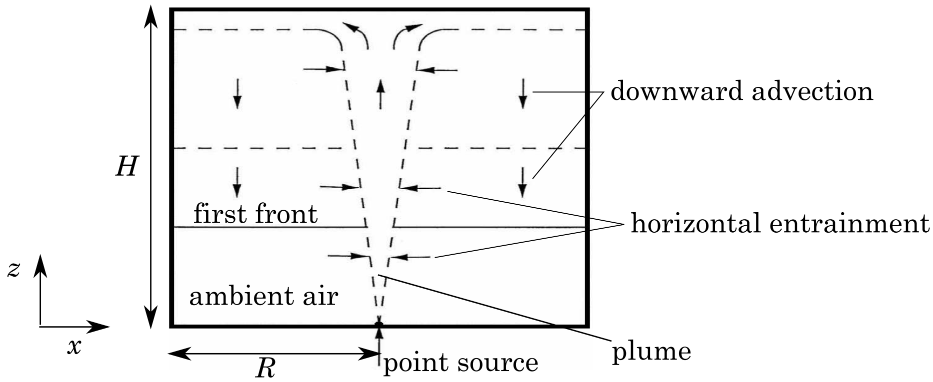

Figure 2.6: Schematic of the filling box model of Baines & Turner (1969) with arrows showing the flow direction of the plume, the environment and the entrainment. The position of the first front is marked at two times (continuous and dashed lines).

a layer of warm air that deepened in time. The validity of this assumption is discussed in Section 2.2. An expression for the position of the first front was attained from the volume conservation, provided that the plume volume flux in the unstratified region ahead of the first front was known (Baines & Turner 1969, Cooper & Hunt 2010). Since source conditions directly affect the plume development, the rate of filling is also a function of the source conditions. The key variables, essential to the discussion of the rate of filling in the context of different source geometries, are summarised in Table 2.1.

Source	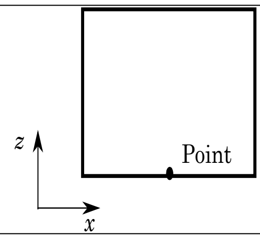	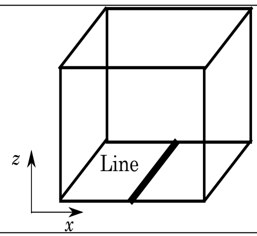	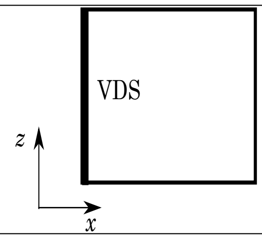
Authors	Baines & Turner	Baines & Turner	Cooper & Hunt
B	$B_0 \sim \left[\frac{L^4}{T^3}\right]$	$B_{L,0} \sim \left[\frac{L^3}{T^3}\right]$	$B_{a,0} \sim \left[\frac{L^2}{T^3}\right]$
Q	$Q = cB_0^{1/3}z^{5/3}$	$Q_L = c_L B_{L,0}^{1/3} z$	$Q_a = c_a B_{a,0}^{1/3} z^{4/3}$
$\mathcal{T}$	$\mathcal{T} = \frac{S}{cB_0^{1/3}H^{2/3}}$	$\mathcal{T}_L = \frac{S}{c_L B_{L,0}^{1/3} L}$	$\mathcal{T}_a = \frac{S}{c_a B_{a,0}^{1/3} H^{1/3} L}$
ζ	$\zeta = \left(\frac{2}{3}\tau + 1\right)^{-3/2}$	$\zeta = e^{-\tau}$	$\zeta = \left(\frac{1}{4}\left(\frac{4}{5}\right)^{1/3}\tau + 1\right)^{-3}$

Table 2.1: Buoyancy flux B, Volume flux Q, characteristic time scale $\mathcal{T}$ and non-dimensional position of the first front $\zeta = z/H$ as a function of non-dimensional time $\tau = t/\mathcal{T}$ for three source geometries.

Table 2.1 shows the dimensions of the buoyancy flux, volume flux, the characteristic time scale and the non-dimensional position of the first front for a point source, a line source and a vertically distributed source (VDS), respectively. Each source is assumed to be within an identical rectangular room of cross-sectional area S and height H. The lengths of a line source and VDS are denoted as L. These three geometries were selected due to their particular relevance to convectors: a point source being a benchmark all the results are compared to, a VDS corresponding to a side wall of a convector and a line source being a possible representation of a plume development in the far field above a convector. Based on the research of Baines & Turner (1969) and Cooper & Hunt (2010), the rate of filling depends on the strength (expressed as the source buoyancy flux B_0), geometry of the buoyancy source (by influencing the entrainment coefficient) and the size of a room. In the filling box with a point source, the rate of filling is a function of height H, the cross-sectional area S, the source buoyancy flux B_0 and the coefficient of proportionality, a function of the entrainment coefficient, c (Baines & Turner 1969). Upon rewriting timescales of the filling box with a line source and a VDS as functions of the source buoyancy flux B_0, the rate of filling in these two cases is a function of the length of the source L, the cross-sectional area S, the source buoyancy flux B_0 and the corresponding coefficient of proportionality c_L (Baines & Turner 1969) or c_a (Cooper & Hunt 2010), respectively. The resulting formulations fit subsequent experimental observations, which indicates that the source geometry influences the rate of room filling. This also appears to be confirmed through comparison of the rates of filling as functions of time. The slowest filling is induced by a VDS, extended from $z = 0$ to $z = H$. A line source is shown to induce faster filling than a point source despite its entirely unrestricted entrainment. By contrast, the strength of the stratification increases with decreasing entrainment. Hence, the slowest filling from a VDS leads to the strongest stratification.

The theoretical predictions of filling rates have been validated by experimental results (Baines & Turner 1969, Cooper & Hunt 2010, McConnochie & Kerr 2016, Caudwell et al. 2016). The theoretical predictions were a good representation of the entire initial filling period for a range of room aspect ratios (see Section 2.2). Baines & Turner (1969) suggested that the two-dimensional plumes are more likely to have large-scale mixing during initial filling. Caudwell et al. (2016) showed that initially there was a significant mixing between the ambient and the front developing in the upper region which became negligible after a stable layer was formed. After the formation of the layer, the mixing was limited to the entrainment of the ambient into the rising plume. Filling during this period was accurately predicted by the filling box model of Cooper & Hunt (2010). Therefore, even in cases when the initial filling is affected by the room boundaries, the actual descent of the first front, after its formation, can be predicted using models.

2.1.5 Stratification

The assumptions of the filling box model imply the immediate development of stable stratification due to the omission of any side wall effects. The filling box model also assumes that, as the filling continues, an increasing portion of the warm layer re-entrains into the plume, hence invariably the warmest air at any instance is the air arriving at the ceiling. Baines & Turner (1969) did not solve the general time-dependent development of stratification. Instead, they described the stratification at large times, when the entire internal environment has at some stage been entrained into the plume. The stratification was calculated by assuming that the temperature distribution with height is fixed in shape in time and there is a linear increase in temperature across the entire height. A numerical procedure to model the evolution of stratification in the filling box at earlier times was developed by Germeles (1975). Worster & Huppert (1983) obtained the approximate analytical solution which is proportional to the solution of Baines & Turner (1969). They based their solution on the assumption that in the unstratified region the plume strength is constant and there is a linear increase in the plume strength in the stratified region above the first front. To validate their solution Worster & Huppert (1983) used a similar approach to Germeles (1975) and their numerical solution was in agreement with the approximate solution.

While the original filling box modelled a heat supply from a steady point source of constant strength located in the centre of a room, the stratification for different source conditions has since been investigated. Germeles (1975) concluded that the same filling box model can be used to describe filling from an off-centred point source when it is away from the side wall such that the plume development is unrestricted. For cases where source is too close to the side wall to avoid interference, Germeles (1975) stated that reduced values of the entrainment coefficient should be used. Killworth & Turner (1982) investigated the effects of cyclic variations of the source strength. They concluded that even though the filling pattern changes in time, due to fluctuations in the source strength, the stable stratification is similar to that of a source of constant strength. Wong & Griffiths (1999) modified the filling box to include multiple well-separated plumes from point sources. From volume conservation, dividing source strength evenly among multiple sources leads to faster advection of the first front. In the case of uneven source strengths, Wong & Griffiths (1999) found that the plume from the strongest source governs the evolution of stratification. Using a case with two sources of unequal strengths as an example, Wong & Griffiths (1999) showed that for any division of source strength, the stable stratification produced by the sources of unequal strengths is similar to the stable stratification from a single point source with the combined source strength. Cooper & Hunt (2010) showed that qualitatively the stratification from a vertically distributed source develops in much the same manner as from a point source, from the initial descent of the first front to the asymptotic state which is achieved when vertical velocities within the entire system tend to zero. Predictions of stratification profiles of Caudwell et al. (2016) were reduced in the stratified region to indicate lower final temperatures compared to Cooper & Hunt's (2010) predictions, see Figure 2.7. The temperature profile in the stratified layer is sensitive to differences in source conditions between the two models. Both models are in reasonable agreement with experiments (Cooper & Hunt 2010, Gladstone & Woods 2014, McConnochie & Kerr 2016, Caudwell et al. 2016). Experiments suggested, however, an approximately linear increase in temperature with height in the stratified region and a continuous temperature profile across the first front, instead of the predicted step change and a non-linear buoyancy profile in the stratified layer (McConnochie & Kerr 2016, Cooper & Hunt 2010). McConnochie & Kerr (2016) suggested that the reason for this discrepancy is due to omitting detrainment in models.

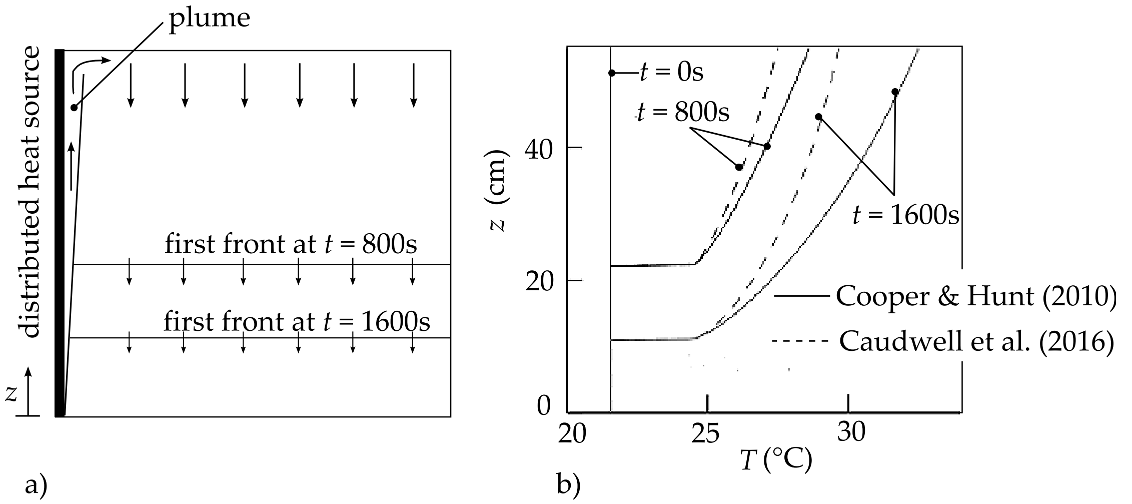

Figure 2.7: Predictions of stratification based on the Cooper & Hunt (2010) and Caudwell et al. (2016): a) development of stratification in a room with a distributed heat source (adapted from Cooper & Hunt 2010), b) ambient temperature profiles as function of time (Caudwell et al. 2016).

2.2 Confinement

There are two aspects to consider in the context of confinement of a room: the location of the heat source relative to the side walls and the room aspect ratio. The location of the buoyancy source directly influences the plume development, whereas the aspect ratio influences initial filling either instantaneously leading to the classic layering as described by Baines & Turner (1969) or the initial large scale mixing prior to the development of stable stratification.

A convector is often a portable device and depending on its location a plume above may develop freely or either partially or entirely along a side wall. Ellison & Turner (1959) modelled wall plumes in a laboratory using saline solutions. Their measurements indicated that the entrainment into wall line plumes is substantially lower than that of unconfined line plumes. Grella & Faeth (1975) performed experiments with wall line plumes from a line gas burner. They showed that the expressions used to predict the development of the unrestrained plume from a horizontal line source may be applied to describe the wall-bounded plume, provided that a smaller entrainment coefficient is applied to account for no entrainment on the wall side. The value of the entrainment coefficient extracted from their experiments is, however, less than half the value for the unrestrained line plume. Grella & Faeth (1975) suggested that unrestrained plumes may entrain additional ambient fluid through the large-scale swaying motion which is absent in restrained plumes. The reduced entrainment, as opposed to the skin-friction coefficient of the wall, was shown to have a major influence on the local flow properties (fluxes). In cases, of partially free and partially restricted development, Germeles (1975) suggested reducing the entrainment coefficient from the impingement onwards.

The aspect ratio of the box determines the extent of any side wall vertical intrusions into the plume outflow. Experimental evidence suggests that there are three basic patterns of filling

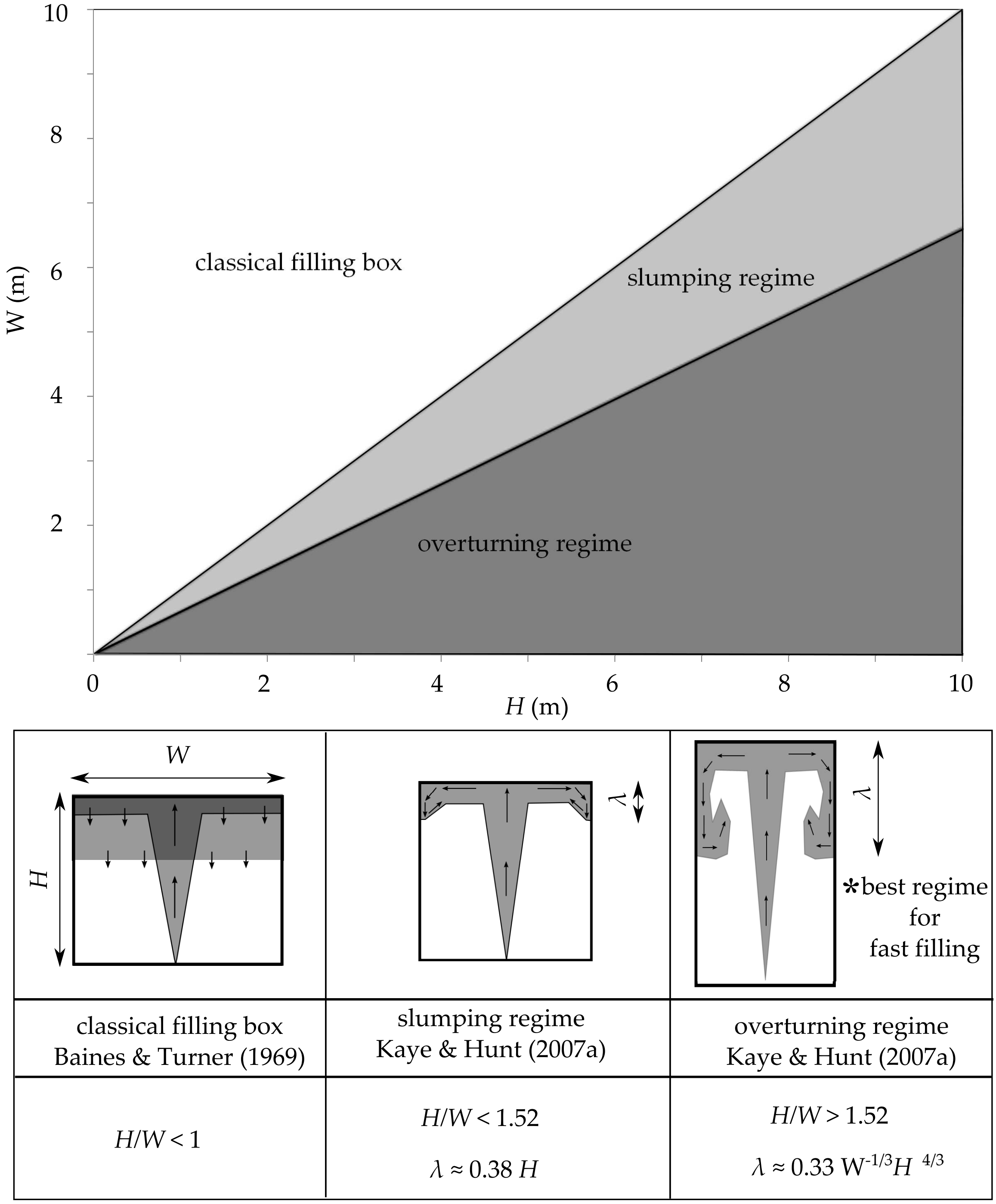

Figure 2.8: Pattern of filling as a function of room aspect ratio.

that may occur: 'layering' without any significant side wall vertical intrusions (Baines & Turner 1969), 'slumping' where limited side wall intrusions are observed in the early transients (Kaye & Hunt 2007a) and large-scale 'overturning' often observed in the early transients (Kaye & Hunt 2007a, Caudwell et al. 2016). Figure 2.8 shows a simplified nomogram which allows the estimation of the pattern of filling as a function of the room height H and the room width W for a point source. The nomogram and the corresponding schematics are based on the research of Baines & Turner (1969) and Kaye & Hunt (2007a). Baines & Turner (1969) observed that during the filling box experiments with a point source in wide boxes, where $H/W < 1$, there are hardly any vertical intrusions upon the impingement of the plume outflow on the side walls. This observation led them to restrict the application of their idealised filling box model to boxes with aspect ratios such that $H/W < 1$. Manins (1979) considered the requirements for the application of Baines & Turner's filling box model. He showed that because the filling is driven primarily by advection and not diffusivity, the Rayleigh number[1] has to be large (tending to infinity) in order for the model to be valid. In turn, Kaye & Hunt (2007a) investigated the physics of vertical intrusions along the side wall in a filling box with a point source. They modelled the plume outflow in two parts: a radial gravity current and a vertical intrusion against the side wall. They showed that the maximum penetration depth of the vertical intrusion depends on the room aspect ratio. Kaye & Hunt (2007a) gave scalings of penetration depth λ for tall (where $H/W > 1.52$) and short (where $H/W < 1.52$) rooms. In tall rooms, the horizontal current (the plume outflow) is not fully developed upon impingement on the side wall, hence the penetration depth of the vertical intrusion is proportional to $(W/H)^{-1/3}$ and overturning flows occur. Kaye & Hunt (2007a) described overturning as a 'rolling' flow that propagates towards the plume. In short rooms, the horizontal current (plume outflow) is fully developed upon impingement and the penetration depth of the vertical intrusion is a function of room height H only. Large-scale overturning does not occur, but instead a slumping flow can occur, which does not engulf additional ambient fluid, as the overturning flow does, but create waves on the interface of the first front (Kaye & Hunt 2007a). Subsequently, Kaye & Hunt (2007b) considered the influence of room shape and source location on the vertical penetration of side wall intrusions. They indicated that vertical penetrations are restricted, both in the case of a rectangular sectioned room and for a decentralised buoyancy source. Consequent time lags in the plume outflow reaching different sections of the ceiling perimeter cause the flow to advect along the wall and prevent immediate reflection towards a source as occurs in a cylindrical room with a source in the centre. Also, the system asymmetry caused by non-centrally located sources is expected to result in an additional overturning in the direction of the closest wall and a reduced overturning in the opposite direction (Kaye & Hunt 2007b). In a follow-up study, the influence of room geometry on the rate of filling, in the context of overturning flows due to a room fire, was explained by Giannakopoulos et al. (2013). They showed that at large times, the rate of filling in taller rooms is faster than in shorter rooms. To investigate the upper limits of the aspect ratios, Barnett (1991) conducted experiments for large aspect ratios (up to $H/W \approx 27$). Barnett established that for large aspect ratios, the counterflow in the ambient environment affects the plume development and finally breaks down the plume flow for $H/W \approx 5.8$. While vertical intrusions along side walls in the filling box with a point source have recently received considerable attention, vertical intrusions from other source geometries remain widely unex-

[1] The Rayleigh number, defined in eq.(4.1), is a dimensionless parameter, which expresses the balance between the driving buoyancy force and the two diffusive processes which retard the convective flow, see Section 4.2.2 for reference.

plored. Based on the previous research, however, there is no doubt that vertical intrusions have the potential of increasing the rate of filling.

Caudwell et al. (2016) observed, using PIV and temperature laser induced fluorescence methods, rapid buoyancy-driven filling induced by a heated wall in a tank of freshwater at early transient times: the starting plume, the horizontal current, the side-wall vertical intrusions and the reflections (secondary horizontal currents) of the front until the wavy interface is established. Their work demonstrated the usefulness of PIV to gain an understanding of mixing mechanisms which can affect filling and which are otherwise undetected using standard visual experimental methods. The sequence of these flows is shown in Figure 2.9. Wong et al. (2001) found that whilst the internal gravity waves (shearing motions) significantly influence the horizontal velocity field, they have minor/no influence on the stratification. They concluded that the horizontal plume outflow at the base causes the formation of shearing motions. Their experiments confirmed that the shearing motions affect horizontal outflows of weaker plumes at intermediate depths such that weak outflows are forced to propagate with the internal wave in which they are spreading.

2.3 Efficiency of filling

Efficiency of filling is a term that refers to using less energy input to achieve the same end-effect, expressed in terms of the rate of filling and stratification. In a discussion on energy efficiency, Patterson (1996) noticed that while there is no universal measure of efficiency, generic indicators can be used to quantify any changes in parameters influencing the efficiency. He also stated that not enough attention is given to define indicators and to ensure their successful application. Tanaka (2008) reviewed different methods to measure energy efficiency performance ranging from absolute energy performance to thermal efficiency. He emphasised the importance of proposing reliable, feasible and verifiable indicators. Tanaka (2008) concluded that there is no ideal method to assess energy efficiency. Instead, the assessment method should be adjusted to fit individual application and purposes.

2.3.1 Occupant-response-driven evaluation and temperature set-points

One method of evaluating energy efficiency of filling is by understanding the occupants response to thermal conditions imposed by design conditions, such as temperature set points. Van Treeck (2011) provides a comprehensive review of occupant-response-driven assessment methods in the context of engineering practice. Heating can be assessed based on the occupants' response to thermal conditions, including their health, well-being and physical activity. There are a large number of variables affecting the occupants' perception of thermal conditions, including activity level, clothing, air temperature, humidity, air velocity and radiation (Fanger 1972, Jones 2002). Fanger (1972) developed a model to assess occupants' satisfaction (the predicted mean vote, PMV) with the thermal environment. Fanger (1972) used statistical methods to relate the physiological responses of large number of people to their perception of thermal sensation. Subsequently Fanger (1977) suggested that local thermal conditions (i.e.

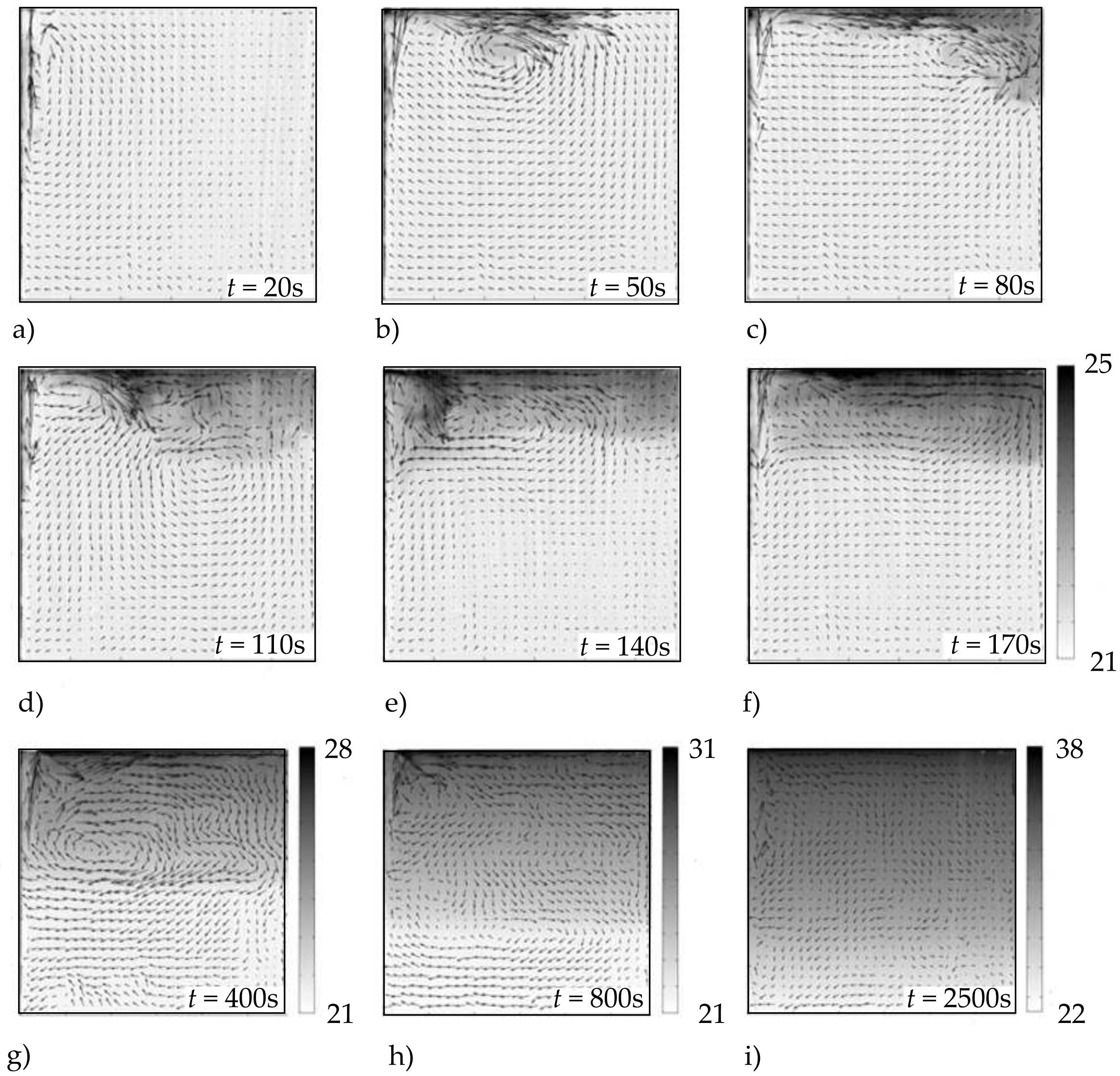

Figure 2.9: Filling flows recorded during small-scale experiments using PIV and temperature laser induced fluorescence methods: a) starting plume, b) horizontal current, c) vertical intrusion, d) overturning, e) reflection, f)-i) descent of the first front. Grey shading represents temperature field (grey levels to indicate temperature in °C) and arrows to indicate the velocity field. Replicated from Caudwell et al. (2016).

vertical temperature gradients, Olesen et al. 1979) should also be accounted for in the analysis. In practice, thermal conditions are often expressed in terms of temperature, instead of PMV (d'Ambrosio Alfano et al. 2014). Currently, the two widely-applied thermal comfort standards BS EN 7730 and ASHRAE 55 are based on Fanger's model. In the context of filling efficiency, both standards are useful to inform a design (i.e., temperature set points), however, they do not provide any indication of the energy efficiency of delivery of thermal comfort through filling.

2.3.2 Performance-driven evaluation

The general trend towards reducing carbon footprint and energy demand for heating drives initiatives of governing bodies aimed at prioritising energy efficiency (e.g. European Directive for Energy Performance of Buildings, EPBD, Directive 2010/31/EU). Typically building energy simulation tools do not enable detailed modelling of heating systems (Maivel & Kurnitski 2014). To establish performance-driven evaluation of strategies involving buoyancy-driven flows, Coffey & Hunt (2007a) developed indicators to quantify the buoyancy accumulated globally and locally, at any height of interest, relative to the benchmark case (Coffey & Hunt 2007b), see Table 2.2. Their performance indicators assess the efficiency of buoyancy-driven ventilation but similar concepts might also apply to buoyancy-driven heating. The global indicator E is the ratio of the total buoyancy $B(t)$ concentrated within a room over a time interval δt and the cumulative buoyancy in a sealed room, B_i, over the same time interval δt. The cumulative buoyancy represents the thermal gains in a room, where a buoyancy source releases the same (maximum) amount of heat B_i at every instant and after δt, there is $B_i \cdot \delta t$ accumulated within the room. The indicator E is therefore used to evaluate how efficient buoyancy removal is over a time interval δt. Note that E is in the range 0 to 1, where $E = 0$ corresponds to the sealed room and $E = 1$ is reached when all excess heat is removed from the room instantaneously at $t = 0$. This time-averaged indicator compares the actual ability of the system to flush buoyancy from a room with benchmark conditions corresponding to the maximum buoyancy gains. Coffey & Hunt (2007a) also developed a local measure $[E(\delta t)]_{h_1}^{h_2}$, which allows a local evaluation of buoyancy accumulation within any given layer over a time interval δt to detect regions with either buoyancy deficiency or excess compared to the room average.

Range	Period	Symbol	Equation
global	time- averaged	E	$1 - \dfrac{\int_0^{\delta t} B(t)\,\mathrm{d}t}{B_i \cdot \delta t}$
local	time-averaged	$[E(\delta t)]_{h_1}^{h_2}$	$1 - \dfrac{1}{\delta t}\int_0^{\delta t} [\mathbf{B(t)}]_{h_1}^{h_2}\,\mathrm{d}t$

Table 2.2: Indicators developed by Coffey & Hunt (2007a,b).

2.4 Summary

The literature review has established that, while there is no holistic study on convector-induced flows, a significant body of research has been conducted on buoyancy-driven flows. Existing theoretical models, developed and validated experimentally, can be used to predict the plume development driven by buoyancy sources of simple geometries, i.e., point, line and wall. It has also been shown that the filling box model combined with physical modelling in the laboratory can be quite successful in describing the buoyancy-driven filling rate and stratification. Using different plume models to inform the filling box model, hence leads to reasonable predictions of filling rate and stratification induced by these simple buoyancy sources. Thus, it is hoped that a similar approach for the convector-induced flow could give a useful insight into the filling mechanisms in heated rooms.

Unlike in previous studies on vertical heat sources, where the investigation stopped at the trailing edge of the source, this investigation of the convector-induced filling will be limited by the room boundaries only. Since the bulk flow from a convector is expected to be fully-turbulent, consideration of turbulent buoyancy-driven plume flows with varying source conditions in the near and far field enables insight into the rate of room filling and the stratification that develops.

There is an obvious lack of knowledge of the fundamental mechanisms that drive convector-induced flows. Questions arise with regard to the governing parameters that may either strengthen or weaken the rate of filling and stratification. By understanding what governs convector-induced filling, one could potentially be able to control and adjust the efficiency of filling. To evaluate efficiency of convector-induced filling, there is a necessity to define a performance indicator suitable to the application, potentially based on Coffey & Hunt's (2007a) indicators.

Transient convector-induced filling has not been investigated and the mechanisms governing the interplay between filling and developing stratification have not been described either. In order to attempt a holistic description of the flows induced by a convector, there is a necessity to address these gaps.

Chapter 3

Aim and objectives

3.1 Aim and objectives of thesis

The ultimate goal of this thesis is to provide a deep understanding of filling and stratification induced by a convector, in order to heat rooms rapidly and effectively.

To reach this goal the following five objectives are identified:

1. To specify the governing parameters of convector-induced flows based on the literature review and a dimensional analysis.
2. To investigate the influence of these governing parameters on the rate of filling and the stratification by conducting small-scale experiments.
3. To investigate if convector-induced filling flows may be simplified to two-dimensional flows or if they have additional complexity.
4. To develop a strategy for evaluating the efficiency of filling flows.
5. To apply newly-developed strategy and to propose set of guidelines aimed at improving the performance of convector-room systems.

3.2 Approach

There is a wide range of possible shapes of rooms and convectors. In this thesis a basic case of a rectangular room with a rectangular convector is investigated. Figure 3.1 shows an example of a system configuration, such that the convector is located above the floor and away from the wall. The focus of the investigation is on the buoyancy distribution induced by a convector only, thus a room envelope (ceiling, walls, floor) is considered to be adiabatic and any external (to the room) disturbances are negligible. The experimental set-up has to be thus carefully developed to ensure the accuracy of the convector-room system modelling.

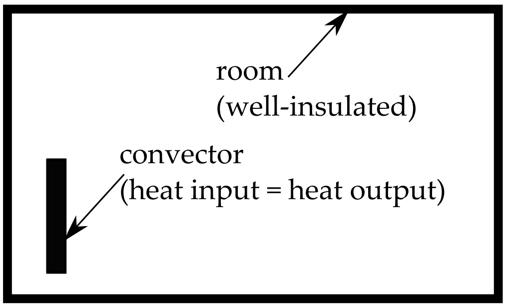

Figure 3.1: Research problem: filling flows in a two-component system consisting of a room and a convector (in elevation).

Buoyancy-driven flows cannot be accurately modelled in air at small scale due to increased viscous effects leading to dynamic dissimilarity with the full-scale application. In air, experiments have to be performed at the full scale, which can be limiting and costly. In the 1990s, at the University of Cambridge, a new small-scale experimental technique using saline-in-water has been established and has been successfully used since (e.g. Linden et al. 1990, Cooper & Hunt 2010). The small-scale in water models enable flow visualisation for evaluation of filling rates and for evaluation of thermal stratification, measurements of the velocities and the salt concentrations, where the latter is the counterpart of the thermal distribution. Crucially, the small-scale filling flows in water and the full-scale filling flows in air approximate dynamic similarity and so the results can be readily scaled to make qualitative and quantitative predictions of the full-scale flows. Approximate dynamic similarity is achieved by ensuring that the Rayleigh number is very large (well above $> 10^9$) in both cases. To ensure that the laboratory physics reflect the full-scale convector-room application, a constant fluid volume in the tank is maintained and the system net flow (inflows and outflows) during saline-in-water experiments are closely controlled.

Chapter 4

Experimental design and methods

The experimental facility is designed to physically model, at a small-scale, a typical domestic room with a typical domestic convector. An example is shown in Figure 4.1.

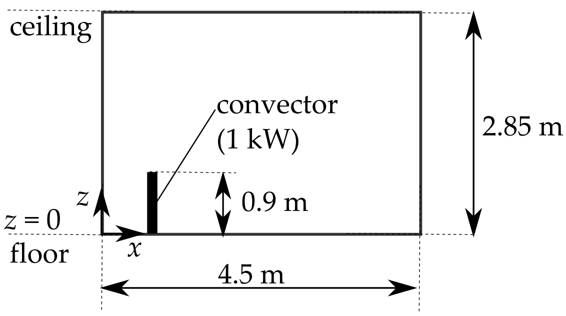

Figure 4.1: Application (schematic in elevation): a typical domestic room (4.5 m × 3 m × 2.85 m) with a typical domestic convector of 1kW strength.

4.1 Vertical reference frame

The experimental arrangement is designed to model filling flows in a room heated by a convector. In a cool environment, less dense, warm air rises and fills a room from the ceiling in a downward direction. During the experiments, saline solutions at room temperature are released in a tank of fresh water at the same temperature. In contrast to a thermal heat-air case, in saline-water experiments, saline solution, being denser than fresh water, descends and fills the tank from the bottom in an upward direction (Baines & Turner 1969). As a result, the vertical reference frame between heat-air and saline-water cases is reversed. Figure 4.2 shows a comparison between vertical reference frames of these two cases, where the origin $z = 0$ is set at floor level in heat-air cases and at the maximum water level for the laboratory experiments. The reversal of reference frame could be avoided by reversing fluids in experiments. A saline-in-water case could be changed into a water-in-saline case, where stained water would be released into a tank of saline solution. This reversal would, however, significantly increase the cost of experiments and waste.

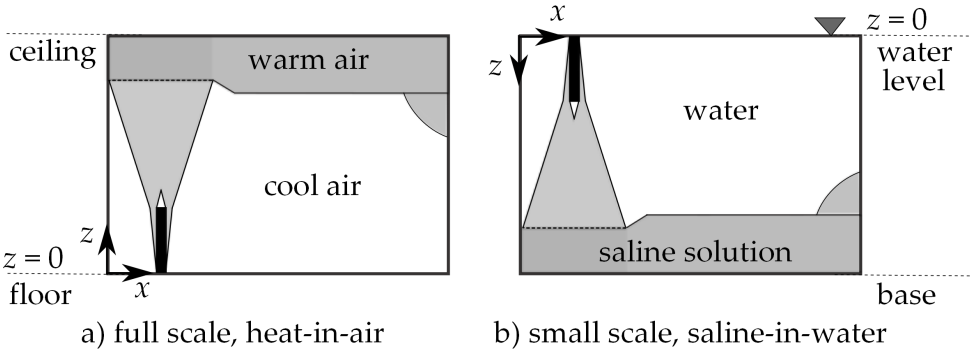

Figure 4.2: Vertical reference frames for a) room heating and b) laboratory experiments.

4.2 Similarity

According to Bradshaw (1970), in fluid mechanics, experimental results can be representative of flows at different scales or even in different fluids, provided that the two systems under consideration are similar without qualification. To share similarity without qualification, the two systems must be geometrically, kinematically and dynamically similar (Munson 1990). Requirements of dynamic similarity are the most restrictive and guarantee geometric and kinematic similarities. Similarity without qualification is, thus, in fact equivalent to dynamic similarity. The filling flows during buoyancy-driven convection could not be modelled physically at small scales in air due to larger viscous effects, which would result in a dynamic dissimilarity between full-scale and small-scale systems. To achieve approximate dynamic similarity, small-scale physical modelling in water was performed. The use of a saline solution, instead of heat, in water-based experiments also provided clear flow visualisation of transient flows (Linden et al. 1990, Cooper & Hunt 2010). In the text below arguments are outlined to show that the two systems considered in this study, namely the small-scale experiment in water with saline solution and the corresponding full-scale convection from a convector in air, approximate dynamic similarity.

4.2.1 Geometric similarity

Geometric similarity between two systems has two requirements. Firstly, the two systems must have the same shape. Secondly, the ratios between the characteristic lengths of these systems should be constant. These two requirements are met for a single room aspect ratio and convector geometry. The reasons for selecting the system geometry are laid out in in Chapter 3. Each system, as shown in Figure 4.3, consists of two elements: a room and a convector operating within this room. Geometries of these elements are: a box-shaped room of width W, length Y and height H and a box-shaped convector of length L, height $\mathcal{L}$ and width d.

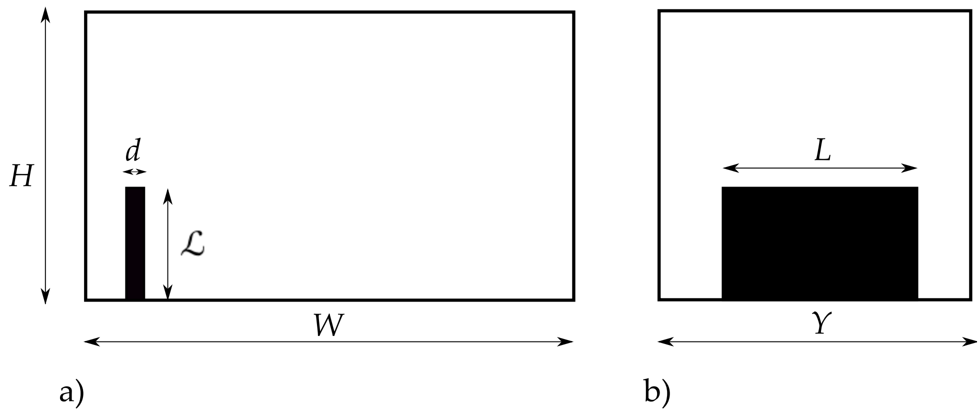

Figure 4.3: System geometry with lengths of a room and a convector in a) a front elevation and b) a side elevation of a room. The system is shown in the vertical reference frame of heat-in-air application.

4.2.2 Dynamic similarity

Two systems approach dynamic similarity when the corresponding forces, which act on fluid particles and boundary surfaces, are of the same order of magnitude. Previous studies of buoyancy-driven convection from heated surfaces (Zierep 1972, Turner 1973, Hibberd & Sawford 1994) identified the dimensionless Rayleigh number as the governing parameter characterising buoyancy-driven convection. The Rayleigh number *Ra* may be expressed as:

$$Ra = \frac{g'\mathcal{L}^3}{\nu D}, \tag{4.1}$$

where g' is the buoyancy, $\mathcal{L}$ is the height of the convector, ν is the kinematic viscosity and D is the thermal diffusivity (Turner 1973). The buoyancy g', a measure of excess heat driving the flow, is defined as:

$$g' = \frac{\Delta\rho}{\rho_0} g \tag{4.2}$$

where g denotes acceleration due to gravity, ρ_0 is a reference density and $\Delta\rho$ is a difference between a density ρ of buoyant fluid and a reference density ρ_0 (Coffey & Hunt 2007a). It is assumed that air in an enclosure behaves as an ideal gas and density differences are caused only by temperature differences. The reduced gravity may be therefore rewritten as:

$$g' = -\frac{\Delta T}{T_0} g \tag{4.3}$$

where ΔT and T_0 denote the corresponding temperature difference and a reference temperature, respectively (Coffey & Hunt 2007a).

The Rayleigh number, as defined in (4.1), expresses the balance between the driving buoyancy force and the two diffusive processes which retard the convective flow. For low *Ra*, the convective flow is laminar and it undergoes transition into turbulent flow at higher Ra. As the values of Ra increase, the flow is amplifying disturbances, until Ra reaches the critical value of approximately 10^9 and the flow becomes fully turbulent (Rogers & Mayhew 1994). The Rayleigh number is thus used to determine how disorderly buoyancy-driven convective flows are (Rogers & Mayhew 1994).

Comparison of dynamic similarity scales

In order to have a better idea of the type of flow regime expected, the Rayleigh numbers anticipated in full scale and model scale (1:3) are approximated based on the assumptions outlined in Table 4.1.

Variable	Units	Small scale	Full scale
$H = H_*$	cm	95	285
$\mathcal{L} = \mathcal{L}_*$	cm	30	90
$W = W_*$	cm	150	450
$L = L_*$	cm	60	180
$d = d_*$	cm	5	15
$g' = g'_*$	cm s^{-2}	27	81
$B_0 = B_{0,*}$	cm^4 s^{-3}	1350	4050
ν	cm^{2}s^{-1}	$\approx 10^{-2}$	$\approx 10^{-1}$
D	cm^{2}s^{-1}	$\approx 10^{-5}$	$\approx 10^{-1}$

Table 4.1: List of values of variables in the reference case at both scales.

The full-scale system considered consists of a room of height 285 cm with a convector of height 90 cm and a temperature difference between the convector surface and ambient environment of 24 °C, where the temperature of the ambient environment is set at 20 °C prior to heating. The room is rescaled using a 1:3 scale model of room height 95 cm and the model convector of height 30 cm. The density difference between the saline solution and water, both at 20 °C (room temperature), is 0.028 gcm^{-3}. Herein, the full scale is denoted by the subscript f and the small scale by the subscript m. The following values for constants are used in the estimation of the Rayleigh numbers: gravitational acceleration $g \approx 10^3$ cms^{-2}; kinematic viscosities $\nu_f \approx 10^{-1}$ cm^{2}s^{-1} and $\nu_m \approx 10^{-2}$ cm^{2}s^{-1}; diffusivities $D_f \approx 10^{-1}$ cm^{2}s^{-1} and $D_{s,m} \approx 10^{-5}$ cm^{2}s^{-1}. Using equations (4.2) and (4.3), the buoyancies are calculated as: $g'_m \approx 27$ cms^{-2} and $g'_f \approx 81$ cms^{-2}. Thus, equation (4.1) gives the Rayleigh numbers in the room as $Ra_f \approx 10^{11}$ and $Ra_m \approx 10^{14}$. The flows characterised by very high magnitudes (10^{10} and above) of Rayleigh number are fully turbulent and, moreover, independent of any subsequent increase in the Rayleigh number (Niemela et al. 2000). Thus, an approximation of dynamic similarity between the small-scale buoyancy driven saline convection in water and the full-scale buoyancy driven convection from a heated surface in air seems reasonable.

4.2.3 Kinematic similarity

Kinematic similarity is guaranteed when two systems share geometric and dynamic similarity (Munson 1990). In other words, when the characteristic lengthscales and the balance of the forces are similar, the flow velocities in these systems are also similar. This is also represented by the velocity scaling $\sqrt{g'l}$, where l is a characteristic lengthscale (Linden et al. 1990). The velocity fields of two systems are similar, when the ratios of the corresponding velocity components are constant. The small-scale experiment in water and the case of full-scale convection in air share geometric and approximate dynamic similarity, hence by definition they are also kinematically similar. As a result, velocity vector fields, which were extracted from PIV data in this research, can also provide information on the flows in the full scale in a heated room. Figure 4.4 depicts three regions within the heated room with different types of motion: a plume region, a buoyant layer region and an ambient environment.

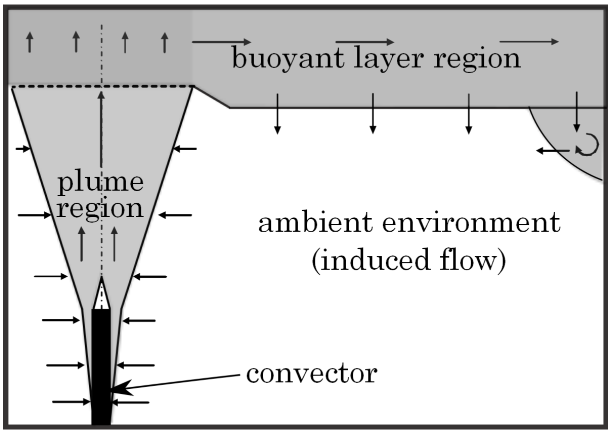

Figure 4.4: Three characteristic regions where different filling flows are observed: the plume region, where the plume flow develops along both sides of the convector and above the convector; the buoyant layer region which advects at a filling rate that depends on the plume volume flux; and the ambient environment in which flows are induced as a result of the plume flow.

4.3 Conversion of small-scale results to full-scale application

In order to convert the results obtained during a small-scale water-tank experiment to the relevant full-scale heat-in-air case, ratios of length and buoyancy between the two scales can be used.

4.3.1 Scaling of length

The dimensionless quantity that results from the scaling of characteristic lengths, denoted as LS, may be expressed as:

$$LS = \frac{l_m}{l_f}, \tag{4.4}$$

where l denotes a length symbol.

4.3.2 Scaling of buoyancy

The dimensionless quantity that results from the scaling of buoyancy, denoted as BS and defined as:

$$BS = \frac{g'_m}{g'_f}, \tag{4.5}$$

is used as a means to compare the source strengths and the developing stratifications at both scales.

4.3.3 Scaling relationships

Nomographs to enable fast conversion between the small-scale results and the full-scale application are enclosed in Appendix C.

4.4 Experimental conditions

Experiments were conducted under controlled and repeatable conditions. The use of measuring instruments, e.g. rotameters, conductivity probes and conductivity meter, results in systematic errors in experimental observations (Taylor 1997). To reduce systematic errors and to estimate random errors, repeat runs were performed. Taylor (1997) explained that random errors are due to unknown and unpredictable changes in the experiment. Precise quantification of errors will be in Sections 4.5.1.7, 4.5.3.9, 4.5.4.5. Averaging data over $\mathcal{N}$ runs reduces the standard error of the mean by $\frac{1}{\sqrt{\mathcal{N}}}$ (Peters 2001, Pitt Ford 2013, Stevens 2015). Typically in this work, five repeat runs were conducted to follow the position of the first front and every density data point was averaged over 10 conductivity measurements, which reduces the random error by approximately 0.45 and 0.32, respectively. Regular calibrations of measuring equipment were performed (e.g. salinity probes were calibrated before each experiment) and independent measuring techniques were used (volume flow rate, density) to control systematic errors.

4.4.1 Experimental set-up

Small-scale experiments were conducted in the Fluid Mechanics Laboratory at the Department of Engineering, University of Cambridge. A schematic of the tank facility is shown in Figure 4.5.

The glass tank has an internal cross-sectional area of 150 cm × 100 cm and a height of 100 cm. The tank was filled with fresh water. The water-air interface represents the floor of the room. The aspect ratio:

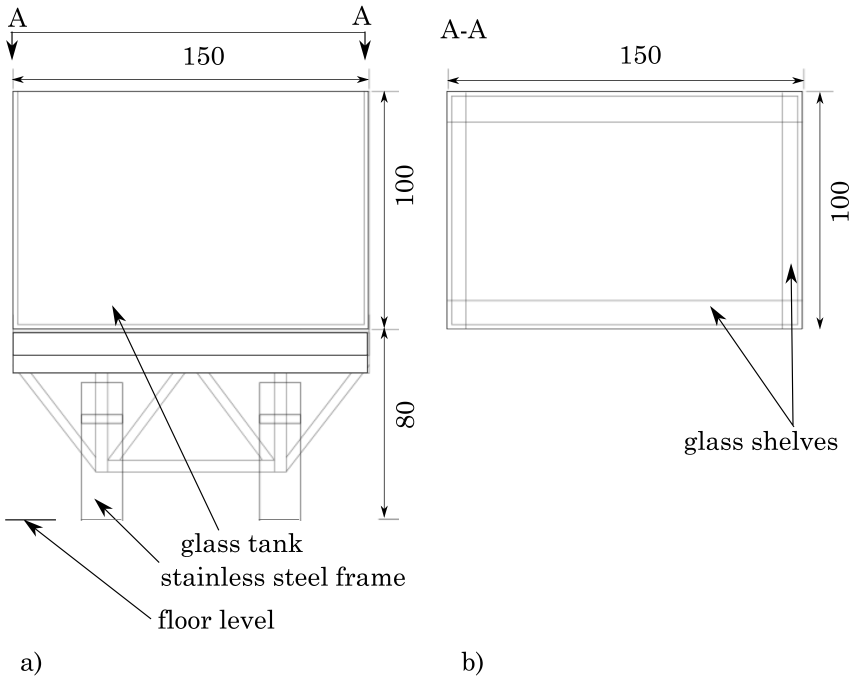

Figure 4.5: Schematic of tank facility with dimensions (in cm): a) the elevation b) the plan view.

$$Æ = H/R \tag{4.6}$$

(where $R = W - a - 1/2d$ is the characteristic horizontal length and a denotes a horizontal distance from the closest side wall to the point A, see Figure 4.6) of the model room was changed by varying the water depth and the location of the convector model. Distances between the leading (top) and trailing (bottom) edges of the convector and the base of the tank are H and $H - \mathcal{L}$, respectively. The position of the convector is defined by a point A, where the x-coordinate defines the horizontal position of the convector and the z-coordinate its vertical position, see Figure 4.6. Horizontal and vertical positions of the convector in each experiment are listed in Tables A.1 and A.2 in Appendix A, together with the source conditions and aspect ratios Æ. In the result chapters variables defining system configuration (lengths, convector strength and position) are expressed in terms of the reference values outlined in Table 4.1.

The model convector, shown in Figure 4.7, was designed to be analogous to a standard household convector. It was designed by Professor Gary Hunt and Peter Holland (ServoRad) prior to the beginning of the project. The dimensions of the model convector are 60 cm (length), 30 cm (height), 5 cm (width). The convector consists of a stainless steel frame of dimensions 60 cm × 30 cm × 5 cm and two sintered stainless steel side plates, approximately 0.5 cm thick with pore sizes in the range 5-40 μm. The pore size of the sintered plates was selected to enhance uniformity of saline distribution across each plate and to ensure relatively low pressure losses. To generate a more uniform saline distribution and to avoid time lags in saline supply the interior of the device was filled with glass marbles and filter foam sponges.

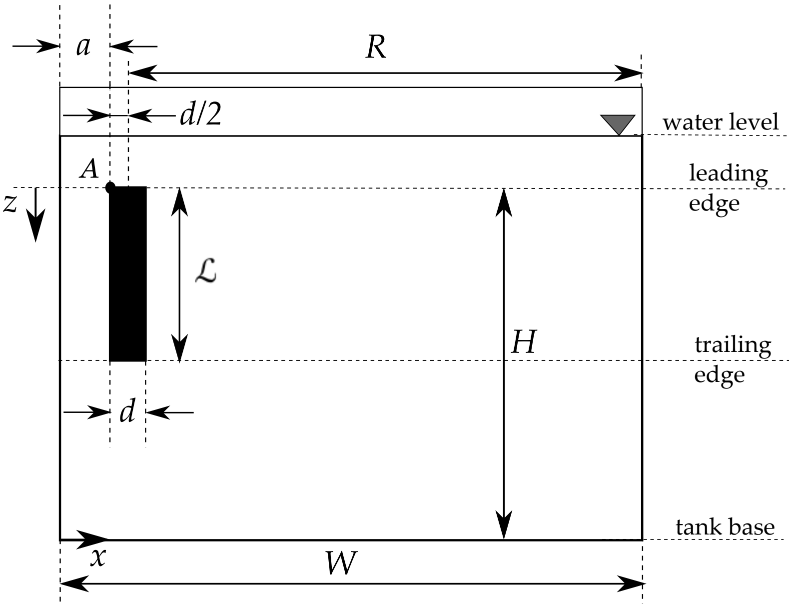

Figure 4.6: Basic geometry of the experiment with characteristic lengths and levels. The system geometry is presented in the vertical reference frame of the experiment. The distance between the water surface and $z = 0$ is in the range 1 to 3 cm.

Figure 4.8 presents the experimental set-up schematically. For further description see Appendix B. The convector was suspended in the tank a few centimetres below the water surface (position typical for domestic convectors). In this thesis, two different convector orientations are investigated. These are a horizontal and vertical orientation, respectively. The horizontal orientation refers to the convector height 30 cm ($\mathcal{L}/\mathcal{L}_* = 1$), whereas the vertical orientation corresponds to the convector height 60 cm ($\mathcal{L}/\mathcal{L}_* = 2$). For a given tank size and a convector size, this means that a change in convector orientation results in changes in the ratios of the convector length L to the tank length Y and the relative heights of both far and near fields in the context of the tank aspect ratio. The orientation and hence relative position of the convector to the boundaries may have an influence on the flow observed. The convector horizontal orientation is treated as a baseline case.

The model was located at various positions within the tank. Saline solution was supplied to the convector from a reservoir via a submersible 240V saltwater pump at volume flow rates $\dot{Q}_0$ in the range 12.5 cm^{3}s^{-1} to 67.0 cm^{3}s^{-1} (range dictated by rig capability and model convector construction). To ensure a uniform saline supply to the model convector, the saline level was maintained in the saline reservoir (i.e. constant pressure head). Two independent flow meters were used to measure volume flow rates during the experiment: an Apollo LowFlo Flowmeter (accuracy of ±1% of full scale) coupled with a Contrec 202 Digital Totaliser (accuracy of 0.05% of full scale) and a Cole-Parmer Valved Acrylic Flowmeter (accuracy of ±5% of full scale). The latter was also used to regulate the flow rate as it had a control valve for control of the volume flow rate.

Fluid was continuously removed from the tank during each experiment via an overflow

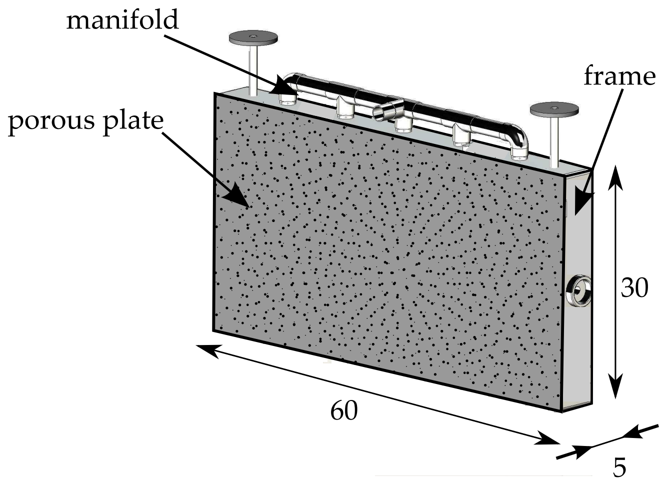

Figure 4.7: Schematic of convector used during experiments (dimensions in cm). When in horizontal orientation (as shown above) the model convector was suspended on two threaded rods. When in vertical orientation ($\mathcal{L}$ = 60cm), the model convector was suspended on one central threaded rod. In both cases the convector was aligned vertically.

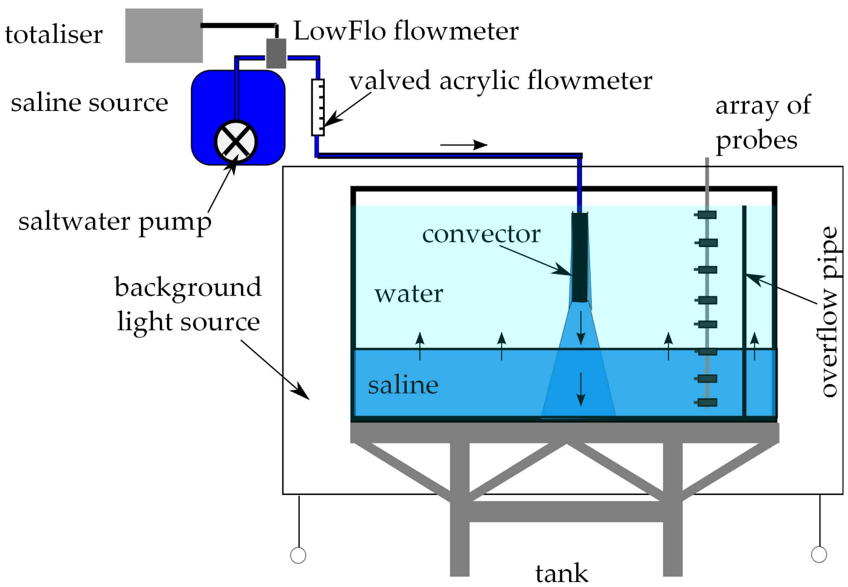

Figure 4.8: Schematic of equipment layout for a filling box experiment (in elevation), arranged for: the dye-attenuation technique and the multiple-point conductivity measurements.

pipe (with the outlet at the top edge of the pipe) so that the water depth, and thus the volume V_{tank}, remained constant. Before each experiment, two properties of the saline solution and the water were measured: density, using an Anton Paar DMA 5000 Densitometer (to an accuracy of 5×10^{-6} gcm $^{-3}$), and temperature, using a Fisher Scientific Traceable Digital Thermometer (to an accuracy of 0.05 °C). The density measurements prior to each experiments were performed to ensure the saline source was not stratified and to record the initial (prior to experiment) densities of the saline source and the water. The temperature measurements were taken to ensure that the temperature difference between the saline and the water was less than the critical value set at ± 1K to ensure the accuracy of the conductivity measurements, see Section 4.5.4. During experiments, measurements of density were taken using ServoRad conductivity probes connected to a ServoRad Conductivity Meter. SalAnalyser25 software, developed to control the conductivity probes, was used to calibrate the system and record data. The chosen location of the probes depended on the depth H and the location of the convector. A maximum of 25 probes was used during an experiment.

4.4.2 Flow control - expected performance of the rig

In small-scale experiments, the constant fluid volume in the tank (mixture of saline solution and water) and the significantly smaller portion of the supplied saline solution compared to the entrained fluid into the plume are crucial to ensure the laboratory physics (saline solution supplied to the tank of freshwater) reflect the full-scale application (room heating induced by a convector). To ensure that the experimental rig operates under conditions meeting these requirements, two aspects of flow control are considered when designing/setting the experiment: a) the net flow of the system referring to the balance of the inflows into the system $\dot{Q}_0$ (in cm^{3}s^{-1}) and the outflows from the system $\dot{Q}_{dr}$ (in cm^{3}s^{-1}), and b) the breakdown of the filling flows into the flow supplied to the system, corresponding to the source volume flux Q_0 (in cm^{2}s^{-1}), and the flow entrained, due to the density difference between the saline inflow and water, in the near field Q_a (in cm^{2}s^{-1}) and the far field Q_L (in cm^{2}s^{-1}).

To ensure a constant water level during the experiments, an overflow pipe was installed in the tank. Prior to each experiment, the tank was filled to the top edge of the outflow pipe. At the beginning of each experiment, the drain valve was opened and the supply pump switched on. The volume flow rate drained $\dot{Q}_{dr}$ was equal to the volume flow rate supplied at a steady rate $\dot{Q}_0$ for the duration of each experiment, see Figure 4.9. The influence of the system configuration was investigated through experiments with different tank aspect ratios, where the height H and the convector position were varied. The room height was varied by using different lengths of the outflow pipe. These modifications in the room aspect ratio changed the volume of fluids kept constant in the tank V_{tank}. The smaller volume V_{tank} resulted in a bigger relative influence of the saline volume supplied on the rate of filling. The volume of saline supplied to the system may be expressed as $V_{sup} = \dot{Q}_0 t$, where t denotes the duration of the experiment. The relative influence of the supplied saline volume V_{sup} may be defined as the ratio $\mathcal{R}_{exp} = V_{sup}/V_{tank}$. With no previous guidance on the maximum acceptable value of the ratio $\mathcal{R}_{exp}$, the critical value is set at $\mathcal{R}_{exp} = 0.2$ to maintain a low inflow into the system, while observing all the crucial periods of the development of stratification. Setting the critical value $\mathcal{R}_{exp}$ allows the estimation of the maximum permissible duration of each experiment, as a function of the volume of fluids and the volume flow rate supplied, $t = 0.2V_{tank}/\dot{Q}_0$. Depending on the experimental conditions the maximum permissible duration of each experiment varies between 500 s and 6000 s.

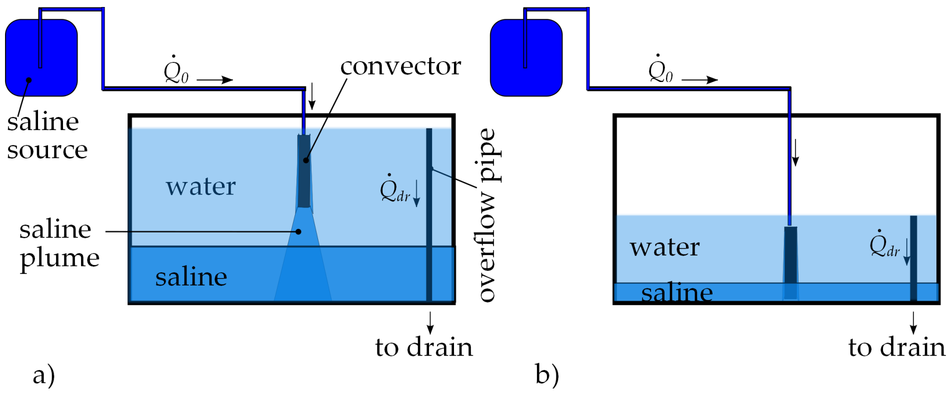

Figure 4.9: Schematics of the saline-in-water experiments (in elevation) showing the net flow of each system for two cases: a) the maximum room height H = 95 cm and b) the minimum room height H = 30 cm.

Preliminary calculations are performed to determine the performance of the rig and to set the acceptable source conditions (buoyancy fluxes and volume fluxes) which ensure that the supplied flow is negligible compared to the entrained flow. The predicted breakdown of the filling flows into the supplied and entrained is considered in two cases: a) the plume development in the unstratified environment and b) the ascent of the first front. These are considered in the near and far field of the convector. Figure 4.10 shows two schematics of plume development as expected in an experiment (a) and as used to estimate the ratio of the volume fluxes supplied and entrained (b).

Simplifications are applied in the preliminary calculations. The width of the convector is assumed to be negligible. Therefore, two plumes are assumed to merge into one upon detachment from the trailing edge (TE) of the convector. It is also assumed that the plume development below the trailing edge is that of a plume developing from a virtual origin of a line source of buoyancy flux only and zero source volume and momentum flux. The location of the virtual origin is estimated using expressions derived by Van den Bremer & Hunt (2014) and also used by Lynch (2012). The coordinates of the virtual origin are $(0, \mathcal{L} - z^*)$, where the horizontal coordinate $x = 0$ denotes the convector's axis and the vertical coordinate $\mathcal{L} - z^* = 0.66\,\mathcal{L}$, where $\mathcal{L}$ denotes the convector's height.

The volume flux entrained in the near field is estimated using solutions derived by Cooper & Hunt (2010), for a convector of strength $B_0 = 2\left(\frac{B_a}{2}\mathcal{L}\right)$ and an evenly distributed buoyancy on both side plates. The volume flux per unit of height of one side of the plate (cm^{2}s^{-1}) is:

$$Q_a = \frac{3}{4}\left(\frac{4}{5}\right)^{1/3} \alpha_a^{2/3}\left(\frac{B_a}{2}\right)^{1/3} z^{4/3} \tag{4.7}$$

where α_a denotes the 'top-hat' entrainment coefficient for a plume developing adjacent to a vertical buoyancy source ($\alpha_a = 0.03$, Cooper & Hunt 2010), B_a is the buoyancy flux per unit area

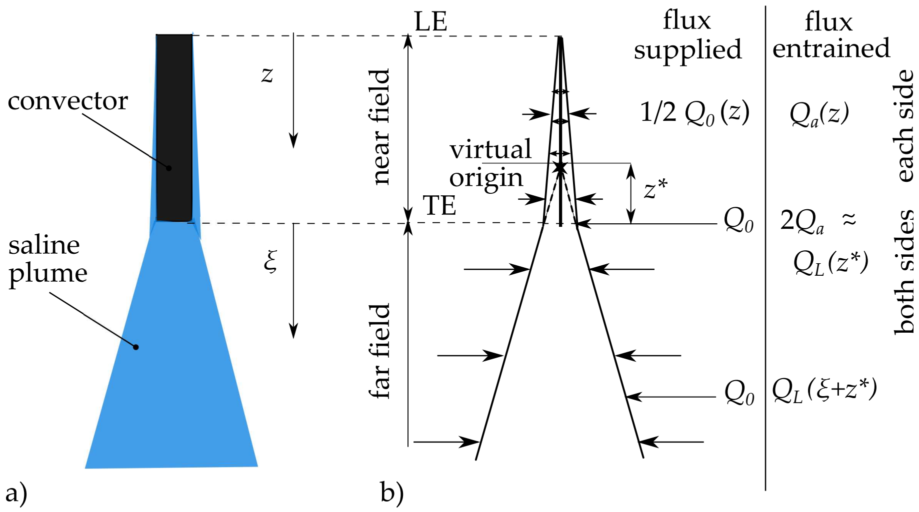

Figure 4.10: Volume fluxes in the near field and in the far field of the experiment: a) a schematic of the saline plume developing from the convector (not to scale), b) a schematic of the saline plume development used to estimate the volume fluxes supplied and entrained in the near and far field.

and z is the vertical distance from the origin. The volume flux in the near field is estimated for $0 \leq z \leq \mathcal{L}$.

With the position of the source virtual origin z^* defined, the volume flux entrained in the far field, above the convector, is estimated, based on the similarity solution for the virtual plume given by Lee & Emmons (1961). It was expressed, in terms of the buoyancy flux per unit length $B_L = B_0/L$, as:

$$Q_L = (2\alpha_L)^{2/3} B_L^{1/3} (\xi + z^*) \tag{4.8}$$

where α_L denotes the 'top-hat' entrainment coefficient of the unconfined plume ($\alpha_L = 0.23$, Lee & Emmons 1961) and ξ denotes the vertical distance from the trailing edge.

To evaluate the influence of the fluxes supplied and entrained two source conditions are used, namely: a) the source buoyancy flux $B_0 = 180$ cm^{4}s^{-3} and the supply volume flux $Q_0 = 0.21$ cm^{2}s^{-1}, b) the source buoyancy flux $B_0 = 1800$ cm^{4}s^{-3} and the supply volume flux $Q_0 = 0.83$ cm^{2}s^{-1}. These source buoyancy fluxes have been selected to account for the full range of source strengths that will be used during experiments. The volume flux supplied Q_0 is assumed to be split equally between the two sides of convector and to be uniformly distributed with height. The influence of the volume fluxes supplied and entrained in the near and far field is assessed on the basis of two dimensionless ratios $\mathcal{R}_1$ and $\mathcal{R}_2$. The first ratio $\mathcal{R}_1 = (1/2Q_0(z))/Q_a \times 100\%$ is used to estimate the fluxes along one of the sides of convector. The second ratio $\mathcal{R}_2 = Q_0/Q_L(\xi + z^*) \times 100\%$ is used to estimate the far field influence. Figure 4.11 shows the predicted values.

A continuous descending trend of ratios $\mathcal{R}$ is predicted with a distance z from the leading

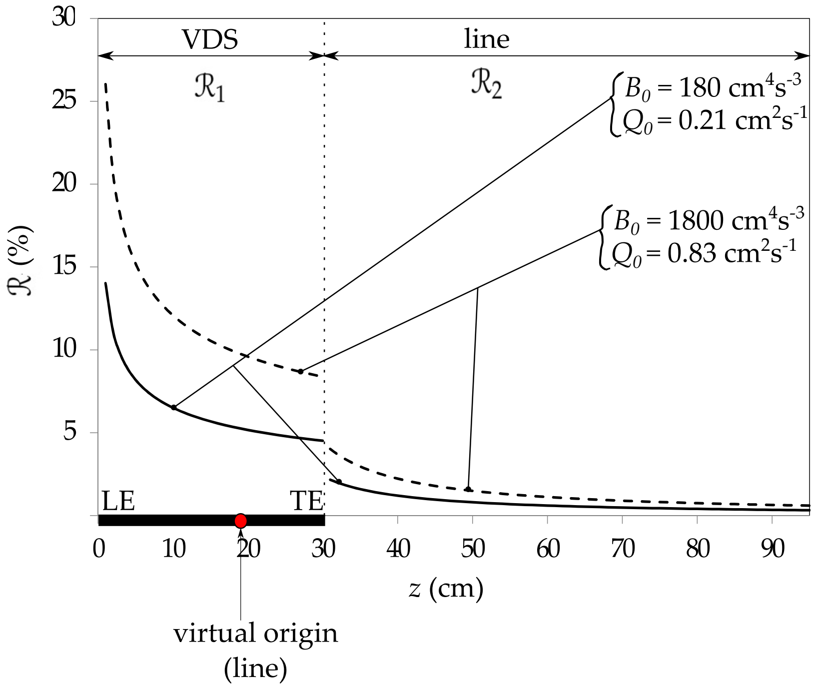

Figure 4.11: Dimensionless ratios $\mathcal{R}_1$ and $\mathcal{R}_2$ as functions of the vertical distance z, in range 0 cm (leading edge of convector, LE) to 30 cm (trailing edge, TE), in the near field and the vertical distance ξ in the far field, in the range 30 cm to 95 cm (tank base), corrected by $z^* = 10.2$ cm. Ratios $\mathcal{R}_1$ and $\mathcal{R}_2$ are used to predict the influence of non-zero source volume flux (supplied) on the plume development.

edge of convector. This indicates that the influence of the volume flux, on the plume development, decreases with height. The significant step change at the trailing edge is caused by the way the estimation of the flux entrained in the far field is set with the virtual origin correction.

The expected impact of the supply volume flux Q_0 on the rate of filling in the buoyant layer region is estimated from a third ratio $\mathcal{R}_3 = h_{sup}/(H - h_{ent})$, where $H = 95$ cm is the tank height from the base to the leading edge of convector, $h_{sup} = V_{sup}/S$ is the predicted depth of the layer due to the saline supply and $(H - h_{ent})$ is the predicted depth of the layer due to entrainment. The layer depth due to entrainment is calculated by applying volume conservation to the buoyant layer and using equations (4.7) and (4.8), respectively. Figure 4.12 shows the ratio $\mathcal{R}_3$ as function of time t for the same two cases used to estimate ratios $\mathcal{R}_1$ and $\mathcal{R}_2$. The expected values of the third ratio $\mathcal{R}_3$ increase with time due to the expected continuous supply of the saline.

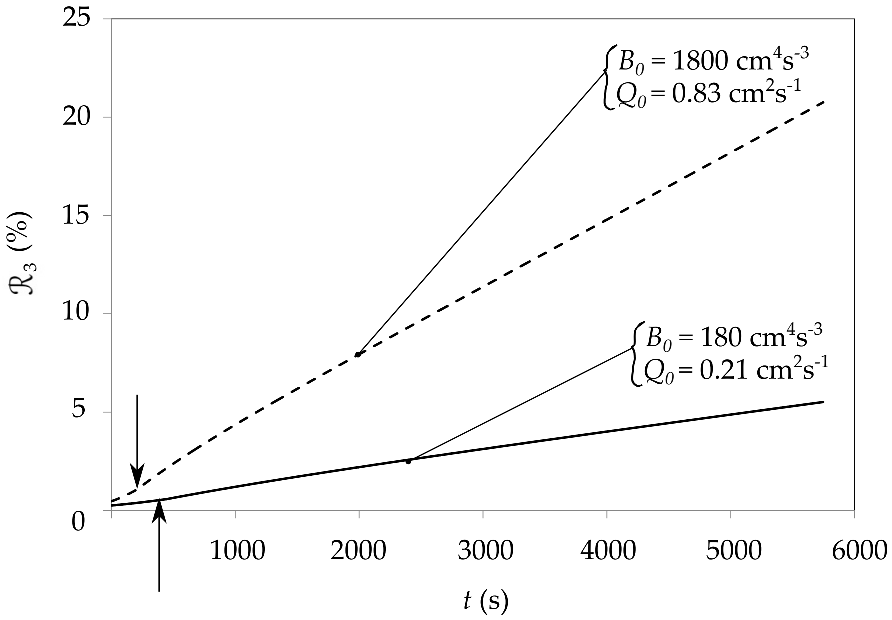

Figure 4.12: Rate of filling estimated from values of the ratio $\mathcal{R}$ as function of time. Arrows indicate reaching the trailing edge of the convector.

4.4.3 Comment on the flow structure

For the model convector $\mathcal{L} = 30$ cm, based on eq. (2.1), transition to turbulence is expected to complete at $z \simeq 3$ cm and thus most of the convector flow is assumed to be turbulent. Figure 4.13 confirms that the structure of the flow developing on the sintered surface is fully turbulent for the entire extent of the model convector and below the trailing edge.

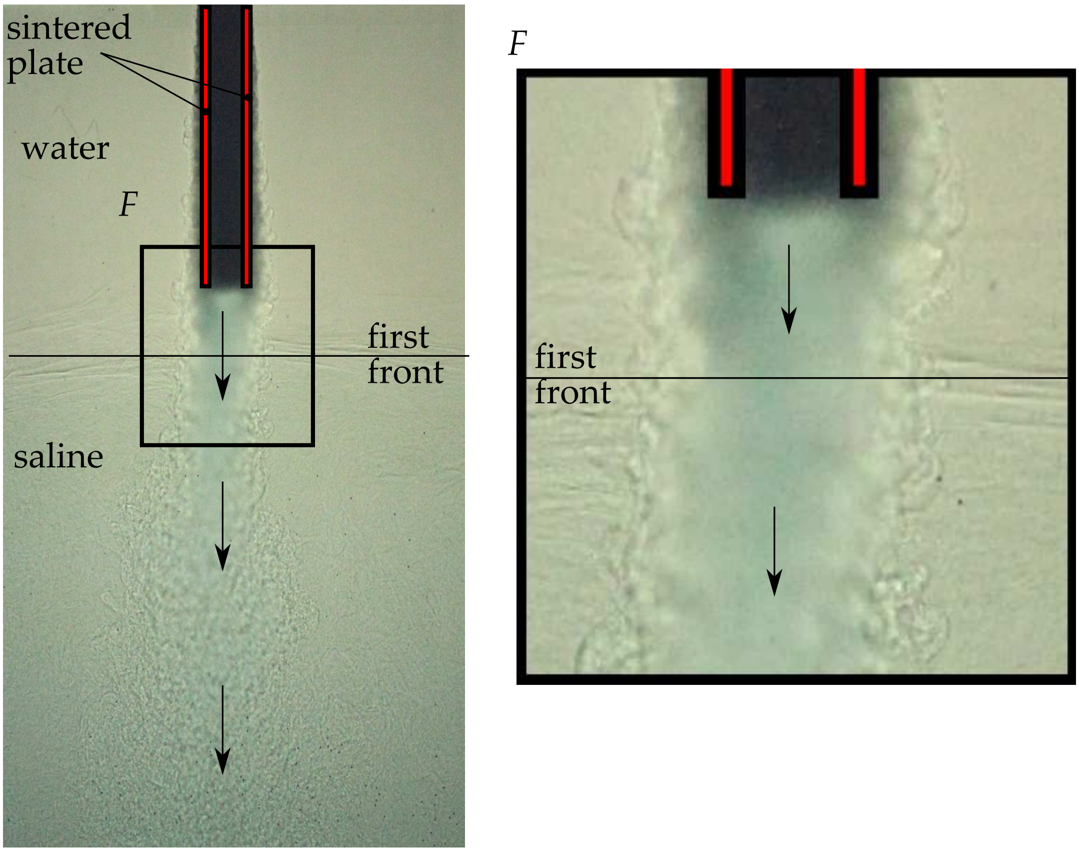

Figure 4.13: Turbulent saline plume flow developed on sintered surfaces of model convector (marked as red rectangles, not to scale). Image *F* shows the region about the trailing edge of convector magnified (as marked). Arrows show general plume flow direction.

4.4.4 Repeatability

In general, the application-specific experimental methods offer a good repeatability of results, see Figure 4.19 for reference. The limiting factor preventing averaging data sets from different experiments is a lack of a precise trigger to commence the experiment. This can lead to slight time shifts between corresponding data sets from run to run.

4.5 Diagnostics

Four independent experimental methods have been used to gather qualitative and quantitative data: a shadowgraph technique, a dye attenuation method, PIV and a salinity method with conductivity probes. Below, each method is described, the required experimental set-up outlined and the application of the method explained.

4.5.1 Dye-attenuation technique

A dye-attenuation technique is applied when there is a need for non-intrusive density measurements (Cenedese & Dalziel 1998, Allgayer & Hunt 2012). This visualisation technique is based on the principles of spectrophotometry and is used to estimate depth-averaged dye concentrations and thereby to infer density. The fundamental principles of the dye-attenuation technique are reviewed in brief below, based on the paper by Allgayer & Hunt (2012) in which this technique is explained in detail.

4.5.1.1 Background

The human eye is sensitive to electromagnetic radiation in the range 360 to 780 nm, within which individual wavelengths are seen as colours. The colour of a solution stained with a chemical dye is a result of the absorption of a given portion of incident radiation within the visible spectrum. The opacity of the stained solution depends on the proportion in which the radiation is absorbed and is represented by its transmittance Tr. Transmittance is the ratio between the intensity of radiation after passing through the solution $\mathscr{I}$ and before passing through the solution $\mathscr{I}_0$. The properties of the solution are related to transmittance by the following expression:

$$ln(Tr) = ln\left(\frac{\mathscr{I}}{\mathscr{I}_0}\right) = -\epsilon Y \mathcal{S}, \tag{4.9}$$

where ϵ denotes the coefficient of molar absorption (ppm m)$^{-1}$, Y is the distance travelled through the solution (m) and $\mathcal{S}$ is the concentration (ppm). The expression (4.9) may be rewritten in the form of the Lambert-Beer law:

$$\mathcal{A} = -ln(Tr), \tag{4.10}$$

where $\mathcal{A}$ is the absorbance of the solution. The main application of (4.9) and (4.10) is to depth-averaged measurements of concentrations. For a known chemical dye and path length Y, measurements of $\mathscr{I}/\mathscr{I}_0$ can be used to estimate the concentration $\mathcal{S}$. These measurements are carried out with a light source, whose specifications are discussed below, and a photometer, here a CCD camera.

4.5.1.2 Comment on dye-attenuation limitations

There are two restrictions of the Lambert-Beer law. Firstly, the expression (4.10) holds for small concentrations $\mathcal{S}$. The large increases in $\mathcal{S}$ trigger interactions between the molecules which result in the absorbance $\mathcal{A}$ becoming non-linear. Secondly, the coefficient of molar absorption ϵ is specific to the chemical used and to the wavelength of radiation. Hence, the use of a monochromatic light source is required. In practice, a polychromatic light source may be used if the unwanted wavelengths can be removed by coloured filters positioned between the photometer and the set up. The colour of the filter should represent a narrow range of wavelengths at the peak of the absorption spectrum of the solution. Figure 4.14 shows the absorption spectrum of methylene blue, which was a chemical used in this research to stain saline solution. The absorption spectrum, represented by the molar extinction coefficient, is a fraction of incident light absorbed by the substance over a range of wavelengths. The advantage of selecting a range of wavelengths around the peak is that small changes in the wavelength correspond to small variations in the light absorbance.

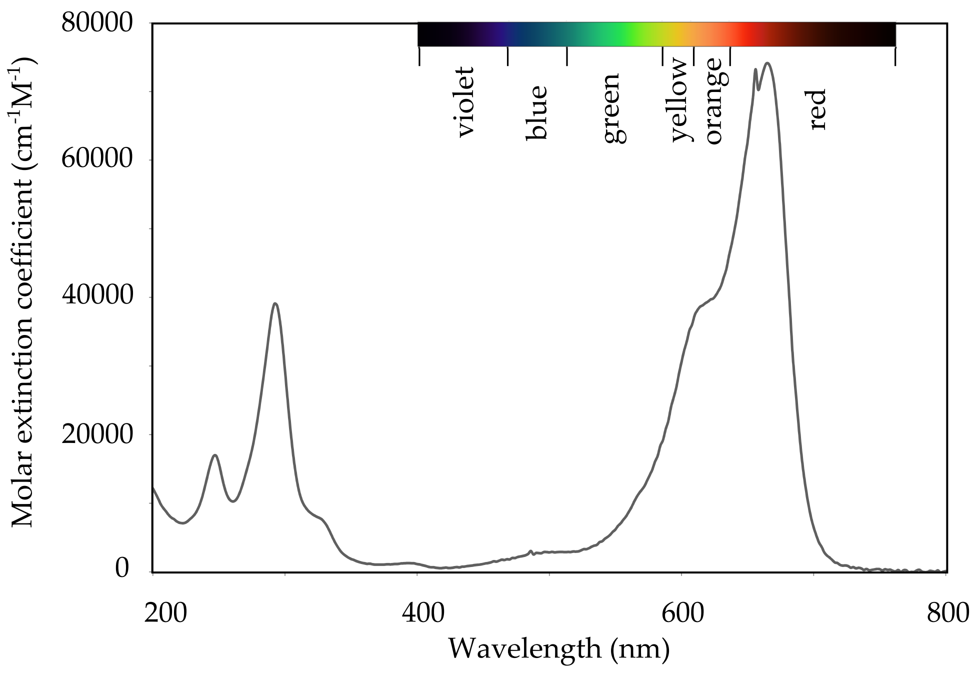

Figure 4.14: Absorption spectrum of methylene blue (replicated from measurements of Scott Prahl, Oregon Medical Center). Molar extinction coefficient is proportional to the coefficient of molar absorption. Visible light range replicated from Bruno & Svoronos (2005).

4.5.1.3 Application of dye-attenuation technique

The dye-attenuation technique was applied by staining the saline solution with methylene blue to a concentration of approximately 0.005 ± 0.0005 mgcm $^{-3}$. This concentration was achieved by adding 2.5l of methylene blue solution of concentration 1gl $^{-1}$ to 500l of saline solution. In this application, due to very low concentrations, methylene blue is a passive tracer chemical, which dilutes in water in a similar way to saline solution (Allgayer & Hunt 2012). The absorption spectrum of methylene blue has a peak in the visible spectrum at 660 nm, see Figure 4.14, hence a red filter with a range from 620 nm to 750 nm (Bruno & Svoronos 2005) was selected. Figure 4.15 shows the set-up used for the dye-attenuation experiments. The tank was backlit by a light box, made of high frequency fluorescent tubes, see schematic in Figure 4.16. On its own, each tube would produce a relatively bright vertical line. To help achieve a uniform light output, the light box was made of opalescent sheets that diffused the light.

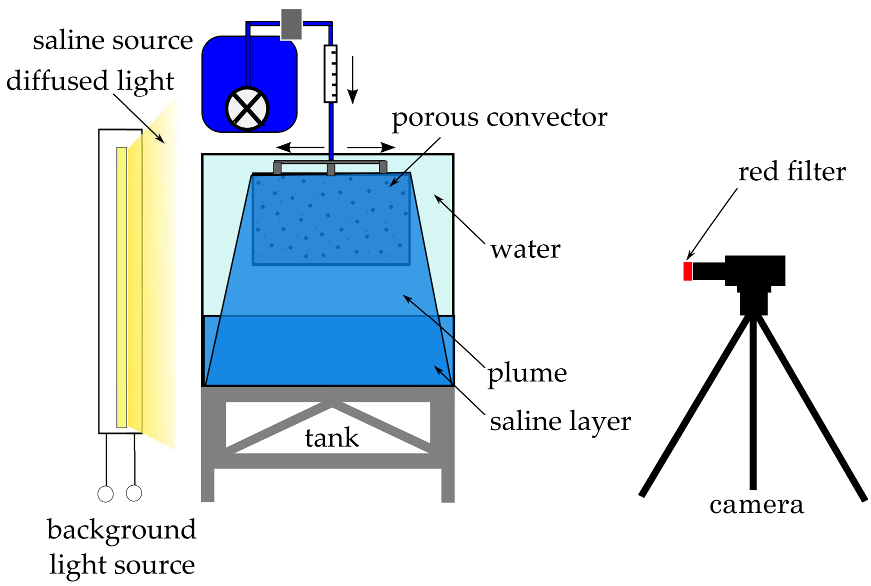

Figure 4.15: Schematic of experimental set-up for dye-attenuation technique during a filling box experiment.

4.5.1.4 Recording

Images were recorded using a CCD camera with a resolution of 1372 × 1024 pixels, with a Pentax 12.5-75 mm 1:1.8 TV ZOOM lens and a Hoya R(25A) red filter, see Section 4.5.1.3. The camera was positioned 3 m from the tank. Sequences of frames were saved as 8-bit bitmap image files at a frequency of 3 frames per second and stored with a BitFlow R3 frame grabber card. Each experiment was conducted for a duration δt varying from 1000 s to 7200 s.

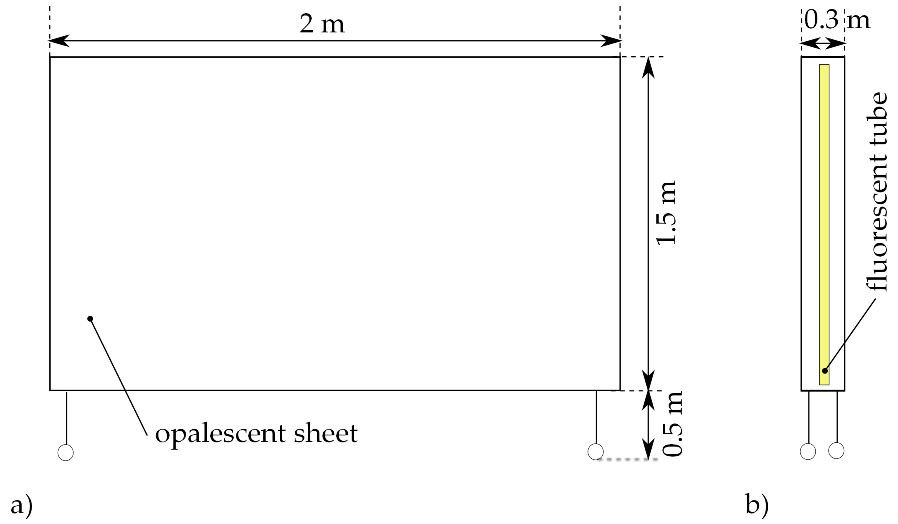

Figure 4.16: Light box: a) front view in elevation; b) side view in elevation.

4.5.1.5 Processing

In order to enable qualitative observations of the filling flows, a digital movie was created from captured frames for each experiment. Data processing was required to gather quantitative information on the rate of filling and on the depth-averaged density fields. This was done in Matlab and involved the following steps: to start with, the intensity of greyscale images was adjusted to ensure that the intensities were recorded using the full range of 256 shades of grey. The initial minimum and maximum intensities were found and the range was rescaled to ensure that black was digitised as 0 and white as 255. The second step involved normalising the pixel intensities of the images with respect to the pixel intensities of the background image. The background subtraction was performed to remove any non-uniformities due to uneven lighting or optical distortions. An example of the effects of background subtraction is shown in Figure 4.17. Images post-background-subtraction were used both to prepare time series and to compute the density field.

First front position

To create a time series, each image was converted into a vertical column of pixels that was produced by averaging the pixel light intensities horizontally, corresponding to averaging in x. Averaging in x is conducted to ensure that each column of pixels comprising a time series captures an instantaneous stage of filling within the tank[1]. A time series of the position of the front for each experiment was then created by positioning all the averaged vertical pixel columns from each captured image next to each other. The position of the first front was extracted from each time series by finding the external contour of the layer. An example of a time series and the relevant contour is shown in Figure 4.18. Contours, extracted in the following way, were used to determine the rate of filling. Time series of line-averaged pixel intensities were presented scaled in the non-dimensional form. The first front position h was

[1]Tracking of the peak vertical intrusion (as shown in Figure 4.17) was conducted separately as part of the analysis of the filling flows.

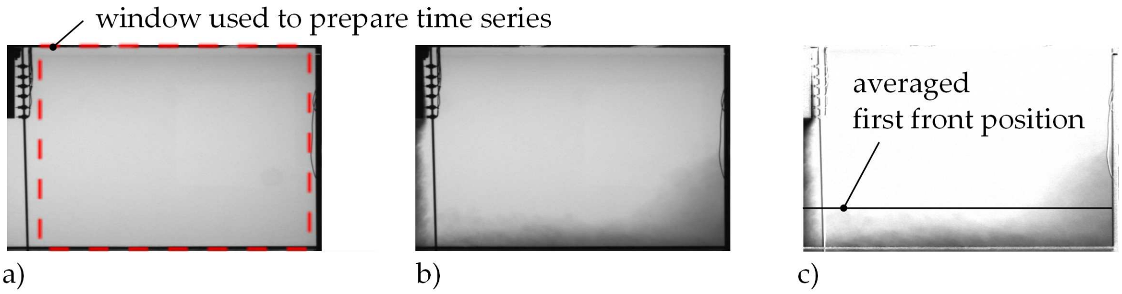

Figure 4.17: Greyscale images from a filling box experiment: a) background with a typical window used to create time series, b) unprocessed image of the experiment, c) resulting processed image with indicative averaged first front position. The pixel intensities of the unprocessed image were divided by the corresponding pixel intensities of the background. The processed image only shows regions in which pixel densities are darker than in the reference frame. All the images were mapped to a 256 grey scale.

scaled on the height H, whereas time was scaled either on the experimental timescale:

$$\mathcal{T}_{exp} = \frac{S}{B_0^{1/3}\mathcal{L}^{1/3}H^{1/3}} \tag{4.11}$$

or the equivalent time scale $\mathcal{T}_a$ developed by Cooper & Hunt (2010), see Section 2.1.4.

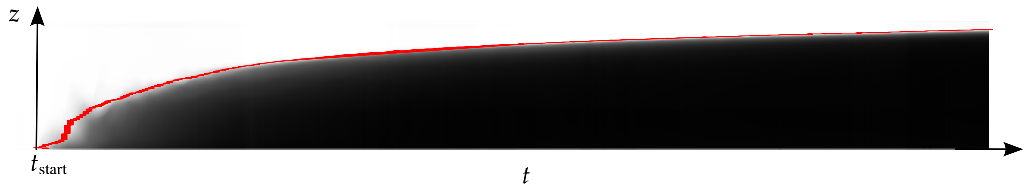

Figure 4.18: Time series of line-averaged pixel intensities with the contour marking the position of the first front. Each vertical column of pixels represents one processed image.

Figure 4.19 shows the time series of interface position captured in 4 experimental runs with the system configuration: convector in the centre (14.5 d), $Æ = 1.26$, $H/H_* = 1$, $Q_0/Q_{0,*} = 1$ and $g'/g'_* = 0.85$. In general, there is a good repeatability in recording the interface position.

Entrainment coefficient

The plume development in near and far fields was analysed individually in each experiment to establish values of entrainment coefficient. Table 4.2 summaries the expressions used to determine the entrainment coefficient. The values of entrainment coefficient were extracted by substituting the experimental data (the position of the first front in time) into the theoretical expression, describing the first front position as a function of time (derived from the filling box model). This implies that the filling box model is applicable to approximate the first front position during convector-induced filling. The validity of this assumption is discussed in Section 5.1. The first front position in time in the near field, during convector-induced filling, is

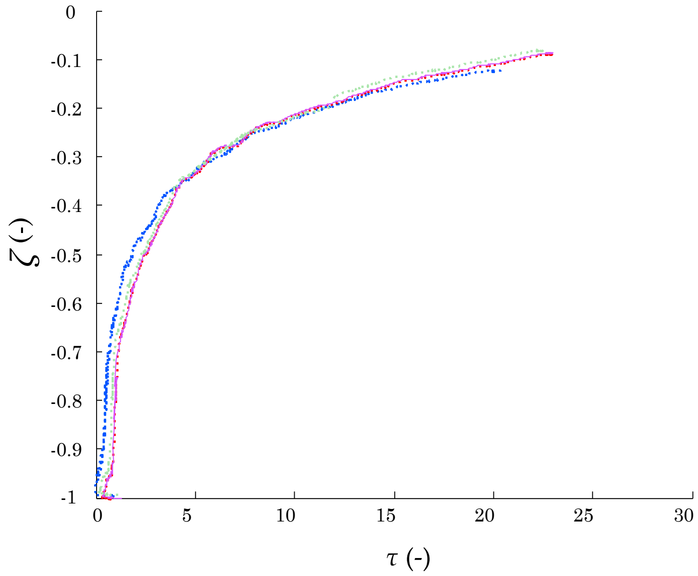

Figure 4.19: Repeatability of recording the position of the interface. Non-dimensional position of the interface as a function of time non-dimensionalised by experimental timescale $\mathcal{T}_{exp}$, see eq.(4.11) for reference, in 4 experiments with: convector in the centre (14.5 d), $Æ$ = 1.26, H/H_* = 1, $Q_0/Q_{0,*}$ = 1 and g'/g'_* = 0.85.

successfully matched with the predictions of the filling box model with the vertically distributed source by Cooper & Hunt (2010), whereas in the far field with the predictions for the line source of Lee & Emmons (1961), see Sections 2.1.2 - 2.1.4 for reference.

Source	Equation: f = $\Bbbk t$,
VDS	$\zeta^{-1/3} - 1 = \frac{1}{4}\left(\frac{4}{5}\right)^{1/3} \frac{\alpha_a^{2/3} B_a^{1/3} \mathcal{L}^{1/3} L}{S} t.$
Line	$ln\zeta^{-1} = \frac{(2\alpha_L)^{2/3} B_L^{1/3} L}{S} t$

Table 4.2: Equations used to determine slope $\Bbbk$, derived from the filling box model, see Table 2.1 for reference.

Substituting the temporal measurements of the interface position into the equations from Table 4.2 allows the determination of the slope $\Bbbk$ of the best fit by using a linear regression. The data is fitted using Matlab Basic Fitting. An example of such a fit is shown in Figure 4.20, where in (a) the data is plotted as f(t) (circles) with a linear least squares fit (red line) and (b) contains a plot of residuals, which are the signed differences between the experimental data and the fitted values.

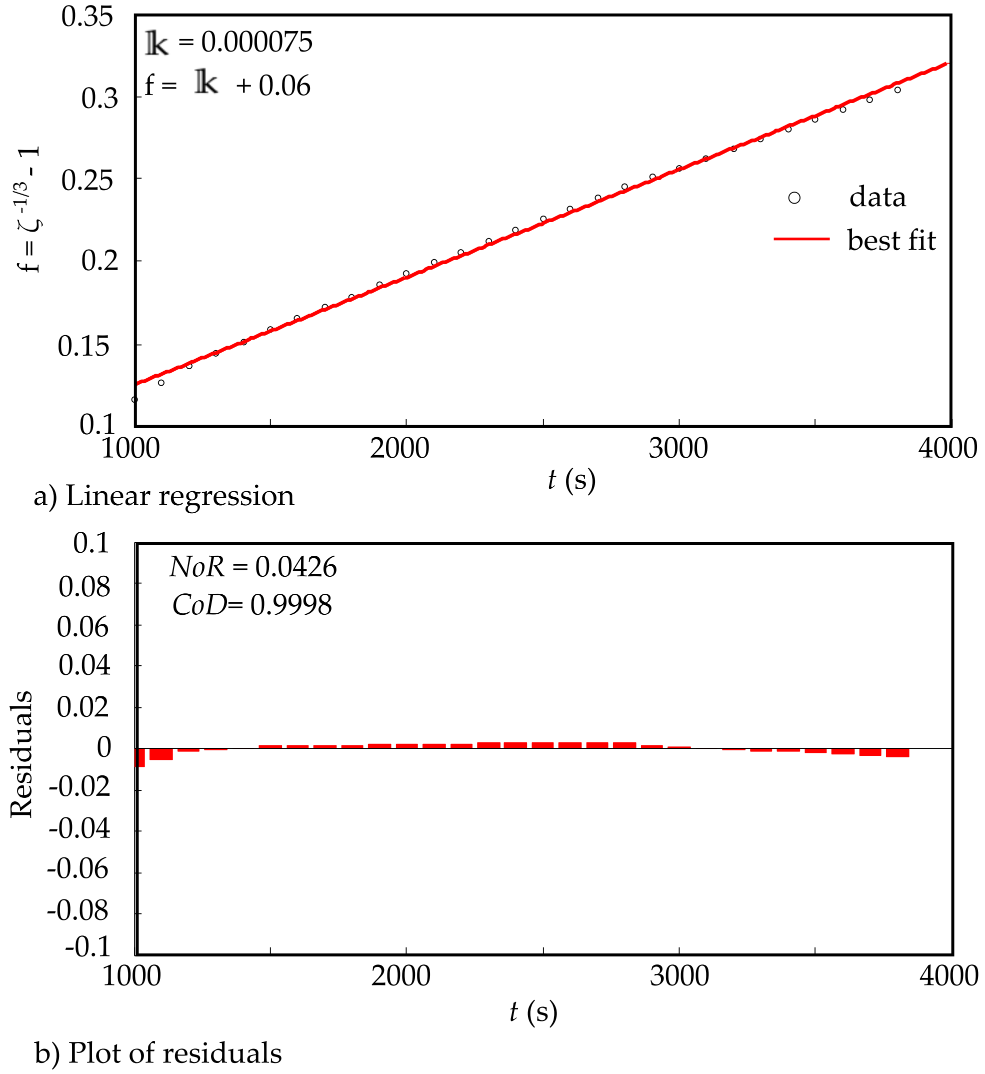

Figure 4.20: Linear least squares fit of data, plotted as f(t), where f $= \zeta^{-1/3} - 1$, to extract entrainment coefficient of VDS.

In order to evaluate the quality of fitting, the norm of residuals *NoR* and the coefficient of determination *CoD* are calculated from:

$$\begin{aligned} NoR &= \sum\left(\sqrt{Res^2}\right) \\ CoD &= 1 - \frac{NoR^2}{(n-1)Var} \end{aligned} \tag{4.12}$$

where *Res* denotes residuals, n is the number of measurements, Var is the variance of f. In the example from Figure 4.20, $CoD = 0.9998$, hence a linear least squares fit of the data shows an excellent agreement with the data. This confirms that the near-field plume from the convector may be accurately described by Cooper & Hunt's (2010) filling box model. Also, the linear regression may be performed on the experimental data in order to extract values of the entrainment coefficient. In the example, the corresponding entrainment coefficient α_a is estimated from the expression:

$$\alpha_a = \left(4\left(\frac{5}{4}\right)^{1/3} \frac{S}{B_a^{1/3}\mathcal{L}^{1/3}L}\mathbb{k}\right)^{3/2}, \tag{4.13}$$

resulting in $\alpha_a = 0.013$. A typical uncertainty of $\pm$ 0.002 of the results occurs due to the measurement of the interface position, the selection of the window to prepare the time series and the choice of contour to reflect the interface position.

Density field

Another application of the images post-background-subtraction was to extract the concentration values and subsequently the density field. The background subtraction enabled transforming the intensity data into the transmissivity data, so that the image pixel intensities are in range 0 to 1 (Allgayer & Hunt 2012). The equal intensity of the image and its background corresponds to a transmissivity of 1, whereas any pixels that were darker than their background correspond to smaller transmissivity. Following Allgayer & Hunt (2012) transmissivity data was converted to the tracer dye concentration data using the Lamber-Beer law, see (4.9-4.10) and assuming the molar absorption $\epsilon = 0.218$ for methylene blue. The concentration field data was then converted into the density field data using a simple formula (Allgayer & Hunt 2012):

$$\rho = \frac{\mathcal{S}}{\mathcal{S}_i}\Delta\rho_i + \rho_i \tag{4.14}$$

where ρ and $\mathcal{S}$ are the density and concentration at the given pixel, $\Delta\rho_i$ denotes the initial density between the saline solution and water in the experiment. The subscript $_i$ denotes initial values of the quantities considered, corresponding to values at $t = 0\,\text{s}$. Figure 4.21 shows an example of the resulting density field data presented as a 256 false-colour scale image.

4.5.1.6 Comment on error associated with parallax

Parallax error has an important impact on the accuracy of interface position measurements. In an ideal case, the camera would be very far from the tank (ideally at infinity) so that the light

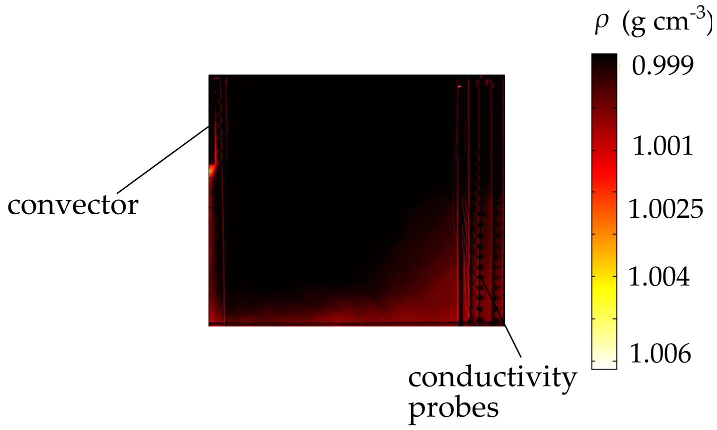

Figure 4.21: An example of a density field extracted from dye attenuation with a false-colour legend, where black corresponds to density of water and white to the most concentrated saline solution.

beams are parallel to each other and perpendicular to the camera. In practice, however, light beams scatter and the angles of the light beams, which track the interface position at the front and the back of the tank, vary. The interface position when below and above the camera level was therefore represented by a thin layer, as opposed to a sharp line. Assumptions used to estimate parallax error: H = 95 cm, Y = 100 cm, the distance between focal point in range 1.25 - 7.5 cm, the distance between tank and the focal point in range 100-500 cm. The maximum parallax error in estimating the interface position varied from 0 to 10% of H during experiments as a result of variation in relative position of camera (fixed) and interface (dynamic). Figure 4.22 shows a crude method of how this estimation of the parallax error was achieved. To reduce parallax error over long timescales, the camera was positioned, as in Figure 4.22 a), at the trailing edge of the convector for every experiment conducted.

4.5.1.7 Comment on error associated with dye-attenuation technique

The results from the dye-attenuation technique have inherent errors. These arise from the design of the set-up, equipment inaccuracies, measurement errors and post-processing errors. The density field extracted from the dye attenuation was locally compared with the vertical density profiles extracted from the conductivity measurements, see Section 4.5.4 for details of the conductivity measurement method. Figure 4.23 shows an example of dye-attenuation data with the density profile superimposed onto the figure. There is an obvious difference between the extracted density data, namely the density field averaged across the depth of field Y from dye attenuation and the local density data points from the conductivity measurements. Comparisons of the corresponding density points, however, show that both methods have good general agreement. The maximum absolute error in results is approximately 10^{-3} gcm^{-3}. The maximum relative error, using the salinity reading as a reference is approximately ±24% of salinity reading at z = 55 cm.

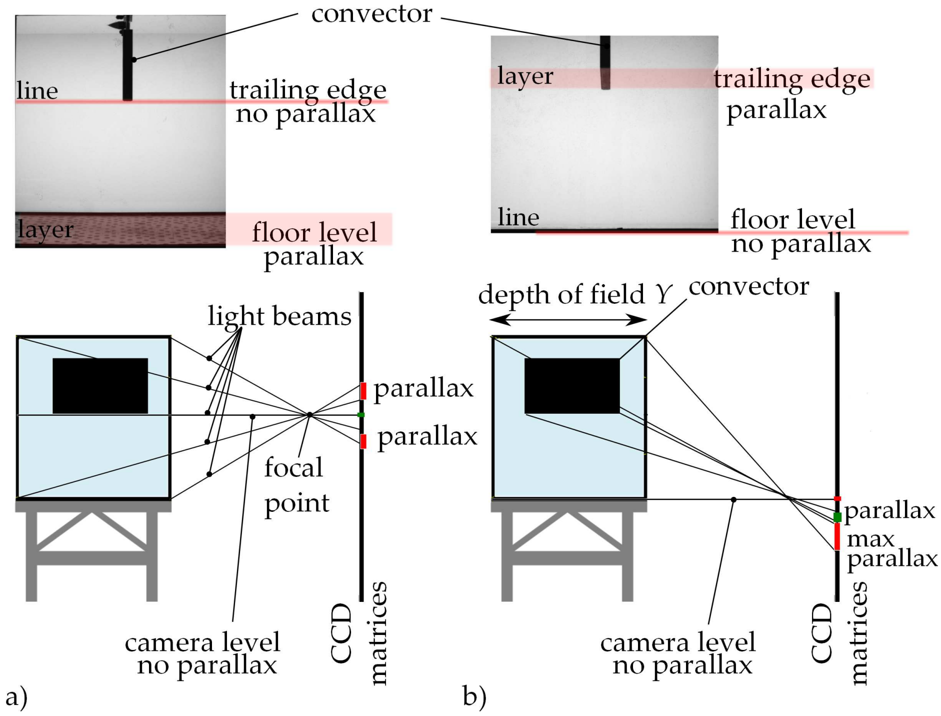

Figure 4.22: Schematic to convey how parallax errors were estimated for two positions of the camera: a) camera at the level of trailing edge and b) camera at the level of tank base. The upper greyscale images show a front view of tank in elevation. These show how parallax changes with vertical distance from 0 at the camera level to its maximum value farthest from the camera level. Selecting one of tank edges as a camera level was thus undesirable. The trailing edge was the optimal camera level, due to its intermediate position relative to the tank edges. The lower images show a side view of tank in elevation. These show schematically representative light beams and corresponding parallax errors on the CCD matrices.

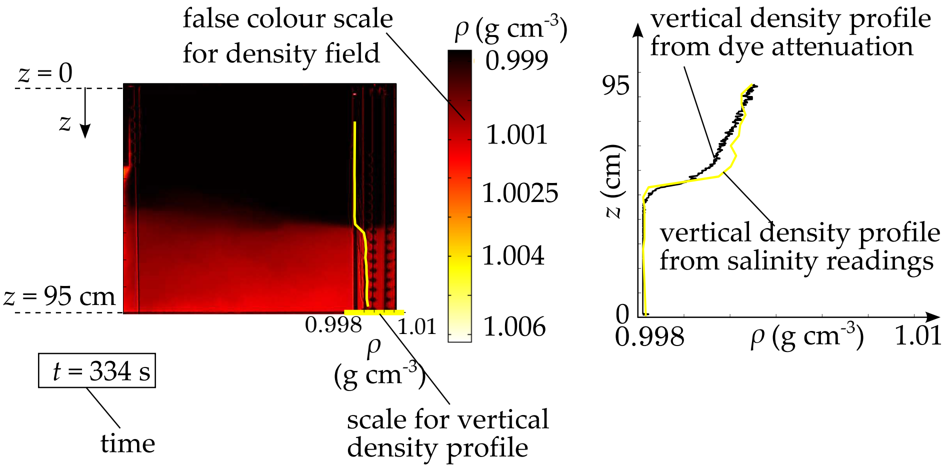

Figure 4.23: Results of the dye attenuation (averaged density field) and conductivity measurements (vertical density profile made of multiple point measurements) superimposed (left-hand-side) and compared (right-hand-side). The location of the density profile corresponds to the location of the probes.

4.5.2 Shadowgraph technique

Shadowgraph imagery is a visualisation technique, used for observation of a flow, whereby light passes through the flow from one side of the tank to the other allowing the density field to be visualised as a shadow pattern on a vertical screen attached to the opposite side of the tank (Bradshaw 1970, Settles 2012).

4.5.2.1 Background

When a parallel beam of light, travelling in the horizontal y-direction passes through a region with a gradient of refractive index in the vertical z-direction, each light ray is deflected vertically through an angle according to:

$$\varphi = \int_{\wp} \frac{1}{\phi} \frac{\partial \phi}{\partial z} dy, \tag{4.15}$$

where $\wp$ is the path length of light ray, $\phi = \mathcal{C}_v/\mathcal{C}$ denotes the refractive index, where $\mathcal{C}_v$ and $\mathcal{C}$ correspond to the speed of light in a vacuum and the speed of light in the medium, respectively. Note that $(\phi - 1)$ is proportional to density ρ of a fluid (Gladstone-Dale relationship, Gladstone & Dale 1863) and the density field can be obtained from the light refraction. Here, however, shadowgraph images were exclusively used to obtain qualitative information on filling flows. Each shadowgraph image potentially consists of light and dark regions, see for example Figure 4.13. When light rays travel through regions with a density gradient, they are deflected towards a region of higher density. On the screen, light illumination is increased where the rays converge, corresponding to a light region and negative values of $\frac{\partial \varphi}{\partial z}$ or $\frac{\partial^2 \phi}{\partial z^2}$, and illumination is decreased when the rays diverge, corresponding to a dark region and positive values of $\frac{\partial^2 \phi}{\partial z^2}$. The intensity variations are given by the following expression (Laufer 1996):

$$\frac{\Delta \mathscr{I}}{\mathscr{I}} = \wp \int \left(\frac{\partial^2 \rho}{\partial x^2} + \frac{\partial^2 \rho}{\partial z^2} \right) dy, \tag{4.16}$$

where $\mathscr{I}$ corresponds to the light intensity that would be observed on the screen in the case of no deflection (here this corresponds to zero density gradient) and $\Delta \mathscr{I}$ is the difference between $\mathscr{I}$ and the observed intensity.

4.5.2.2 Application

Figure 4.24 shows a schematic of the experimental set-up used for the shadowgraph imagery. The camera was positioned 3 m from the tank. A light source was at a distance from the tank, in this case, an overhead projector (OHP) was positioned 5 m from the tank. By using OHP, a bright light passed through the fluid and casted sharp shadows on the screen corresponding to the light ray displacement from the deflection (Settles 2001). The shadowgraph images showed salient features of the filling flows such as flow direction, mixing and disturbance.

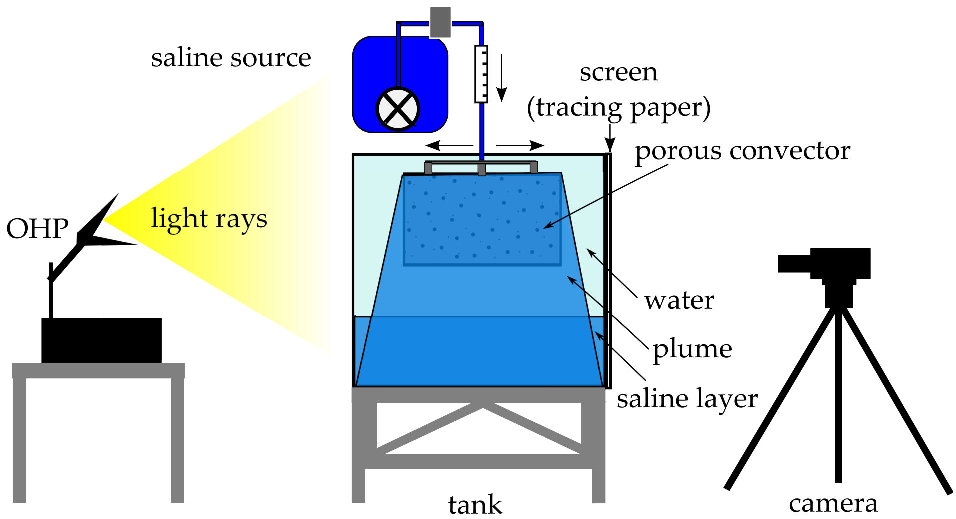

Figure 4.24: Experimental set-up for flow visualisation using shadowgraph imagery.

4.5.2.3 Comment on tracking direction of a flow

In order to follow the flow direction in the environment at different heights, strings, dyed with methylene blue paste[1], were attached to bars, stretched across the tank, and dropped into the tank. To ensure fast alignment of each string, a weight was tied to the end of each string. When immersed, each string started releasing dye that was advected by the induced flows established in the environment. Figure 4.25 shows a sample shadowgraph image used to track the flow

[1]Methylene blue paste was prepared in-house from methylene blue crystals.

direction.

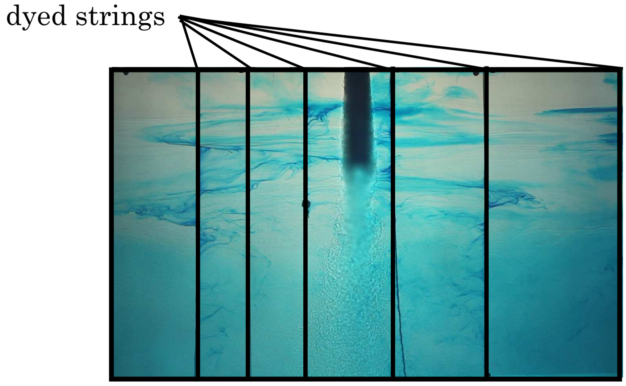

Figure 4.25: Sample shadowgraph image.

4.5.3 Particle Image Velocimetry

To complement the concentration measurements, in which a tracer chemical dye is used to visualise the filling flows, PIV experiments were performed to obtain instantaneous velocity measurements. The method used was a 2D planar PIV, referred to as PIV from now on. PIV vector fields allowed a representation of the motion of the fluid outside the filling flows. PIV measurements are also useful here because they can help to understand the significance of flow three-dimensionality and to what extent any 2D approximations are valid.

4.5.3.1 Background

PIV is a flow diagnostic technique used to measure flow velocities. The basic PIV system is shown in Figure 4.26. The fluid is seeded with tracer particles which ideally should closely follow the movement of the flow, see Section 4.5.3.3 for full details on the tracer particles selected. The particles are illuminated (see Section 4.5.3.4 for details on light source) and an image frame is recorded, as described in Section 4.5.3.6. Subsequently, a second frame is captured a small time Δt after the first, which enables calculation of a velocity vector (Raffel et al. 2007). The basic principles of PIV are now outlined based on the descriptions of Fincham & Spedding (1997), Raffel et al. (2007) and Brossard et al. (2009).

4.5.3.2 Application of PIV

The PIV set-up is shown schematically in Figure 4.27. The set-up comprised of the visualisation tank with the model convector, a light projector and a CMOS camera which has a resolution of 1280×800 pixels, and a maximum frame rate capability of 3260 Hz at full resolution. The PIV experiments were performed in the same visualisation tank as described in Section 4.4.1. The saline solution was not stained and the water was seeded as described in Section 4.5.3.3. To increase the visibility of white particles a black background was arranged by affixing the

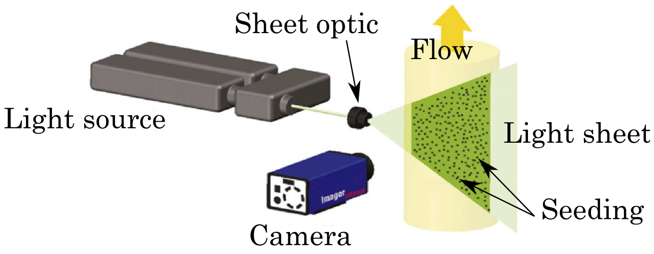

Figure 4.26: System components of a typical PIV arrangement (adapted from La Vision GmbH 2010).

black matt sheet of rubber to the back wall of the tank. The light sheet was formed by allowing a limited propagation of light through the slot in the blanked side wall, as described in Section 4.5.3.4.

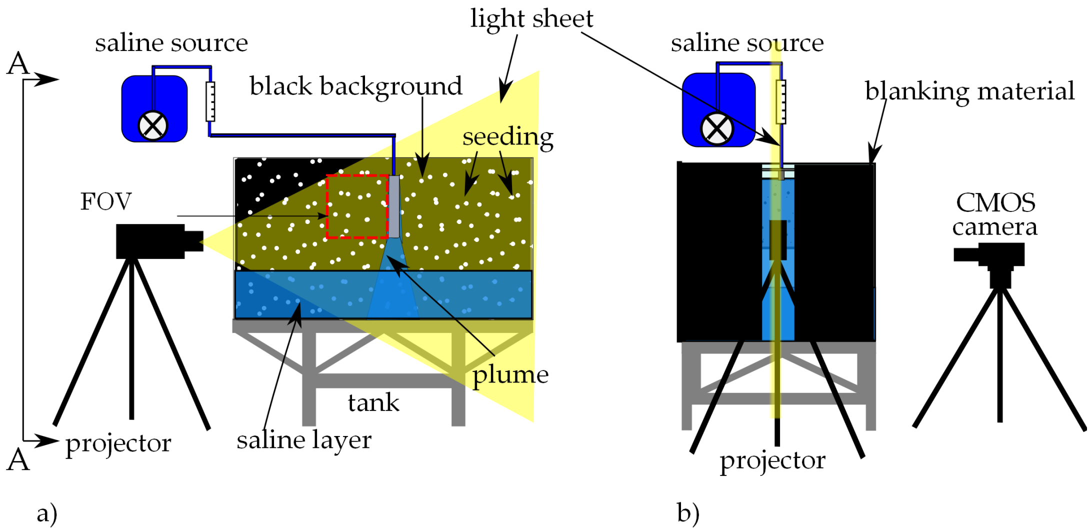

Figure 4.27: The experimental set-up for the PIV experiments: a) front elevation; b) side elevation.

4.5.3.3 Seeding

PIV vector calculations are based on algorithms that consider the statistical average movements of groups of seeding particles. The selection of appropriate seeding (material, concentration, size) is therefore crucial to ensure good quality data. The selected seeding has to meet a number of criteria with regard to its visibility, movement and concentration, each of which is now considered (Westerweel 1997). PIV experiments were conducted with titanium dioxide (TiO_2). The particle size was of the order of 10^{-4}cm.

Visibility

Firstly, the seeding should be easily detectable by the camera. For a black background used, this requires bright particles, i.e. which scatter enough light such that the particle image size exceeds a pixel. This results in a variation in pixel illumination intensity and a pseudo-Gaussian fit to the sub-pixel particle displacement may be applied to ascertain the particle position with an accuracy of better than a single pixel.

If the light reflected by the particle occupies less than the size of a pixel on the imaging sensor, pixel locking may occur (Fincham & Spedding 1997). Pixel locking is a pixel displacement bias error leading to the displacements being biased towards integer values (Westerweel 1997, Raffel et al. 2007). It may be detected by investigating whether there is an inclination in particle displacement towards integer values in the displacement histogram. In case of pixel locking, a histogram is distorted with a number of peaks about integer values. This informs that the systematic errors are larger than the random noise in displacement estimates (Raffel et al. 2007). Figure 4.28 shows an example of a pixel locking histogram from this work. This sample indicates that the particle image was free from pixel locking due to the lack of increased samples at integer displacement values, hence the size of particles was correct and not too small.

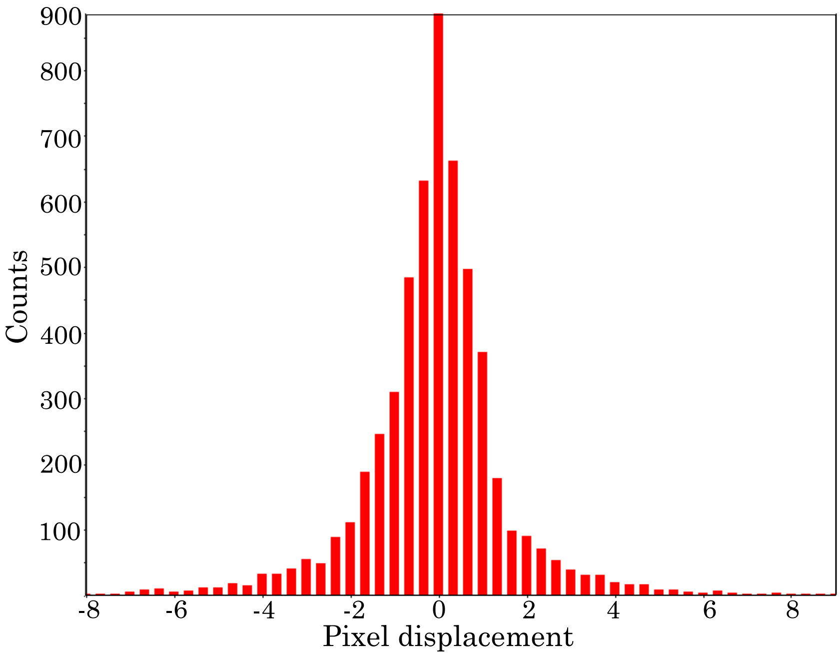

Figure 4.28: Histogram of actual pixel displacement data obtained from a single pair of images of filling box experiment. Counts denote a number of vectors with a corresponding pixel displacement.

Movement

Secondly, as the fluid is invisible to the camera, the particles should be chosen so as to follow the flow direction as closely as possible. Therefore, in the fluid at rest, the particles should stay in suspension for a time significantly longer than duration of an experiment. Otherwise, buoyant particles would rise to the top or sink to the base, which would result in non-uniform distribution of particles before an experiment and introduce errors in the velocity. This requirement corresponds to having a small settling velocity of particles relative to the fluid velocity in experiments. The settling velocity may be calculated from (Adrian & Westerweel 2011):

$$w_{sv} = \frac{\overline{\rho} - 1}{\overline{\rho}} \frac{g t_{sv}}{\chi} \tag{4.17}$$

where $\overline{\rho} = \frac{\rho_p}{\rho}$ is a ratio of the particle density ρ_p to the fluid density ρ, $t_{sv} = \frac{\rho_p \mho^2}{18\nu\rho}$ is a time constant (s), $\mho$ denotes a particle diameter (cm), ν is a kinematic viscosity of a fluid ($\mathrm{cm^2 s^{-1}}$) and χ is a correction function for particle dynamics used to modify the Stokes law for steady, low-Reynolds-number[1] drag on a motionless solid sphere to unsteady flow, where $Re_p = \frac{w_{sv}\mho}{\nu}$ and $\chi = 1 + \frac{3}{16}Re_p$ (valid for $Re_p < 0.01$, Clift et al. 1978). The settling velocity was calculated in two approximations, first for $\chi = 1$ and second for χ calculated from the first approximation of w_{sv}. The titanium dioxide particles used in this work had a settling velocity of approximately $1.8 \times 10^{-4}\mathrm{cms^{-1}}$, which is equivalent to a particle descending by 0.6 cm per hour[2]. Given the fact that the experiment lasted less than an hour, and each recording of sequence of images took less than a minute, the influence of settling velocity on the particle position was negligible. Also a settling velocity was negligible when compared with the velocity scaling of the buoyancy-driven flow ($\sqrt{g'H} = 50.6$ $\mathrm{cms^{-1}}$, for $H = 95$ cm and $g' = 27$ $\mathrm{cms^{-2}}$). The low particle Reynolds number $Re_p \approx 1.78 \times 10^{-6}$ corresponds to the small inertia of particles, which are thus able to respond to different flows and follow them closely.

Velocity magnitudes of induced flows, in different periods and FOVs, are compared based on the parameter m of each velocity vector field defined as:

$$m = \sqrt{(\overline{u})^2 + (\overline{w})^2} \tag{4.18}$$

where $|\overline{u}|$ and $|\overline{w}|$ correspond to the mean magnitudes of the horizontal and vertical velocity components, respectively. The settling velocity was also negligible when compared to the mean velocity magnitude of the induced flows from the velocity vector field, which was in the range 10^{-1} to 10^{-2} $\mathrm{cms^{-1}}$, see Chapter 7.

Concentration

The concentration of particles should be low enough, so as not to affect the properties of the fluid. The amount of particles should, however, also be sufficient to ensure an even distribution that still allows reliable vector computation. The mass ratio of particles and fluid, for particles of the order of a micron in diameter, must not exceed 10^{-3}(Raffel et al. 2007). The particles should also be spherical to avoid any dependencies between the orientation of particles and the flow direction (Hubner 2004).

To improve suspension in water, the particles of titanium dioxide were first premixed in 100 ml of water and then gently released into the tank of fresh water. For more uniform dis-

[1]The Reynolds number is a dimensionless number, which expresses the balance between the inertial and viscous forces.

[2]Assumptions used to estimate a settling velocity: $\rho_p = 4.23$ $\mathrm{gcm^{-3}}$, $\rho = 1$ $\mathrm{gcm^{-3}}$, $\nu = 1.004 \times 10^{-2}$ $\mathrm{cm^2 s^{-1}}$ and $\mho = 10^{-4}$cm.

tribution of particles, water was stirred and left to settle. This was done to allow the ambient turbulence intensity to drop off to an acceptable level that is no longer distinguishable in the velocity vector field. It was determined by Jones (2010) that for a similar water tank facility the ambient turbulence intensity[1] dropped to an acceptable level after 20 min. Figure 4.29 shows a vector plot of the instantaneous velocity field of the ambient environment, within the field of view, prior the start of the experiment, after 20 minutes of settling. After 20 minutes some marginal movements were still evident in the instantaneous vector plot of velocity field, where the maximum magnitudes of the horizontal and vertical velocity components were equal to 0.11 and 0.19 $\mathrm{cms^{-1}}$. To ensure that these movements have no effect on the results the settle time was extended. The tank prior to convector-induced filling box was left to settle for approximately an hour, three times the duration recommended by Jones (2010). This is because the magnitude of the velocity vectors that are of interest in this work is quite small and comparable to the ambient turbulence even after 20 minutes. After an hour, these marginal movements were restricted further and the maximum magnitudes of the horizontal and vertical components were reduced to 0.06 and 0.08 $\mathrm{cms^{-1}}$. Figure 4.30 shows a raw image of the field of view taken prior to the experiment after 60 minutes of settling and a corresponding vector plot of the instantaneous velocity field of the ambient environment, within the field of view, also prior the start of the experiment, after 60 minutes of settling.

To avoid clogging the pores of the model convector, particles were not added directly to the saline solution. Instead, the tank of fresh water was seeded with particles and the induced flow tracked. As a result, notably at the beginning of an experiment, before any particles were entrained into the plume, there were significant discrepancies between the seeding density of the plume and the seeding density of the freshwater. This was evident by darker region of the plume flow in the raw image of particle distribution and the lack of vectors in the plume region of the vector plot. Figure 4.31 a) displays a raw image of particle distribution for the developed plume in the unstratified environment, and Figure 4.31 b) contains the corresponding vector plot of the velocity field. Due to a lack of sufficient seeding, the vectors may not be determined within the plume. The edges of the plume were defined and vectors were estimated outside the plume. In this thesis, PIV experiments are primarily used in a discussion of the flows induced in the ambient environment outside the plume flow.

4.5.3.4 Illumination

Most modern PIV systems take advantage of high-power lasers to provide a source of illumination. Despite the advantages of lasers, they are expensive to purchase and potentially dangerous to operate. As a result, cheaper and safer sources of illumination were sourced for research such as the LED-based illumination used by Willert et al. (2010) as an alternative to laser-based illumination to create the light sheet in their PIV experiments. This work used a light sheet of white light, formed from a projector incandescent lamp source. The projector lamp source (40 W) is both inexpensive by comparison and offers adequate illumination of the seeding particles. A simpler light sheet could be used in this study because the flow velocities

[1]Turbulence intensity is measured quantitatively using the time-average of the oscillating turbulent velocities ($\overline{u'^2}, \overline{v'^2}, \overline{w'^2}$) (Schlichting 1979).

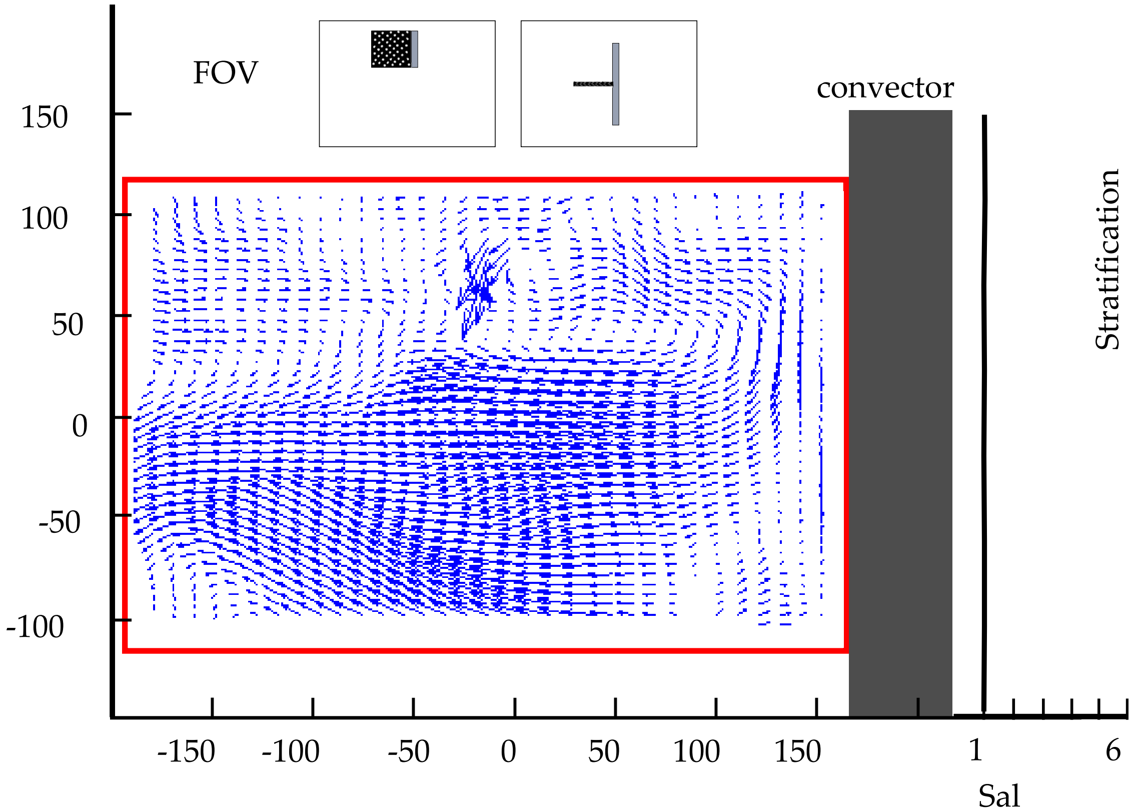

Figure 4.29: Field of view before an average experiment: a vector plot of velocity field indicating marginal particle movement after 20 min settle time (m = 1.89×10^{-2} cms^{-1}).

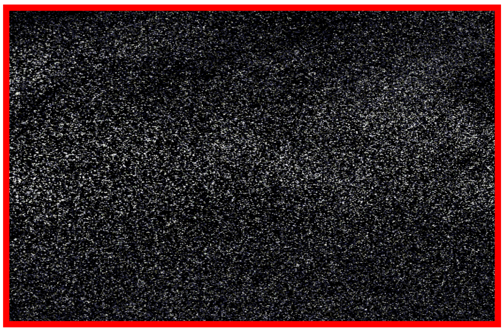

a)

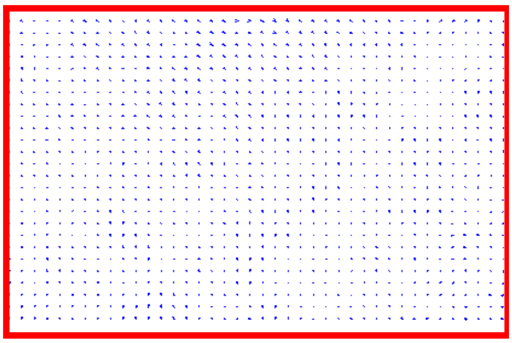

b)

Figure 4.30: Field of view before an average experiment: a) a raw digitised image of a field of view displaying an average degree of seeding; b) a vector plot of velocity field indicating lack of particle movement after 60 min settle time (m = 2.18×10^{-3} cms^{-1}).

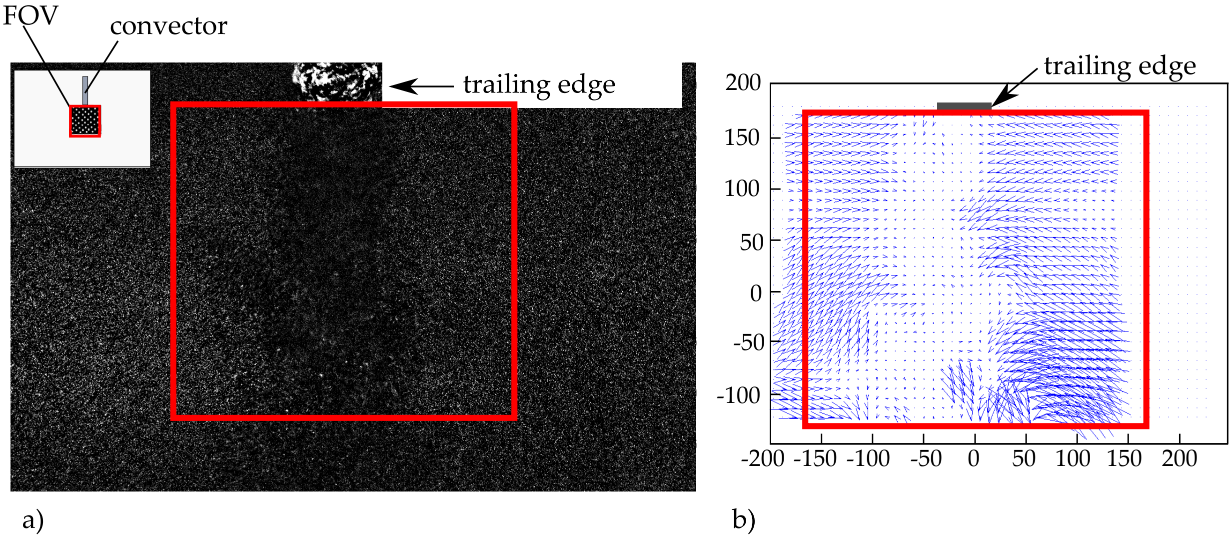

Figure 4.31: Plume development in the far field: a) raw image of uneven particle seeding in a field of view with a developed plume; b) vector plot of velocity field. Field of view (FOV) was directly below the convector, as shown in the schematic showing the tank elevation with the calibration plate marking the FOV.

were quite slow and particles were quite large resulting in good visibility.

The light sheet was formed using a transparent rectangular slot in the side wall blanking material affixed to the end face of the tank, see Figure 4.27. Typically a thin (submillimeter) light sheet is best for a two-dimensional flow as it captures the flow and avoids the errors due to capturing out-of-plane velocities (Raffel et al. 2007, Adrian & Westerweel 2011). An estimate of the thickness of the light sheet is therefore useful. The average light sheet thickness across the field of view (FOV) was calculated to be approximately 1.35 cm thick from the minimum and the maximum thickness of the light sheet in the FOV as shown in Figure 4.32. Measurements of the light sheet give an error of approximately ±10% (±1 mm).

The light sheet was considerably thicker than what is typically used for planar PIV in order to illuminate more particles. A thicker light sheet was used as it was assumed, that the flows of interest were relatively two-dimensional (however, the velocity vector fields extracted indicate that there might be an additional complexity to the induced flows). It was difficult to determine the exact centre of the light sheet and it was assumed that the camera was carefully focused on the FOV plane, which was within the light beam, see Figure 4.32. The light sheet thickness was still relatively thin, which ensured that particles out-of-focus were not seen and not a lot of depth of field was needed. As a result, when the camera was focused, the largest aperture setting was used, which ensured that there was a small depth of field. An additional benefit of a large aperture setting was that more light entered the camera, which was also helpful given the low power of the light source used.

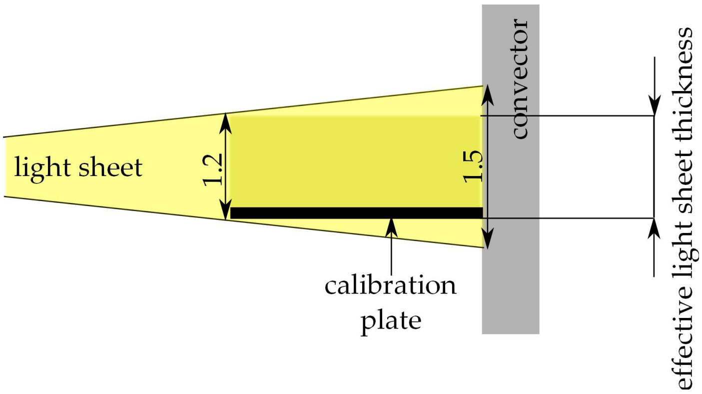

Figure 4.32: Top view of light sheet (dimensions in cm). Divergence angles exaggerated for clarity.

4.5.3.5 Calibration

A calibration was required to scale the camera pixel dimensions to those of the actual FOV. The set-up required for calibration is shown in Figure 4.33. The calibration ensured particle movements were scaled for vector calculation and that the image plane was de-warped. A FOV of dimensions 300 mm × 300 mm was selected. A calibration plate was then positioned in the selected FOV. A calibration plate is a planar calibration target with a uniformly spaced grid of dots which is placed exactly at the position of the light sheet (Wieneke 2005). The calibration plate has a defined separation of marks (dots) (La Vision GmbH 2010). The camera position was adjusted to achieve the correct FOV, perpendicular to the plate with the camera lens level with the centre of the plate. The camera was focused on the calibration plate such that the white dots were in focus and the image scaling was obtained from the known distances between white dots on the plate. The deduced vectors were results from the measured 'in-light-sheet-plane' displacement and the projection onto the light-sheet plane of the out-of-plane component of velocity. The latter is an inherent error which was unrecoverable and may lead to erroneous interpretation of out-of-plane velocities as a non-zero in-plane displacement.

4.5.3.6 Recording

The high speed camera (up to 3260 Hz at full resolution) used was manually triggered to record the illuminated particles in a plane of the flow a number of times within a short time interval. Stevens (2015), based on La Vision GmbH 2010, stated that the frame rate dt to ensure an appropriate particle movement between image frames for vector calculation may be estimated from the following expression:

$$dt = \left(\frac{pix_{shift_x}}{pix_x}\right)\left(\frac{FOV_x}{\mathscr{U}}\right) \tag{4.19}$$

where pix_{shift_x} is a pixel shift, in the range 5-7, pix_x is the width of FOV (in pixels), FOV_x is a width of FOV (in m) and $\mathscr{U}$ is a velocity (ms $^{-1}$).

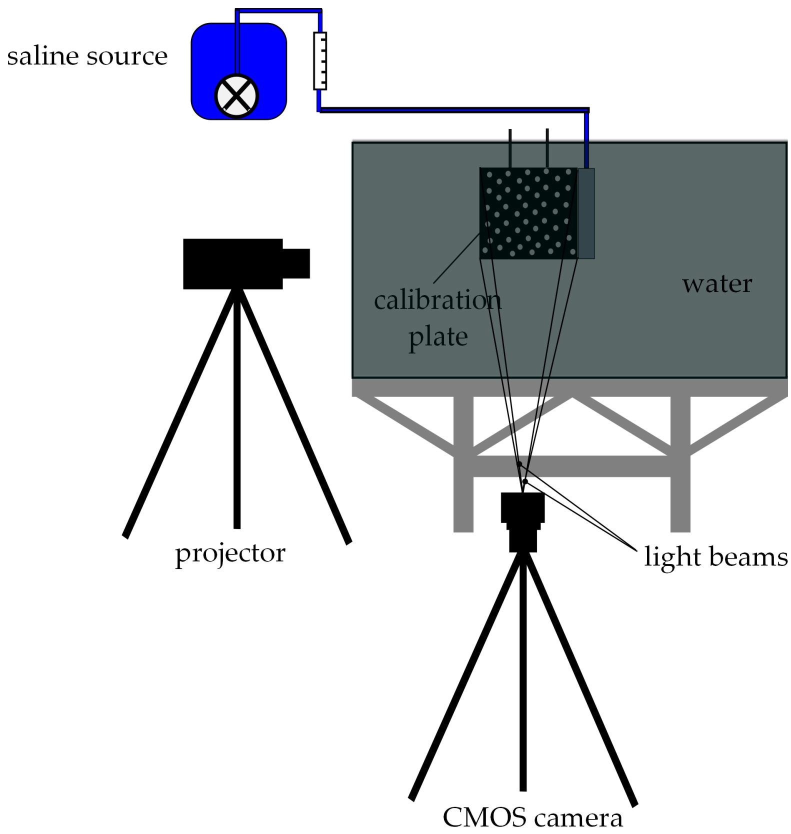

Figure 4.33: Calibration set-up prior to each experiment (black background prepared for the experiments). Calibration was conducted with the tank filled with water and the projector switched off.

The light dispersed by the tracer particles was recorded at the minimum camera acquisition frequency, corresponding to 200 Hz, and a background subtraction with a sliding average of 10 images was conducted to remove any artificial reflection. For all of the PIV results presented, the frequency of acquisition, $\frac{1}{dt}$, was 40 Hz (this was calculated based on the following estimated values: $pix_{shift_x} = 5$, $pix_x = 1280$ pixels, $FOV_x = 0.3$ m and $\mathscr{U} = 0.05\,\mathrm{ms}^{-1}$). Hence the data was oversampled and the correct dt was achieved between every fifth image. The vector calculation was thus performed using every fifth image.

4.5.3.7 Post-processing

DaVis version 8 software was used for velocity vector calculation. Each PIV recording was split into small interrogation windows for post-processing. All the tracer particles within one interrogation window were assumed to move homogeneously (together) between two frames. The local displacement vector was estimated for each interrogation window, based on the statistical method of cross-correlation (Raffel et al. 2007). As a result, a two-component velocity vector was calculated. In this investigation, datasets were not ensemble averaged. This avoids erroneous velocity vector fields caused by the lack of a precise recording trigger, which could result in averaging datasets at slightly different stages of filling. The FOV which was perpendicular to the convector in the central plane was processed with an interrogation window size of 16×16 pixels with 0% overlap, which gives 80 vectors in the x-direction of the FOV. The other FOVs investigated were processed with 24×24 pixels and 0% overlap, which gave 54 vectors in the x-direction of the FOV. Two different resolutions were used for convenience of the set-up. For the FOV of dimensions 300 mm × 300 mm the spacial resolution was 4 pixels/mm. Note that some of the vector-field data contained in this thesis was down-sampled for clarity of presentation.

4.5.3.8 Vorticity, ω

Vorticity ($\omega = \nabla \times \overrightarrow{u}$) is the curl of the velocity field (Batchelor 2010) and is often used to analyse unsteady flows to detect vorticies. Since vorticity requires differentiation of the PIV vector field, any noise in the data will be amplified. The usefulness of vorticity for analysis of the flows of interest in this research is evaluated in Section 7.4, where an example of a distorted vortical structure from the experimental data is shown. In general, however, the calculation of vorticity on the PIV data acquired gave a very noisy field.

4.5.3.9 Comment on PIV error

There are a number of errors associated with the PIV technique (Brossard et al. 2009), including human-related and non-human-related errors. The human-related errors, which are likely to be similar in any experimental technique, may be related to the experimental set-up, measurement inaccuracies, post-processing errors and statistical errors. The non-human-related errors may be caused by external disturbances, such as changes in background lighting, incident stray light reflections, reflections caused by the silver surface of the convector device and out-of-plane motions of the tracer particles (Raffel et al. 2007). Herein, the total experimental error was estimated following the approach undertaken by Stevens (2015) which uses Raffel's Monte Carlo simulation predictions (Raffel et al. 2007). The total estimated error $\mathscr{E}_{tot}$ consists of systematic errors $\mathscr{E}_{bias}$ and residual errors $\mathscr{E}_{rms}$:

$$\mathscr{E}_{tot} = \mathscr{E}_{bias} + \mathscr{E}_{rms}. \tag{4.20}$$

In PIV, errors due to the cross-correlation technique are among the systemic errors. According to Raffel (2007), the systematic errors are predictable due to their constant trend and can be thus removed or accounted for in contrast to the residual errors. An example of a systematic error $\mathscr{E}_{bias}$, due to out-of-plane motion of the tracer particles, resulting in the loss of particle image pairs, was approximately -0.01, based on the Raffel's simulation. This error was based on a 16×16 interrogation window size.

The random error may be broken down into three groups of errors, namely, due to particle image diameter $\mathscr{E}_{rms_0}$, due to particle image displacement $\mathscr{E}_{rms_{dis}}$ and interrogation window particle density $\mathscr{E}_{rms_\rho}$:

$$\mathscr{E}_{rms} = \mathscr{E}_{rms_0} + \mathscr{E}_{rms_{dis}} + \mathscr{E}_{rms_\rho}, \tag{4.21}$$

where based on Raffel's Monte Carlo simulations (Raffel et al. 2007) $\mathscr{E}_{rms_0} \approx 0.01$, $\mathscr{E}_{rms_{dis}} \approx 0.01$ and $\mathscr{E}_{rms_\rho} \approx 0.025$ (estimated assuming average of 10 particles per interrogation window). The sum of all error estimates is the total error $\mathscr{E}_{tot} = 0.035$ pixels which was, assuming $pix_{shift_x} = 5$,[1] equivalent to an error of 1% in velocity.

4.5.4 Salinity measurements with conductivity probes

Salinity conductivity probes were used for instantaneous measurements of density, locally, at a given point of interest. The density results are based on the conductivity measurements of electrolytes in a solution.

4.5.4.1 Background

The Salinity Analyser (aka Conductivity Meter) was designed by Jonathan Fall and Peter Holland (Personal Communication) to measure the conductivity G (μS cm^{-1}) of diluted saline solutions.

4.5.4.2 Application

Figure 4.34 shows schematic of the apparatus required for conductivity measurements. The apparatus consisted of a PC with SalAnalyser Software, a Conductivity Meter, referred to herein as a Salinity Analyser, 25 conductivity probes and a mounting arrangement to hold the probes

[1] A pixel shift in the range 5 to 7 is recommended to ensure a reliable cross-correlation peak (Raffel et al. 2007), thus $pix_{shift_x} = 5$ was deemed appropriate.

in position.

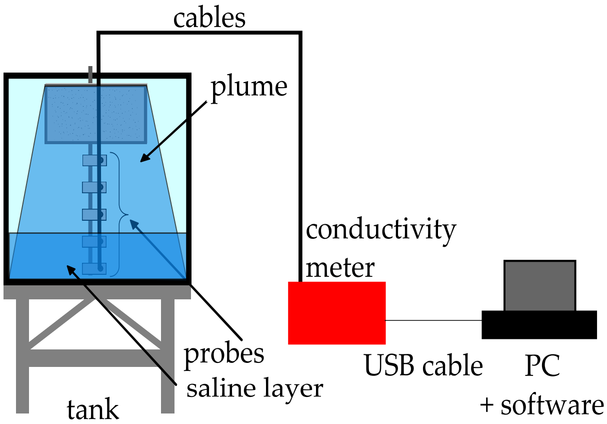

Figure 4.34: Set-up during experiments with salinity probes showing how the apparatus was connected for conductivity measurements. To avoid noise hum the entire electric circuit (conductivity meter, PC) was connected to and charged by the uninterruptible power supply.

4.5.4.3 Measurements

These results were converted into density (in ppt - parts per thousand) in the SalAnalyser Software, based on the following relationships between the units (Weiner 2000):

$$1\ \mu\text{S cm}^{-1} \equiv TDS_{NaCl} \cdot 1\ \text{ppm} \equiv 0.5\ \text{ppm}$$
$$1\ \text{ppt} \equiv 1000\ \text{ppm}$$

In other words, the conductivity G (μS cm^{-1}) was multiplied by the TDS-factor, which for NaCl is equal to 0.5 (Weiner 2000), and divided by 10^3 to convert from ppm to ppt.

Conductivity measurements were taken for the duration of experiment. Figure 4.35 a) shows an example of raw salinity data extracted from a single probe in time. To compare readings from different probes in one figure and to track the increasing trends more closely, the salinity data, shown in Chapter 6, was smoothed using Matlab moving average filter, see examples in Figure 4.35 (b-c). In Chapter 6, whenever smoothed data is shown, a span used is given.

The set of data points from all probes constituted a sample. To ensure that each sample was a good representation of the instantaneous local stratification a relatively short loop time of 2 seconds per sample was chosen. The loop time is the time required to read all the probes (here measurements of each probe were taken 10 times per sample) and create a sample of mean values converted into density. The loop time was less than 1% of the experimental timescale as defined in (4.11). On average samples were taken continuously (every 2 s) with no breaks between sampling.

Samples were also used to create vertical density profiles, see Figure 4.36. Each vertical density profile was a result of interpolation between data points. Each data point within a profile was marked to indicate the position of the corresponding probe. The set of data points

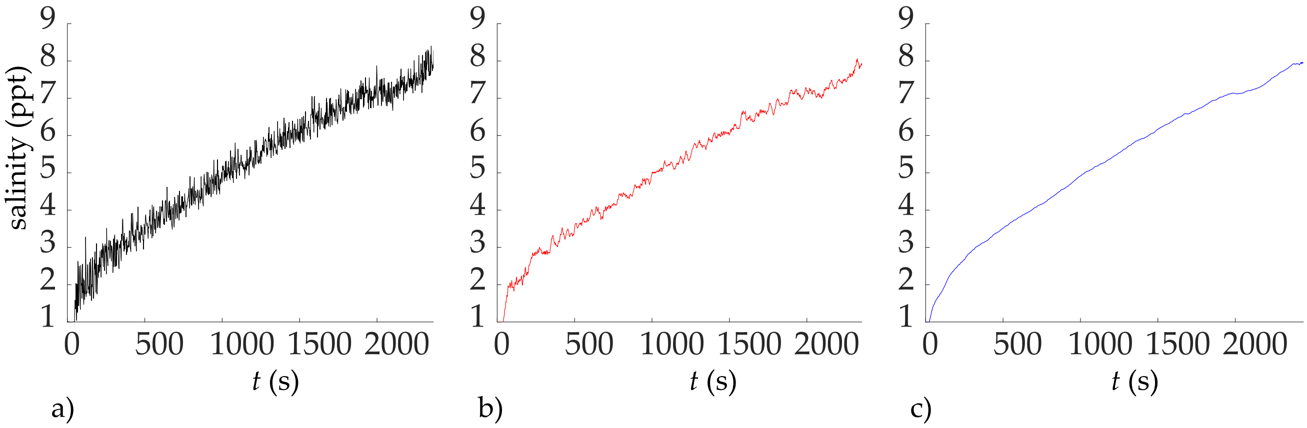

Figure 4.35: Salinity readings from one probe as function of time: a) raw, unsmoothed, data; b) data smoothed using moving average filter with span 9; c) data smoothed using moving average filter with span 99.

from one profile constituted a sample.

4.5.4.4 Calibration

Prior to the start of each experiment the conductivity meter was calibrated. The conductivity meter contained accurate, fixed resistors of known resistance.

4.5.4.5 Comment on salinity measurement error

Averaging each data point over 10 measurements reduced the standard error of the mean by $\frac{1}{\sqrt{10}}$. Independent salinity measurements using a refractometer (Hanna Instruments HI 96821 Sodium Chloride Refractometer) and a densitometer (Anton Paar DMA 5000) were taken prior to each experiment, during selected runs and at the end of each experiment to compare with readings from salinity probes and to ensure reduction of systematic errors.

The calibration curve was continuously updated during each experiment. This dynamic adjustment, while taking measurements, reduced the effects of the temperature changes on electronics. The effect of temperature change on the conductivity readings was observed in the preliminary tests, and found to be approximately 2% per 1 °C. The freshwater and saline solution were prepared a day before experiments to ensure stable thermal conditions. Under these stable thermal conditions, where the temperature difference between the freshwater and saline solution was less than 1 °C, the accuracy of readings was within 1%. Appendix B contains a description of the procedures performed prior to each experiment and relevant additional set-up details, which were added to the basic set-up to control the temperatures of the water and saline solutions.

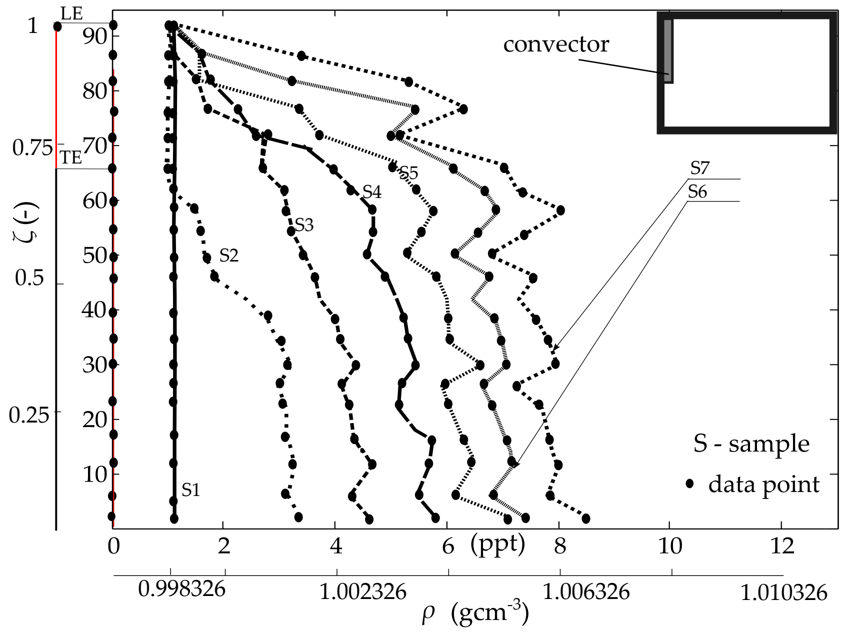

Figure 4.36: Seven vertical density profiles based on seven samples extracted during conductivity measurements. Each profile shows density (in ppt and gcm^{-3}) as a function of vertical position (in cm and non-dimensional, scaled on the height H). Location of the convector shown in tank front elevation. Label'Sx' refers to the sample number taken at a given time instance.

4.6 Statistical methods

Statistical methods were used to systematically quantify and interpret the influence of governing parameters on the rate of room filling and stratification. This was achieved by deriving power-law functions describing the rate of filling and stratification in terms of the non-dimensional governing parameters, where each coefficient of regression represented the influence of a corresponding governing parameter. Based on values of coefficients of regression, governing parameters were classified as either dominant or subordinate.

In order to derive equations describing the filling rate at five subsequent filling periods[1], the output data from all the experiments, referred to as the population, was organised into five subpopulations, based on changes in the flowfield. Figure 4.37 shows an example sequence of filling consisting of five subsequent filling periods corresponding to the five subpopulations: (1) a starting plume, (2) a horizontal current, (3) a vertical intrusion, (4) a horizontal reflection and (5) a vertical filling. Each experiment was divided into these five subsequent periods. The literature survey revealed that all these filling periods were observed in previous filling box experiments (e.g., Baines & Turner 1969, Cooper & Hunt 2010, Caudwell et al. 2016), thus it was expected that each convector-room configuration will go through these five filling periods. Figure 4.38 contains schematics of filling for four convector-room system configurations, where five subsequent filling periods are marked. Figure 4.39 depicts the structure of the population. Each experiment consisted of a number of observations. An observation was a set of results

[1]These relationships are shown in Section 5.3.

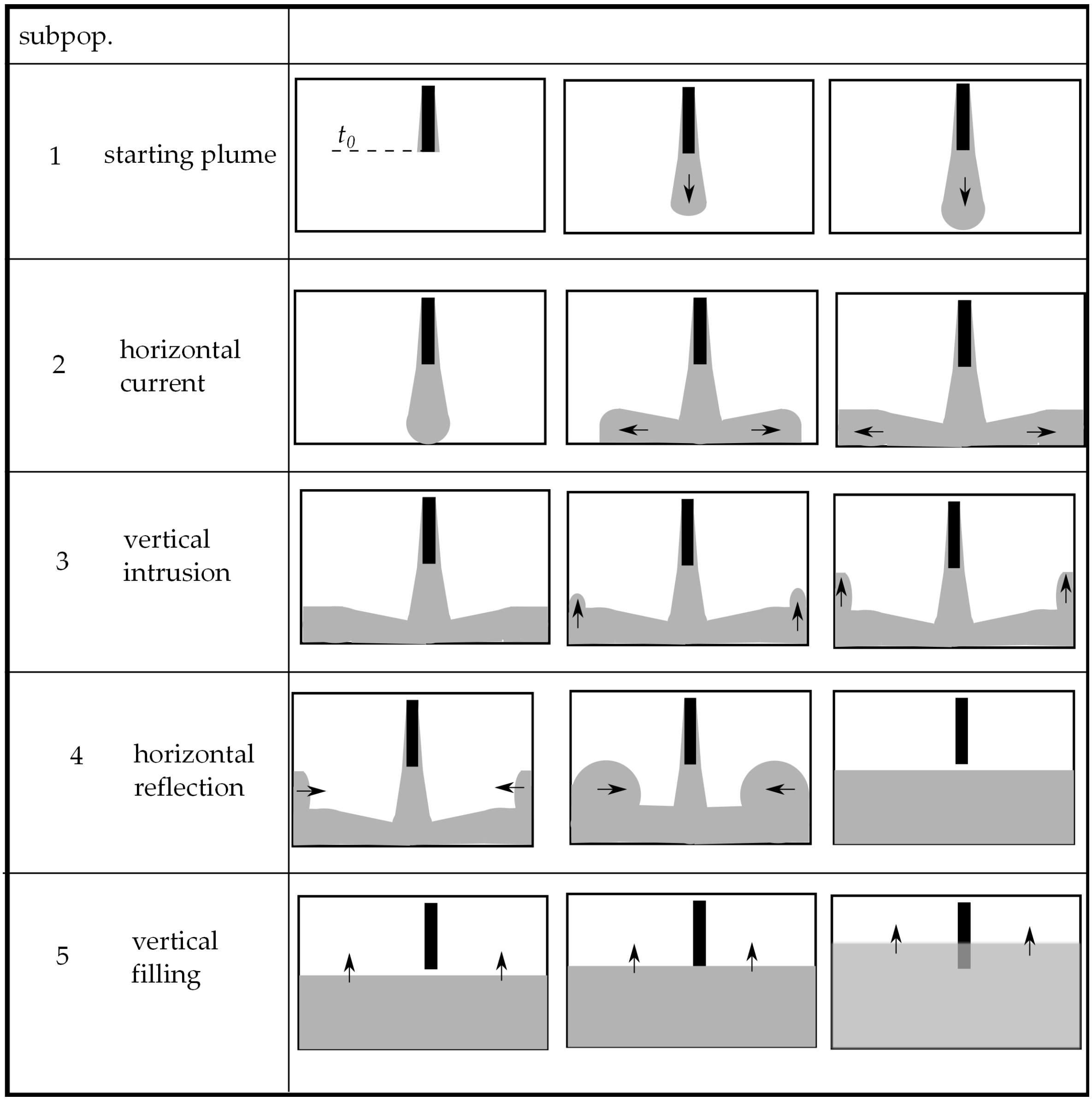

Figure 4.37: Filling periods.

from a time interval Δt, where Δt was contained in one subpopulation, so that each observation was assigned to a specific subpopulation. The equation describing the stratification[1] was derived using the entire population.

The statistical analysis performed consisted of the following five steps:

1. Description of the subpopulation aimed at describing governing parameters.
2. Dimensional analysis based on the Buckigham Π theorem aimed at establishing the non-dimensional governing parameters.
3. Data collection and organisation aimed at preparing experimental data for application in the statistical model.
4. Multiple non-linear regression aimed at finding the power-law functions describing the rate of filling and stratification in terms of the non-dimensional governing parameters.
5. Analysis of the significance of the coefficients of regression and correlation aimed at ensuring that the results are statistically significant.

These steps were performed on each subpopulation. For full description of each step see Przydróżny (1983) and for details of the approach undertaken see Szűcs (1972) and Zierep (1972). The essential elements of the statistical method, which are specific to the application to the convector-induced filling, are now discussed.

4.6.1 Step 1: Description of subpopulations

Figure 4.40 comprehensively summarises each subpopulation by providing a number of observations used in the analysis and presenting schematics corresponding to the beginning, the end and an intermediate state of each subpopulation. For the purposes of the statistical analysis, the beginning of the starting plume was assumed at t_0 (see Figure 4.37), when the plumes developing on each face of the convector descended to the trailing edge, as shown in Figure 4.40. The start of this period was therefore not equivalent to the start of the experiment t_{start}, see Figure 4.18. The time lag between t_{start} and t_0 was caused by the supply pipework filling with saline and air bubbles releasing from the convector pores upon switching on the supply pump. The time lag was proportional to the height of the convector $\mathcal{L}$. For the horizontal orientation ($\mathcal{L}$ = 30 cm) an average time lag was 5 s, whereas for the vertical orientation ($\mathcal{L}$ = 60 cm) 15 s. The end of subpopulation 1, corresponding to the beginning of subpopulation 2, was marked by the impingement of the starting plume on the base of the tank. The end of subpopulation 2 was marked by the impingement of the horizontal current on the side wall of the tank, whereas the end of subpopulation 3 corresponded to the vertical intrusion reaching its maximum height. Finally, establishing an even horizontal interface across the tank marked the end of subpopulation 4 and the subpopulation 5 lasted until the experiment was terminated.

[1]The relationship is shown in Section 6.3.

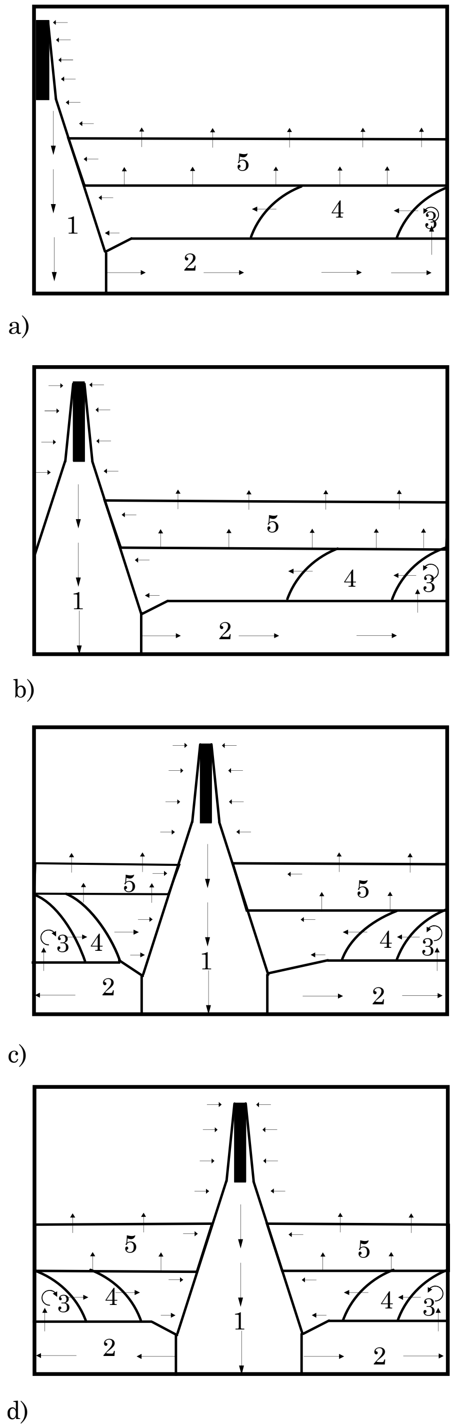

Figure 4.38: Filling flows: 1 - starting plume, 2 - horizontal current, 3 - vertical intrusion, 4 - horizontal reflection, 5 - vertical filling; a) confined case - wall-mounted convector, plume attached to the side wall (1) and unidirectional bulk flows in (2-4); b) semi-confined case - convector in close proximity to side wall, plume partially confined by the side wall (1) and unidirectional bulk flows in (2-4); c) unconfined case - convector far from side wall, unrestricted plume (1) and bidirectional bulk flows in (2-4); d) unconfined symmetrical case - convector in the middle and bidirectional bulk flows and symmetrical in (2-4). Arrows indicate flow direction.

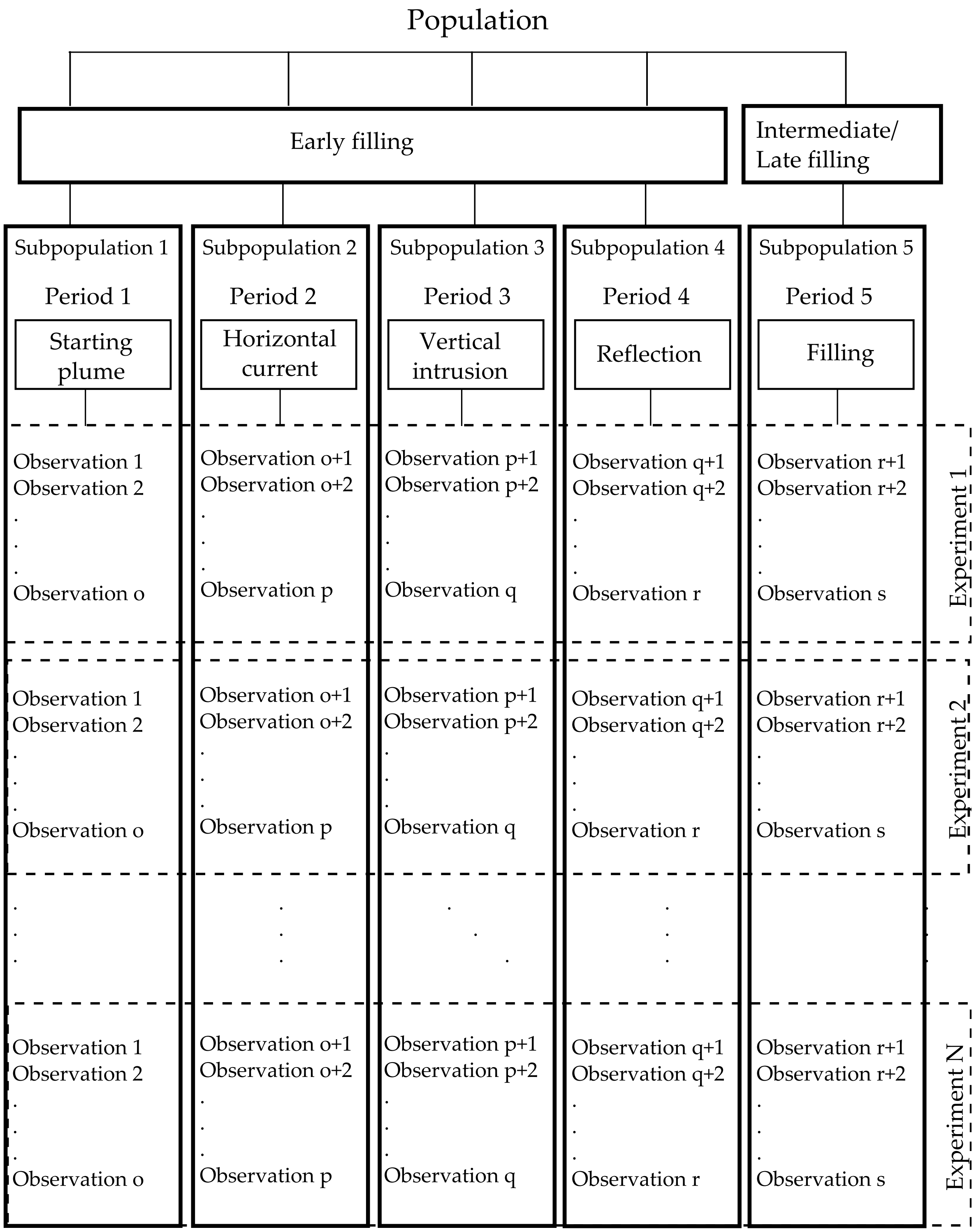

Figure 4.39: Experimental data set prepared for statistical analysis. Population consisted of 5 subpopulations. Each subpopulation was created from a number of observations. A number of observations o≠ p-o ≠ q-p ≠ r-q ≠ r-s was not identical for each experiment and depended on the experimental set-up.

subpop.	no. observations	start of subpopulation	intermediate	end of subpopulation
1	1582	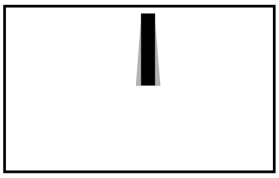	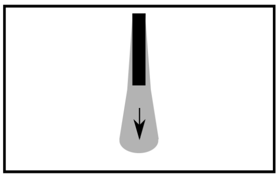	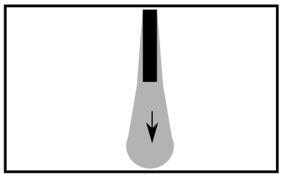
2	4196	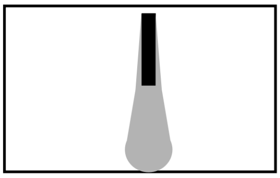	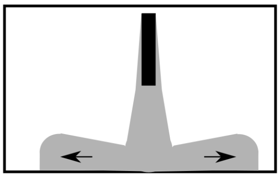	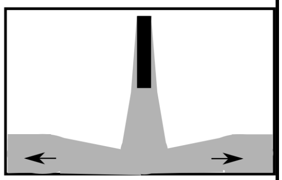
3	1105	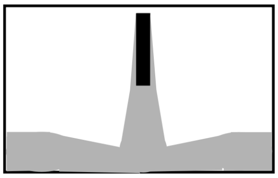	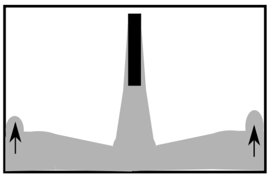	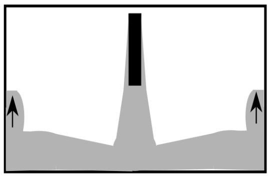
4	3050	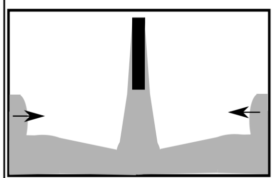	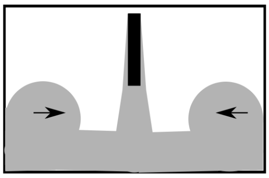	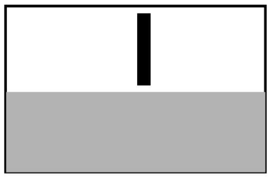
5	108979	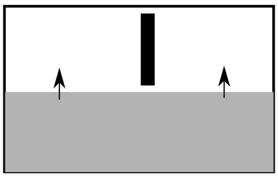	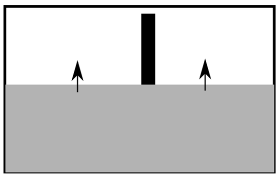	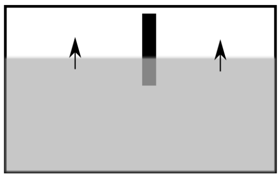

Figure 4.40: Filling periods (subpopulations) considered during statistical analysis: a number of observations, the beginning, the end and an intermediate state.

4.6.2 Step 2: Dimensional analysis

The dimensional analysis undertaken consisted of the following six steps (Munson et al. 1990):

1. Making a list of all the variables describing the flow in each subpopulation.
2. Expressing each variable by the basic units.
3. From Buckingham Π theorem determining the number of Π terms required.
4. Selecting the repeating variables
5. Forming the non-dimensional Π term by multiplying a non-repeating variable by the product of the repeating variables, each raised to an appropriate exponent to meet the requirement of non-dimensionality of the combination. Performing this step on each non-repeating variable and ensuring that all the Π terms are non-dimensional.
6. Expressing the final equation as a relationship between the Π terms.

Dimensional analysis is a common technique used in variety of engineering applications, therefore a detailed breakdown of each step is not included in the thesis. A crucial and unique to convector-induced experiments is a list of variables used to describe the flow in each subpopulation, see Table 4.3.

The dimensional analysis was concluded by establishing the following expressions used to describe filling rate ($\mathfrak{R}$) of horizontal flows (subpopulations 2 and 4) and vertical flows (subpopulations 1, 3 and 5), and stratification ($\mathfrak{I}$) of the entire population:

$$\mathfrak{R} = \beta_0 \Delta Ra^{\beta_1} \mathcal{B}^{\beta_2} \mathcal{G}^{\beta_3} \mathbf{T}^{\beta_4}. \tag{4.22}$$

$$\mathfrak{R} = \beta_0 \Delta Ra^{\beta_1} \mathcal{B}^{\beta_2} \mathcal{G}^{*\beta_3} \mathbf{T}^{\beta_4}. \tag{4.23}$$

$$\mathfrak{I} = \beta_0 Ra^{\beta_1} \mathcal{B}^{\beta_2} \mathcal{G}_{pr}^{\beta_3} \mathbf{T}^{\beta_4}. \tag{4.24}$$

The filling rate of each subpopulation was described in terms of the non-dimensional parameter:

$$\mathfrak{R} = \frac{\Delta\rho}{\rho_0} \cdot \frac{g\Delta t^2}{\Delta z} = \frac{g'\Delta t}{\Delta u} \tag{4.25}$$

where Δu is a rate of displacement. The $\mathfrak{R}$ number is therefore a ratio of the velocity induced by the buoyancy input and the resulting rate of displacement.

The stratification was described by the non-dimensional parameter:

$$\mathfrak{I} = \frac{\Delta\rho}{\rho_0} \tag{4.26}$$

which is a ratio of density difference (captured by salinity probes) and the ambient density. Both numbers, $\mathfrak{R}$ and $\mathfrak{I}$, are dependent variables, therefore they were represented as functions

variables	subpop. 1	subpop. 2	subpop. 3	subpop. 4	subpop. 5
Δt	√	√	√	√	√
t_{cum}	√	√	√	√	√
$\mathcal{T}_{exp}$	√	√	√	√	√
g	√	√	√	√	√
H	√	√	√	√	√
$H-\mathcal{L}$	√	√	√	√	√
a	√	√		√	
B_0	√	√	√	√	√
$\Delta\rho$	√	√	√	√	√
ρ_0	√	√	√	√	√
ν	√	√	√	√	√
D	√	√	√	√	√
Δz	√				
Δx		√			
$\Delta z'$			√		
$\Delta x'$				√	
$\Delta z''$					√

Table 4.3: List of variables to describe the flow in each subpopulation, where: Δt - time of observation, t_{cum} - cumulative time from t_0 to the end of the observation, $\mathcal{T}_{exp}$ - time scale of filling, see eq.(4.11), g - acceleration due to gravity, H - vertical distance between the convector leading edge and the base of the tank, $H-\mathcal{L}$ - vertical distance between the trailing edge and the base of the tank, a - horizontal distance between closer side wall and convector face, B_0 - buoyancy flux of convector, $\Delta\rho$ - density difference, ρ_0 - density of ambient fluid, ν - kinematic viscosity, D - diffusivity, Δz - vertical displacement of starting plume during observation, Δx- horizontal displacement of horizontal current during observation, $\Delta z'$ - vertical displacement of vertical intrusion during observation, $\Delta x'$ - horizontal displacement of horizontal flow reflecting during observation, $\Delta z''$ - vertical displacement of front ascending during observation.

of four independent, non-dimensional governing parameters:

- the non-dimensional accumulation $\mathcal{B}$;
- the non-dimensional Rayleigh number Ra;
- one of the non-dimensional geometric parameters: $\{\mathcal{G} = \frac{a}{H-\mathcal{L}}, \mathcal{G}^* = \frac{H-\mathcal{L}}{H}, \mathcal{G}_{pr} = \frac{z_{pr}}{H}\}$;
- the non-dimensional time $\mathbf{T}$.

This particular non-dimensional governing parameters were selected, during the dimensional analysis, instead of other possible groups, as they are sensible on physical grounds, take into account sequencing of the filling flows and can be easily varied between the experiments. The definition of geometric parameter varied in expressions describing vertical flows, horizontal flows and stratification (see Section 4.6.2.3).

4.6.2.1 Non-dimensional accumulation

The non-dimensional accumulation:

$$\mathcal{B} = \frac{B_0 \Delta t^3}{\Delta z^4}, \tag{4.27}$$

was calculated for each observation, where the buoyancy flux of the convector B_0 was scaled on the displacement $\{\Delta z, \Delta x, \Delta z', \Delta x, \Delta z''\}$ and time Δt of the observation.

4.6.2.2 Rayleigh number

Rayleigh number, defined in Section 4.2.2, is a ratio of forces that are driving and retarding flows. To define $\mathfrak{R}$, a local formula of Rayleigh number:

$$\Delta Ra = \frac{g' \Delta z^3}{\nu D}, \tag{4.28}$$

was used, where a displacement $\{\Delta z, \Delta x, \Delta z', \Delta x, \Delta z''\}$ over Δt, measured for each observation, is a characteristic length and g' is the source buoyancy. The local ΔRa was used to track the instantaneous changes in the balance of the driving and retarding forces and to investigate the influence of the force balance on the displacement rate of each filling flow.

The non-dimensional stratification parameter $\mathfrak{I}$ is a function of the global Rayleigh number:

$$Ra = \frac{g' H^3}{\nu D}, \tag{4.29}$$

with the height H as a characteristic length. As a result, the global Rayleigh number was constant in $\mathfrak{I}$ and represented the influence of the system configuration.

4.6.2.3 Non-dimensional geometric parameter

A non-dimensional geometric parameter is a ratio representing the dependency of a given filling flow on the system configuration. The non-dimensional geometric parameter was, thus, defined individually for vertical flows and horizontal flows. The position of the convector, relative to the side wall and the base of the tank, had an impact on the starting plume. In order to understand the influence of the vertical and horizontal position of the convector on the starting plume, two statistical analyses were conducted, so that two different definitions of geometric parameter could be used. The definition of the geometric parameter used in the global $\mathfrak{I}$ varies from the definition used to define flow in subpopulations and corresponds to the relative vertical position of the salinity probe in the tank.

Vertical flows

For vertical flows, such as a starting plume (subpopulation 1), a vertical intrusion (subpopulation 3) and filling (subpopulation 5), the geometric parameter was expressed as a ratio of the vertical distance between the trailing edge of convector and the base of the tank, $H - \mathcal{L}$, relative to the height H:

$$\mathcal{G}^* = \frac{H - \mathcal{L}}{H}. \tag{4.30}$$

Horizontal flows

For horizontal flows (subpopulations 2 and 4) the geometric parameter was the ratio between the distance of the convector to the side wall a and the vertical distance $H - \mathcal{L}$:

$$\mathcal{G} = \frac{a}{H - \mathcal{L}}. \tag{4.31}$$

Comment on horizontal position of the convector

A starting plume may be: confined, partially confined and unconfined, depending on the convector's position relative to the side wall (see Figure 4.38). As a consequence, despite being a vertical flow, a starting plume was expected to be influenced by both vertical and horizontal geometric parameters. The influence of both geometric parameters was tested during two independent statistical analyses.

Comment on characteristic length for salinity measurements

An example of statistical analysis performed on the non-unidirectional flow was when the entire population was used to find $\mathfrak{I} = f(\mathcal{B}, Ra, \mathcal{G}_{pr}, \mathbf{T})$. With the instantaneous readings from salinity probes $\Delta\rho$, the geometric parameter used is:

$$\mathcal{G}_{pr} = \frac{z_{pr}}{H} \tag{4.32}$$

where z_{pr} is a position of a probe, scaled on the height H. Each probe had an individual value of $\mathcal{G}_{pr}$, hence the position of the probe was accounted for in the statistical analysis.

4.6.2.4 Non-dimensional time

The non-dimensional time used in the statistical analyses is defined as:

$$\mathbf{T} = \frac{t_{cum}}{\mathcal{T}_{exp}}, \tag{4.33}$$

where t_{cum} is a cumulative time from t_0, when plumes developing on each face of the convector descended to the trailing edge, to the end of a given observation, and $\mathcal{T}_{exp}$ is the characteristic time scale of an experiment, for definition see Section 4.5.1.5.

4.6.3 Step 3: Data collection

The next step in the statistical analysis was the preparation of the output data. The data collected during the experiments was organised in a matrix. All variables were recorded during each observation. Consider a starting plume, Figure 4.41 shows how the flow displacement Δz in time Δt (= 1s) was extracted from each recording. The following method was applied to each subpopulation.

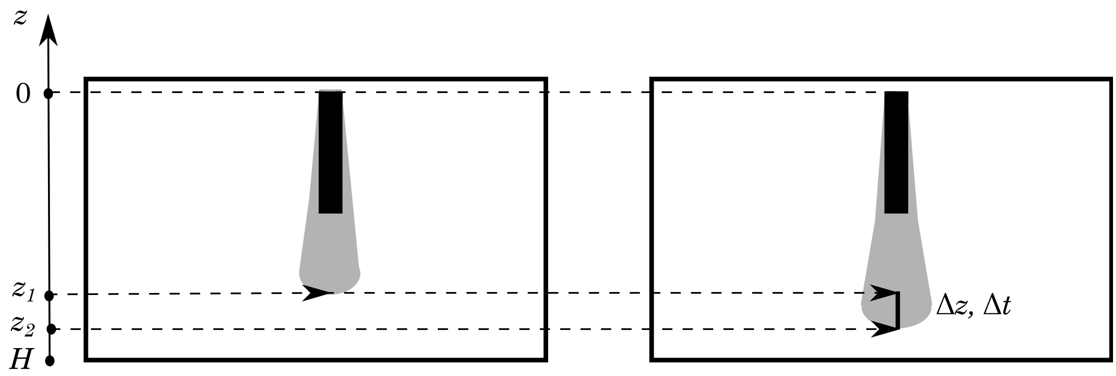

a) Vertical intrusion z_1 at time t_1 b) Vertical intrusion z_2 at time t_2

Figure 4.41: Schematic of technique used measure flow displacement Δz in time Δt.

4.6.4 Step 4: Multiple non-linear regression

Once, the data set was collected and organised, the method of non-linear regression was used to find β-coefficients to complete the empirical expressions derived. Consider $\mathfrak{R}$ (the same method was used to close expression $\mathfrak{I}$), the logarithm of equation (4.22) was taken:

$$ln(\mathfrak{R}) = ln(\beta_0) + \beta_1 ln(Ra) + \beta_2 ln(\mathcal{B}) + \beta_3 ln(\mathcal{G}) + \beta_4 ln(\mathbf{T}). \tag{4.34}$$

Say

$$\begin{aligned} y &= ln(\mathfrak{R}) \\ x_1 &= ln(Ra) \\ x_2 &= ln(\mathcal{B}) \\ x_3 &= ln(\mathcal{G}) \\ x_4 &= ln(\mathbf{T}) \end{aligned}$$

then the equation (4.34) may be rewritten as:

$$y = ln(\beta_0) + \beta_1 x_1 + \beta_2 x_2 + \beta_3 x_3 + \beta_4 x_4. \tag{4.35}$$

Due to the the large number of observations and sufficient operational memory of a computer, calculations of coefficients β_i and analysis of significance of these coefficients were carried out in Matlab. The formula (4.35) was saved as a function in Matlab. Then, a multiple non-linear regression was performed in Matlab using nlinfit. The outcomes of the non-linear regression were the closed empirical expressions describing the filling and stratification. Also, the classification of governing parameters into dominant and subordinate was established. These results are discussed in Sections 5.3 and 6.3.

4.6.5 Step 5: Analysis of significance of coefficients of regression and correlation

To evaluate the results of non-linear regression, an analysis of significance of coefficients of regression and correlation was performed. Equations used herein are commonly used to verify statistical results (Montgomery & Runger 2011, Spiegel & Stephens 2011). For each empirical equation, the coefficient of multiple correlation R was calculated to measure a degree of correlation of the dependent variable to the independent variables:

$$R = \sqrt{\left(1 - \frac{\sum_{l=1}^{n}(y_l - \hat{y}_l)^2}{\sum_{l=1}^{n}(y_l - \overline{y})^2}\right)}, \tag{4.36}$$

where
y_l - the value of dependent variable in the l-th observation;
$\overline{y}$ - the arithmetic mean of dependent variable;
$\hat{y}_l$ - the value of regression of the dependent variable in the l-th observation.

The value of coefficient of multiple correlation R may be between 0 and 1, where correlation improves as R approaches 1.

In order to estimate quality of each coefficient of regression in each empirical expression derived, additional measures, which are commonly used in statistical analyses, were calculated. The mean squared error was estimated from:

$$s^2 = \frac{\sum_{l=1}^{n}(y_l - \hat{y}_l)^2}{n - k - 1}, \tag{4.37}$$

where n is a number of observations and k denotes a number of independent variables.

Subsequently, the s^2 - values were used in the analysis of significance of coefficients of regression to calculate the standard deviation of each coefficient. The analysis of significance of each coefficient of regression was performed based on verification of the zero - hypothesis $\mathcal{H}_0$: $\beta_i = 0$, in relation to the alternative hypothesis: $\beta_i \neq 0$. For each coefficient of regression β_i the hypothesis $\mathcal{H}_0$ was made and the value of statistic t_{Stu} was calculated from the following formula:

$$t_{Stu} = \frac{\beta_i - 0}{s_{\beta_i}} \tag{4.38}$$

where β_i denotes the coefficient of regression and $s_{\beta_i} = \sqrt{s^2_{\beta_i}}$ is the standard deviation of coefficient of regression, which was estimated from:

$$s_{\beta_i} = \sqrt{s^2 d_{ii}}, \tag{4.39}$$

where d_{ii} is the i-th diagonal element of $(\mathbf{X}^T\mathbf{X})^{-1}$ matrix. Here $\mathbf{X}$ expresses the matrix of independent variables (values of x_i that will be extracted from experiments). The size of the matrix is $n \times 5$, with n the number of observations. The first four columns will be populated by the independent variables and the last column of ones (this is how a variable is assigned to a free coefficient $ln(\beta_0)$). Let n be a number of observations. Hence,

$$\mathbf{X} = \begin{bmatrix} x_{11} & x_{12} & \dots & x_{14} & 1 \\ x_{21} & x_{22} & \dots & x_{24} & 1 \\ \dots & \dots & \dots & \dots & 1 \\ x_{n1} & x_{n2} & \dots & x_{n4} & 1 \end{bmatrix} \tag{4.40}$$

The statistic defined by eq. (4.38), when $\mathcal{H}_0$ is true, has a t-student distribution with $n-k-1$ degrees of freedom. From the t-Student distribution table for $n-k-1 \approx \infty$ degrees of freedom and for the level of significance $\gamma = 0.05$ (5%), the critical value $t_{Stucr} = 1.645$ (Lindley & Scott 1984).

The analysis of significance of coefficients of correlation was based on F-statistic, calculated from:

$$F = \frac{R^2(n-k-1)}{(1-R^2)k} \tag{4.41}$$

where:
F - F - statistic;
R - multiple correlation coefficient.

For the zero - hypothesis $\mathcal{H}_0$: $\mathcal{R} = 0$, the F-statistic, defined in eq. (4.41), has the F-Snedecor distribution and no correlation between dependent and independent variables. To verify the zero - hypothesis, the values of F-statistic were compared with the critical F-value for $n-k-1$ degrees of freedom and for the level of significance $\gamma = 0.05$ (5%), $F_{cr} = 5.63$ (Lindley & Scott 1984).

The confidence intervals of coefficients of regression were calculated based on the standard deviations eq. (4.39):

$$l_{\beta_i} = \pm t_{\infty,\gamma} \cdot s_{\beta_i} \tag{4.42}$$

where:
l_{β_i} - confidence limits of coefficient of regression β_i;
$t_{\infty,\gamma}$ - critical value of t-student distribution for ∞ degrees of freedom and level of significance γ;
s_{β_i} - standard deviation of coefficient of regression.

The average confidence interval was calculated based on the standard deviation of regression:

$$l_y = \pm t_{\infty,\gamma} \cdot s \tag{4.43}$$

where:
l_y - mean confidence limits of regression;
$t_{\infty,\gamma}$ - critical value of t-Student distribution for ∞ degrees of freedom and level of significance γ;
s - standard deviation of regression.

4.7 Performance evaluation

The literature review revealed that there is no dedicated strategy to evaluate the efficiency of convector-induced filling and stratification. If there are two identical rooms, each with a convector of identical strength but with different size and location, the question arises as to how an objective assessment can be made as to which convector is better at heating the room. In this thesis, two methods of evaluating efficiency are proposed and applied to saline-in-water experiments. Firstly, the corresponding filling rates are compared, based on the first front position in time, and stratifications are compared, based on density measurements. These comparisons enable the establishment of relationships between increasing the filling rate and developing a more uniform environment, and the system configuration. As a consequence, the interplay between the stratification and filling rate can be confirmed. The results of the analysis, based on this methodology, are outlined in the next two chapters. Secondly, there is a need for performance indicators dedicated to the assessment of the entire convector operation. Indicators, developed by Coffey & Hunt (2007a), inspired establishing new performance indicators, based on the ability to accumulate buoyancy.

4.7.1 Room-averaged performance indicator I_R

The global performance indicator I_R is defined to assess how much buoyancy is accumulated within the entire room, relative to a benchmark case, where, at $t = 0$, the entire volume would be uniformly filled with fluid of design density ρ_d and the convector would maintain the room density at ρ_d ($\Delta\rho = \rho_d - \rho_0 = \text{const}$) for the time interval δt. The room-averaged performance indicator I_R is defined as:

$$I_R = \frac{\int\limits_{t}^{t+\delta t} S \int\limits_{0}^{H} g'(z,t)\mathrm{d}z\mathrm{d}t}{\int\limits_{t}^{t+\delta t} S \int\limits_{0}^{H} g'_d \mathrm{d}z\mathrm{d}t}$$

where $g'(z,t)$ denotes buoyancy at height z and time t. This expression assumes a lack of horizontal stratification and a buoyancy change in vertical direction only. For cases where the buoyancy changes with (x,y) the expression can be modified accordingly. Without any loss of generality the time origin can be shifted and new limits defined as: $t_1 = 0$ and $t_2 = \delta t$. Assuming that the design buoyancy, $g'_d(z,t) = g'_d = \text{const}$, is independent of both time t and vertical position z, the room-averaged performance indicator may be rewritten as:

$$I_R = \frac{1}{\delta t g_d' H} \int_0^{\delta t} \int_0^{H} g'(z,t)\, \mathrm{d}z\mathrm{d}t. \tag{4.44}$$

The global parameter allows the evaluation of the filling opportunities that a given convector provides and a comparison with other convectors. For fixed values of total buoyancy accumulated, the value of I_R would be lower in 'taller' rooms. Note that, unlike the Coffey & Hunt's (2007a) indicators, the global room-averaged performance indicator I_R is unrestrained, hence in the limit as $\delta t \to \infty$, $I_R \to \infty$. Nevertheless, the current definition of I_R does not restrict its application because, in a well-insulated room, when left to overheat, at $t \gg 0$, the room temperature may approach the temperature of the surface of the convector, which is much higher than T_d, hence $I_R \gg 1$. Defined in this way, the global performance indicator I_R fails to provide any information on the stratification. Consider two identical spaces, one which is stratified and one which is well-mixed. These spaces may have identical room-averaged indicators, provided that the same amount of buoyancy accumulates in each space. As a result, there is a need for a local assessment of stratification.

4.7.2 Local zone indicator I_Z

The local performance indicator I_Z, applied to assess stratification within a room, is defined as:

$$I_Z = \frac{1}{\delta t g_d'(z_2 - z_1)} \int_0^{\delta t} \int_{z_1}^{z_2} g'(z,t)\mathrm{d}z\, \mathrm{d}t. \tag{4.45}$$

The local performance indicator defined in the following way allows an assessment of how much heat is accumulated in a horizontal slice (zone), between heights z_1 and z_2, over a time interval δt. I_Z is scaled similarly to the global performance indicator I_R, except that the height H is replaced by the vertical distance $(z_2 - z_1)$. The selection of the zones to evaluate using I_Z is driven by the application. The convector-room system is an example of occupied space. The use of a convector is thus dedicated to ensure the comfort of people occupying the space. Two basic zones to test within any occupied space are: the occupied zone and the above occupied zone. The occupied zone corresponds to a location within a space where occupants usually reside (ASHRAE 2015). The depth of each zone depends on the room height, the occupants' location and position (sedentary or standing). Figure 4.42 outlines the extent of occupied zone in accordance to ASHRAE Standard 55. The main objective of convector operation is to rapidly establish and subsequently maintain comfort within the occupied zone. The comfort conditions correspond to establishing design conditions (application specific) and ensuring that the vertical temperature (density) difference between the head and ankle levels is not above the acceptable level (ASHRAE 2015). In order to verify how uniform the occupied zone is, sub-zones within the occupied zone can be evaluated, such as: the 'breathing' zone (level of head) and the 'walking' zone (level of ankles). In this thesis, the performance indicators, within these four zones, namely the occupied zone (OZ), the above occupied zone (AOZ), the breathing zone (H) and the walking zone (F) were simulated during small-scale experiments and evaluated.

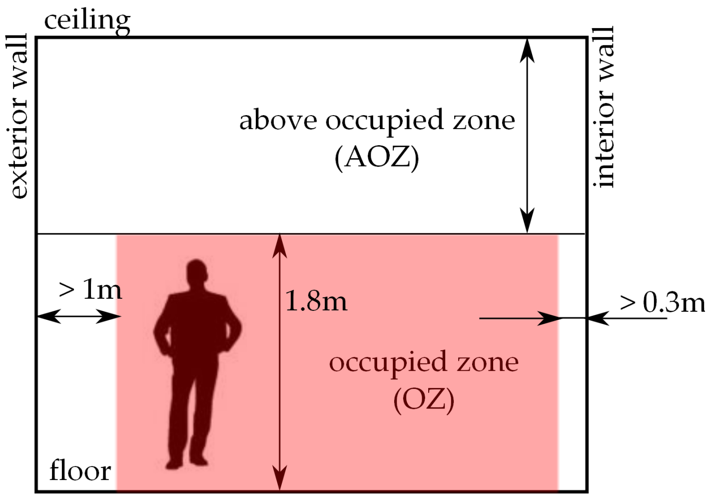

Figure 4.42: Extent of occupied zone (based on ASHRAE 2015).

4.7.3 Scaling of performance indicators

Universal interpretation of any indicators relies on transparency of the scaling applied. Scaling is a crucial element of defining each performance indicator, because it allows instantaneous, quantitative comparisons between different performance indicators. Performance indicators are time-, space- and strength-averaged. This scaling enables direct comparisons between the performance of convectors in spaces of different sizes as well as direct comparisons of buoyancy accumulation within distinct zones of a space. Values of performance indicators can be either positive or negative, to account for buoyancy gains and losses. A value of performance indicator $I = 1$ corresponds to accumulating enough buoyancy to ensure design conditions within a zone for a time interval δt. The shorter the time required to reach this state, the better is the convector. A state at $I = 1$ is not however equivalent to design conditions. To establish $I = 1$, 'overperformance' is required, to account for a time lag in reaching the design conditions.

4.7.4 Rosette Diagram

The rosette diagram was developed to convey the results of efficiency evaluation in a more comprehensive way. Figure 4.43 shows an example of a rosette developed, based on salinity readings, where I_R corresponds to the global performance indicator, I_{OZ} - (local) occupied zone performance indicator, I_{AOZ} - (local) above occupied zone indicator, I_{max} - (local) performance indicator monitoring zone with maximum buoyancy accumulation (herein = I_{AOZ}), I_H - (local) breathing zone performance indicator, I_F - (local) walking zone performance indicator. A rosette diagram consists of lines that extend radially from the origin, set at $I = 0$. These half lines are axes that are used to display values of selected performance indicators. Each axis is assigned to a specific performance indicator. Instead of drawing separate scales on each axis, a global scaling, in the form of concentric circles with the centre at $I = 0$, is used. The absolute values of indicators increase as the radius increases. For time t, instantaneous results of performance indicators are displayed as points on the designated axes. These points are connected to create contours, referred to as the instantaneous room signature. A rosette may consist of either a single (as shaded in example in Figure 4.43) or many signatures. The order of performance indicators on the rosette is predetermined. The right side of the rosette is for performance indicators that quantify layers in the occupied zone and the left side depicts performance indicators of layers above the occupied zone. A comparison between the right and left-hand sides enables evaluation of the filling efficiency. The right side displays useful buoyancy that directly improves comfort and the left side depicts unused, accumulated buoyancy that is stored in inaccessible, upper regions. In principle, by inspection, i.e. looking at the shape of the signatures, it can be seen as to whether the room is strongly stratified or not. For instance, regular shapes of the signatures correspond to well-mixed enclosures (Figure 4.44 a), whereas sharp, irregular shapes imply thermal stratification (Figure 4.44 b).

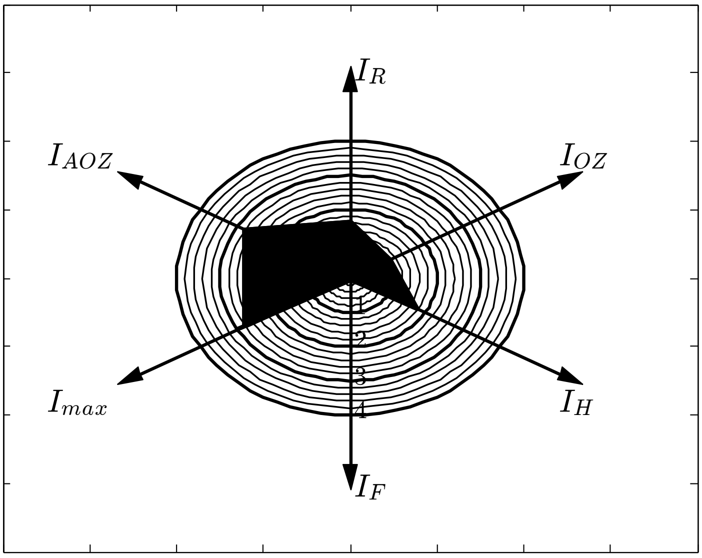

Figure 4.43: Example rosette

4.8 Summary

Experimental methods, introduced in this chapter, have been designed for small-scale buoyancy-driven convector-induced filling flows. Small-scale saline-in-water experiments will be conducted to ensure large Rayleigh numbers. Qualitative data will be obtained from two visualisation techniques: dye-attenuation and shadowgraph. Quantitative data will be obtained from dye-attenuation, PIV and salinity measurements. The density field will be obtained from dye-attenuation and density profiles from salinity measurements. Interface position will be estimated from time series extracted from dye-attenuation recordings. A PIV arrangement with a single high speed camera and single light sheet of white light will be used for velocity measurements. Table 4.4 summarises the estimated errors of the three quantitative methods. The statistical method has been designed to derive empirical expressions describing the filling rate

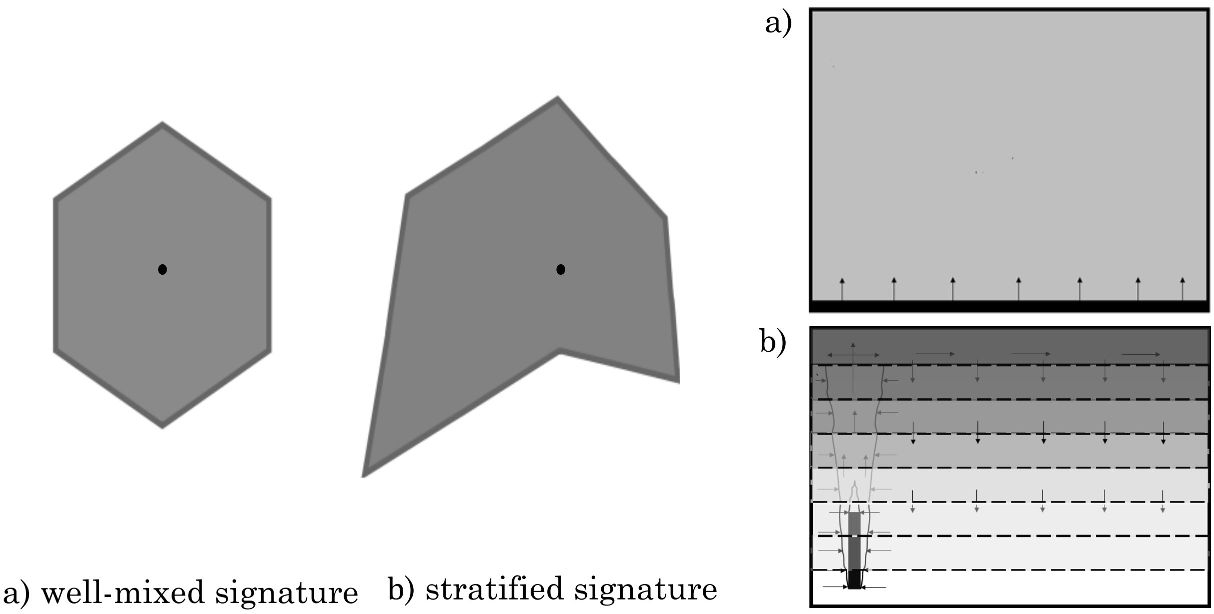

Figure 4.44: Interpretation of rosettes.

at different stages of filling and the developing stratification. The non-linear regression allows closing the expressions and verifying the impact of each governing parameter on the filling rate and stratification. Finally, two methods of evaluating the efficiency of convector-induced filling have been developed. The first method relies on the direct comparisons of data extracted from experiments and assesses the instantaneous performance of convector. The second method is based on the newly-developed performance indicators that have been developed to evaluate the operation of convector through the history of filling.

Method	Variable	Maximum Error
Dye-attenuation	Interface position	10%
Dye-attenuation	Density (field)	24%
PIV	Velocity	1%
Salinity measurement	Density (multiple points)	1%

Table 4.4: Error estimates for quantitative measurements during small-scale experiments.

Chapter 5

Convector-induced filling

This chapter discusses results of small-scale saline-in-water experiments, which were performed to model a typical household convector of 1kW strength. The emphasis is on the influence of the system configuration on the filling rate.

5.1 General observations

In general, in a room heated by a convector, the convector location is typically against the side wall close to the floor level. It is not at all obvious, however, if this location results in the fastest filling, or if moving the convector away from the side wall could lead to the increase in the filling rate. Also, the standard design approach is based on the convector strength meeting the design requirements, while the convector size is chosen based on the space available and visual preferences. The experimental investigation presented is used to look beyond the standard approach and to attempt to enhance convector performance, i.e. filling rate, by adjusting the configuration of the room-convector system[1]. The convector against the side wall is taken as the baseline case and the other system configurations are compared to it, therefore the physics of the convector-induced filling are initially described in the context of the wall-mounted convector.

To start with, consider a typical sequence of filling flows. Figure 5.1 shows filling flows induced by the convector against the side wall and the aspect ratio $\mathcal{AR} = 0.64$, where the convector height $\mathcal{L}$ is approximately a third of the room height.[2] After turning on the convector supply, a plume of saline develops on a porous face of the convector. After detaching from the trailing edge, the plume continues descending to the base of the tank in a plume-like flow restricted by the side wall (as in Figure 5.1 a). After impinging on the base (Figure 5.1 b), the body of buoyant fluid spreads outwards (Figure 5.1 c) forming a horizontal intrusion. Upon reaching the side wall, the horizontal current ascends vertically and overturns (Figure 5.1 d). This unstable intrusion collapses under gravity (Figure 5.1 e), causing secondary horizontal currents

[1] In this context the system configuration refers to the location of the convector relative to the horizontal and vertical boundaries, the convector strength and orientation, and the room size.

[2] Note that varying the convector horizontal position results in a variation of the aspect ratio defined as the ratio of height H, dependent on the convector vertical position, and horizontal extent R, dependent on the convector horizontal position, see Section 4.4.1 for reference.

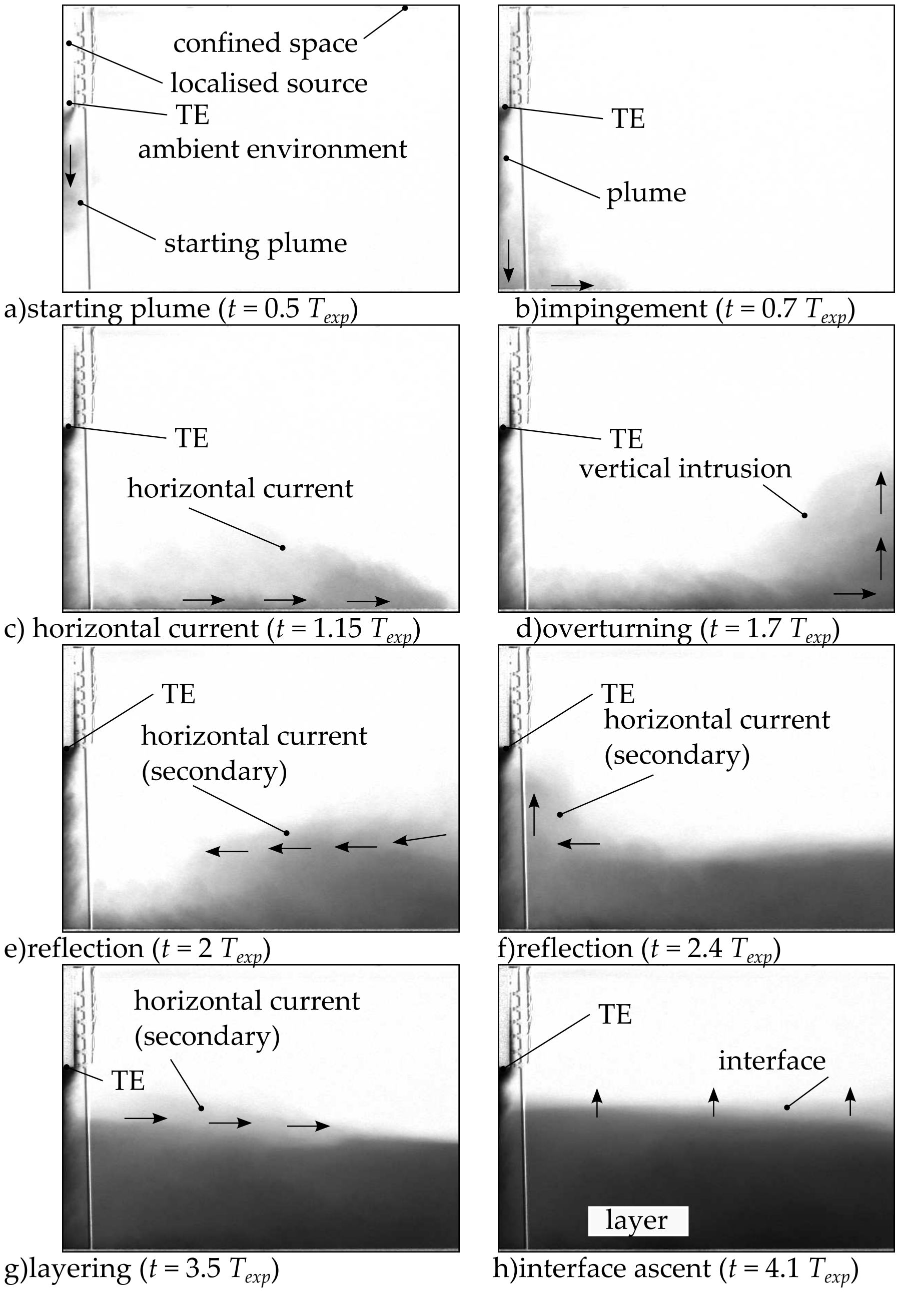

Figure 5.1: Early filling period (a-h) with the wall-mounted convector, captured during a small-scale experiment (system configuration: $B_0/B_{0,*} = 1$, $Æ = 0.65$, $H/H_* = 1$). Arrows in bulk flows indicate direction of the flow. Legend: TE - trailing edge.

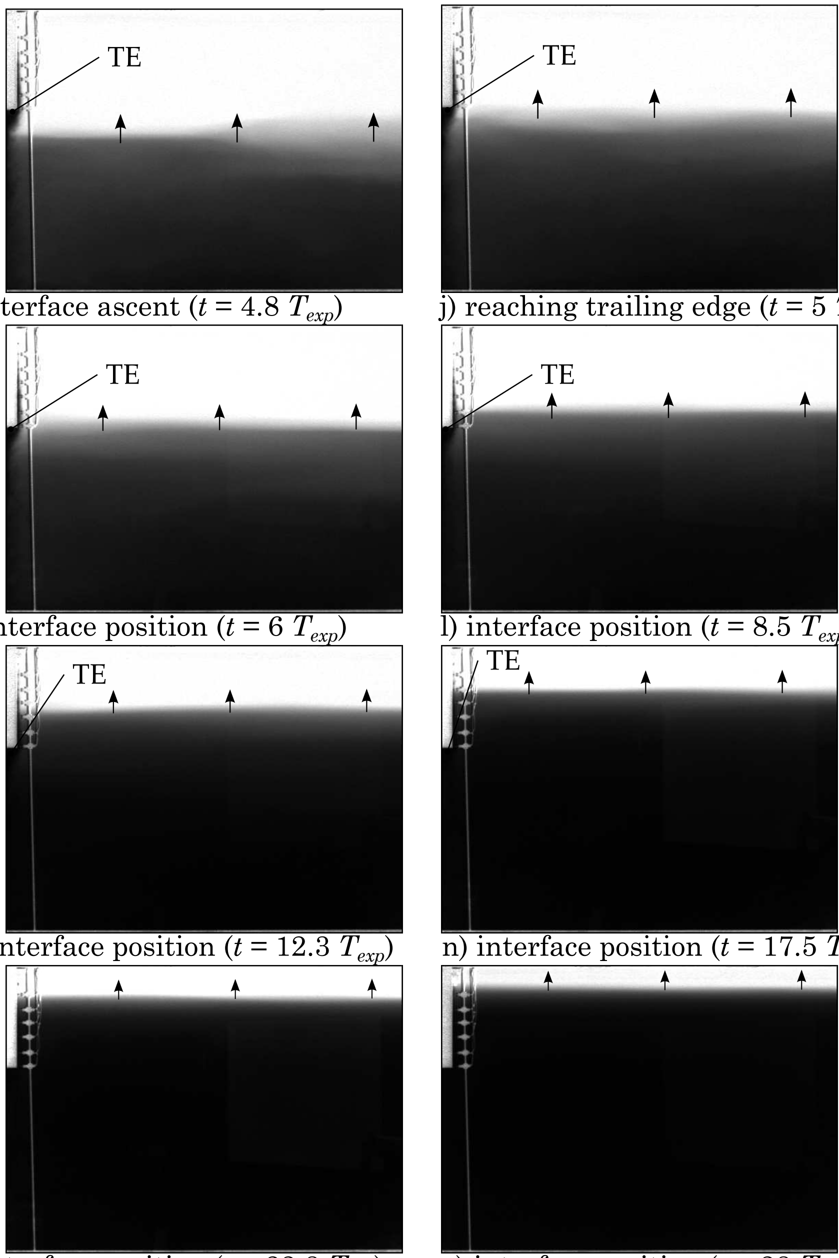

i) interface ascent (t = 4.8 T_{exp}) j) reaching trailing edge (t = 5 T_{exp})

k) interface position (t = 6 T_{exp}) l) interface position (t = 8.5 T_{exp})

m) interface position (t = 12.3 T_{exp}) n) interface position (t = 17.5 T_{exp})

o) interface position (t = 22.8 T_{exp}) p) interface position (t = 28 T_{exp})

Figure 5.1: Intermediate and late filling periods (i-p) with the wall-mounted convector, captured during a small-scale experiment (system configuration: $B_0/B_{0,*} = 1$, $\AE = 0.65$, $H/H_* = 1$). Arrows in bulk flows indicate direction of the flow. Legend: TE - trailing edge.

where the vertical intrusion reflects back (Figure 5.1 f) and forth (Figure 5.1 g) between the plume and the side wall until a levelled smeared interface forms (Figure 5.1 h). The smeared interface becomes sharper (Figure 5.1 i) as it continues ascending towards the trailing edge (Figure 5.1 j). The pattern of filling, as shown in Figure 5.1, is seen in every experiment. The direction of filling flows[1] is governed by the buoyancy forces, inertia and confinement of the tank. The extent of filling flows and the resulting filling rate, however, vary depending on the convector's location, strength and orientation, as will be demonstrated and explained in Section 5.2.

A qualitative classification into three filling periods, early, intermediate and late periods, is proposed to distinguish the significant changes in the development of filling flows. Namely, turning on the convector marks the beginning of the early filling period, whereas formation of a smeared, levelled interface and ascent to the trailing edge are treated as the beginnings of the intermediate and late periods, respectively. In general, early and intermediate periods occur in the time interval 0 to 5τ (scaled on $\mathcal{T}_{exp}$, see eq. (4.11)) with the early period lasting between 2.5τ-4τ (from 0 to up to 4τ) and the intermediate period between 1τ-2.5τ (between 2.5 τ and 5τ). The exact duration of each period depends on the system configuration and the interface position relative to the trailing edge upon the beginning of the intermediate period. The higher the interface position upon establishment is, the shorter the intermediate period. Figure 5.2 shows schematics of filling at three time instances, where schematic (a) shows the filling observed during an early period and schematics (b-c) correspond to filling in an intermediate period and a late period, respectively.

The early period (Figure 5.2 a) comprises filling flows such as a starting plume (Figure 5.1 a), a horizontal current (Figure 5.1 b), and a side wall vertical intrusion (Figure 5.1 d) followed by secondary horizontal currents (Figure 5.1 e-g). This period is therefore likely to involve large-scale mixing, particularly during the development of a horizontal current and a subsequent vertical upward motion against buoyancy, for example, where energy from inertia could be transferred into a mixing process. Once the early period is completed, a wavy interface is established across the tank, marked by limited (to ± 2.5%)[2] differences in a vertical coordinate of the first front. As a result, an area of contact between the buoyant fluid and ambient fluid is also reduced and mixing likely occurs only between the plume and the surroundings and across the ascending interface. The intermediate period (Figure 5.2 b) is, thus, dominated by a unidirectional ascent of the first front (Figure 5.1 h-j).

The interface ascent in the intermediate period (for different system configurations) can be compared to the filling induced by a virtual line source of buoyancy. To extract values of entrainment coefficient[3], from the volume conservation of the buoyant layer, Lee & Emmons (1961) equation for the plume volume flux is used: $ln\zeta^{-1} = \frac{(2\alpha_L)^{2/3}B_L^{1/3}L}{S}t$, where $\alpha_L = \alpha_{FF}$ is the entrainment coefficient in the far field. Figure 5.3 shows the plume entrainment coefficient α_{FF} in the convector far field as a function of maximum vertical intrusion λ along a side wall, scaled on vertical distance $H - \mathcal{L}$. If we ignore one data point outside the shaded area, all the

[1]The term 'filling flows' refers to the bulk flows of buoyant fluid, i.e. a starting plume, horizontal currents, vertical intrusions.

[2]Percentage corresponds to the maximum height $H/H_* = 1$. Criterion developed by the author based on qualitative data.

[3]Section 4.5.1.5 shows an example of calculation of the α value and an example evaluation of the fitting quality.

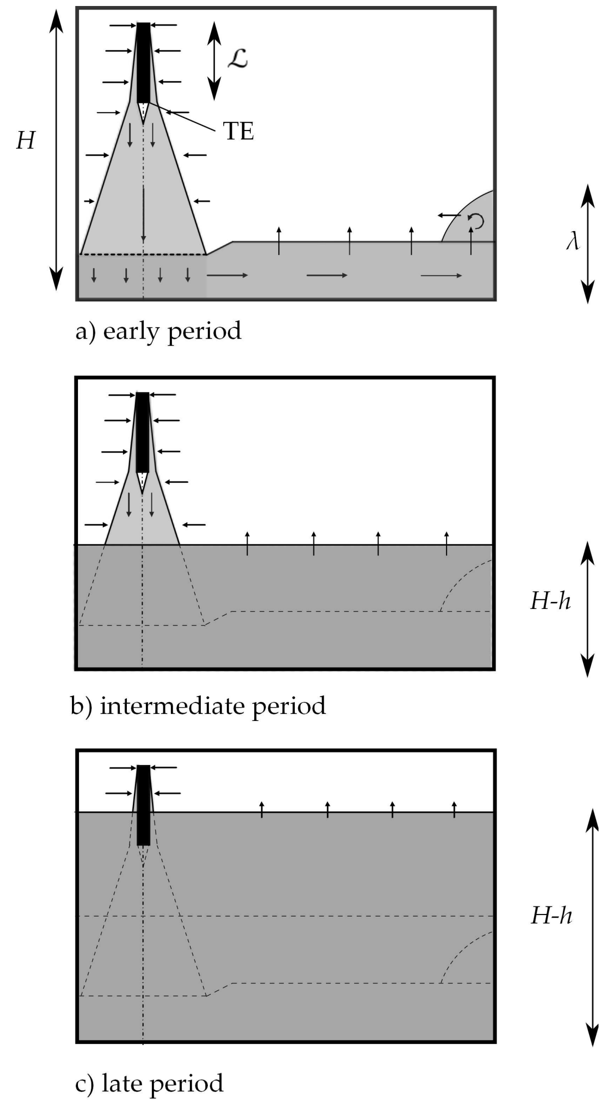

Figure 5.2: Schematics of filling at three instances: a) early filling box characterised by a maximum depth of a side wall vertical intrusion λ; b) intermediate filling box with buoyant layer depth $(H-h) < (H-\mathcal{L})$; c) late filling box with buoyant layer $(H-h) > (H-\mathcal{L})$. Legend: TE - trailing edge.

remaining data suggest a stable increase in the uncertainty of α-value with λ. An increased spread in derived α-values, as shown in Figure 5.3, for instance in the range 0.0088 to 0.055 for $\lambda/(H-\mathcal{L}) = 1$, appears to confirm that other components of the system configuration, i.e. the convector position relative to the wall, affect the plume development and thus the filling rate. Also, values of entrainment coefficient in the convector-induced intermediate period are 2-3 times lower than typical values extracted for line sources (see Figure 2.4 in literature review), which could mean that due to limited vertical distance $H-\mathcal{L}$ the flow has never fully developed and self-regulated to reflect a plume from a line source.

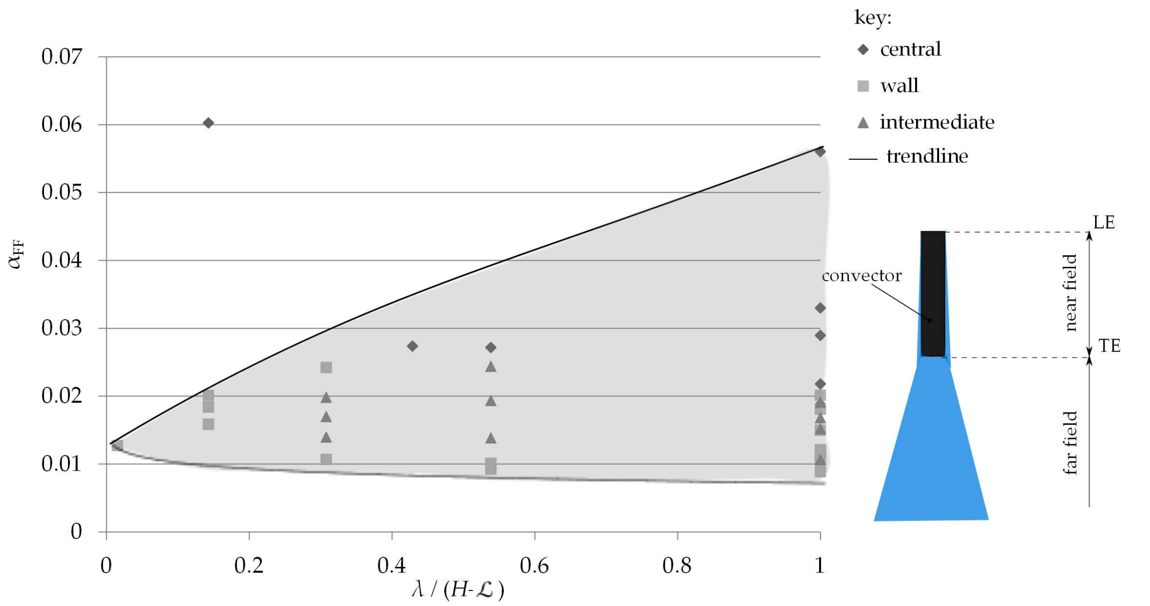

Figure 5.3: Top-hat values of entrainment coefficient α in convector far field as a function of maximum vertical intrusion λ along side wall, scaled on vertical distance $H-\mathcal{L}$. Values derived, using Lee & Emmons (1961) equation, see eq. (4.8), from interface ascent data in intermediate period for wall-mounted, intermediate and central convector positions. Each data point is a result of linear regression. Quality of fitting has been evaluated (through calculation of the norm of residuals and the coefficient of determination). Here each data point has *CoD* exceeding 0.95.

The late period (Figure 5.2 c), similarly to the intermediate period, is characterised by the unidirectional ascent of the interface (Figure 5.1 k-p), where the rate of ascent depends on the plume development. Figure 5.4 shows the plume entrainment coefficient α_{NF} in the convector near field as a function of maximum vertical intrusion λ along a side wall, scaled on vertical distance $H-\mathcal{L}$. The plume entrainment coefficients for the convector near field case are derived similarly to the far field, where Cooper & Hunt (2010) expression for the plume volume flux is used, so that $\zeta^{-1/3}-1 = \frac{1}{4}\left(\frac{4}{5}\right)^{1/3}\frac{\alpha_a^{2/3}B_a^{1/3}\mathcal{L}^{1/3}L}{S}t$. The system configuration also appears to influence α-values, which are in range 0.00681 to 0.06619. On average α-values are 10-20% lower in the late period compared to the intermediate period. There are few exceptions where α-values are comparable or slightly (up to 10%) higher in the late period, which could be attributed to the transitional state of the developing plume (plume detachment from the trailing edge, plume merging) at levels that correspond to the interface positions in the intermediate period. The

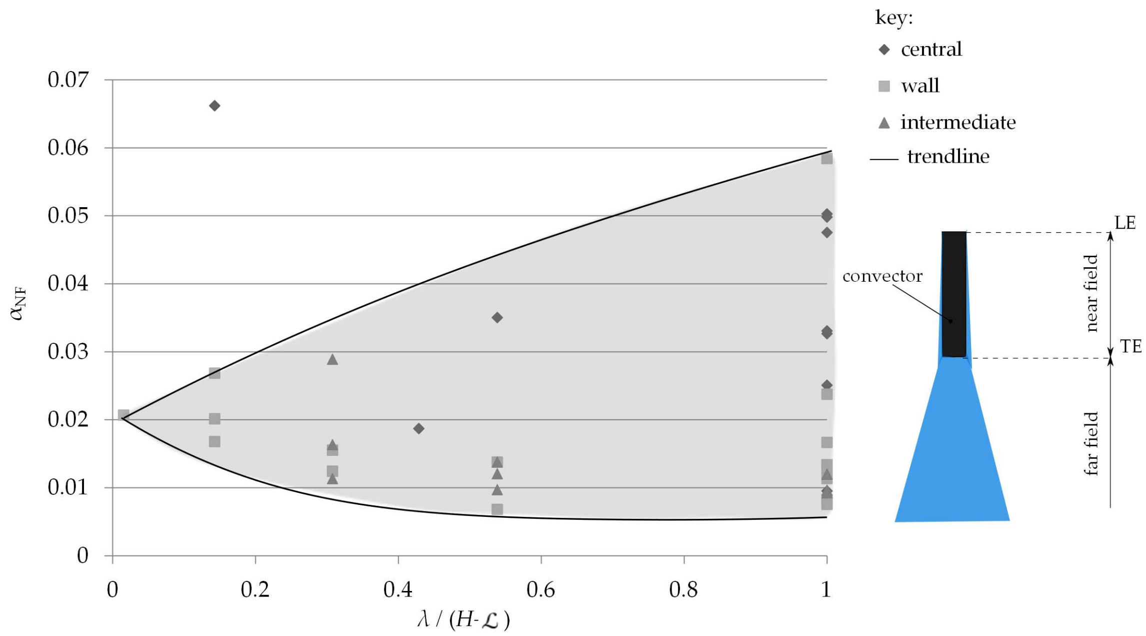

Figure 5.4: Top-hat values of entrainment coefficient α in convector near field as a function of maximum vertical intrusion λ along side wall, scaled on vertical distance $H-\mathcal{L}$. Values derived, using Cooper & Hunt (2010) equation, see eq.(4.7), from interface ascent data in late period for wall-mounted, intermediate and central convector positions. Each data point is a result of linear regression. Quality of fitting has been evaluated (through calculation of the norm of residuals and the coefficient of determination). Here each data point has CoD exceeding 0.95.

α-values derived in the near field are in good agreement with values derived previously by other authors for vertically-distributed buoyancy sources (see Figure 2.4).

The variability of the entrainment-coefficient results implies that the simple filling box model is not sufficient and changes in geometry must be accounted for. The results of the experiments are now compared with the results of Cooper & Hunt (2010) for a vertically distributed source. Figure 5.5 shows the non-dimensional interface position in the near field during the late period as a function of non-dimensional time τ_a. The interface position has been scaled on the convector's height $\mathcal{L}$ and time has been scaled on the timescale of the vertically distributed source $\mathcal{T}_a = \frac{S}{c_a B_{a,0}^{1/3} \mathcal{L}^{1/3} L}$ (see Section 2.1.4). To enable comparisons between experimental results and the theoretical predictions of Cooper & Hunt (2010), the experimental curves have been shifted, so that at $\tau = 0$, the interface level reached the trailing edge of the convector $\zeta_{NF} = 1$. The experimental curves are in good agreement (±10%) with the theoretical predictions of Cooper & Hunt (2010). The agreement can be further improved if the time scale is rescaled using H as a characteristic length $\mathcal{T}_{a_{mod}} = \frac{S}{c_a B_{a,0}^{1/3} H^{1/3} L}$. Figure 5.6 shows the resulting relationships between the non-dimensional interface position and rescaled time. The obvious success of this non-dimensionalisation suggests that the room height H is a critical parameter in the filling process.

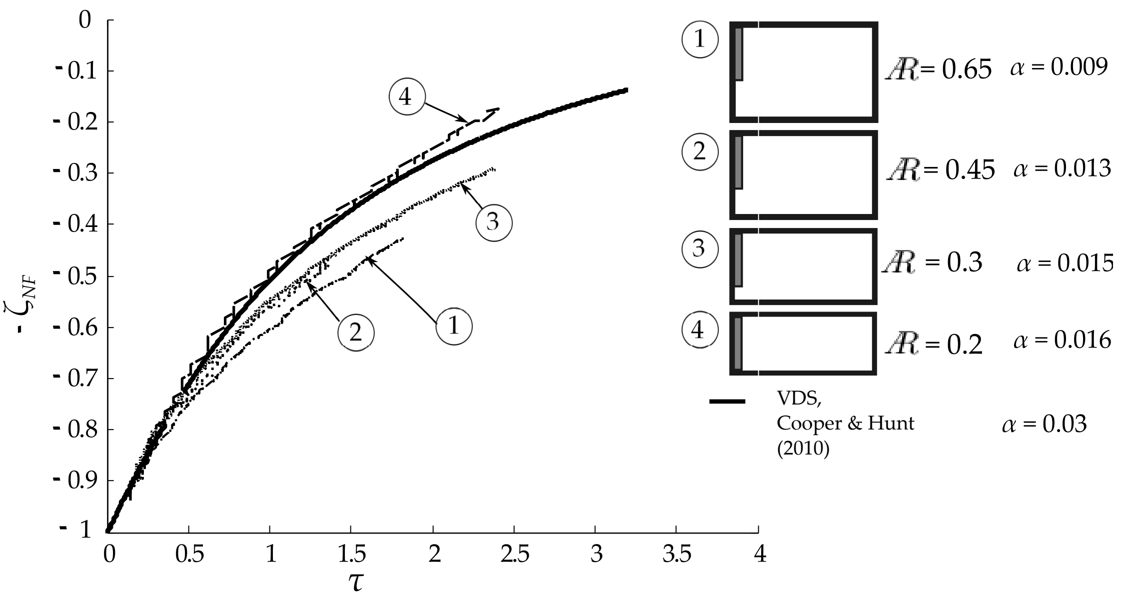

Figure 5.5: Non-dimensional position of the interface in the near field, scaled on $\mathcal{L}$, as a function of non-dimensional time, scaled on $\mathcal{T}_a$.

5.2 Influence of system configuration on the filling rate

The impact of the system configuration, i.e. the convector location, orientation and strength, on the rate of filling is now considered based on the non-dimensional time series of the first front

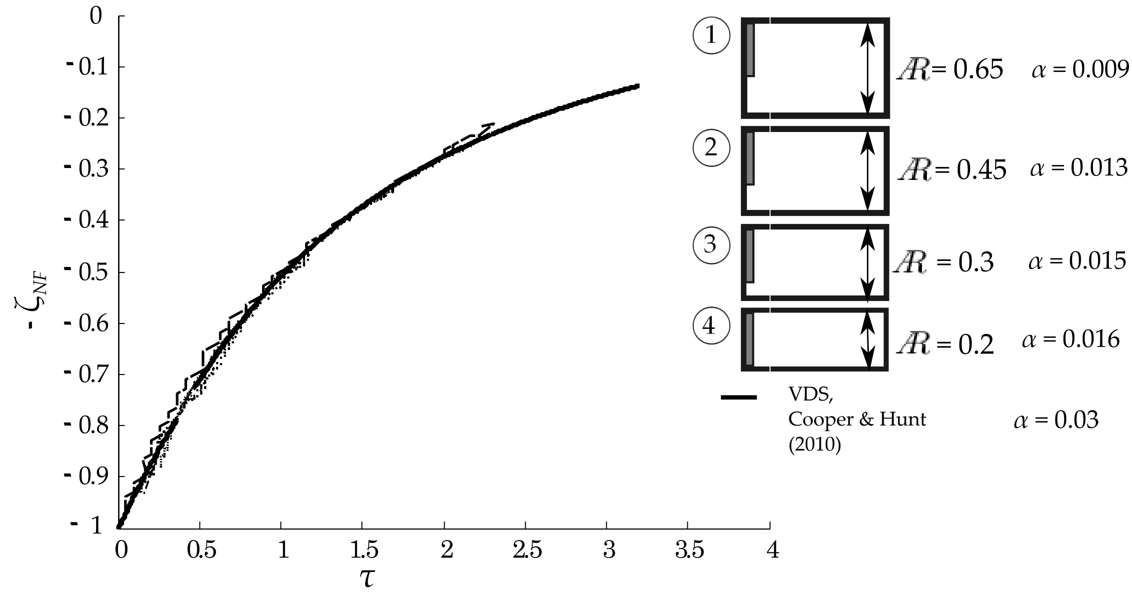

Figure 5.6: Non-dimensional position of the interface in the near field, scaled on $\mathcal{L}$, as a function of non-dimensional time, scaled on $\mathcal{T}_{a_{mod}}$.

position[1].

5.2.1 Convector horizontal position

Figure 5.7 shows sequences of development of filling flows in the early period for three horizontal positions of the convector, namely against the side wall (a), in the tank centre (c) and in the intermediate position (b), $2d$ from the side wall, for system configuration: $B_0/B_{0,*} = 1$ and $H/H_* = 1$. Depending on the convector horizontal position, the plume development through entrainment of the ambient fluid, is restricted from one side (wall-mounted position), partially restricted (intermediate case in the figure) or free (central case in the figure). A vertical plume descent towards the tank base is observed in the two limiting cases (arrows indicating the direction of the bulk flow are marked in subplots (a)VI-VIII and (c)VII-VIII), whereas in the intermediate case the descending plume inclines towards the wall, allowing for an additional plume development (as shown in subplots (b) VI-VIII). As a result, in the intermediate case, the plume outflow width (of $8d$) upon impingement is greater than in the wall case ($4d$, 50% narrower than in (b)) and the central case ($7.8d$, 2.5% narrower than in (b)), respectively. These differences in the plume outflow width appear to affect the height of the horizontal current and the maximum vertical penetration along a side wall (marked in Figure 5.7 subplots: (a) XV, XXIV; (b) XV, XXIV; (c) XVI, XXIV). The maximum heights are observed in the intermediate case, where the horizontal current height is approximately $0.65(H - \mathcal{L})$ and the maximum vertical intrusion is $1.1(H - \mathcal{L})$. The height of horizontal current is reduced approximately by 40% (wall) and 55% (centre) compared to the intermediate case, whereas the vertical penetration by 30% (wall) and 40% (centre), respectively. Subsequently, the horizontal position of

[1] Details on how time series have been extracted and scaled are in Section 4.5.1.5

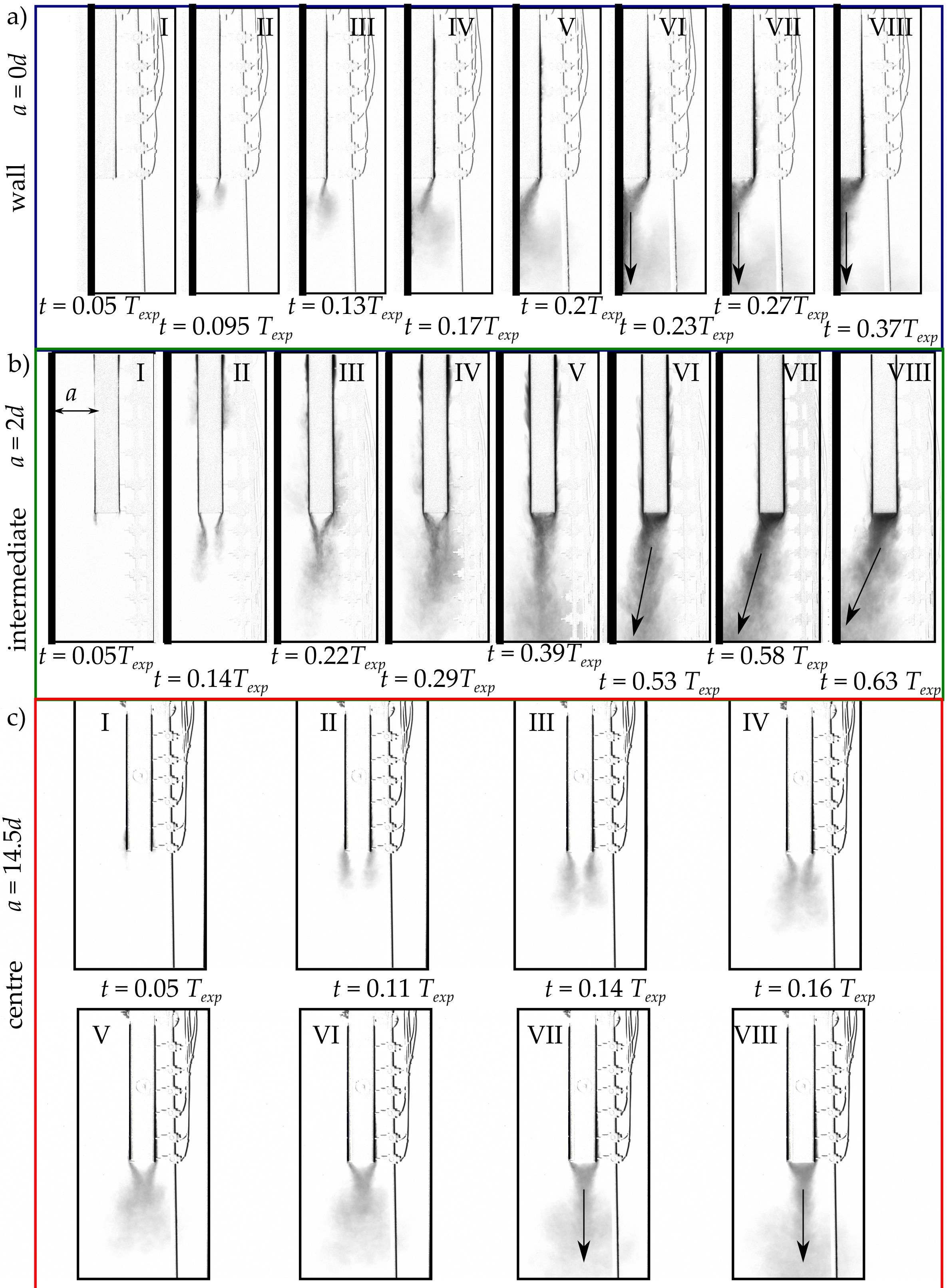

Figure 5.7: Development of starting plume as function of convector's horizontal position relative to side wall (horizontal orientation). Sequence of normalised frames in order of appearance. Arrows indicate direction of the bulk flow.

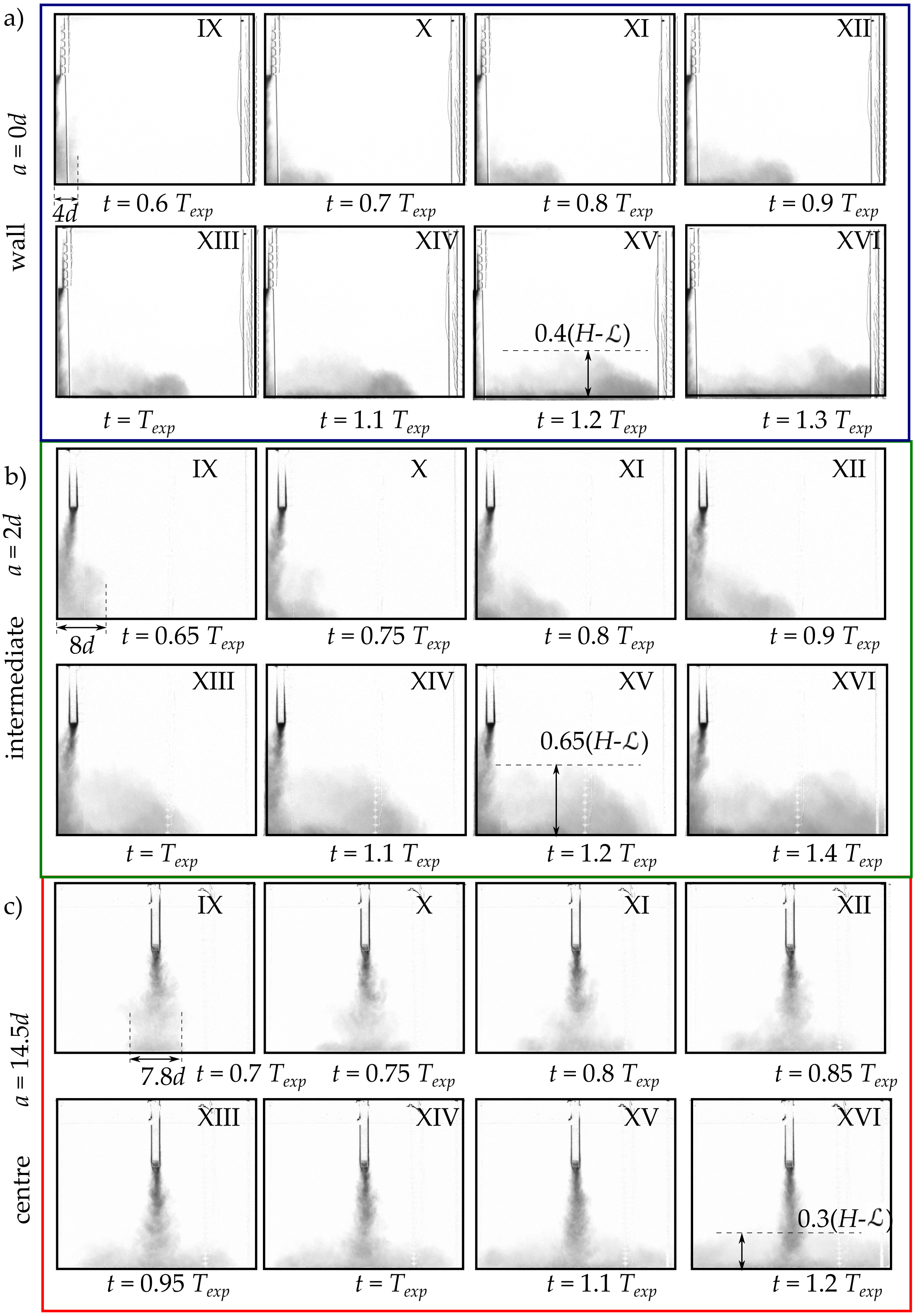

Figure 5.7: Development of horizontal current. Sequence of normalised frames in order of appearance. Measured lengths: IX plume outflow width, XV and XVI horizontal current height.

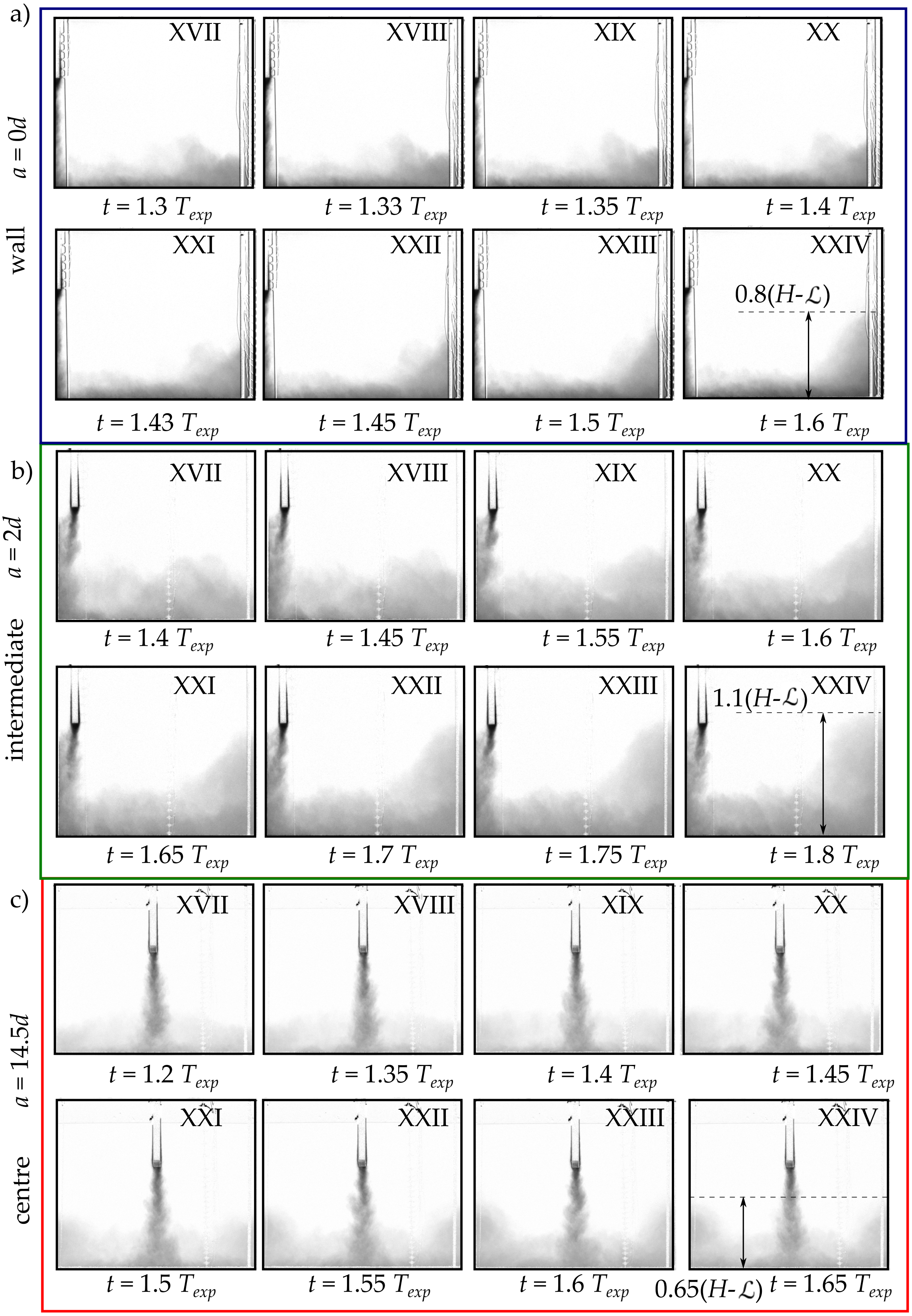

Figure 5.7: Development of vertical intrusion. Sequence of normalised frames in order of appearance. Measured lengths: maximum side wall vertical penetration.

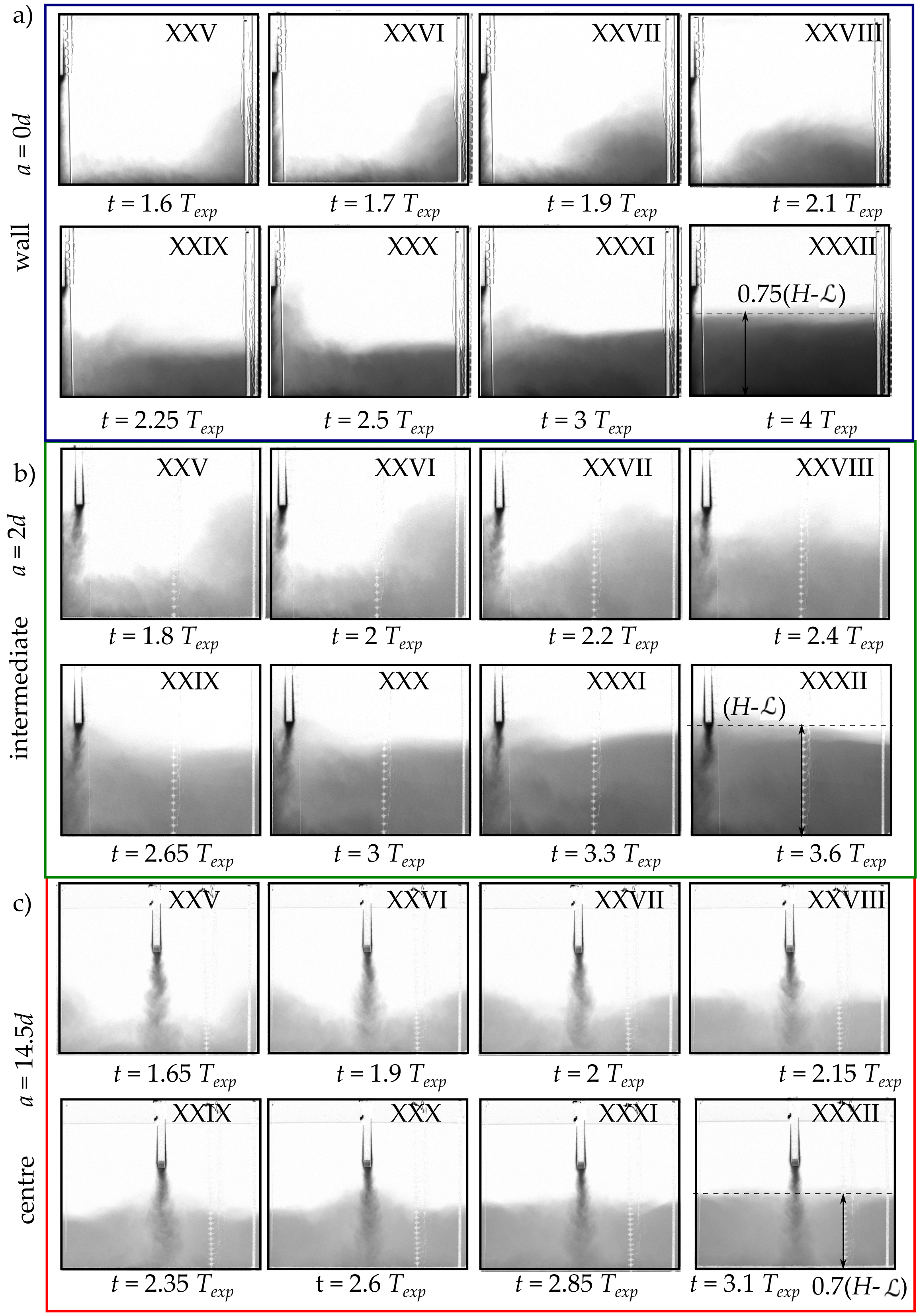

Figure 5.7: Horizontal reflection. Sequence of normalised frames in order of appearance. Measured lengths: first front position upon formation.

the interface upon its establishment is the highest in the intermediate case (approximately at the level of the convector trailing edge, subplot (b) XXXII), whereas by comparison in the wall (subplot (a) XXXII) and central (subplot (c) XXXII) cases it is lower by 25% and 30%, respectively.

Figure 5.8 shows the non-dimensional position of the interface as a function of a non-dimensional time and horizontal position relative to the side wall. Seven horizontal positions are compared: on the wall (0*d*), in the centre (14.5*d*) and at five intermediate positions: *d*, 2*d*, 4*d*, 8*d* and 12*d* from the wall, , for system configuration: $B_0/B_{0,*}$ = 1 and H/H_* = 1. The extracted curves indicate that the interface position continuously ascends with time. The rate at which the interface ascends, however, varies both with time (as filling continues) and convector horizontal position. The filling rate decreases with time, based on decreasing increments $\Delta\zeta$ in subsequent time intervals $\Delta\tau$ of equal length. For instance, in a wall-mounted case (1), for $\Delta\tau$ = 5, during the first time interval (0 - 5τ) $\Delta\zeta$ = 0.6 corresponding to an average rate of ascent $\frac{\Delta\zeta}{\Delta\tau}$ = 0.12. Subsequently, during the second time interval (5τ - 10τ) the increment decreases to $\Delta\zeta$ = 0.15 and $\frac{\Delta\zeta}{\Delta\tau}$ = 0.03, corresponding to 75% slower rate of ascent. This decelerating continues during the third time interval (10τ - 15τ) with the increment $\Delta\zeta$ = 0.1 and the rate of ascent $\frac{\Delta\zeta}{\Delta\tau}$ = 0.01, corresponding to 84% slower ascent than in the first time interval. In general, the filling rate in the early period is 5 - 6 times faster than in the late period.

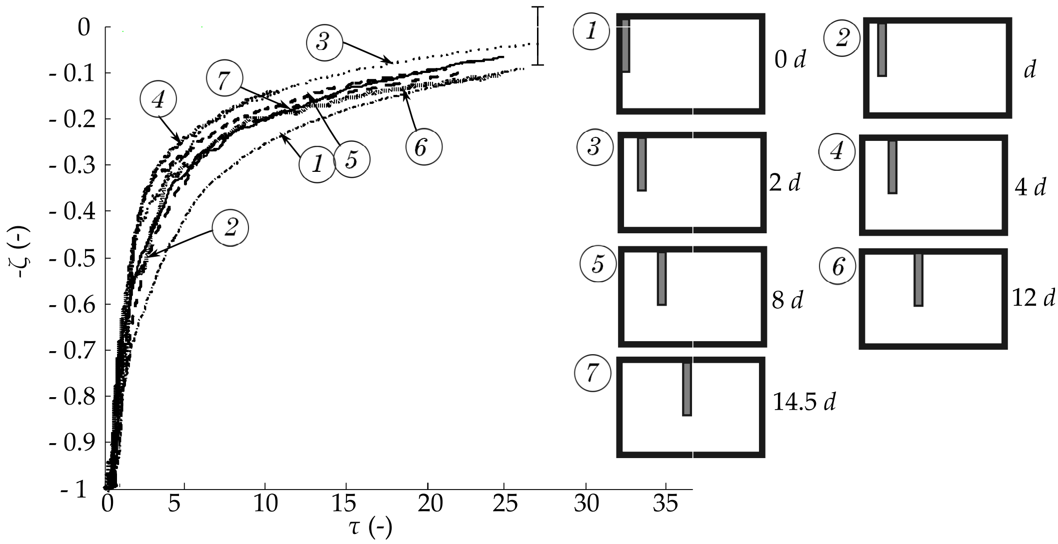

Figure 5.8: Non-dimensional position of the interface as a function of time non-dimensionalised by experimental timescale $\mathcal{T}_{exp}$, see eq.(4.11) for reference, and a horizontal position - 7 cases: on the wall (0*d*), 5 intermediate cases: *d*, 2*d*, 4*d*, 8*d*, 12*d* and in the centre (14.5 *d*). System configuration: Æ = 0.64 - 1.3, H/H_* = 1, $B_0/B_{0,*}$ = 1. The vertical line corresponds to the maximum error.

The wall-mounted convector induces the slowest filling (case 1), due to restrictions in the plume development. Moving the convector away from the side wall initially leads to the faster filling for convector horizontal positions not exceeding 4*d* (cases 2-3). The fastest filling for a = 4*d* (case 4) leads to 30% higher interface position in the early period (peak value) and 10%

higher interface position for the duration of intermediate and late periods compared to the wall-mounted case. Moving the device even further from the side wall ($a > 4d$) leads to gradually slower filling (cases 5-7). The interface position in the central case (7) is approximately 20% lower in the early period and 5% lower for the remainder of experiment compared to the $a = 4d$ intermediate case. The deceleration of the interface ascent over a course of filling appears to be caused by large-scale mixing dissipation and restriction of the entrainment into the plume.

Salinity probe rake and associated wires are visible in some of the images. Figure 5.9 shows the vertical intrusion against the side wall as a function of convector horizontal position for six cases (1-5 and 7) from Figure 5.8. The fastest filling for $a = 4d$ (case 4 in Figure 5.8) corresponds to the closest horizontal position of the convector to the side wall that allows entirely free development of the plume and the highest side wall vertical penetration of $1.12(H - \mathcal{L})$, see Figure 5.9 (d). For $a < 4d$ (as shown in Figure 5.9 a-c), the penetration depth and the filling rate decrease with a decreasing distance a (cases 1-3 in Figure 5.8). For $a > 4d$ the vertical penetration depth and the filling rate decrease with an increasing a. It appears that two horizontal distances a and $W - a$, relative to each side wall influence the vertical intrusion, thus also the filling rate. The increase in $W - a$ results in a higher momentum flux for the horizontal current upon impingement on the side wall, which results in the higher penetration depth of the vertical intrusion. When the convector is in the intermediate horizontal position ($0 < a \leq 4d$), the spreading rate of the horizontal current is greater than in the two limiting cases, resulting in higher penetration depths. The maximum vertical penetration $\lambda = (H - \mathcal{L})/H = 0.68$ occurs for $H/H_* = 1$ and $a = 4d$.

When considering the entire process of filling, adjusting the horizontal position of the convector may result in an increased filling rate, which in turn leads to 30 % higher position of the interface during the early filling period and up to 10 % steady difference at any given time in the intermediate and late periods (qualitative estimation). In other words, the same buoyancy flux may be distributed in the tank but in such a way that it fills the tank faster. The faster filling of a more diluted saline also corresponds to a less stratified environment (see Chapter 6).

5.2.2 Convector vertical position

Figure 5.10 shows sequence of images presenting the development of filling flows in the early filling period for the wall-mounted convector and two heights $H/H_* = 0.32$ and 0.68, whereas for the height $H/H_* = 1$, see Figure 5.7. There is a significant difference in the development of early-period flows between the three wall-mounted cases. For $H/H_* = 0.32$ (case a in Figure 5.10), early transients are barely developed. The plume outflow width upon impingement on the tank base ($0.03d$, subplot I) is over 13 times narrower than the width of the plume outflow in the wall-mounted case, where $H/H_* = 1$ (Figure 5.7 (a) IX). The height of horizontal current and the side wall vertical intrusion are approximately 10 times smaller for $H/H_* = 0.32$, compared to $H/H_* = 1$.[1] The development of the early-period flows in the case, where $H/H_* = 0.68$ is intermediate, between development observed in cases where $H/H_* = 0.32$ and $H/H_* = 1$. The reduced developments of the horizontal current and the subsequent early period flows for the decreasing H/H_* can be attributed to the less developed plume outflow upon impingement on

[1]Qualitive estimation, based on estimates from Figures 5.7 (a) XIV, XXIV and 5.10 (a) VIII and XII.

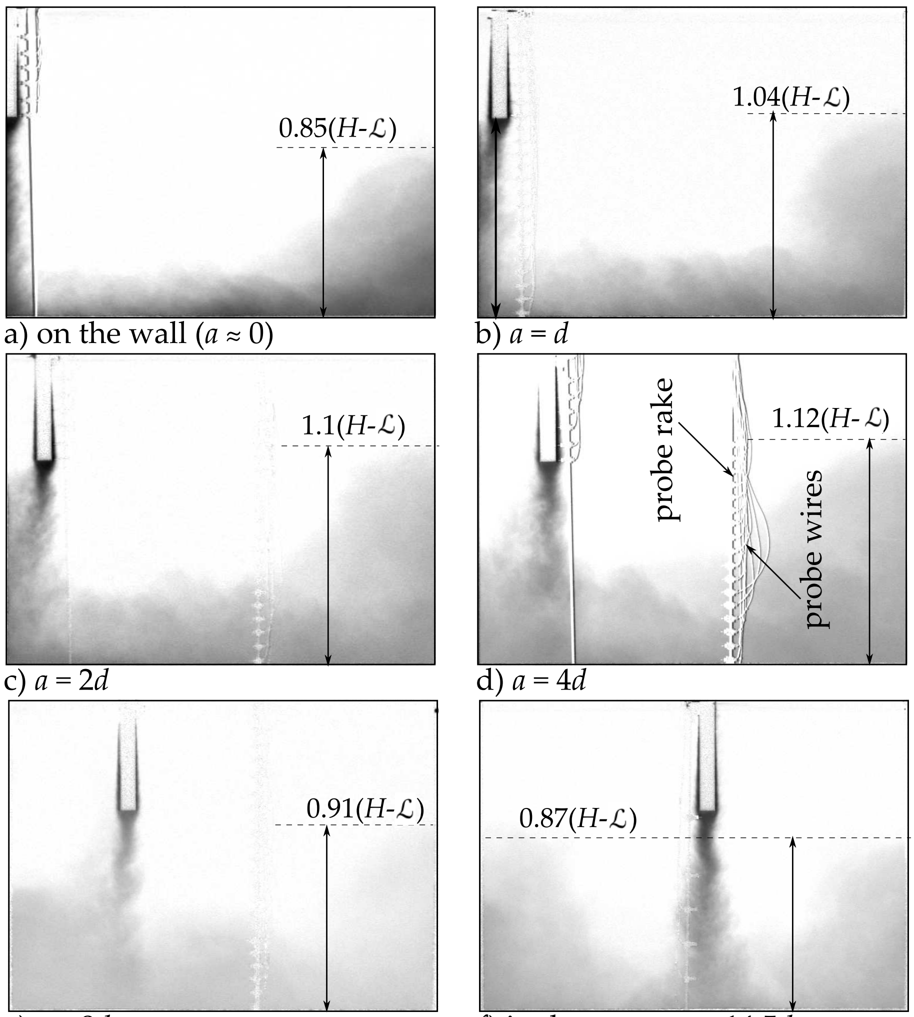

Figure 5.9: Vertical intrusion against side wall as a function of convector horizontal position. Salinity probe rake and associated wires are visible in some of the images.

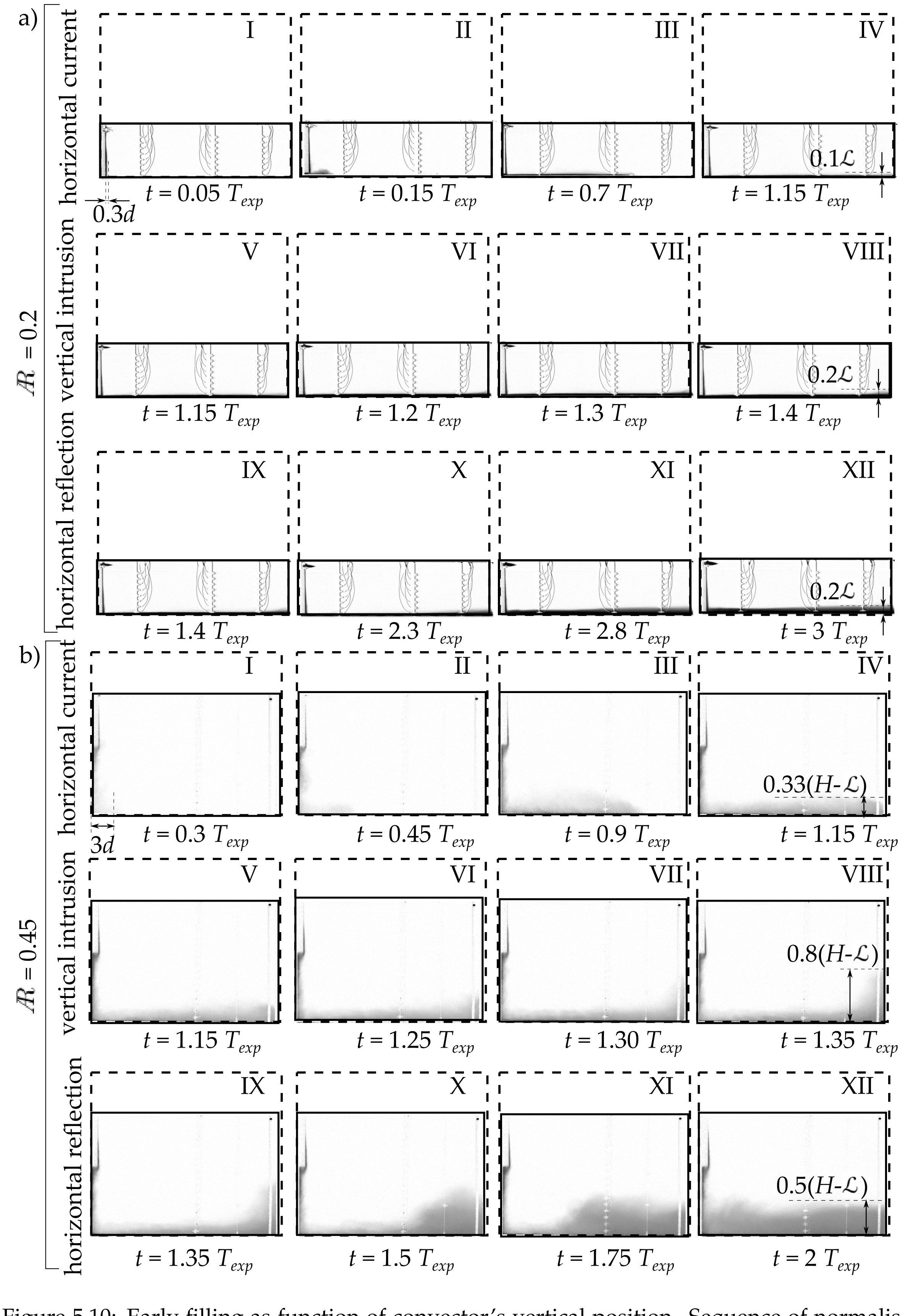

Figure 5.10: Early filling as function of convector's vertical position. Sequence of normalised frames in order of appearance.

the base of the tank, such that the plume outflow is less diluted and the volume flow rate is lower.

Figure 5.11 shows the vertical intrusion along the side wall for four heights H: $H/H_* = 0.32$, $H/H_* = 0.47$, $H/H_* = 0.68$ and $H/H_* = 1$. The vertical intrusion appears to increase with increasing $H - \mathcal{L}$, corresponding to H/H_* tending to 1. This can be explained by the dependency between the height of the vertical intrusion and the force balance of bulk flow between a stabilising buoyancy force and a destabilising momentum force. In general, the greater the momentum force is, compared to the buoyancy force, the higher the vertical intrusion against the side wall. The buoyancy force decreases as the flow develops, whereas the momentum force increases. As a result, the greater the height H is, the higher may be the vertical penetration along a side wall λ. For $H < 1.3\mathcal{L}$ (e.g. Figure 5.11 c-d), the vertical intrusion slumps, whereas for $H > 1.3\mathcal{L}$ (e.g. Figure 5.11 a-b) the vertical intrusion overturns. Figure 5.12 shows the experimental vertical penetrations, scaled on $H - \mathcal{L}$, as functions of distance $H - \mathcal{L}$, scaled on the convector height $\mathcal{L}$. The trendline marks an approximate relationship between the non-dimensional maximum penetration depth and the non-dimensional vertical position. The grey field corresponds to the error band ±5% (±0.5). The maximum penetration $\lambda = 0.897\left(\frac{H-\mathcal{L}}{\mathcal{L}}\right)^{-0.562}$, which is a best fit, appears to exponentially decrease with decreasing $H-\mathcal{L}$. For the horizontal orientation, when $H > 1.3\mathcal{L}$ the flow overturns and $\lambda \leq 1.2(H-\mathcal{L})$. In the cases where the flow slumps, $H \approx \mathcal{L}$ and $\lambda \geq H-\mathcal{L}$.

Figure 5.13 shows the non-dimensional interface positions as functions of non-dimensional time for four heights $H/H_* = 0.32$, $H/H_* = 0.47$, $H/H_* = 0.68$ and $H/H_* = 1$ and the convector in the centre; two additional time series of interface positions are included corresponding to the wall-mounted convector for two heights $H/H_* = 0.32$ and $H/H_* = 1$. The time series of the interface position indicate that faster filling can be achieved by increasing H/H_*, thus also increasing the distance $H - \mathcal{L}$. Cases 4 and 4a lead to the lowest interface position at any given time, where there is an average 10% difference between the interface position in the central and wall-mounted horizontal positions for $H = \mathcal{L}$. The filling rate decreases from $\frac{\Delta\zeta}{\Delta\tau} = 0.038$ in 0 - 5τ to $\frac{\Delta\zeta}{\Delta\tau} = 0.02$ in 5 - 25τ. For $H/H_* = 0.47$ (case 3), the interface position is up to 35% higher than for $H/H_* = 0.32$, due to faster filling by approximately a factor of 2.6 ($\frac{\Delta\zeta}{\Delta\tau} = 0.1$) in the early and intermediate periods (in 0 - 5τ). In the late period (from 5τ), the rate of ascent decelerates to $\frac{\Delta\zeta}{\Delta\tau} = 0.02$ and the two curves (for cases 3 and 4) remain parallel. Heights $H/H_* = 0.68$ and $H/H_* = 1$, correspond to doubling and quadrupling the distance $H-\mathcal{L}$ compared to $H/H_* = 0.47$. Increasing H/H_* enables further development of early-period flows, which results in the further increase in the filling rate (by 20% (case 2) and 50% (case 1) compared to case 3) in the early and intermediate periods (0 - 5τ), with the additional ascent of the interface by 15% and 25%, respectively. In the late period the rate of ascent decelerates to $\frac{\Delta\zeta}{\Delta\tau} = 0.02$ and the relative positions of the interface level off and remain 10% (case 2) and 15% (case 1) above the curve representing case 3. This indicates that the effects of faster interface ascent due to varying the distance $H - \mathcal{L}$ are achieved in the early and intermediate periods. In the late period, the rate of ascent (in the near field) is similar in each case.

The reduced development of the early-period filling flows leads to a lower position of the interface at the end of the early period and ultimately a slower relative filling. The results give the conclusion that for a given room height H, it is beneficial to select a shorter convector, in order to maximise the vertical distance $H - \mathcal{L}$ and to make use of early-period mixing to ensure

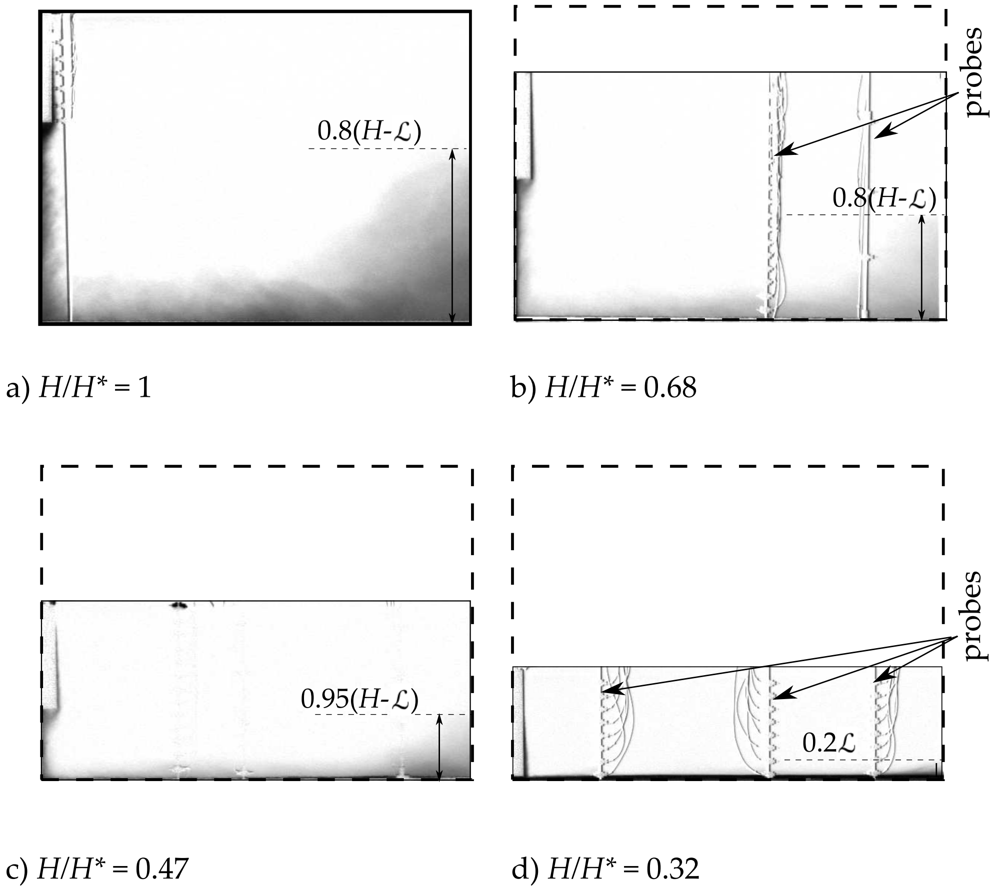

Figure 5.11: Vertical intrusion along side wall as a function of convector vertical position.

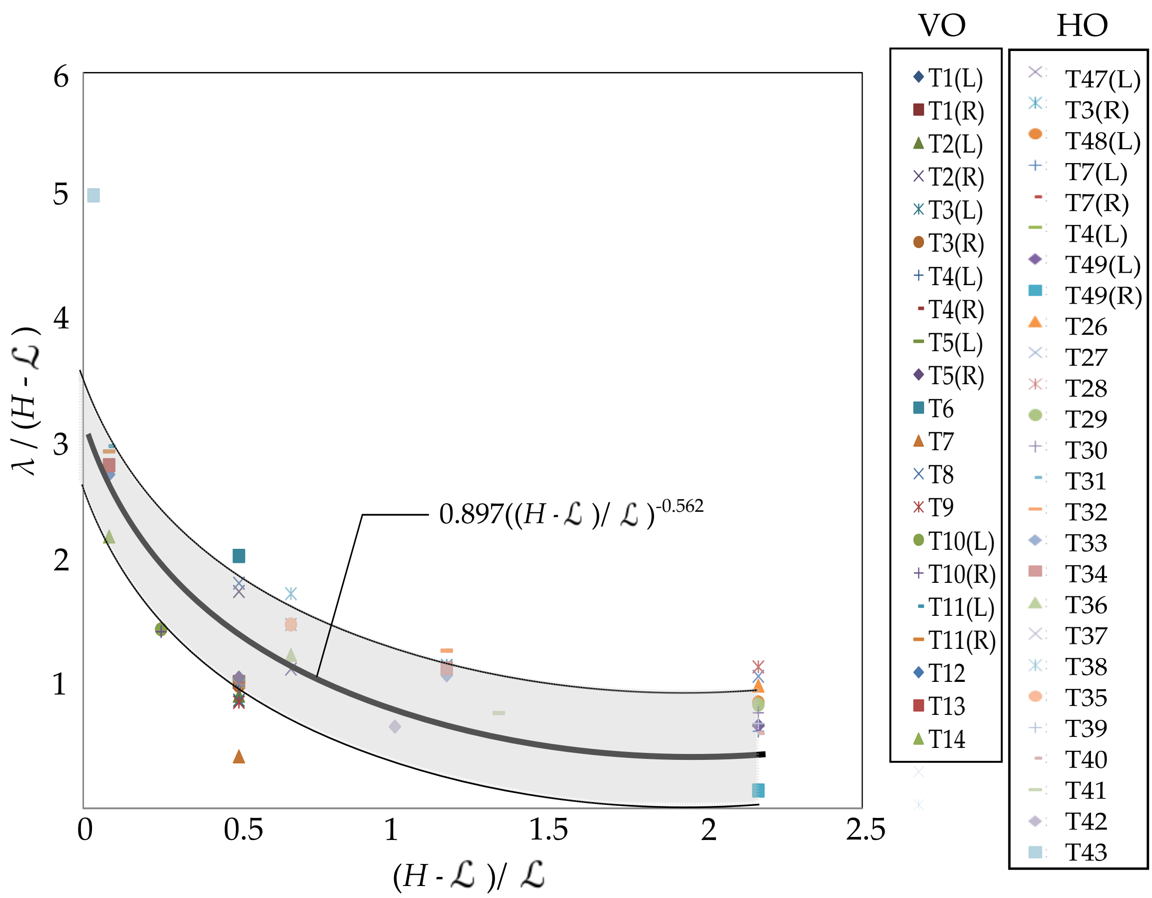

Figure 5.12: Maximum penetration depth λ of a side wall intrusion, scaled on $H - \mathcal{L}$ as a function of a vertical distance $H - \mathcal{L}$, scaled on $\mathcal{L}$. Penetration depth decreases exponentially with increasing $(H - \mathcal{L})/\mathcal{L}$. For the horizontal orientation (HO) $\lambda \leq (H - \mathcal{L})$ with exception of cases when $(H - \mathcal{L}) \approx 0$ ($\leq 1/6H$). For the vertical orientation (VO), in each experiment $(H - \mathcal{L}) \leq 1/2\mathcal{L}$ and $\lambda \geq 0.5(H - \mathcal{L})$.

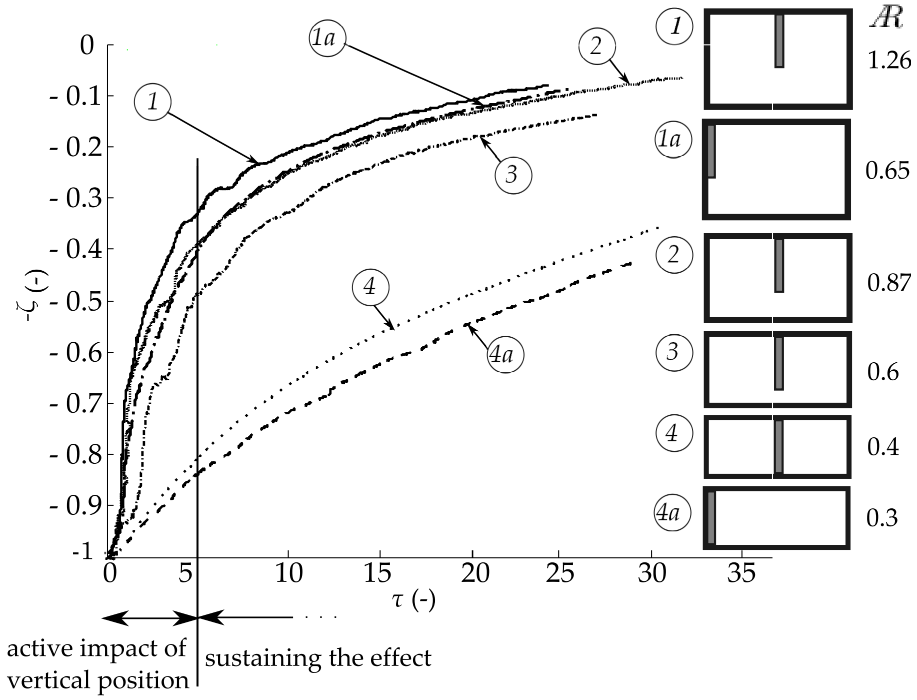

Figure 5.13: Non-dimensional position of the interface as a function of time, non-dimensionalised as in Figure 5.8, and a height H for four vertical distances $H - \mathcal{L}$ and the convector in the centre.

faster filling.

5.2.3 Convector orientation

Both a horizontal and vertical orientation of one convector of fixed size is used, see Section 4.4.1. The relative position of the convector to the tank boundaries in each orientation may affect the flow physics, which may include phenomena such as the occurrence of three-dimensionality. It is not immediately obvious here how the convector orientation influences the flow physics. Figure 5.14 shows the development of filling flows in the early period for the convector in the vertical orientation for two horizontal positions, wall-mounted (a) and centrally-located (b). The plume outflow width induced by the convector in the vertical orientation equals $3d$ in the wall-mounted case and $5.5d$ in the central case, corresponding to the 25% and 30% narrower plume outflow compared to the convector in the horizontal orientation. Also, the vertical distances of horizontal current, vertical penetration and horizontal reflection are 2-3 times lower for the convector in the vertical orientation than in the horizontal orientation.[1]

Figure 5.15 shows the non-dimensional positions of the interface as functions of the non-dimensional time for the convector in the horizontal and vertical orientation. The filling rates appear to be equivalent, corresponding to $\frac{\Delta\zeta}{\Delta\tau} = 0.12$ (±5%) in both cases, prior to reaching the trailing edge in the vertical orientation (TE VO). After reaching TE VO, the filling rate induced by the convector in the vertical orientation decelerates to $\frac{\Delta\zeta}{\Delta\tau} = 0.02$ and the differences between the filling rates in two orientations are more explicit. These differences increase with time. Upon experiment termination the difference between interface positions corresponds to 30%. For a fixed strength of the convector, selecting the shorter convector, in order to increase the distance $H - \mathcal{L}$, appears to be thus crucial to ensure faster filling.

5.2.4 Convector strength

Figure 5.16 shows the non-dimensional position of the interface as a function of a non-dimensional time and the device's strength (7 cases). To investigate the influence of varying the density of saline solution supplied to the convector on the filling rate, five distinct buoyancy ratios g'_s/g'_{s*} are used, ranging from 0.125 to 4. Three volume flow rates $\dot{Q}_0/\dot{Q}_{0*}$, 0.5, 1 and 2, are used in the experiments during which the source buoyancy g'_s/g'_{s*} is set at 0.5. In general, an increase in the convector strength leads to faster filling. Similarly to system modifications considered in previous sections, the effects of varying the convector strength on the filling rate are particularly discernible in the period 0 - 5τ. During this time interval inclination of curves (representing interface position) vary, which represents different filling rates ranging from $\frac{\Delta\zeta}{\Delta\tau} = 0.064$ (4) to $\frac{\Delta\zeta}{\Delta\tau} = 0.16$ (7). The acceleration of the filling may be explained by an increase in the forces driving the flows (buoyancy and inertia). In the late period, in spite of the convector strength, the filling rate levels off and remains at $\frac{\Delta\zeta}{\Delta\tau} = 0.02$. On average, at a given time, doubling the strength, either by increasing the buoyancy or the volume flow rate,

[1]Qualitative estimation from Figure 5.7 and Figure 5.14, where $(H-\mathcal{L})/(H-\mathcal{L})_* = 1$ for the horizontal orientation and 0.54 for the vertical orientation.

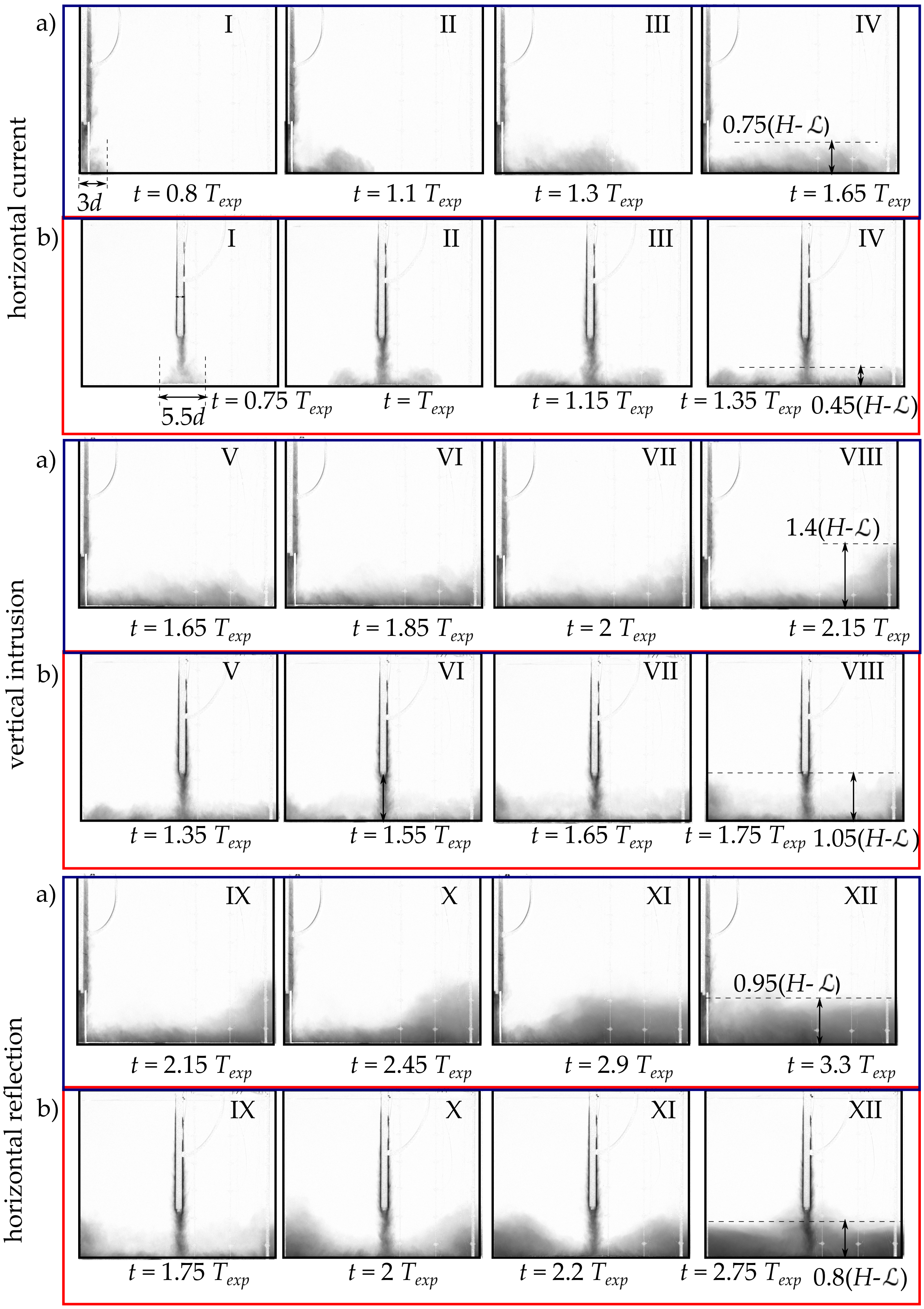

Figure 5.14: Early filling period from horizontal current to horizontal reflection for convector in vertical orientation as a function of convector's horizontal position relative to side wall: a)wall-mounted case, b) central case. Sequence of normalised frames in order of appearance.

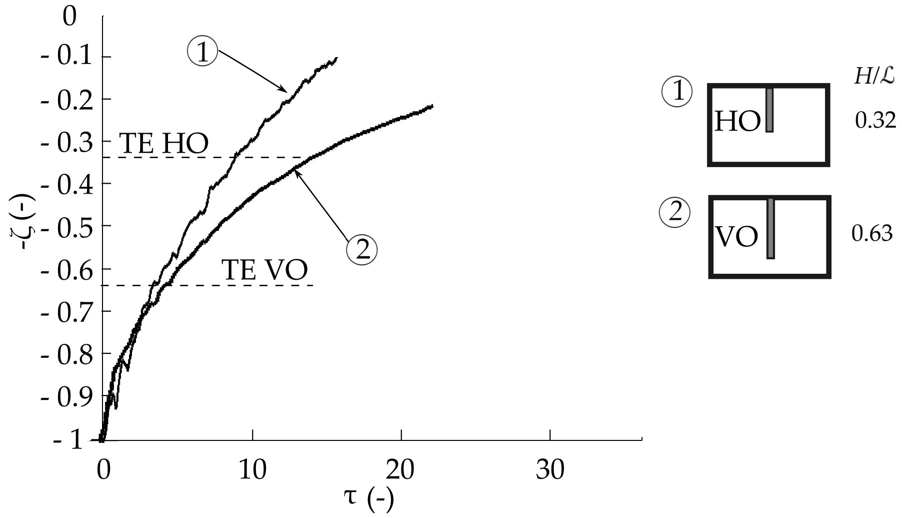

Figure 5.15: Non-dimensional position of the interface as a function of time, non-dimensionalised as in Figure 5.8, and convector orientation for timescale $\mathcal{T}_{exp}$ = 95 s. The interface position is scaled on height H. Dashed lines correspond to levels of trailing edges (TE).

results in an approximately 10-20% higher position of the interface. For the interface to ascend at any time instance to a level 50% higher, the convector strength has to be increased by a factor of 8.

5.3 Results of statistical analysis

The previous section focused on the experimental investigations into changing one component of the room-convector system, namely the convector location, orientation or strength. By targeting one system component in each investigation, several opportunities to increase the filling rate have been unveiled. To complete the investigation into the filling rate, the interdependency of the effects achieved by simultaneous modification of a few components of the room-convector system is investigated and the relative importance of individual system components is revealed. This is achieved by a statistical analysis performed on the experimental data[1], which is divided into five subpopulations, namely the starting plume, the horizontal current, the vertical intrusion, the reflection and the vertical filling, to monitor how these interdependencies vary in time, see Section 4.6 for details of the method. The outcome of the statistical analyses are the empirical expressions, $\mathfrak{R} = \beta_0 Ra^{\beta_1}\mathcal{B}^{\beta_2}\mathcal{G}^{\beta_3}\mathbf{T}^{\beta_4}$, which are derived to describe each stage of filling in terms of the non-dimensional governing parameters: the non-dimensional accumulation $\mathcal{B}$, the Rayleigh number Ra, the geometrical parameter $\{\mathcal{G}, \mathcal{G}^*\}$ and the time $\mathbf{T}$. These particular non-dimensional governing parameters have been selected, during the dimensional analysis, instead of other possible groups, as they are sensible on physical grounds, take into

[1]The experiments used in the statistical analysis are listed in the Appendix A.

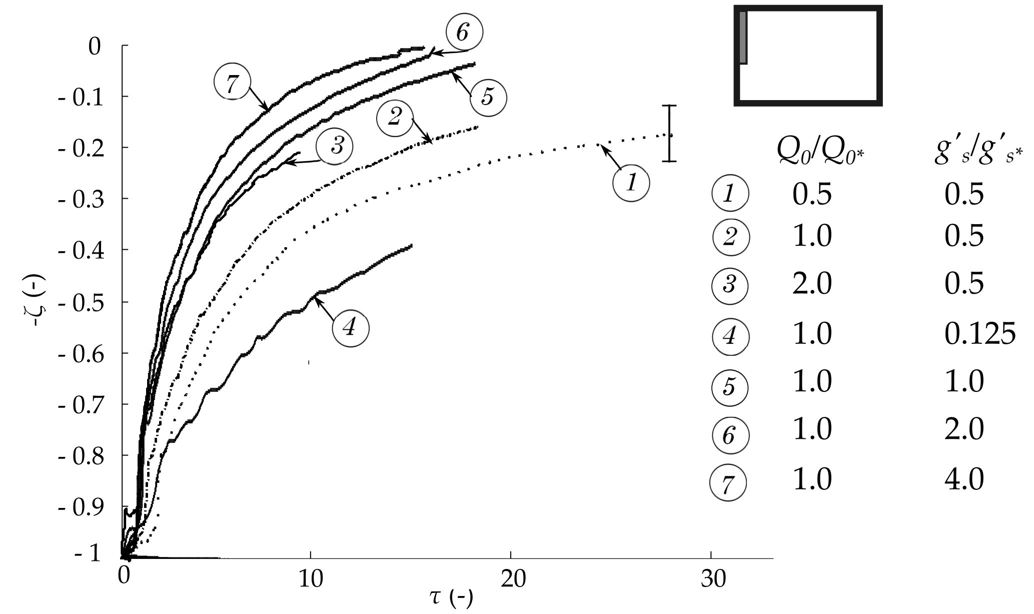

Figure 5.16: Non-dimensional position of the interface as a function of time, non-dimensionalised as in Figure 5.8, and the convector's strength.

account sequencing of the filling flows and can be easily varied between the experiments. The β-coefficients of regression correspond to the impact of a given governing parameter on the flow, thus enabling the classification of the governing parameters into the dominant and subordinate.

In Table 5.1 coefficients of regression for each governing parameter in each subpopulation are listed. The statistical analysis identifies two dominant governing parameters, the non-dimensional accumulation $\mathcal{B}$ and the Rayleigh number Ra, and two subordinate governing parameters, the dimensionless geometrical parameter $\{\mathcal{G}, \mathcal{G}^*\}$ and the dimensionless time $\mathbf{T}$.

5.3.1 Dominant parameters

The influence of two dominant governing parameters, the non-dimensional accumulation $\mathcal{B}$ and the Rayleigh number Ra, on the filling rate appears to be maintained at a constant level for the entire sequence of filling. Values of both dominant parameters depend on the convector strength. The parameter $\mathcal{B}$ relates the accumulated buoyancy released by the convector and the resulting rate of displacement, whereas Ra is a ratio of forces driving and retarding filling flows with the convector strength affecting the balance. The invariable impact of both dominant parameters on the filling rate is thus consistent with the results in Section 5.2.4, where the increase in the convector strength is shown to result in the stable increase in the ascent rate of the interface position for the duration of filling. An average value of the coefficient of regression of the non-dimensional accumulation $\mathcal{B}$ is 0.575 ±1%, whereas an average value of the coefficient of regression of the local Rayleigh number Ra is 0.425 ±6%. A greater value of each dominant governing parameter corresponds to a greater value of $\mathfrak{R}$, thus faster filling, which is yielded by the increased influence of buoyancy on the filling flows.

Subpopulation	β_1	β_2	β_3	β_4
1	0.57	0.4	0.0026	0.012
1	0.57	0.4	0.036	0.012
2	0.57	0.42	-0.008	-0.006
3	0.59	0.45	0.002	0.0145
4	0.58	0.44	0.00014	0.0006
5	0.57	0.43	-0.0000255	-0.000011

Table 5.1: Coefficients of regression β extracted from statistical analysis on five subpopulations.

5.3.2 Subordinate parameters

The influence of the subordinate parameters seems to decrease in each subsequent subpopulation. An average value of the coefficient of regression of each subordinate parameter is 0.005 $\pm O(10^2)$%. Decreasing trends of values of coefficients of regression of dimensionless geometry and time are in agreement with the results in Sections 5.1 and 5.2. By adjusting the convector-room system, the faster filling rates are achieved in the early period, contributing to the overall faster filling. In the late period the differences between filling rates for different system configurations tend to level off. In other words, the contribution of the flows to the overall filling rate seems to decrease in each subsequent subpopulation and the filling rate decreases with time. This is reflected by the decreasing values of exponents of the non-dimensional time. The influence of geometry on the rate of filling is crucial in the early period, during which the large-scale mixing may be extended by adjusting the convector location and height. With the decreasing rate of filling, the instantaneous impact of the geometry decreases, which justifies the decreasing trend in values of coefficients of regression of $\{\mathcal{G}, \mathcal{G}^*\}$.

5.3.3 Error of the Statistical Analysis

Table 5.2 summarises the results of analysis of significance (see Section 4.6.5 for details of the method). Coefficients of multiple correlation R are approximately 1 in each analysis, indicating noteworthy agreement between the newly defined power functions and the experimental results. Each value of statistic t-distribution is higher than the critical value (t_{Stucr} = 1.645), thus each variable used in the statistical analysis is significant. The values of F-statistics are significantly higher than the critical value (F_{cr} = 5.63), thus the zero - hypothesis $\mathcal{H}_0$: R = 0 is rejected and the alternative hypothesis $\mathcal{H}_1$: $R \neq 0$ applies, thus there is correlation between dependent and independent variables. The confidence intervals are small, which provides additional justification of the form of empirical equations developed. The analysis of significance thus confirms that each coefficient of regression is significant.

	Sub. 1 (with $\mathcal{G}$)	Sub. 1 (with $\mathcal{G}^*$)	Sub. 2	Sub. 3	Sub. 4	Sub. 5
R	0.991	0.981	0.995	0.995	0.999	0.999
s^2	0.0066	0.0064	0.0022	0.0022	0.00045	0.00002
$t_{Stu\beta 1}$	2.2×10^3	2.4×10^3	1.1×10^4	1.7×10^4	5.6×10^4	1.3×10^7
$t_{Stu\beta 2}$	1.4×10^3	1.4×10^3	7×10^3	9.5×10^3	3.5×10^4	6.6×10^6
$t_{Stu\beta 3}$	21	94	314	34	26	527
$t_{Stu\beta 4}$	44	48	62	177	25	141
F	9.9×10^3	10^4	1.1×10^4	1.8×10^5	4.4×10^4	3.7×10^9
$l_{\beta 1}$	$\pm 4.2 \times 10^{-4}$	$\pm 4 \times 10^{-4}$	$\pm 8 \times 10^{-5}$	$\pm 5.5 \times 10^{-5}$	$\pm 1.7 \times 10^{-5}$	$\pm 7.3 \times 10^{-8}$
$l_{\beta 2}$	$\pm 4.9 \times 10^{-4}$	$\pm 4.8 \times 10^{-4}$	$\pm 9.9 \times 10^{-5}$	$\pm 7.7 \times 10^{-5}$	$\pm 2.1 \times 10^{-5}$	$\pm 1.1 \times 10^{-7}$
$l_{\beta 3}$	$\pm 2 \times 10^{-4}$	$\pm 6.2 \times 10^{-4}$	$\pm 4.2 \times 10^{-5}$	$\pm 9.7 \times 10^{-5}$	$\pm 5 \times 10^{-4}$	$\pm 8 \times 10^{-8}$
$l_{\beta 4}$	$\pm 4.4 \times 10^{-4}$	$\pm 4 \times 10^{-4}$	$\pm 1.6 \times 10^{-5}$	$\pm 1.3 \times 10^{-4}$	$\pm 3.8 \times 10^{-5}$	$\pm 1.3 \times 10^{-7}$
l_y	±0.1337	±0.1314	±0.0772	±0.0531	±0.035	±0.0057

Table 5.2: Filling rate - results of analysis of significance: coefficient of multiple correlation, mean squared error, statistic t-distribution for the zero-hypothesis, F-statistic and confidence intervals of regression.

The experimental data used in the statistical analysis have inherent error due to the experimental methods used (see Chapter 4). The total error of the statistical analysis is therefore a sum of the errors due to the experimental method and the statistical method.

5.4 Summary of Results

The investigation presented here identifies the convector location and relative height (to the room height) as equally important. It is also shown that the effects of increasing the relative filling rate by adjusting either the convector location or the convector relative height may match the effects achieved by increasing the convector strength. Table 5.3 summarises maximum additional relative interface ascent due to system configuration adjustment. The location that encourages faster filling is the convector on the floor and away from the side wall at a distance $2d - 4d$. Limiting the convector height $\mathcal{L}$ improves the filling rate. In cases, where the heat demand is high and only taller convectors provide the sufficient output, selecting two shorter convectors is recommended. Table 5.4 summarises maximum filling rates due to system configuration adjustment.

horizontal pos.	vertical pos.	orientation	strength
10%	40%	30%	45%

Table 5.3: Maximum additional relative interface ascent due to system configuration adjustment.

	period	horizontal pos.	vertical pos.	orientation	strength
max	early + intermediate	0.15	0.136	0.12	0.16
min	early + intermediate	0.12	0.038	0.12	0.064
	late	0.02 ±0.01	0.02 ±0.01	0.02 ±0.01	0.02 ±0.01

Table 5.4: Maximum filling rates due to system configuration adjustment.

The qualitative observations and the investigation of the influence of the system configuration on the filling rate resulted in a set of simple rules that can simplify, the otherwise daunting and often accidental, processes of convector selection and setting out within a room. These can be summarised as follows:

- The convector strength B_0 maintains a steady influence of the filling rate for the duration of filling.
- For a given height H, maximising the vertical distance $H - \mathcal{L}$ should be a priority as it leads to the faster filling.
- Moving the convector away from the side wall, increases the entrainment into the plume, thus leading to the faster filling.
- For $a \leq 4d$, the development of the starting plume and plume is at least partially confined by a side wall and there are two characteristic lengths $H - \mathcal{L}$ and a. For $a > 4d$, $H - \mathcal{L}$ is the only characteristic length.
- The development of the horizontal current depends on a and $H - \mathcal{L}$.
- The maximum penetration λ of vertical intrusion depends on H and $\mathcal{L}$.

- Depending on H and $\mathcal{L}$, vertical intrusion collapses into:
  - overturning for $\left(\frac{H}{\mathcal{L}}\right) > 1.3$;
  - slumping for $\left(\frac{H}{\mathcal{L}}\right) < 1.3$.

It is reassuring that the results of statistical analysis confirm the qualitative results. The statistical analysis allowed examination the interdependencies between the governing parameters, which also led to establishing the dominant and subordinate governing parameters.

Chapter 6

Convector-induced stratification

Stratification is the second parameter used to assess the efficiency of filling and rank the performance of the convector-room system. In terms of stratification, more efficient filling and better system performance corresponds to inducing a weaker stratification (smaller salinity/density differences).

6.1 Developing stratification - discussion

Experiments have been performed to investigate if stratification can be controlled through convector position and strength. Salinity measurements, extracted from each experiment, are used to inform the discussion. The development of stratification is quantitatively assessed by analysing the salinity gradient, corresponding to the rate at which salinity increases, and by considering differences in salinity with height.

6.1.1 Horizontal position

Figure 6.1 shows the location of salinity probes used to investigate the influence of the convector horizontal position on the stratification, for $H/H_* = 1$. Figure 6.2 shows non-dimensional salinity as a function of non-dimensional time τ and convector horizontal position, for the system configuration: $H/H_* = 1$, $B_0/B_{0,*} = 1$. Four horizontal positions are considered: a) wall-mounted convector ($Æ = 0.65$); b) convector d from a side wall ($Æ = 0.67$); c) convector $2d$ from a side wall ($Æ = 0.69$); d) convector in the centre ($Æ = 1.26$).

The development of stratification varies for different horizontal positions of the convector. Linear trendlines in each figure approximate how the development of stratification varies in the early and late period, respectively. The steepest curves, corresponding to the highest salinity increment, are for the wall-mounted-convector case (Figure 6.2 a), where the entrainment rate into the plume decreases due to the limitations imposed by a side wall. Restricting the entrainment thus leads to a stronger stratification at 24τ with non-dimensional salinity varying between 0.26 - 0.3 in the far field (probes 1 - 5) and 0.04 - 0.22 in the near field (probes 6 -

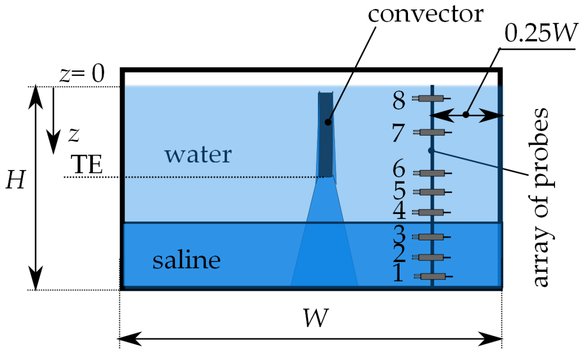

probe	distance	location
1	$0.95H$	far field
2	$0.85H$	far field
3	$0.75H$	far field
4	$0.64H$	far field
5	$0.47H$	far field
6	$0.32H$	trailing edge
7	$0.16H$	near field
8	$0.04H$	near field

Figure 6.1: Location of salinity probes in experiments with varying horizontal position of the convector, for $H/H_* = 1$ (schematic of tank in elevation).

8)[1]. Initially, stratification weakens with increasing horizontal distance from a side wall. For instance, for a convector placed d from a side wall (Figure 6.2 b), the non-dimensional salinity in the far field varies between 0.23 - 0.29, corresponding to up to 10% weaker stratification than for a wall-mounted convector. While in the near field, non-dimensional salinity ranges from 0.11 to 0.218 (up to 3% weaker stratification). Increasing the distance by another d (Figure 6.2 c) causes the stratification to weaken further and non-dimensional salinity varies between 0.21 - 0.24 (up to 20% weaker stratification) in the far field and 0.07 - 0.192 (up to 15% weaker stratification) in the near field. This behaviour of weakening stratification appears to be proportional to the filling rate that tends to increase initially (for distances up to $4d$) with the increasing distance from the side wall (see Section 5.2). Also in the previous chapter, it is shown that the fastest filling occurs when the convector is at the horizontal distance allowing free development of the plume in the near and far field ($2d$ - $4d$). Whereas moving the convector any further from the closer side wall results in a decreased filling rate due to less developed horizontal and vertical currents in the early period. Similarly, the developing stratification is stronger for the centrally-located convector (Figure 6.2 d) than the convector $2d$ from the side wall. The convector in the centre results in non-dimensional salinity between 0.23 - 0.26 in the far field and 0.11 - 0.196 in the near field at 24τ, corresponding to 15% and 12% decrease in salinity concentrations in the far field and near field, respectively (5% and 3% more stratified than in case c).

Similar effects of adjusting horizontal position can be observed for different heights H. Figure 6.3 shows the location of the salinity probes used to investigate the influence of the convector horizontal position on the stratification, for $H/H_* = 0.68$.

Figure 6.4 shows non-dimensional salinity $\mathcal{S}/\mathcal{S}_0$ as a function of non-dimensional time τ, for the system configuration: $H/H_* = 0.68$, $B_0/B_{0,*} = 1$. Three cases are considered: a) wall-mounted convector ($\mathcal{AR} = 0.44$; b) convector d from a side wall ($\mathcal{AR} = 0.46$); c) convector $2d$ from a side wall ($\mathcal{AR} = 0.47$). An insight into the role of vertical distance $H - \mathcal{L}$ for a given convector height is gained by comparing Figures 6.2 and 6.4. Reducing the vertical distance $H - \mathcal{L}$, while maintaining the convector height $\mathcal{L}$, strengthens stratification in both near and far fields. As a result, salinity curves are steeper and more spread in Figure 6.4. However, for a given height H, the relative impact of adjusting convector horizontal position appears

[1]The remaining three cases are compared to the wall-mounted case.

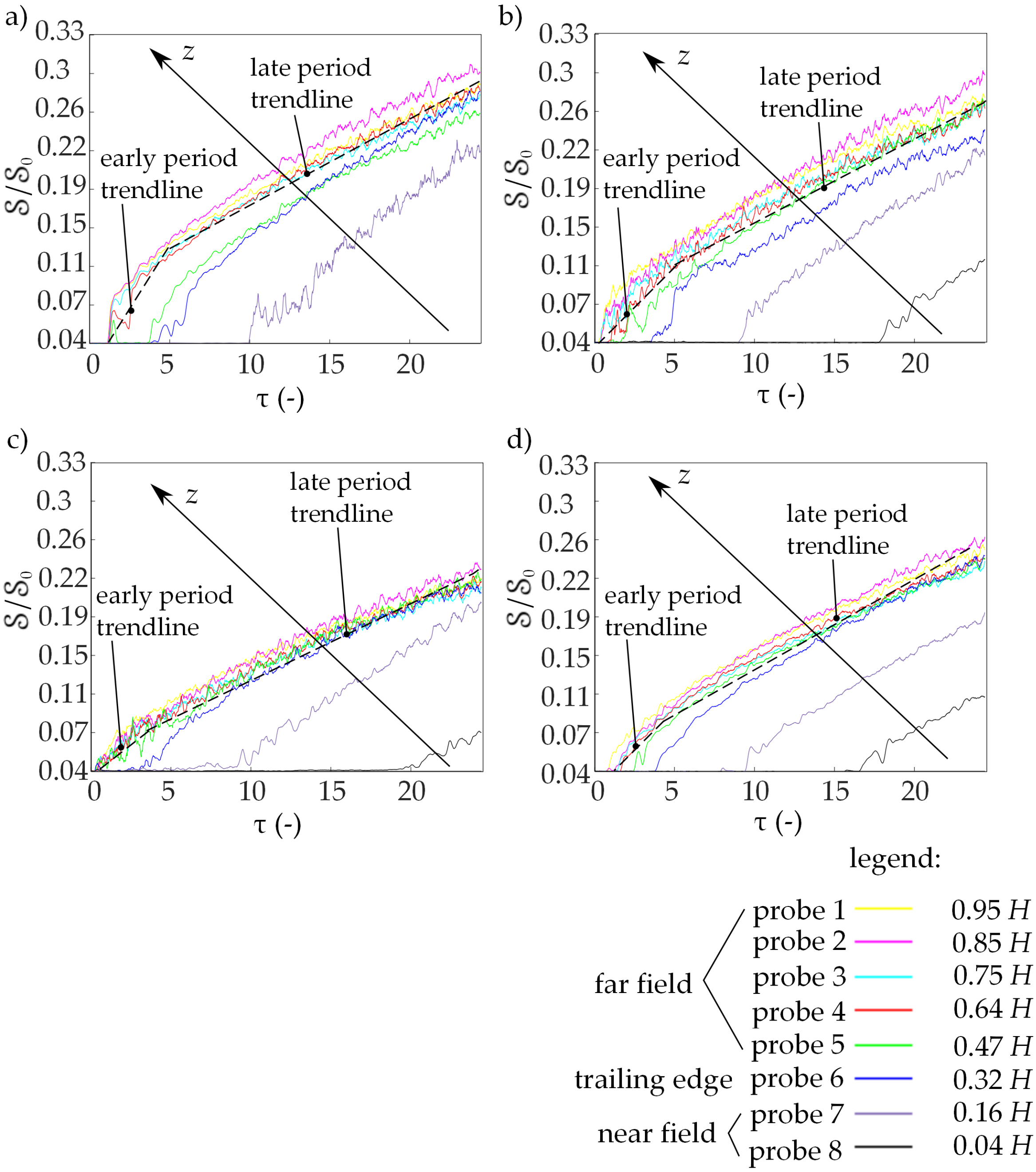

Figure 6.2: Salinity $\mathcal{S}$, scaled on the source salinity $\mathcal{S}_0$, as a function of non-dimensional time τ, scaled on the experimental time scale $\mathcal{T}_{exp}$, and convector horizontal position for $H/H_* = 1$: a) wall-mounted convector ($\AE = 0.65$); b) convector d from a side wall ($\AE = 0.67$); c) convector $2d$ from a side wall ($\AE = 0.69$); d) convector in the centre ($\AE = 1.26$). Vertical z-coordinate is related to the vertical position of the probes, where arrow indicates direction towards the tank base. Data is smoothed using a moving average filter with span equal 9.

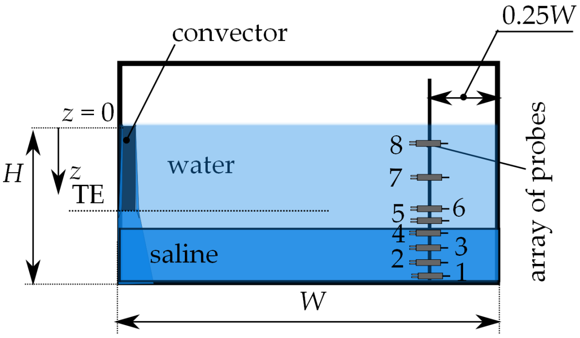

probe	distance	location
1	0.95H	far field
2	0.92H	far field
3	0.75H	far field
4	0.64H	far field
5	0.54H	far field
6	0.47H	trailing edge
7	0.32H	near field
8	0.16H	near field

Figure 6.3: Location of salinity probes in experiments with varying horizontal position of the convector, for $H/H_* = 0.68$ (schematic of tank in elevation).

to have similar influence on the stratification, with 20% and 15% weaker stratification in the far and near fields of convector located 2d from a side wall, compared to the wall-mounted case.

Throughout the early period and the early stages of the late period (approximately 0 - 7τ, subject to system configuration), a stable stratification develops characterised by decreasing salinity with height. As the filling progresses, the stratification destabilises and there are cross-overs between different salinity curves (e.g., in Figure 6.2: (a) probes 3 and 4 at 7.5τ, probes 5 and 6 at 13τ; (d) probes 1 and 2 at 11τ; in Figure 6.4 (a) probes 4 and 5 at 7τ). This irregularity could be caused by additional mixing or salinity detrainment from the plume in the late period. The physics of the process are explained in Section 6.2 and then investigated further in the next chapter, using PIV data. Another aspect of the late-period filling is that there is a trend towards a well-mixed environment, which is faster in the far field than in the near field. Similarly to weakening stratification, this trend initially increases with the distance from a side wall, due to the increase in the entrainment into the plume. The weakening of stratification by adjusting the horizontal position of the convector hence leads to a more uniform surrounding area that tends to well-mixed, although not reaching this state for the duration of filling. The closest to the well-mixed is the far-field stratification induced by a convector 2d from a side wall.

6.1.2 Vertical position

Figure 6.5 shows the location of the salinity probes used to investigate the influence of the vertical position on the stratification.

Figure 6.6 shows non-dimensional salinity $\mathcal{S}/\mathcal{S}_0$ as a function of non-dimensional time τ and convector vertical position, for wall-mounted convector and $B_0/B_{0,*} = 1$; three cases are considered: a) $H/H_* = 0.32, \mathcal{R} = 0.2$; b) $H/H_* = 0.47, \mathcal{R} = 0.3$; c) $H/H_* = 0.68, \mathcal{R} = 0.43$. For a given convector (size, strength, position) limiting the height H, which corresponds to limiting the vertical distance $H - \mathcal{L}$, leads to a stronger stratification reflected by steeper, more spread, salinity curves. The strongest stratification, as shown in Figure 6.6 a), corresponds to the case where $H = \mathcal{L}$ ($H/H_* = 0.32, \mathcal{R} = 0.2$) and the salinity difference between probes 1 and 8 ($\Delta\mathcal{S}/\mathcal{S}_0 = 0.38$) at 24$\tau$ (experiment termination) is 43% higher than in the wall-mounted case for $H/H_* = 1$ (Figure 6.2, $\Delta\mathcal{S}/\mathcal{S}_0 = 0.26$). For $(H - \mathcal{L})/H = 0.33$ ($H/H_* = 0.47, \mathcal{R} = 0.3$) the sur-

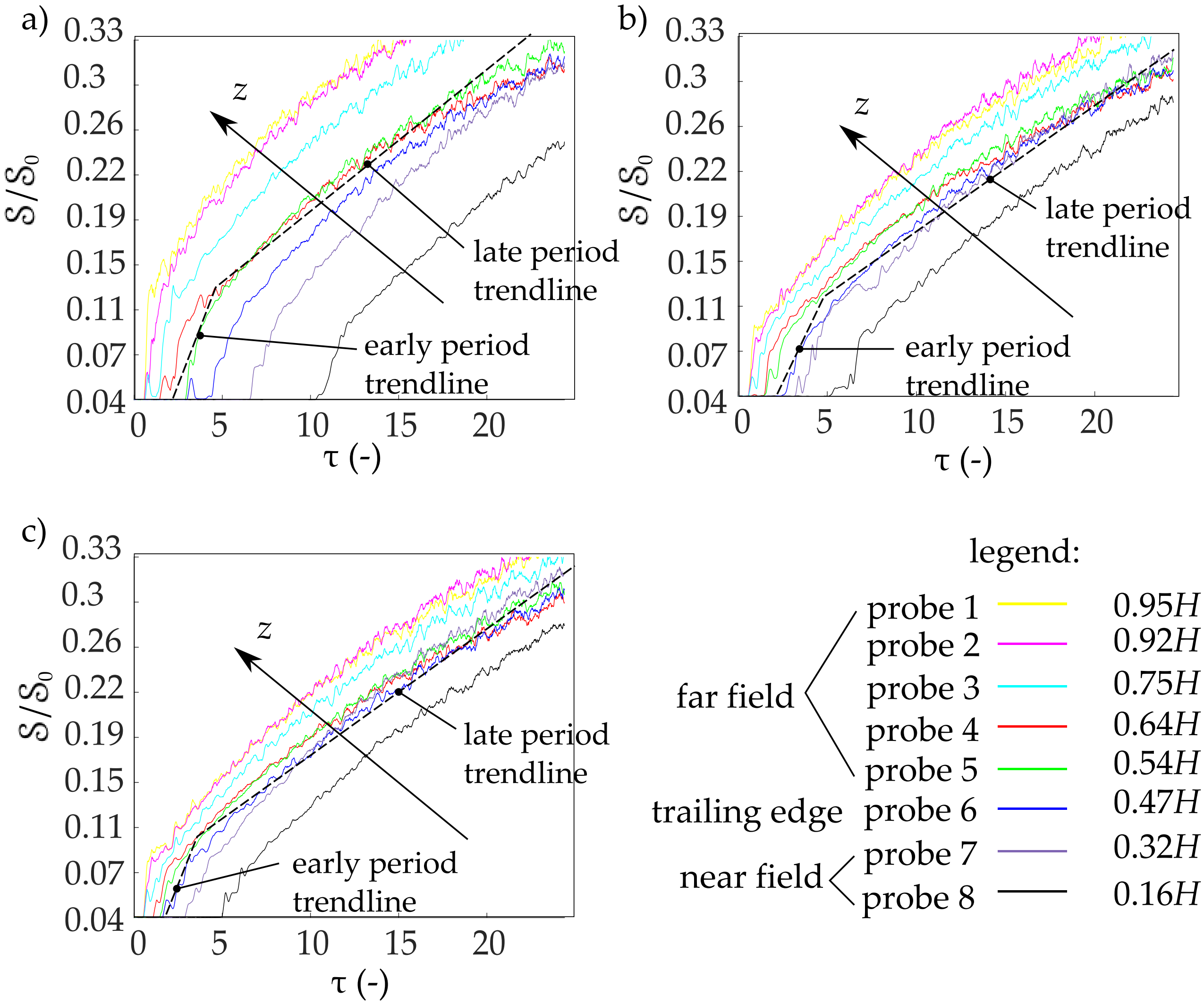

Figure 6.4: Salinity $\mathcal{S}$, scaled on the source salinity $\mathcal{S}_0$, as a function of non-dimensional time τ, scaled as in Figure 6.2, and convector horizontal position for $H/H_* = 0.68$: a) wall-mounted convector ($Æ = 0.44$; b) convector d from a side wall ($Æ = 0.46$); c) convector $2d$ from a side wall ($Æ = 0.47$). Vertical z-coordinate is related to the vertical position of the probes, where arrow indicates direction towards the tank base. Data is smoothed using a moving average filter with span equal 9.

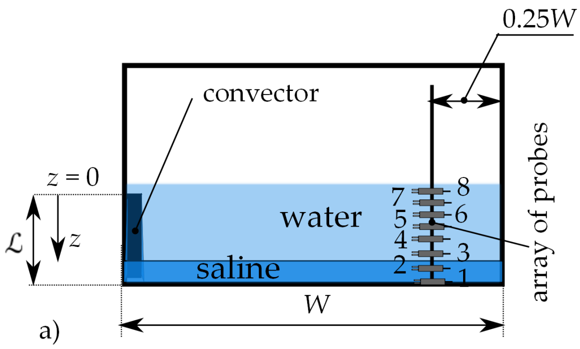

a)

probe	distance	location
1	0.92H	near field
2	0.83H	near field
3	0.66H	near field
4	0.5H	near field
5	0.33H	near field
6	0.24H	near field
7	0.16H	near field
8	0.03H	near field

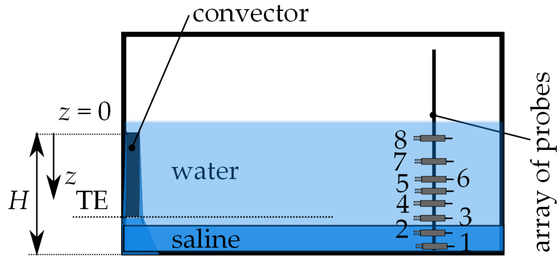

b)

probe	distance	location
1	0.95H	far field
2	0.88H	far field
3	0.66H	trailing edge
4	0.55H	near field
5	0.33H	near field
6	0.22H	near field
7	0.11H	near field
8	0.04H	near field

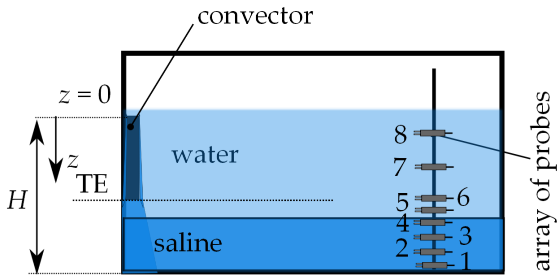

c)

probe	distance	location
1	0.95H	far field
2	0.92H	far field
3	0.75H	far field
4	0.64H	far field
5	0.54H	far field
6	0.47H	trailing edge
7	0.32H	near field
8	0.16H	near field

Figure 6.5: Location of salinity probes in experiments with varying vertical position of the convector, for wall-mounted convector, $B_0/B_{0,*} = 1$: a) $H/H_* = 0.32$, $Æ = 0.2$; b) $H/H_* = 0.47$, $Æ = 0.3$; c) $H/H_* = 0.68$, $Æ = 0.43$ (schematic of tank in elevation).

rounding area remains strongly stratified with a salinity difference $\Delta\mathcal{S}/\mathcal{S}_0 = 0.37$. A reduction in the salinity difference can be observed for $(H-\mathcal{L})/H = 0.54$ ($H/H_* = 0.68$, $\text{Æ} = 0.43$) with salinity curves slowly levelling off (salinity difference of $\Delta\mathcal{S}/\mathcal{S}_0 = 0.33$, accounts for interface not reaching the leading edge of convector). The development of stratification in the near and far fields is compared based on salinity readings from individual probes. Probes 1 and 2, are of particular interest, because in case (a) these are in the near field, whereas in cases (b-c) in the far field. When in the near field (a), the salinity difference between the two probes is $\Delta\mathcal{S}/\mathcal{S}_0 = 0.11$. For $(H-\mathcal{L})/H = 0.33$ the salinity difference decreases to $\Delta\mathcal{S}/\mathcal{S}_0 = 0.01$ (by an order of magnitude) and $(H-\mathcal{L})/H = 0.54$ leads to further reduction in salinity difference to approximately $\Delta\mathcal{S}/\mathcal{S}_0 = 0.002$. These results emphasise the impact of the vertical distance $H-\mathcal{L}$ on the developing stratification. The stratification tending towards well-mixed appears to be achieved when $H-\mathcal{L}$ is greater than the convector height $\mathcal{L}$, e.g. ($H/H_* = 0.68$ and $H/H_* = 1$).

6.1.3 Strength

Figure 6.7 shows non-dimensional salinity $\mathcal{S}/\mathcal{S}_0$ as a function of non-dimensional time τ and convector strength, for system configuration: $H/H_* = 1$ and $\text{Æ} = 0.76$. Three convector strengths are considered: a) $\dot{Q}_0/\dot{Q}_{0,*} = 0.5$, $g'_s/g'_{s,*} = 1$; b) $\dot{Q}_0/\dot{Q}_{0,*} = 1$, $g'_s/g'_{s,*} = 1$; c) $\dot{Q}_0/\dot{Q}_{0,*} = 1.33$, $g'_s/g'_{s,*} = 1$. The increase in convector strength results in an increase in the salinity across near and far fields. The values of non-dimensional salinity $\mathcal{S}/\mathcal{S}_0$ in the far and near fields, at 24τ, for $\dot{Q}_0/\dot{Q}_{0,*} = 0.5$ are in the range 0.16 - 0.23 and 0.04 - 0.16, respectively. Doubling the convector strength, does not lead to a doubling of salinity at any level, but shifts the ranges to 0.22 - 0.26 (far field) and 0.11 - 0.22 (near field). These correspond to a 13% increase in the far field upper limit, a 43% increase in the salinity at the trailing edge of the convector and a 290% increase in the value of the near field lower limit. These changes are caused by faster ascent of the more concentrated saline layer. Increasing the convector strength by a further 66.67% results in additional shifts in ranges of non-dimensional salinity in far and near fields by 29%, 25% and 14% compared to values for $\dot{Q}_0/\dot{Q}_{0,*} = 1$.

6.1.4 Interdependency between filling rate and stratification

Understanding the interplay between the filling rate and stratification is crucial to any assessment of the convector-room system in the context of efficiency of filling flows. Figure 6.8 and Figure 6.9 show the interdependencies between the filling rate and stratification in the early and late filling periods, respectively. The convector against the side wall ($\text{Æ} = 0.64$) of height $H = H_*$ and strength $B_0 = B_{0,*}$ is taken as the baseline case the other system configurations are compared to. In both periods, the coordinates of the baseline case correspond to (1,1), where an abscissa corresponds to the inclination of the interface position and an ordinate corresponds to the inclination of the linear trendline approximating stratification development. An abscissa greater than 1 corresponds to faster filling than the baseline case, whereas an ordinate less than 1 corresponds to weaker stratification. Each point in the diagram corresponds to a different convector-room configuration. Relative efficiency of each convector-room system compared to the baseline case is represented by colours, where points in green correspond to the better configurations (leading to both faster filling and weaker stratification), whereas red indicates worse

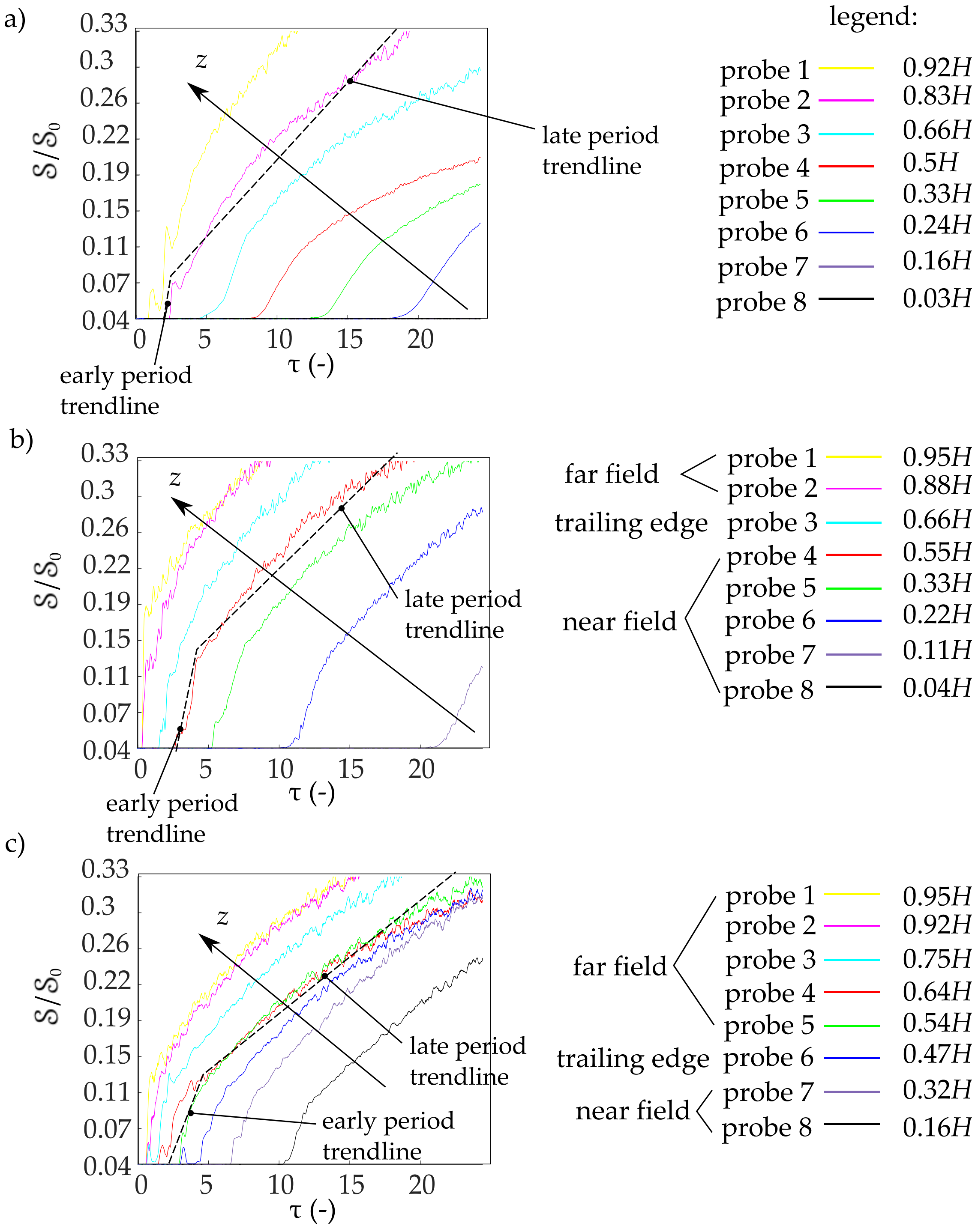

Figure 6.6: Salinity $\mathcal{S}$, scaled on the source salinity $\mathcal{S}_0$, as a function of non-dimensional time τ, scaled as in Figure 6.2, and vertical distance H, for wall-mounted convector, $B_0/B_{0,*} = 1$: a) $H/H_* = 0.32$, $\AE = 0.2$; b) $H/H_* = 0.47$, $\AE = 0.3$; c) $H/H_* = 0.68$, $\AE = 0.43$ (schematic of tank in elevation). Data is smoothed using a moving average filter with span equal 9.

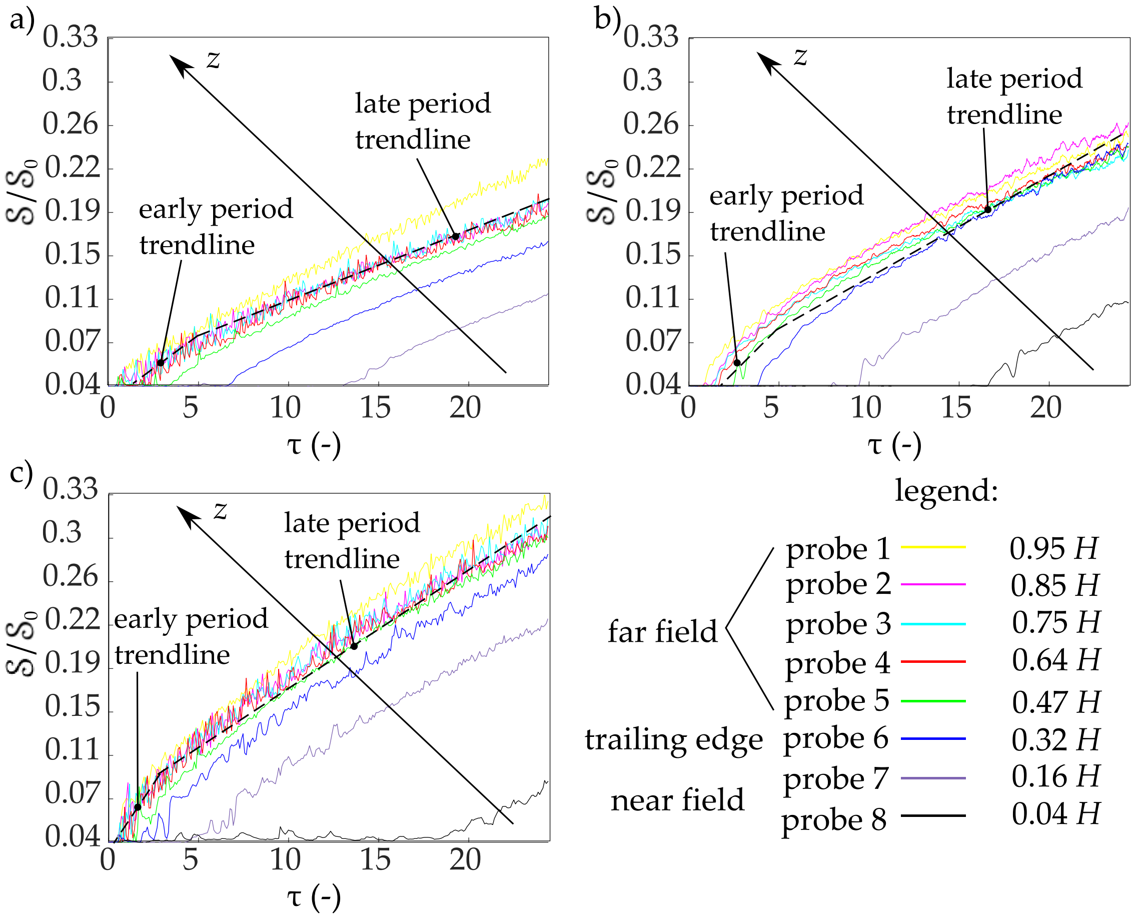

Figure 6.7: Salinity $\mathcal{S}$, scaled on the source salinity $\mathcal{S}_0$, as a function of non-dimensional time τ, scaled as in Figure 6.2, and strength, for $H/H_* = 1$ and convector in the centre, $AR = 0.76$: a) $\dot{Q}_0/\dot{Q}_{0,*} = 0.5$, $g'_s/g'_{s,*} = 1$; b) $\dot{Q}_0/\dot{Q}_{0,*} = 1$, $g'_s/g'_{s,*} = 1$; c) $\dot{Q}_0/\dot{Q}_{0,*} = 1.33$, $g'_s/g'_{s,*} = 1$. Data is smoothed using a moving average filter with span equal 9.

configurations. In the early period, point 4 (1.3, 0.5) represents the best configuration with the convector $4d$ from the side wall and the maximum height ($H/H_* = 1$). Whereas points 13 (0.3, 2.55) (wall-mounted convector, minimum height $H/H_* = 0.32$) and 14 (0.45, 3) (wall-mounted convector in vertical orientation) correspond to the worst configurations.

Design guidelines: horizontal position

Adjusting horizontal position by moving a convector away from a side wall both weakens the stratification and increases the filling rate. These beneficial effects of changing the horizontal position of convector are pronounced both in the early and late filling periods. The interdependency between rate of filling and stratification is confirmed and the increase in the filling rate through adjusting the convector horizontal position results in the less stratified environment. It is therefore recommended to locate convectors away from side walls at a distance that allows free development of the plume, both in the near and far fields - herein this distance corresponds to $2d - 4d$.

Design guidelines: vertical position

The increase in the vertical distance $H - \mathcal{L}$, thus also height H, compared to the convector height $\mathcal{L}$ leads to faster filling and more uniform environment. Herein, for better performance of convector-room system, it is recommended that the vertical distance $H - \mathcal{L}$ is greater than the convector height.

Design guidelines: strength

Increasing the convector strength improves the performance of the convector-room system by ensuring faster filling with portions of more concentrated saline both in near and far fields. The mixing within the buoyant layer remains, however, mainly unchanged subject to modification by adjusting vertical and horizontal position of the convector. No attempts are made to provide recommendations regarding the optimal strength of convector. The outcome of the discussion on both filling rate and stratification is that, for a given convector strength, the buoyancy distribution with height can be improved by adjusting the convector position.

6.1.5 Performance implications

Performance indicators are non-dimensional measures of buoyancy accumulation and are used to evaluate the overall efficiency of operation of the convector-room system through assessing the history of filling (for definitions see Sections 4.7.1 - 4.7.2). The scaling of performance indicators (time-, space- and strength-averaged) allows direct comparisons of accumulation within distinct systems against the benchmark case. For clarity, performance indicators are displayed on rosette diagrams (see Section 4.7.4 for details regarding constructing rosettes).

During an experiment, a vertical array of evenly distributed probes recorded salinity data. To demonstrate a scenario representative of a standard habitable room, rather than separately displaying results from all the probes, probes are grouped into zones, as shown in Figure 6.10:

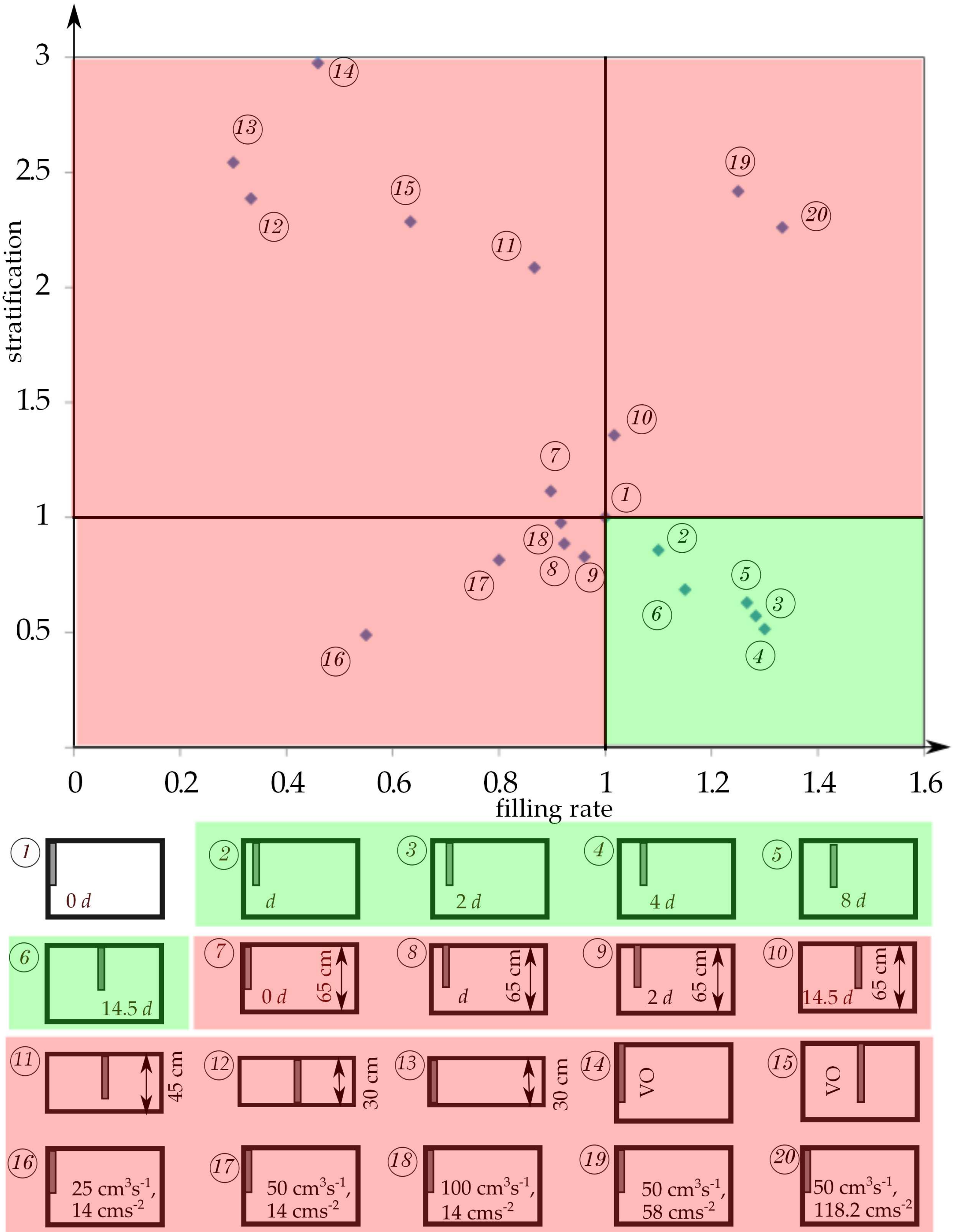

Figure 6.8: Interdependency between filling rate and stratification in early filling period. Legend: green field - better performance than baseline case (1,1); red field - worse performance than baseline case (1,1).

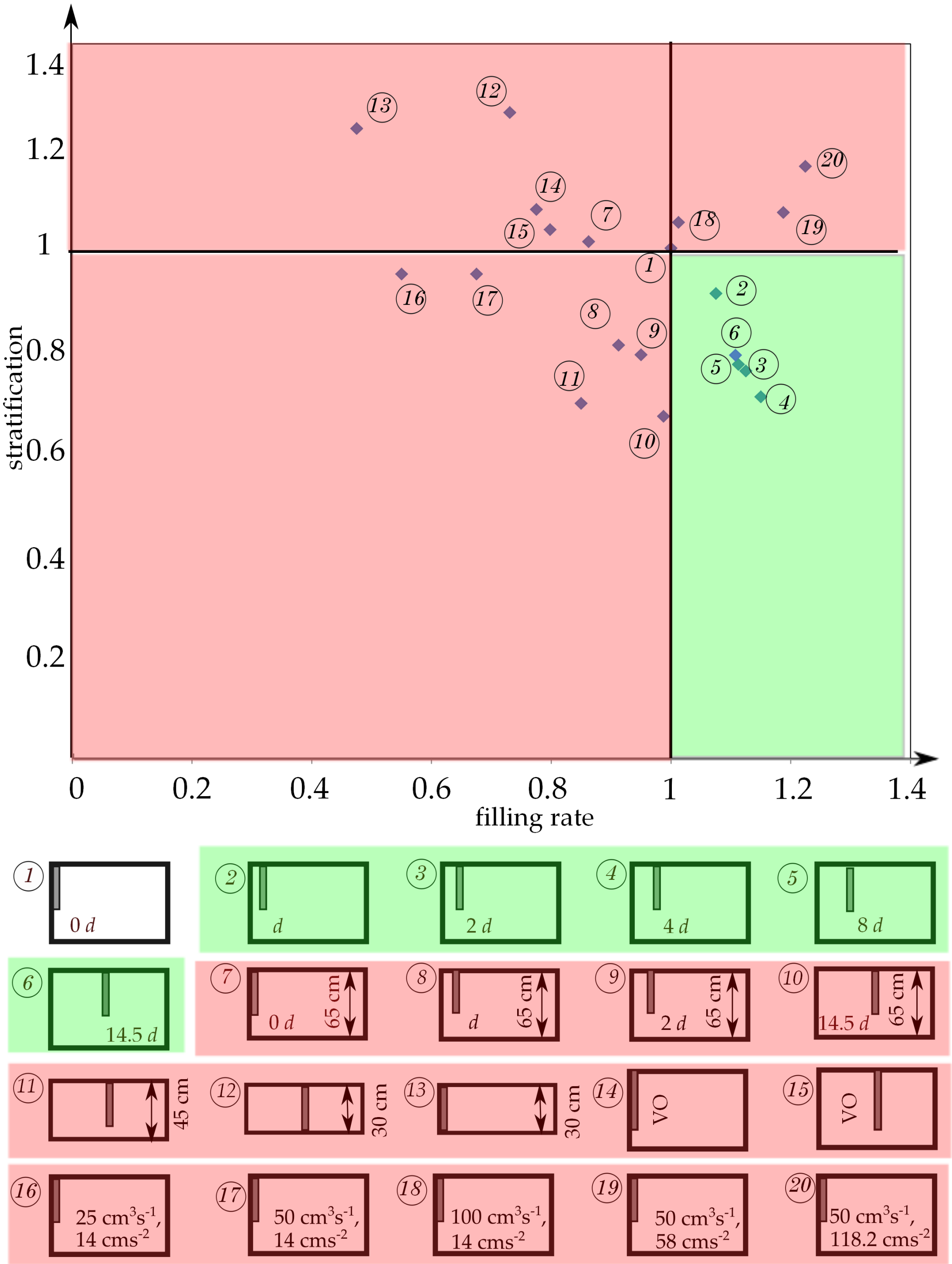

Figure 6.9: Interdependency between filling rate and stratification in late filling period. Legend: green field - better performance than baseline case (1,1); red field - worse performance than baseline case (1,1).

the occupied zone of $0.7H$ depth (from the water level), the above occupied zone of $0.3H$ depth, the breathing zone (level of head) and the walking zone (level of the feet), subsets of the occupied zone, both of $0.3H$ depth and with a well-mixed buoyant layer. At a given instant, the mean density in each zone is an average of measurements from probes grouped within.

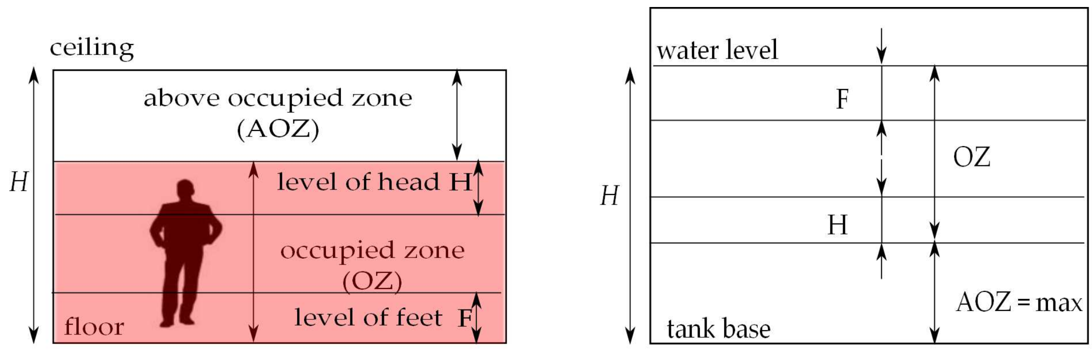

a) b)

Figure 6.10: Performance indicators: a) example application; b) corresponding experimental set-up.

Figure 6.11 demonstrates the application of performance indicators to the saline-in-water experiment, based on salinity measurements. The convector-room configuration is as follows: wall-mounted convector, $H/H_* = 1$ and $B_0/B_{0,*} = 1$. Figure 6.11 shows (a) six performance indicators: I_R, $I_{AOZ} = I_{max}$, I_{OZ}, I_H and I_F as functions of time, and (b) four rosettes corresponding to 15τ, 25τ, 35τ and 45τ. There is an increasing trend in values of all the performance indicators: I_R, $I_{AOZ} = I_{max}$, I_{OZ}, I_H and I_F in time. Increments, however, vary which lead to functions $I = f(t)$ spreading in time. A temporal function of the global performance indicator I_R shows an averaged (smoothed) efficiency of accumulation within the entire space and thus it may be used as a benchmark value to compare to the accumulation within remaining zones. The zones that underperform, thus with a lower than room-averaged capability to accumulate buoyancy, have values lower than I_R, whereas overperforming zones may be identified by values higher than I_R. In the example, *AOZ* is 30% - 40% above average, whereas OZ 20% - 30% below. In *OZ* the discrepancies between H and F are more significant corresponding to 30% - 40% above the average and 70% - 80% below the average, respectively. These trends are mostly maintained for the duration of filling with a slow self-regulating tendency to even out the differences (fluctuations ±10% to 20%). Irregular shapes of rosettes emphasise discrepancies in capability of each zone to accumulate buoyancy. The zone with the highest improvement rate between 15τ and 45τ is F, corresponding to 20%.

Figure 6.12 shows rosettes with performance indicators at 25τ for selected cases from Sections 6.1.1 - 6.1.3, where rosettes (a), (d) and (g) show the buoyancy accumulation as a function of vertical position; rosettes (b), (e) and (h) focus on the implications of the horizontal position; and (c), (f) and (i) show the implications of changing the convector strength. Different shapes of rosettes for different system configurations confirm that the capability to accumulate buoyancy in different locations within space depends on the convector position and strength. For

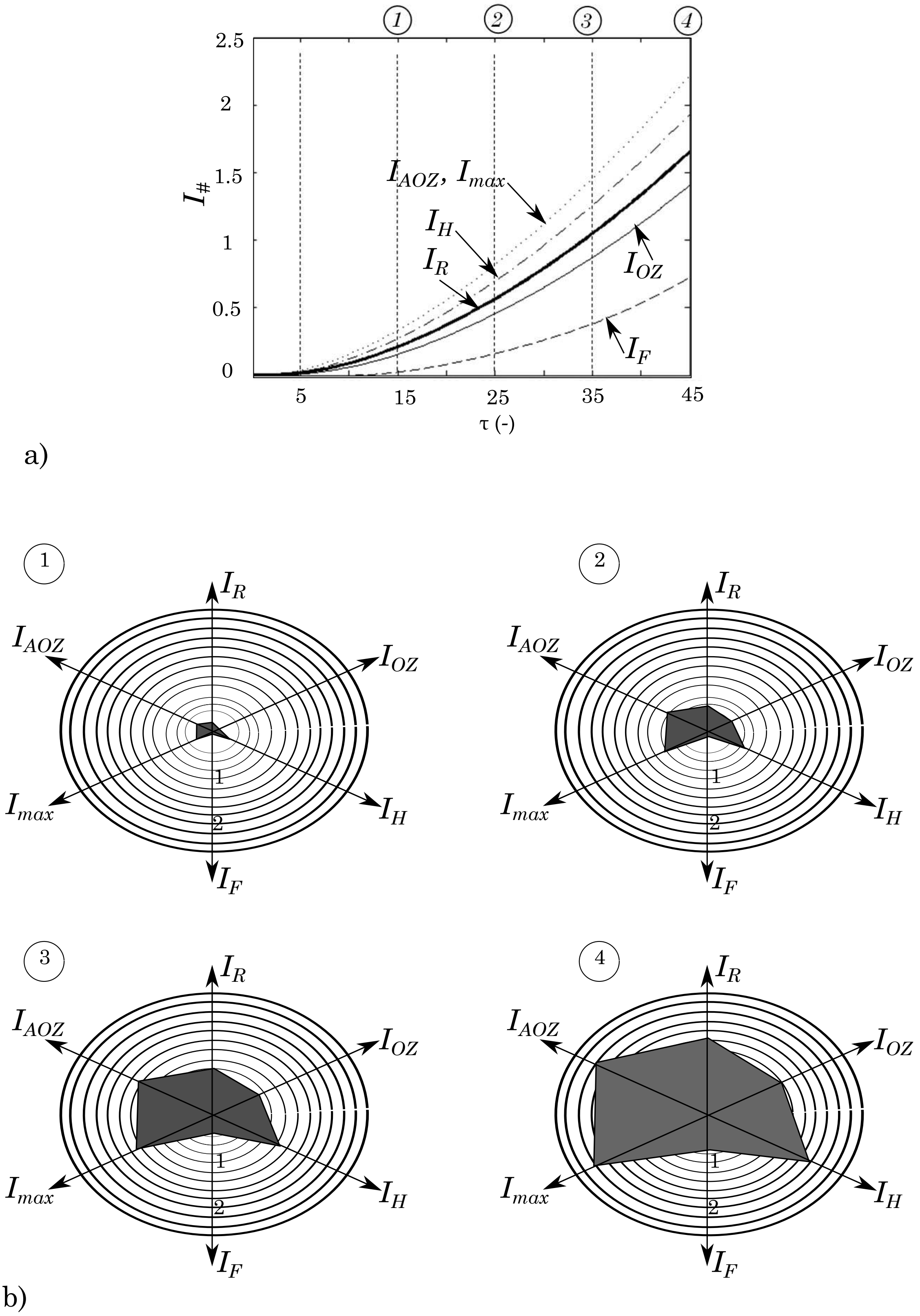

Figure 6.11: Rosette diagrams from experimental data: a) performance indicators, b) experimental rosettes.

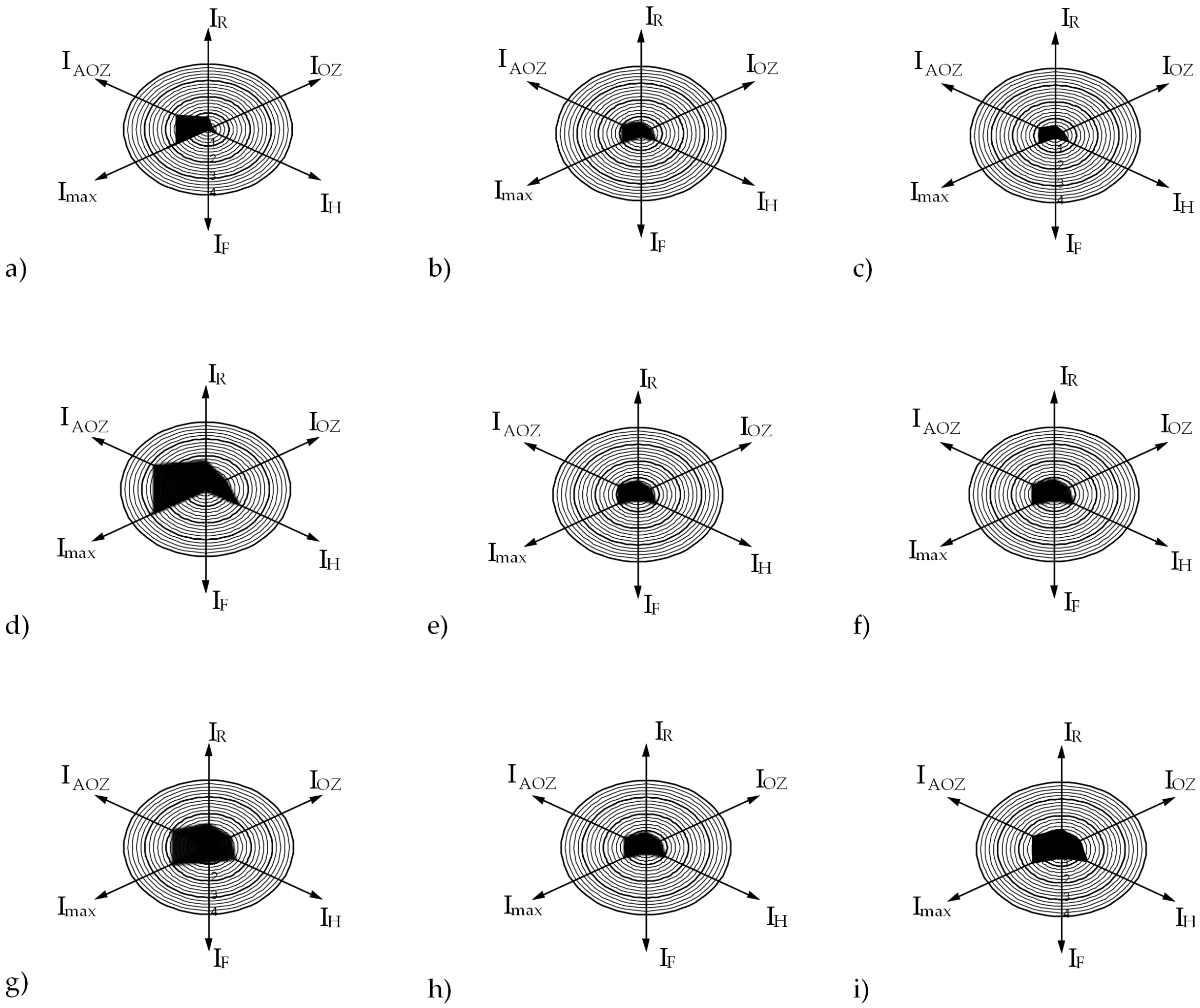

legend:

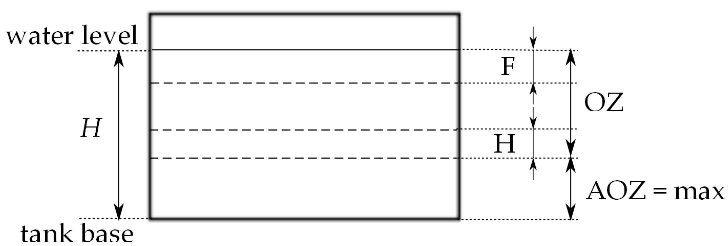

case:	rest	g)	d)	a)
H/H_*	1	0.68	0.47	0.32
OZ	$0.74H$	$0.77H$	$0.67H$	$0.67H$
AOZ	$0.26H$	$0.23H$	$0.33H$	$0.33H$
H	$0.29H$	$0.31H$	$0.33H$	$0.27H$
F	$0.29H$	$0.31H$	$0.22H$	$0.27H$

Figure 6.12: Rosette diagrams with performance indicators: vertical position comparison (wall-mounted convector, $B_0/B_{0,*} = 1$): a) $H/H_* = 0.32$, d) $H/H_* = 0.47$, g) $H/H_* = 0.68$; horizontal position ($H/H_* = 1$, $B_0/B_{0,*} = 1$): b) wall-mounted convector, e) convector ($2d$) from a side wall, h) convector in the centre ($14.5d$); strength comparison (convector in the centre, $H/H_* = 1$, $g_s'/g_{s,*}' = 1$): c) $\dot{Q}_0/\dot{Q}_{0,*} = 0.5$, f) $\dot{Q}_0/\dot{Q}_{0,*} = 1$, i) $\dot{Q}_0/\dot{Q}_{0,*} = 1.33$.

smaller vertical distances $H - \mathcal{L}$, the differences between AOZ and OZ, and H and F increase, which corresponds to more stratified layers. For instance, for $(H - \mathcal{L})/H = 0.68$ the difference in accumulation capability between AOZ and OZ corresponds to 60%, which increases to 65% and 110% for $(H - \mathcal{L})/H = 0.54$ and 0.33, respectively[1]. Moving the convector away from the wall reduces the gap (even by 30% for convector $2d$ away from the wall) in buoyancy accumulation between zones by reducing the capability of AOZ and increasing of OZ. Increasing the convector strength appears to decrease the differences between buoyancy accumulation in different zones (by up to 35%). A trend to equalise capability to accumulate buoyancy within space appears to coincide with increasing the rate of filling and decreasing the stratification.

6.2 Physics of developing stratification

The rescaled dye-attenuation images provide a quantitative representation of stratification and time series of rescaled dye-attenuation images are thus used to assess the development of stratification in the horizontal and vertical directions during filling. Salinity readings are also used to quantify horizontal and vertical stratification. Figure 6.13 consists of 16 frames depicting different stages of filling in a typical experiment with a wall-mounted convector, in order of their appearance. The set-up conditions are: $B_0/B_{0,*} = 1$, $\AE = 0.65$ and $H/H_* = 1$. Each frame, recorded as a grayscale image, is rescaled to a color map to display the density field within the entire tank, averaged across the depth of field, here equal to the width of the side wall of the tank, $W/Y = 1.5$. The colour scheme is identical in each frame, where black corresponds to $\mathcal{S}/\mathcal{S}_0 = 0$ and white to $\mathcal{S}/\mathcal{S}_0 = 0.5$. An array of 18 probes was positioned away from the convector, $0.05W$ from the opposite side wall. The density profiles, the results of interpolation between the measuring points, were created for each frame and superimposed onto the figure. As a result, Figure 6.13 makes it possible to follow the development of stratification. The ratio between the buoyant and the ambient fluid entrained into the plume increases as the stratification progresses and the position of the first front consequently ascends.

At first, the stratification develops both in the vertical and horizontal direction. In subfigures a-e, there is a horizontal stratification with salinity $\mathcal{S}/\mathcal{S}_0$ ranging from 0.04 to 0.11. The horizontal stratification begins to cease during motions of horizontal reflection (f-k) that leads to slow evening of the salinity difference between the less dense region close to the plume (left-hand-side, 0.07 to 0.11) and the buoyant region in the opposite side of tank (0.11 to 0.15). This appears to be achieved at 8.5τ (l), where at any level within the buoyant layer salinity difference is less than 0.04. In period $8.5\tau - 17.5\tau$ balanced stratification establishes. Towards the end of experiment (n-p), local disturbances in density distribution with height begin to appear, first in the right-hand-corner of the tank (n), to subsequently spread across the entire tank (o-p). These could correspond to local detrainments from the plume at heights where a local density equilibrium between the plume and the buoyant layer occurs leading to the release of portion of plume into the environment. Similar trends in the development of stratification are recorded by salinity probes. The density profiles extracted from the experiment are initially regular, which indicates balanced development of stratification (a-l). Interestingly, the late-period intrusions (shearing motions) appear to affect, disturb even, the balanced stratification

[1]Values calculated using the following expression: $\frac{I_{AOZ}-I_{OZ}}{I_R} \times 100\%$

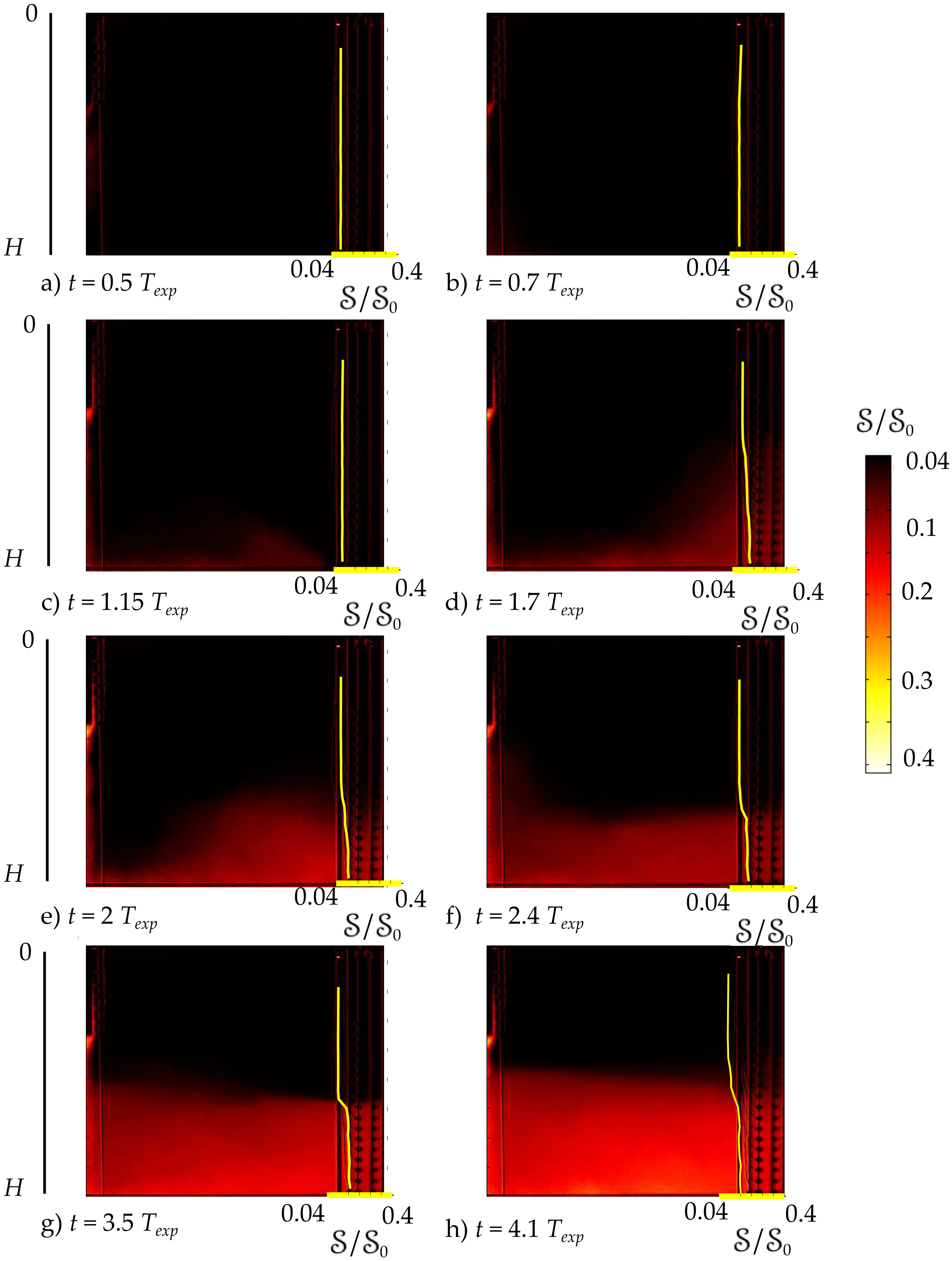

Figure 6.13: Filling flows during early period: a) vertical starting plume, b) impingement, c) horizontal current, d) vertical intrusion, e) horizontal reflection, f) horizontal reflection, g) layering, h) interface ascent. Each subplot consists of two parts: 1) an experimental frame, recorded as a grayscale image, scaled using dye-attenuation technique for depth-of-field-averaged density field (Allgayer & Hunt 2012) and presented as a color map (legend applies to each subplot); 2) a salinity profile. Set-up conditions: $B_0/B_{0,*} = 1$; room parameters: $\mathcal{AR} = 0.65$, $H/H_* = 1$.

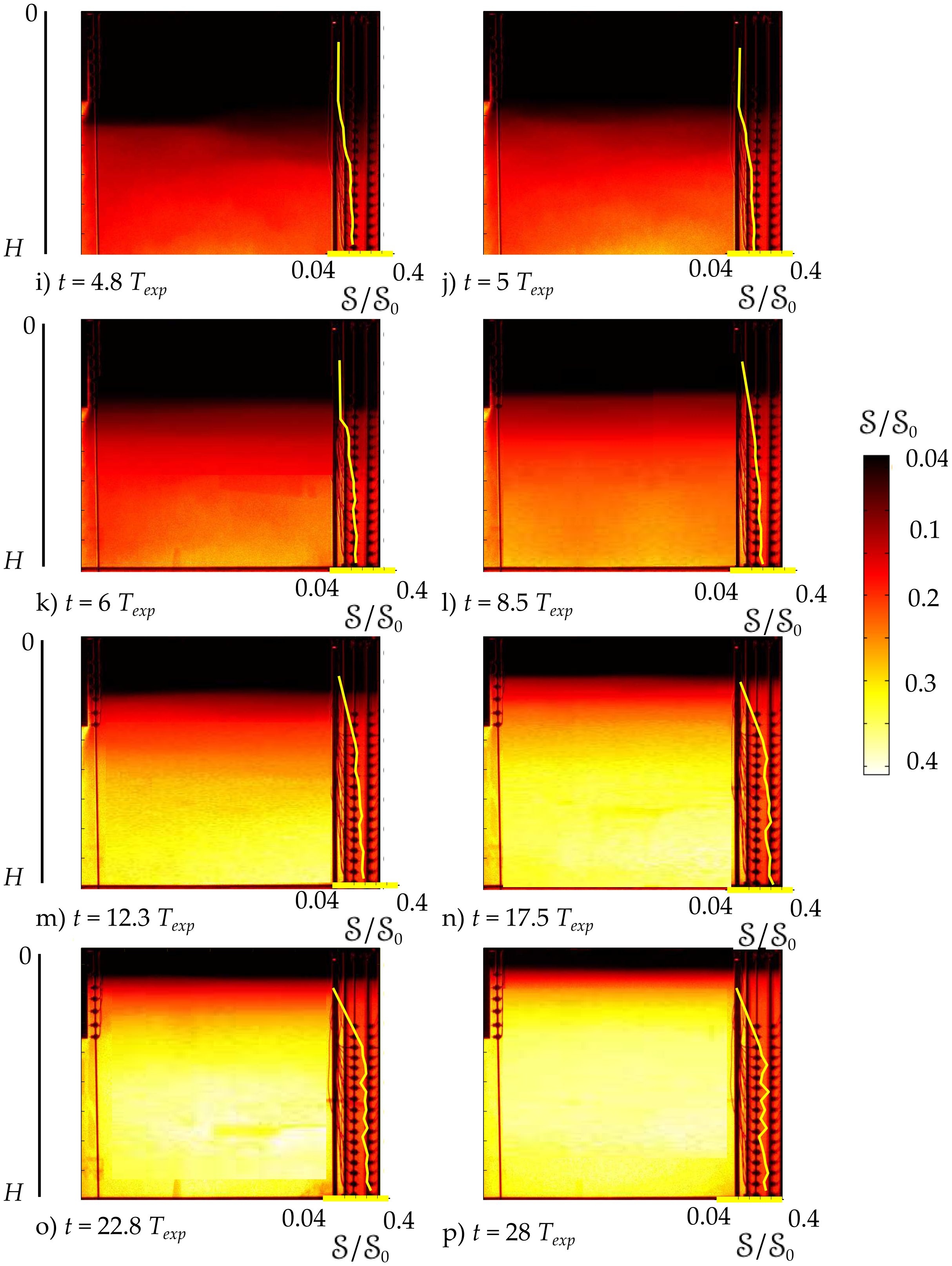

Figure 6.13: Filling flows during intermediate and late period. Each subplot consists of two parts: 1) an experimental frame, recorded as a grayscale image, scaled using dye-attenuation technique for depth-of-field-averaged density field (Allgayer & Hunt 2012) and presented as a color map (legend applies to each subplot); 2) a density profile (values in gcm $^{-3}$ converted from direct measurements of salinity, see Section 4.4). Set-up conditions: $B_0/B_{0,*} = 1$; room parameters: $Æ = 0.65$, $H/H_* = 1$.

with height as evidenced by irregular shapes of density profile with local peaks in density (m-p).

Figure 6.14 shows the development of stratification for the wall-mounted convector and the vertical distance H limited to the convector height $\mathcal{L}$. With the vertical distance $H - \mathcal{L}$ eliminated, the initial horizontal stratification, caused by the motion of the first front, is limited (a-b, $\mathcal{S}/\mathcal{S}_0$ 0.04 to 0.08; c-d, 0.17 to 0.22) and there is a tendency towards layering (from 2τ). In the later stages of filling (e-h), however, shearing motions (irregularities, detrainments) appear to affect the stratification, in a similar way to the horizontal motions captured in the late period in Figure 6.13.

To compare the developing stratification in both cases (Figures 6.13 and 6.14), Figure 6.15 shows density profiles at a few time instances, resulting from interpolation between 18 probes for $H/H_* = 1$ and 8 probes for $H/H_* = 0.32$, with each array of probes $0.05W$ from the side wall. In both cases, initially (S1-S4), the density field is balanced, corresponding to the unidirectional density increase (towards the tank base). At 2τ (S2), for $H/H_* = 1$, two thirds of the tank are stratified, with the bottom two thirds of the buoyant layer at approximately $\mathcal{S}/\mathcal{S}_0 = 0.11$, while the salinity in the top one third of the buoyant layer tends linearly to 0.04 (in the direction away from the tank base). The trend of the bottom $0.42H$ of the buoyant layer to stay uniform remains mostly unchanged for the duration of filling with density increasing evenly across this zone (with the corresponding part of the density profile shifting right, S2-S7). This could be caused by the frequent changes in the direction of the buoyant plume outflow resulting in the intense mixing between the environment and the buoyant fluid in the early (Figure 6.13 d - f) and late periods (Figure 6.13 i - l). The exceptions correspond to density peaks in the late period observed at: $0.95H$, $0.7H$, $0.35H$ and $0.2H$. The peaks in density, for $H/H_* = 0.32$, are within two zones, at: 0.67 - $0.83H$ and 0.16 - $0.33H$, which coincide with density peaks in the near field for $H/H_* = 1$. At 2τ (S2), for $H/H_* = 0.32$, stratification reaches approximately one fifth of H and ranges from $\mathcal{S}/\mathcal{S}_0 = 0.04$ to 0.22. There are no well-mixed regions and the surrounding area tends towards stronger stratification than for $H/H_* = 1$. Differences in vertical stratification, expressed in terms of maximum density range at a given time, for two cases with wall-mounted convector and two limiting vertical distances H, decrease in time from 50% at 2τ (S2) to 25% at 24τ (S7).

Figure 6.16 shows stratification development induced by a convector in the centre. As discussed previously (in Sections 5.2.1 and 6.1.1), adjusting the horizontal position of the convector changes the entrainment into the plume which affects both the rate of filling and stratification. For example, in the central case, horizontal stratification, due to early-period motions, evens out at 6.4τ, which is 25% faster than in the wall-mounted case[1].

Figure 6.17 shows the development of stratification recorded by three arrays of evenly distributed probes located at distances: $0.15W$, $0.25W$ and $0.45W$ from the convector face. Salinity profiles are in agreement with dye-attenuation images indicating initial horizontal stratification (S2-S3) with 0.04 and 0.025 discrepancies at 2τ and 4τ, respectively. The salinity difference decreases to 0.018 at 12τ. The continuous density increase (in direction towards the tank base) follows (S1 - S6) until 20τ when density peaks appear at $0.95H$, $0.5H$ and $0.25H$, which persist

[1] Time required for wall-mounted convector assumed as 100%

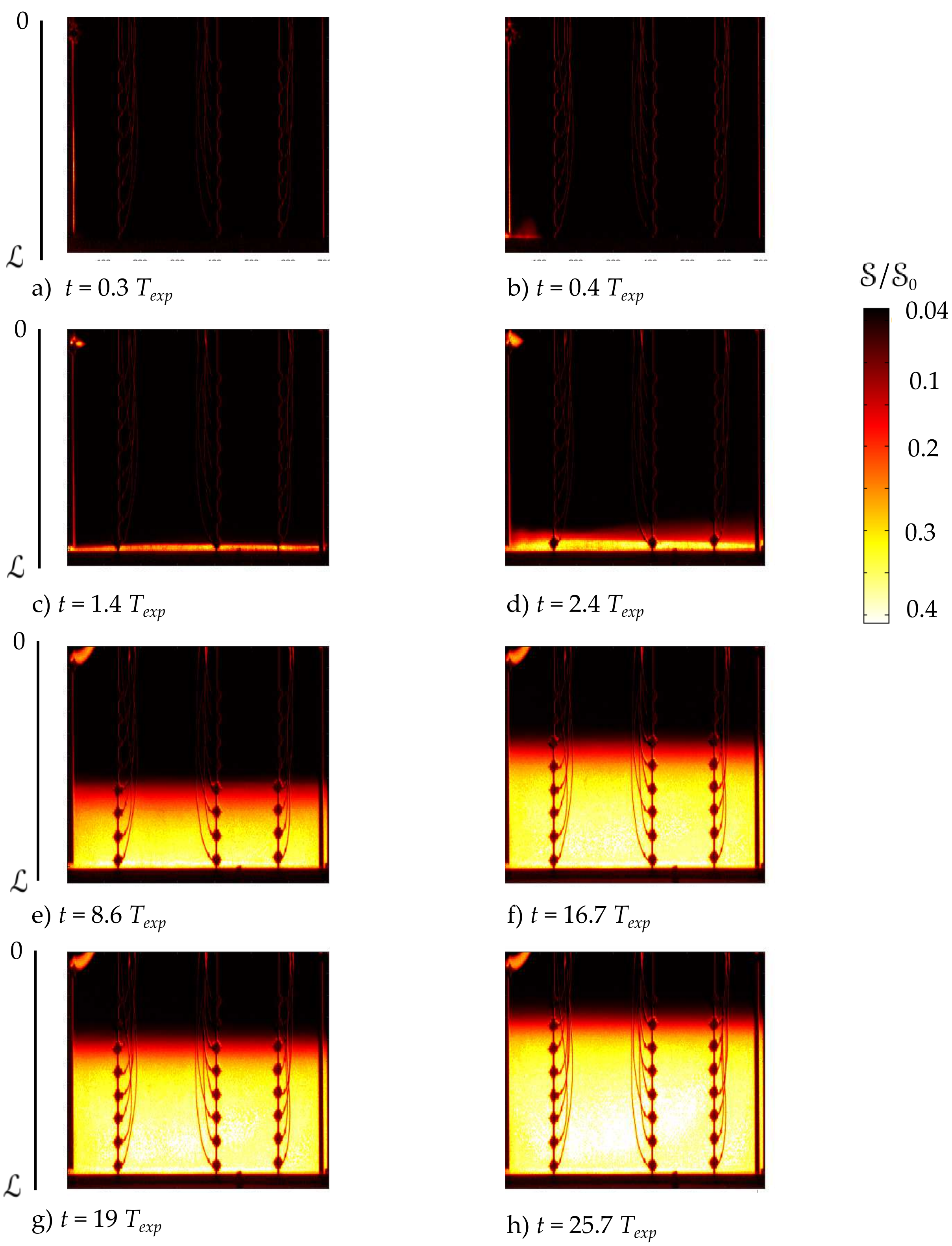

Figure 6.14: Stratification development for wall-mounted convector, $Æ = 0.2$ and $H/H_* = 0.32$. Each subplot is an experimental frame, recorded as a grayscale image, scaled using dye-attenuation technique for depth-of-field-averaged density field (Allgayer & Hunt 2012) and presented as a color map (legend applies to each subplot).

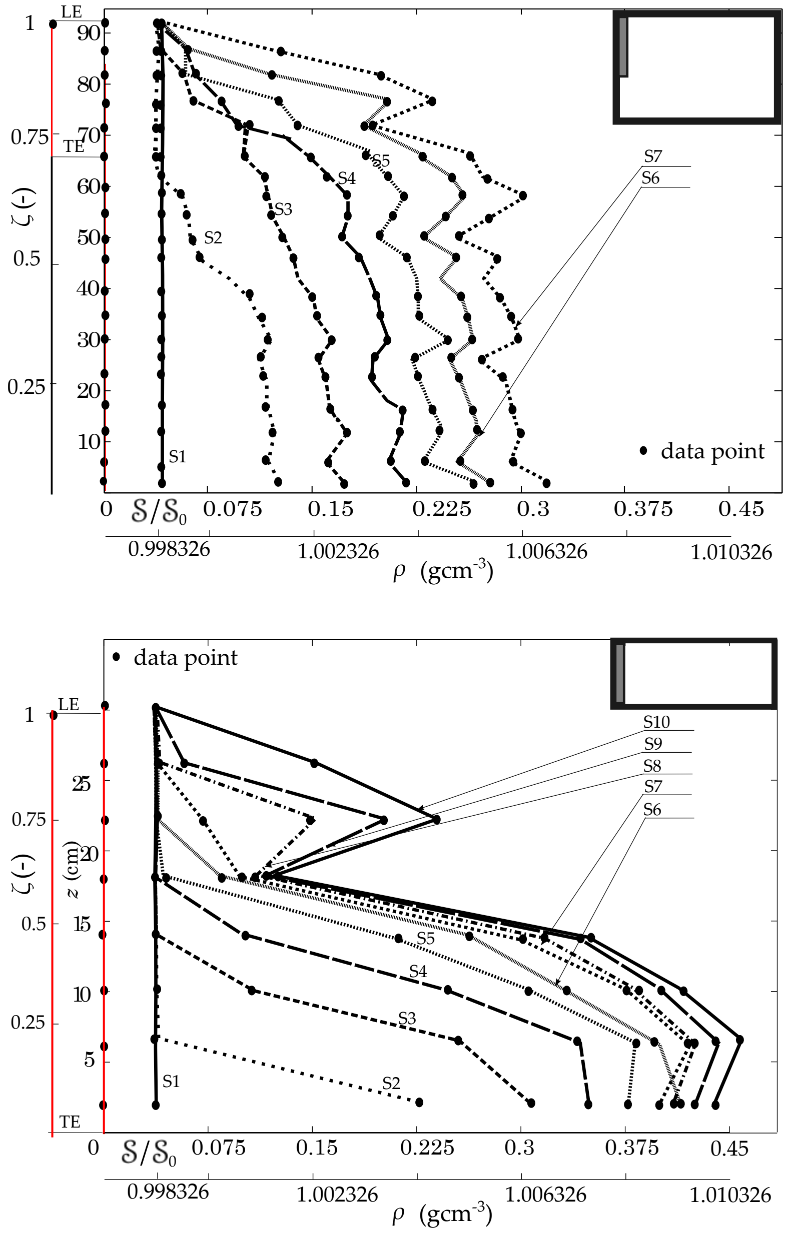

Figure 6.15: Density profiles: a) development of the stratification in the filling box with the convector, where $H/H_{*} = 1$; b) development of the stratification in the filling box with the convector, where $H/H_{*} = 0.32$. Convector strength: $B_0/B_{0,*} = 1$. Time instances: S1 = 0.01τ, S2 = 4τ, S3 = 8τ, S4 = 12τ, S5 = 16τ, S6 = 20τ, S7 = 24τ, S8 = 28τ, S9 = 32τ, S10 = 36τ.

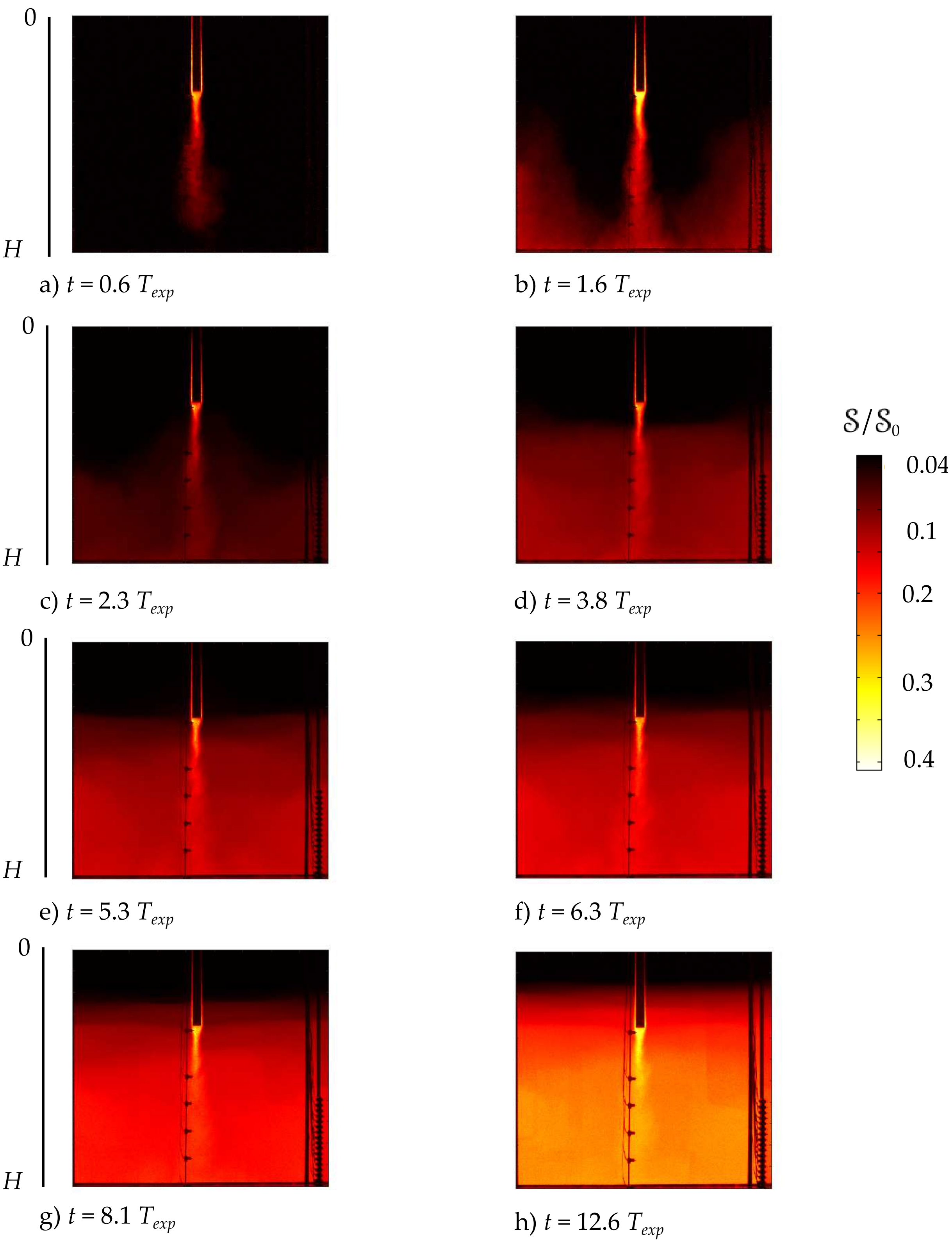

Figure 6.16: Stratification development for convector in the centre, $\mathcal{AR}$ = 1.3 and $H/H_* = 1$. Each subplot is an experimental frame, recorded as a grayscale image, scaled using dye-attenuation technique for depth-of-field-averaged density field (Allgayer & Hunt 2012) and presented as a color map (legend applies to each subplot).

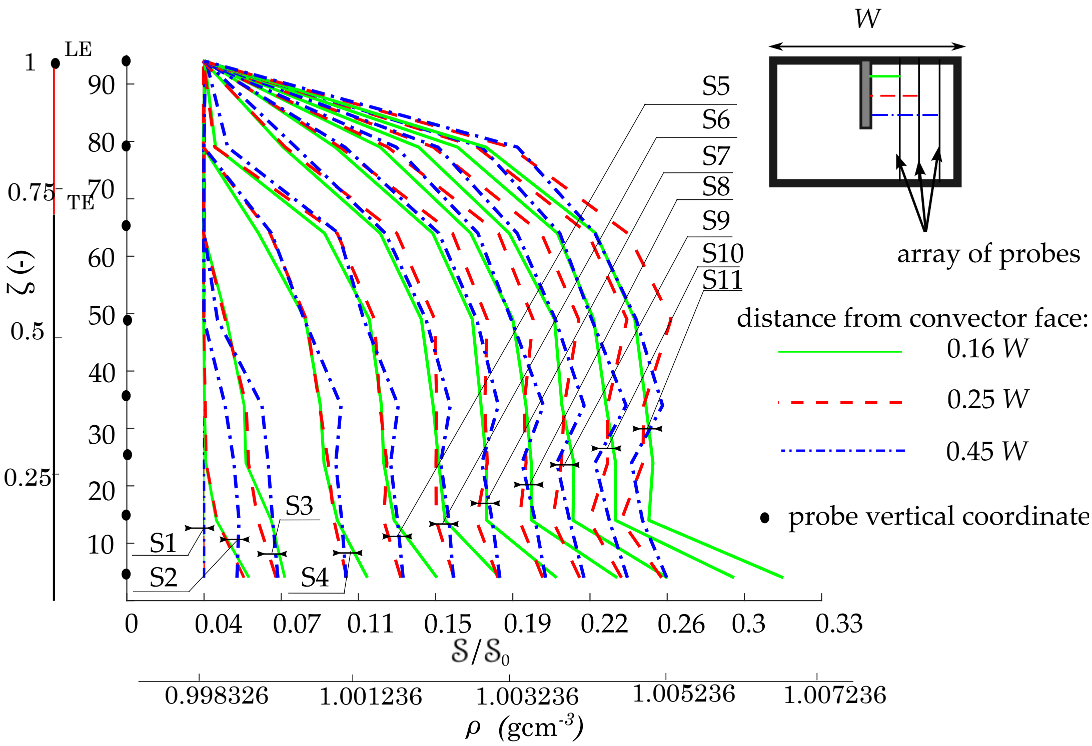

Figure 6.17: Density profiles: development of the stratification in the filling box with the convector, where $H/H_{*} = 1$, $B_0/B_{0,*} = 1$. Time instances: S1 = 0.01τ, S2 = 2τ, S3 = 4τ, S4 = 8τ, S5 = 12τ, S6 = 16τ, S7 = 20τ, S8 = 24τ, S9 = 28τ, S10 = 32τ, S11 = 36τ.

until the filling is completed. Irregular density profiles in the late period prompt a follow-up investigation of horizontal intrusions within a stratified layer. In shadowgraph images motions are tracked using strings with methylene paste (see Section 4.5.2.3). In shadowgraph images in Figure 6.18, arrows, which indicate the flow direction in the surrounding area, confirm that, in the late period, horizontal flows in opposite directions occur both in the far and near fields. The zones with shearing motions coincide with density peaks in the density profiles. Results from each technique analysed thus far appear to confirm that stratification in the late period is affected by shearing motions.

Figure 6.19 shows a composite image of the velocity vector field in the convector near field[1]. PIV results appear to confirm that in the late period (at 28τ) flows induced in the near field are primarily bidirectional (away and towards the convector). There also appears to be a rotational tendency of the flow, not previously identified. A further analysis of these induced flows is presented in Chapter 7.

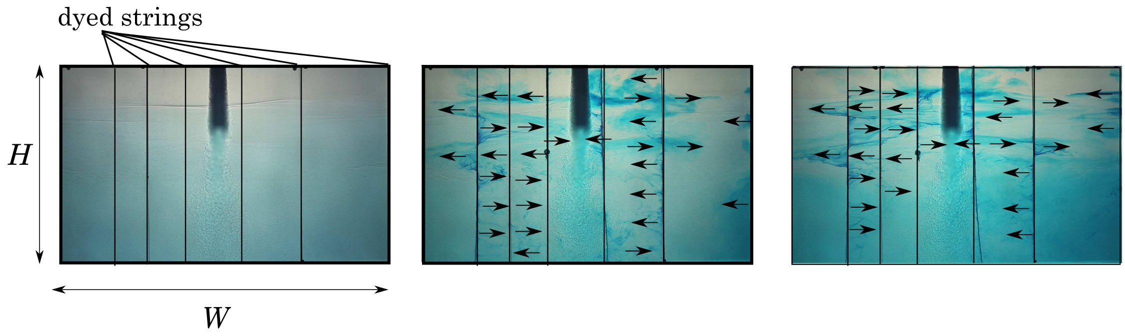

a) b) c)

Figure 6.18: Shadowgraphs of filling in the late period at a) t=27T_{exp}, b) t=27.6T_{exp}, c) t=30T_{exp}. Arrows, which are prepared based on the sequence of frames, indicate flow direction.

6.3 Statistical analysis on stratification

Statistical analysis is used to test the effect of simultaneous adjustment of all the system components. The result of the statistical analysis is an empirical equation describing the development of stratification, based on salinity measurements. Stratification, corresponding to the dependent variable $\Im$ (a ratio of density difference at a given height and the density of the ambient environment), is represented as a power function, see Section 4.6.2. Non-linear regression is performed to establish coefficients representing the impact each governing parameter has on the developing stratification. As a result, eq. (4.24) may be rewritten as:

$$\Im = 0.00001 Ra^{0.036} \mathcal{B}^{0.1} \mathcal{G}_{pr}^{-0.3} \mathbf{T}^{0.21}. \tag{6.1}$$

Based on eq.(6.1), the density increment depends predominantly on three parameters: the vertical coordinate ($G_{pr} = \frac{z_{pr}}{H}$, see Section 4.6.2.3), stage of filling, represented by dimensionless

[1]The composite image was made by stitching three PIV velocity vector fields.

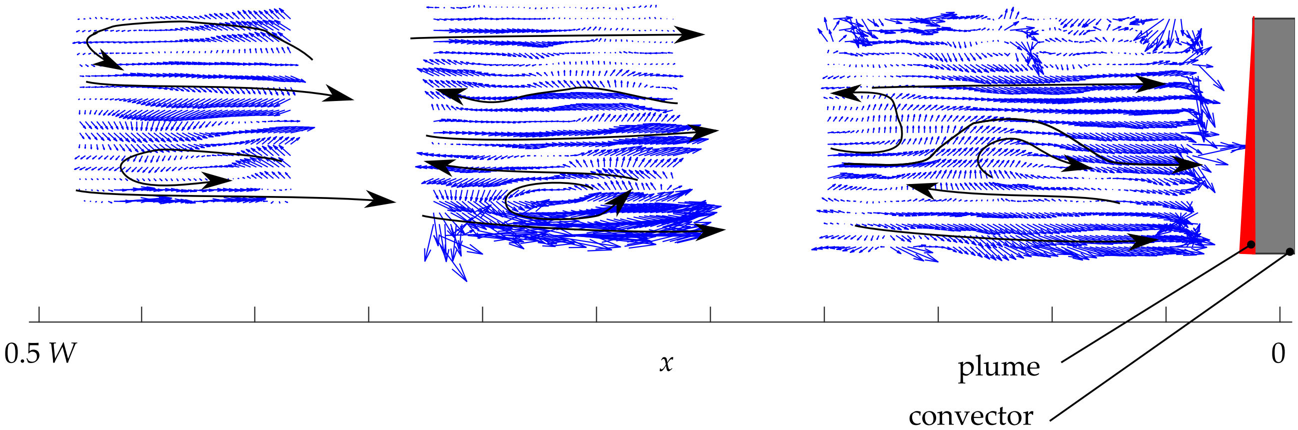

Figure 6.19: PIV composite image of velocity vector field in the convector near field captured at $t = 2800\,\text{s}$. Vector field consists of three stitched PIV vector fields captured in three distinct FOVs at given distances from the convector. Blue arrows correspond to velocity vectors and black arrows indicate direction of the bulk flow.

time parameter ($\mathbf{T} = \frac{t_{cum}}{T_{exp}}$, see Section 4.6.2.4) and the dimensionless accumulation ($\mathcal{B} = \frac{B_0 \Delta t^3}{\Delta z^4}$, see Section 4.6.2.1), whereas the global Rayleigh number ($Ra = \frac{g' H^3}{\nu D}$, see Section 4.6.2.2) is a subordinate parameter. This empirical representation supports conclusions drawn in previous sections. Namely that, at any given height, an increase in the convector strength results in an increase in the buoyancy accumulation, which tends to be evenly distributed with height. One subtlety in the developing stratification not accounted for in the empirical equation is the presence of horizontal intrusions within the buoyant layer in the late period. Instead, eq. (6.1) indicates a strong dependency between the density increment and the vertical coordinate, corresponding to a uniform density increase in direction towards the tank base. This implies, for the duration of filling, a leading role of layering, as a form of stratification development. This is in agreement with experimental observations, as horizontal intrusions appear towards the end of experiments and are limited to a few zones. The lack of representation of the horizontal intrusions in the empirical equation does not limit its application to describe the convector-induced stratification. On the contrary, eq. (6.1) is a conservative representation of the stratification, subject to potential improvement provided that the influence of horizontal intrusions is understood and used to establish a more uniform environment. The irregular density profiles correspond to unbalanced stratification with the surroundings tending to restore a balanced state through mixing between layers. The attempt to identify and describe the flows induced in the environment, based on the PIV data, is discussed in the next chapter.

Table 6.1 summarises the results of the analysis of significance (see Section 4.6.5 for details of the method). For stratification the R-value appears to be lower (but still acceptable) than for previously discussed expressions. The lower R-value could be caused by the initial time lag in undertaking measurements and small relative changes in recorded values. Each value of statistic t_{Stu} is higher than the critical value ($t_{Stucr} = 1.645$), thus each variable used in the statistical analysis is significant. The value of F-statistic is significantly higher than the critical value ($F_{cr} = 5.63$), thus the zero - hypothesis $\mathcal{H}_0$: R = 0 is rejected and the alternative hypothesis $\mathcal{H}_1$: $R \neq 0$ applies, thus there is correlation between dependent and independent variables. The confidence intervals are small, which provides additional justification of the form of empirical equations developed. The analysis of significance thus confirms that each coefficient of regression is significant.

R	0.7023
s^2	0.3009
$t_{Stu\beta1}$	1.8×10^6
$t_{Stu\beta2}$	2.2×10^5
$t_{Stu\beta3}$	2.1×10^6
$t_{Stu\beta4}$	2.6×10^5
F	3.3×10^5
$l_{\beta1}$	$\pm 3.2 \times 10^{-8}$
$l_{\beta2}$	$\pm 7.7 \times 10^{-7}$
$l_{\beta3}$	$\pm 2.4 \times 10^{-7}$
$l_{\beta4}$	$\pm 1.3 \times 10^{-6}$
l_y	± 0.9023

Table 6.1: Stratification - results of analysis of significance: coefficient of multiple correlation, mean squared error, statistic t-distribution for the zero-hypothesis, F-statistic and confidence intervals of regression.

6.4 Summary of Results

The investigation in this chapter reveals that both convector position and strength influence stratification development. This is in agreement with the results observed in the previous chapter, where the impact of both convector position and strength on the filling rate was shown. This chapter extends the knowledge of convector-induced filling further by revealing the interdependency between filling rate and stratification. Diagrams relating these two variables are prepared for the early and late periods, respectively. In general, a trend towards a weaker stratification appears to coincide with a trend towards increased filling rate. The two main design guidelines, which are aimed at improving the performance of the convector-room system through increasing the efficiency of filling, involve adjusting the convector by moving the convector away from the side wall and ensuring that the vertical distance $H - \mathcal{L}$ is greater than the convector height. It has been shown that improved convector performance, compared to the baseline case (wall-mounted convector in a room of height $H = H_*$), is achieved when the relative filling rate is greater than 1 and the relative stratification is lower than 1. The late-period horizontal intrusions have been detected using three independent experimental techniques (salinity measurements, shadowgraph and PIV). These intrusions appear to disturb uniform layering during stratification development. Perhaps a further analysis of fluid mechanical aspects of these flows is needed.

Chapter 7

Induced flows

The aim of this chapter is to show how PIV can be used to visualise flows induced by a convector. Furthermore, flow three-dimensionality and vorticity in the system are also discussed. This is a preliminary study limited to flow snapshots only to demonstrate feasibility of the method and provide some further qualitative insight. In the PIV experiments, only the tank of freshwater was seeded, whereas the saline solution supplied was unstained and unseeded, see Section 4.5.3 for details of the method. Salinity measurements, as described in Section 4.5.4, were also taken continuously during PIV experiments, in order to track the interface position[1].

7.1 Location of PIV planes

Three vertical planes are used during the experiments to assess how induced flows vary in different regions of the tank. Figure 7.1 shows the tank plan view with the locations of vertical PIV planes, where 1 marks the central plane, which is used to investigate induced flows within both the near field, corresponding to the zone extending from the leading edge to the trailing edge of the convector, and the far field, corresponding to the zone below the convector. The size of the central plane, $0.47W$ (w) $\times$ $0.95H_*$ (h) , exceeds the size of the field of view (FOV), $0.2W$ (w) $\times$ $0.32H_*$ (h), and experimental results from eight overlapping FOVs are used to prepare the velocity vector field in half of the tank (see Figure 7.8 and Figure 7.11) and schematics of the induced flows within the central plane (see Figure 7.9 and Figure 7.12). Note that, the composite flowfields produced from multiple FOVs are taken from different runs, rather than simultaneously from the same flow realisation. Both the front plane, which is marked as 2 in Figure 7.1 and the parallel plane, marked as 3, are used to investigate the assumption of two-dimensionality of induced flows within the tank. The size of both planes corresponds to the size of the FOV, $0.2W$ (w) $\times$ $0.32H_*$ (h).

Figure 7.2 defines the legend for Figures 7.3-7.7 and 7.10 in this chapter. The location of the FOV, represented by the position of the calibration plate prior to the experiment is shown above the velocity vector field both in the elevation and in the plan view. Next to the vector plot there is a corresponding salinity/density profile, captured simultaneously to the PIV recording. An array of 8 probes was installed in a location mirroring the FOV (see Figure 7.2 for an example

[1]The interface position is the boundary between the saline layer and the freshwater.

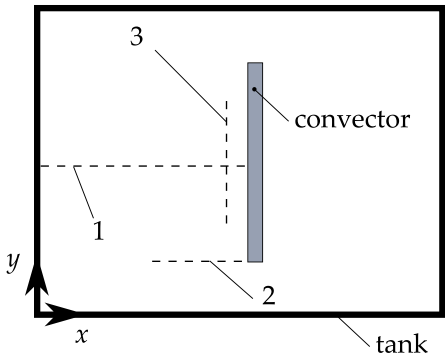

Figure 7.1: Tank in plan view with marked locations of vertical PIV planes (relative to the convector): 1 - central plane; 2 - front plane; 3 - parallel plane.

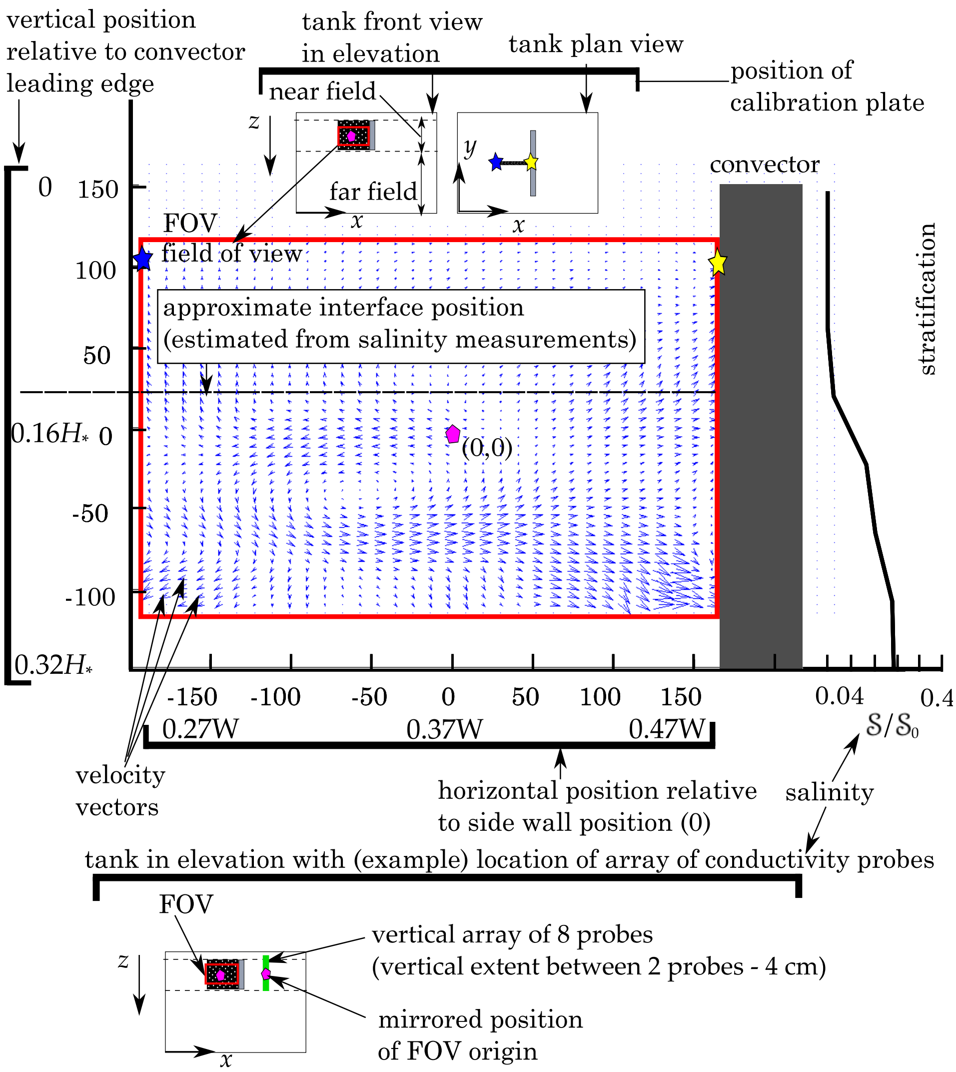

Figure 7.2: Sample velocity vector field based on PIV experiments.

location of the array of probes).

7.2 Early filling period

In each FOV, the flow direction appears to change rapidly within the first $0.6T_f$ of the experiment, perhaps due to initial disturbances such as air bubbles releasing from the pores of the sintered plates. After the initial disturbances cease, the flowfield visibly stabilises and the response of surrounding fluid to the filling flow can be observed. This stabilisation period is not expected to influence the subsequent flowfield observed, since the disturbances are small and rapidly damp out. Velocity magnitudes, in different periods and FOVs, are compared based on the resultant velocity magnitude parameter m, for definition see (4.18) in Section 4.5.3.3.

7.2.1 Near field of convector

After the initial disturbances cease in the near field, the flowfield in the ambient fluid stabilise and remain mostly unchanged in the near field until the interface reaches the convector trailing edge. For all the FOVs in the near field, during the early period, the interface remains below the trailing edge level. As a result, the near field salinity/density profile is a vertical line of $\mathcal{S}/\mathcal{S}_0 \approx 0.04$ corresponding to the salinity of water scaled on the source salinity. The induced flow topology observed in the three different PIV planes are now discussed.

7.2.1.1 Central plane

Figure 7.3 shows a typical vector plot of velocity in the near field in the FOV nearest to the convector in the central plane during the early period at 3τ. Figure 7.3 indicates that the majority of the flow in the plane is directed towards the convector. The bulk flow in the surrounding ambient fluid appears to deviate either upwards or downwards from the horizontal direction. The ratio of mean magnitudes of the velocity components, namely horizontal $|\overline{u}|$ and vertical $|\overline{w}|$, $\frac{|\overline{u}|}{|\overline{w}|} = 2.75$, indicate that the horizontal velocity component is dominant. The field also shows a localised rotational tendency. Particularly, closer to the convector, for x in the range $0.37W$ to $0.47W$ and z in the range $0.1H_*$ to $0.32H_*$, flow appears to rotate locally with vectors moving in anticlockwise direction (as indicated in the figure). These deviations in close proximity to the plume could be due to the shearing motion of the plume[1].

The velocity vector field in the intermediate FOV (Figure 7.4 a) is noticeably different to the velocity vector field shown in Figure 7.3. The entire field shows a rotational tendency with vectors moving in an anticlockwise direction. This may be indicative of a large vortical structure or recirculation zone. This is a particularly interesting result, which is neither included in the classical filling box model, nor detected in the dye-attenuation experiments. The rotational nature could be due to shear stresses within the fluid that may encourage organizing the induced flows into a collection of localised vortical structures or recirculation zones. The vector field of

[1]The turbulent plume flow was observed using the shadowgraph method. See Figure 4.13 for reference.

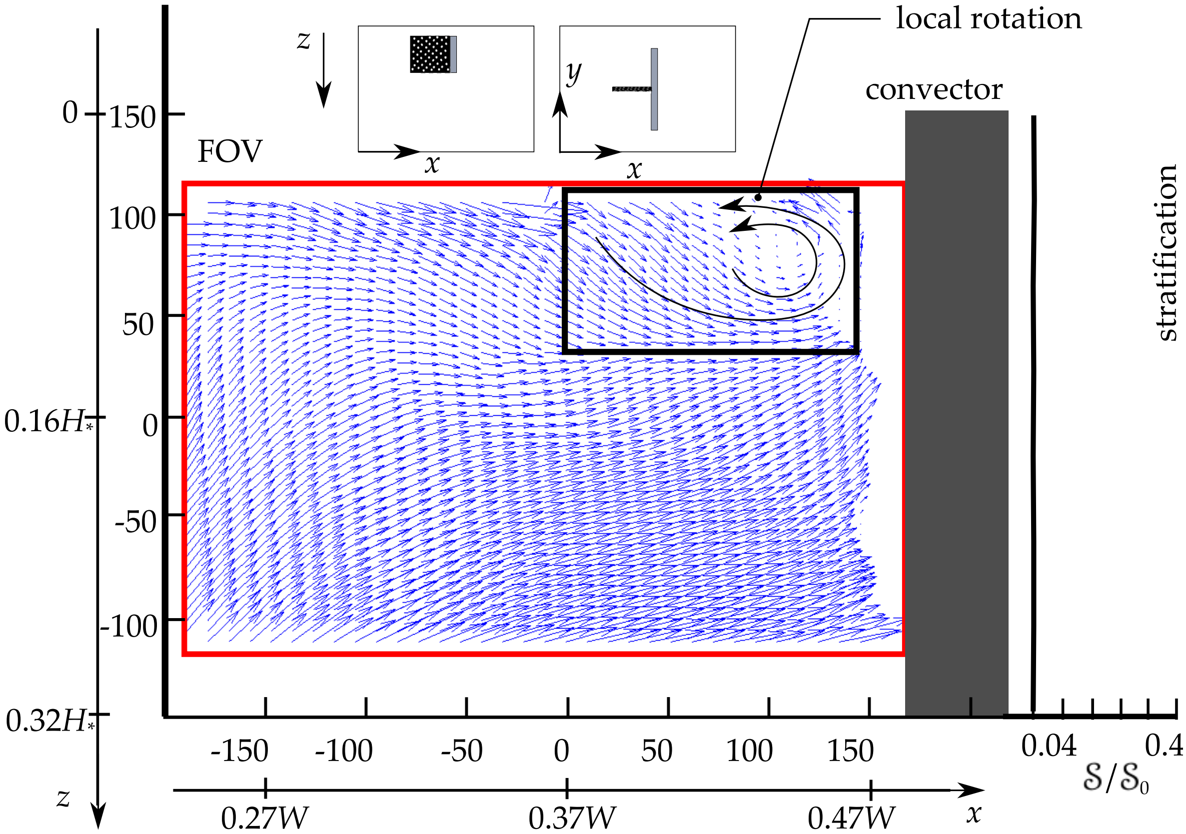

Figure 7.3: Typical velocity vector field in the near field in the central vertical plane in the nearest FOV to the convector ($m = m_{*,ep} = 0.058$ cms^{-1}) and the corresponding salinity/density profile (vertical line) at $t = 3T_{exp}$.

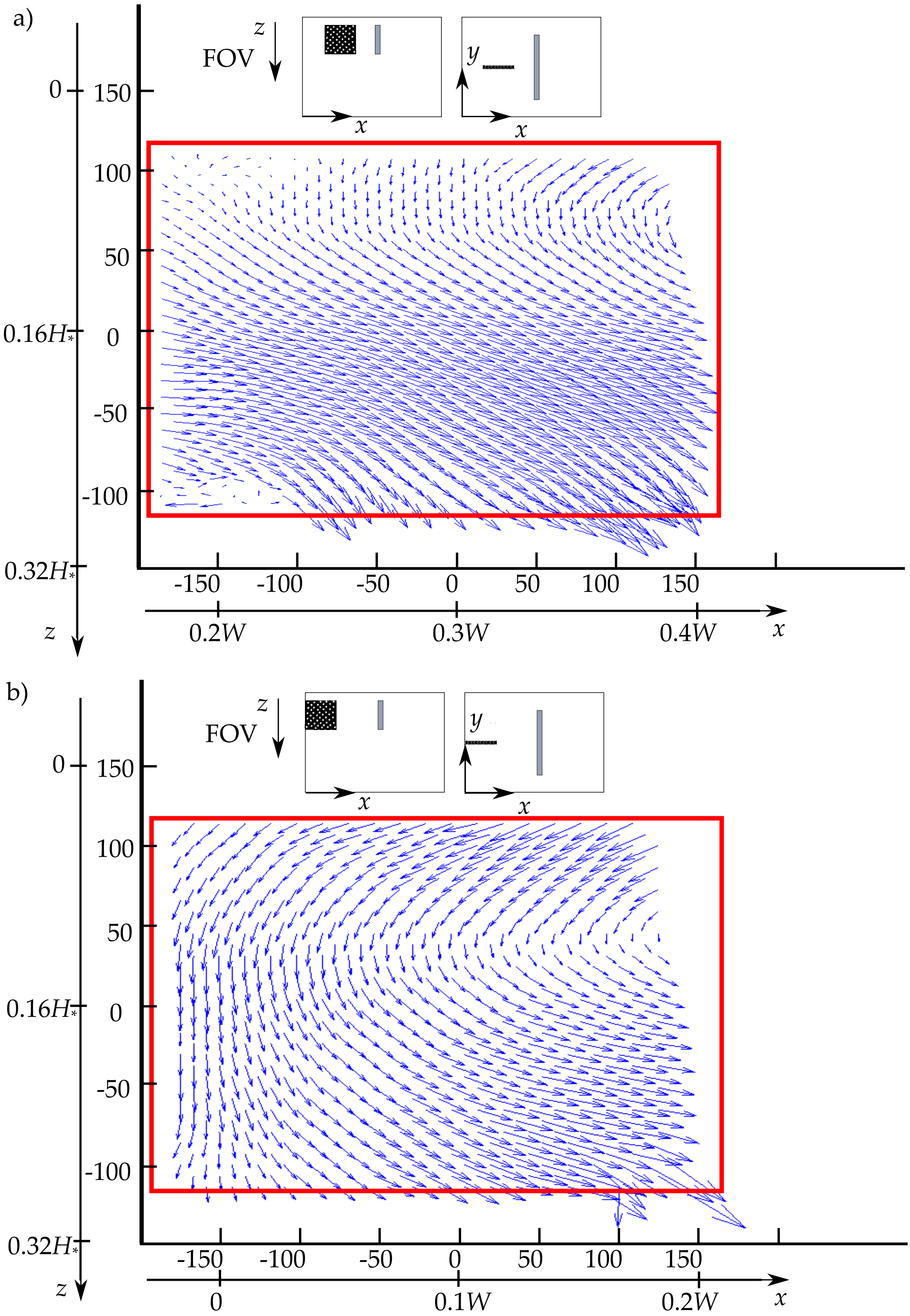

Figure 7.4: Typical velocity field in the near field in the central plane a) in the intermediate FOV, $m/m_{*,ep} = 0.75$) and b) in the furthest FOV from the convector ($m/m_{*,ep} = 0.39$) at $t = 3T_{exp}$.

the FOV furthest from the convector (Figure 7.4 b) again shows an anticlockwise rotational tendency but with downward flow along the side wall (for x in the range 0 to $0.015W$). This again suggests that there may be rotation of the flow within the tank. Values of m in the intermediate FOV, $m/m_{*,ep} = 0.75$, and the furthest FOV from the convector, $m/m_{*,ep} = 0.39$, are lower than in the FOV nearest to the convector, where $m = m_{*,ep}$. It appears that the largest induced velocities are close to the convector. Velocities appear to decrease in the horizontal direction away from the convector.

7.2.1.2 Front plane

Figure 7.5 shows a typical velocity vector field, in the near field, in the front plane, during the early period, captured at 3τ. It can be observed that, similarly to Figure 7.3, the direction of the induced flow is towards the convector. In the front plane the velocity magnitudes appear to be higher on average by 12% than in the central plane ($m/m_{*,ep} = 1.12$). Once more, the velocity vectors deviate from the horizontal direction more noticeably close to the convector ($x = 0.4W - 0.44W$).

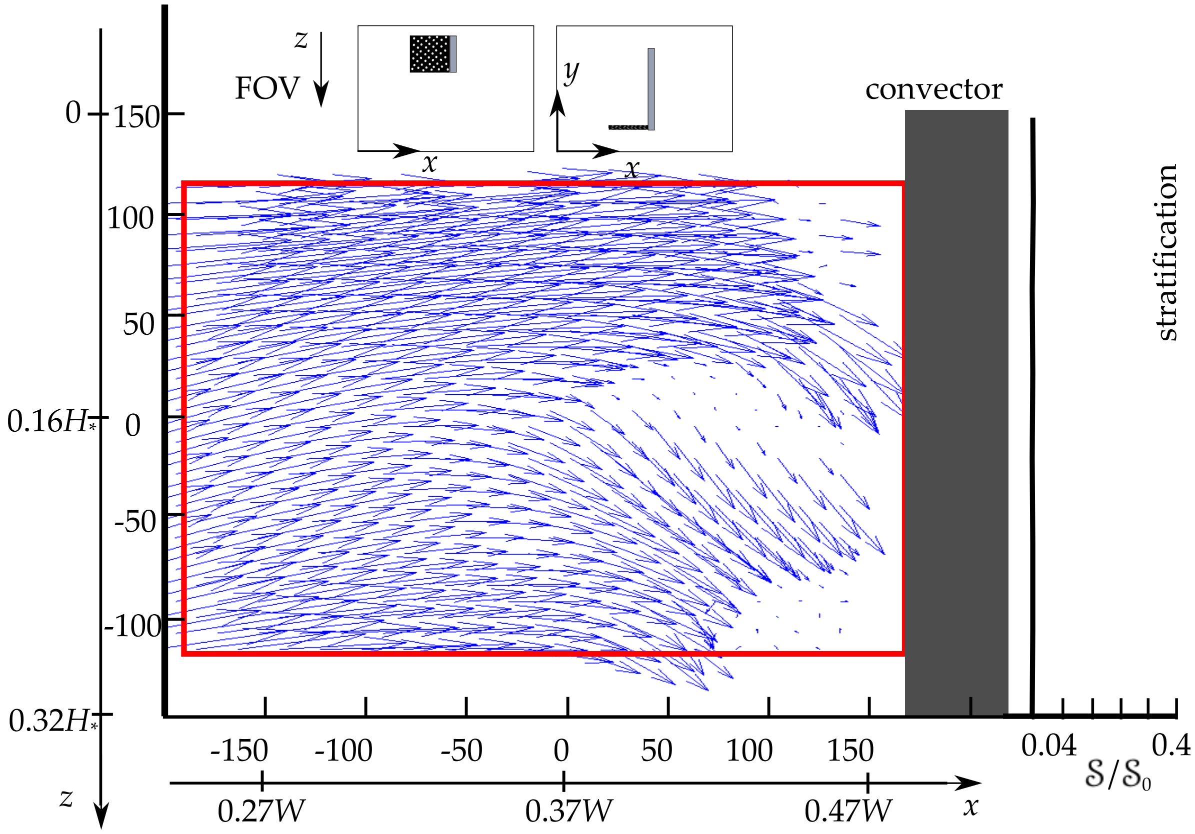

Figure 7.5: Typical velocity vector field in the near field in the front vertical plane ($m/m_{*,ep} = 1.12$) and the corresponding salinity/density profile.

7.2.1.3 Parallel plane

Figure 7.6 shows a time series of vector fields in the near field, parallel to the convector, *d* from the side wall. Secondary flows appear to be induced in the plane parallel to the convector. The flow direction changes in time from downward at 1.2τ, through horizontal at 3τ, followed by upward at 6τ and again horizontal at 18τ . There are also instantaneous local rotations (as indicated in the figure). Values of $m/m_{*,ep}$ decrease in time from 1.17 to 0.32. At 1.2τ m in the parallel plane is higher than in perpendicular planes, from 3τ m are lower than in the planes perpendicular to the convector but the velocity magnitude appears to remain of the same order in all the planes. In order to understand the impact of additional complexity, perhaps a study involving stereoscopic PIV is needed.

7.2.2 Far field of convector

In the far field, during the early period, transient buoyant bulk flows were observed in the dye-attenuation experiments. These are characterised by changes in the flow direction upon impingement on tank surfaces. These flows can affect the direction of the flow in the surrounding area by inducing shearing motions susceptible to changes in the direction of the buoyant bulk flow. These variations in the flow direction in the environment appear to be captured in PIV experiments. Perhaps the most interesting is the flow in the corner of the tank, as demonstrated in Figure 7.7, where velocity vector fields are shown during the early period, at 1.2τ and during the late period, at 18τ. During the early period the entire induced flow in the corner appears to move in a clockwise direction, whereas during the late period the induced flow seems to be more unsteady. In the early period the flow appears to slide along tank surfaces, whereas in the late period there is a tendency towards impingement on the tank surfaces. Based on the values of $m/m_{*,ep}$ in the early and late periods (2.2 and 5.1, respectively), the velocity magnitude increases in the corner of the tank as the stratification develops. This could be caused by intensified shearing motions between layers of buoyant fluid in the stratified environment. Due to rotational nature of the velocity vectors in both periods, vortical structures are expected to be found in a region close to the corner of the tank. This is further discussed in Section 7.4.

7.2.3 Flows induced in early period

Figure 7.8 shows velocity field of the surrounding area induced by the convector in one half of the tank (in elevation) during the early period at 3τ. Here data from eight different FOVs is shown in one global view. Data captured in the ninth FOV (2nd raw, right-hand-side) comprising the central plane (plane 1, as described in Section 7.1, see Figure 7.1 for reference), was unreliable and have thus been omitted. The flow appears to be mainly horizontal towards the plume. There is a distinct difference in the flow between the bottom of the image, where horizontal velocities are relatively high, compared to small velocities at the top. However, an overall trend of the entire flow in the system (both buoyant and ambient) is to circulate where the plume vertically descends, the horizontal current spreads away from the plume, the vertical flow ascends along the wall and the horizontal flow progresses towards the plume. There also appear to be local rotational trends in the ambient environment. Table 7.1 shows values of m for eight vector fields comprising the stitched velocity vector field in the early period at 3τ. In the

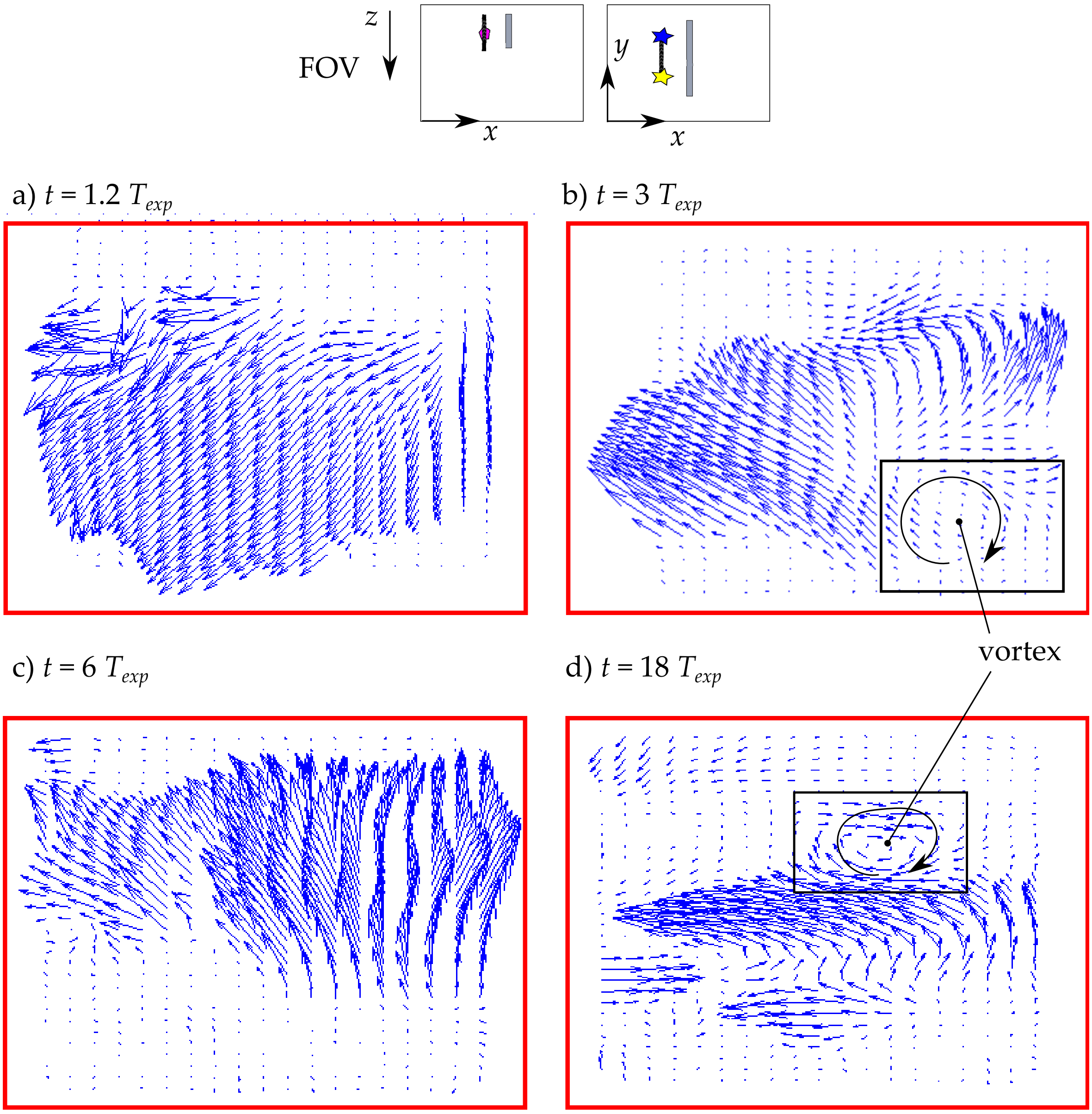

Figure 7.6: Time series of velocity vector fields in the near field parallel to the convector (a-b) during the early period, where at $t = 1.2T_{exp}$ ($m/m_{*,ep} = 1.17$) and at $t = 3T_{exp}$ ($m/m_{*,ep} = 0.45$); and (c-d) during the late period, where at $t = 6T_{exp}$ ($m/m_{*,ep} = 0.39$) and at $t = 18T_{exp}$ ($m/m_{*,ep} = 0.32$).

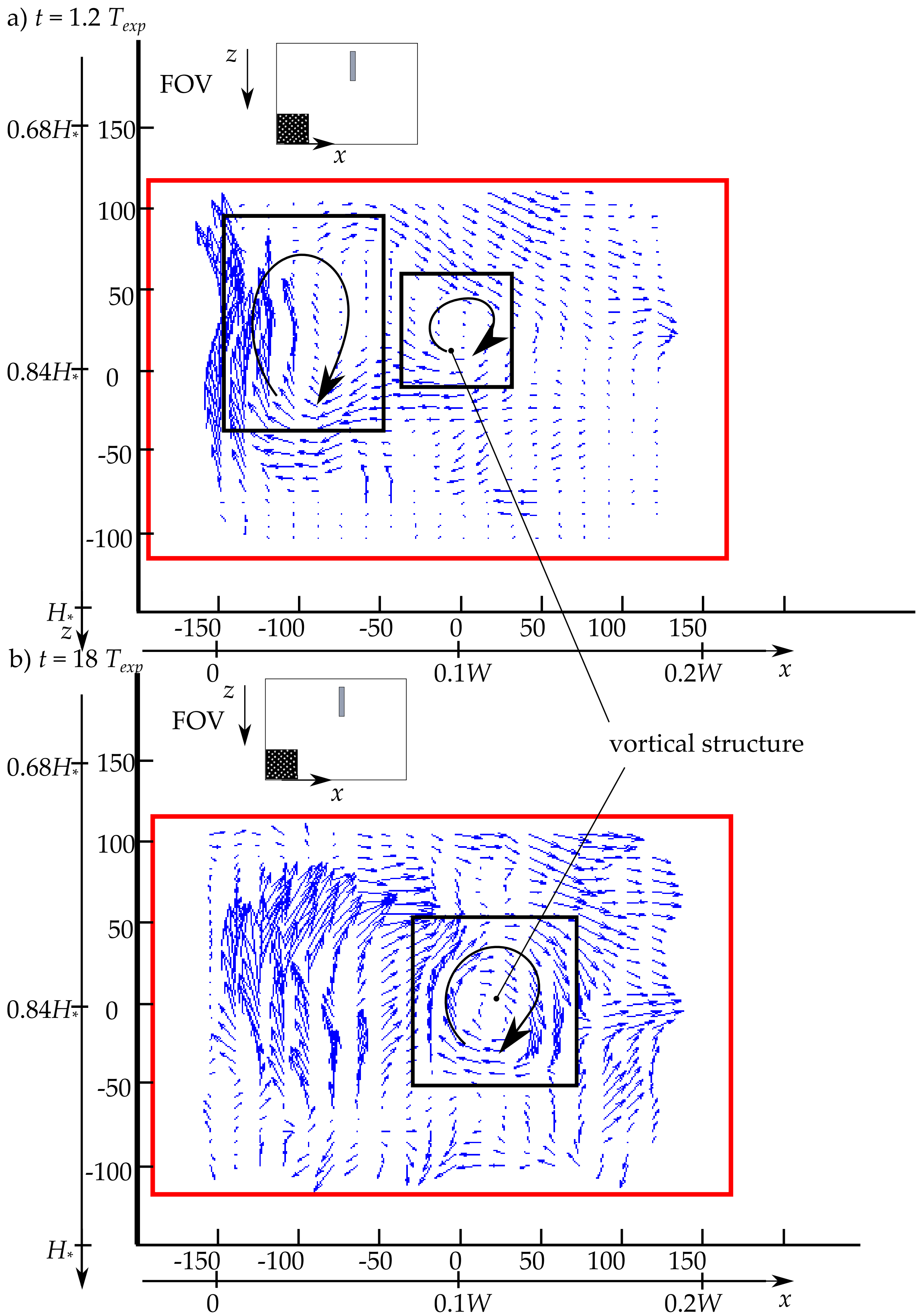

Figure 7.7: Velocity field in the corner of the tank a) during the early period at $t = 1.2T_{exp}$ ($m/m_{*,ep} = 2.2$) and b) during the late period at $t = 18T_{exp}$ ($m/m_{*,ep} = 5.1$).

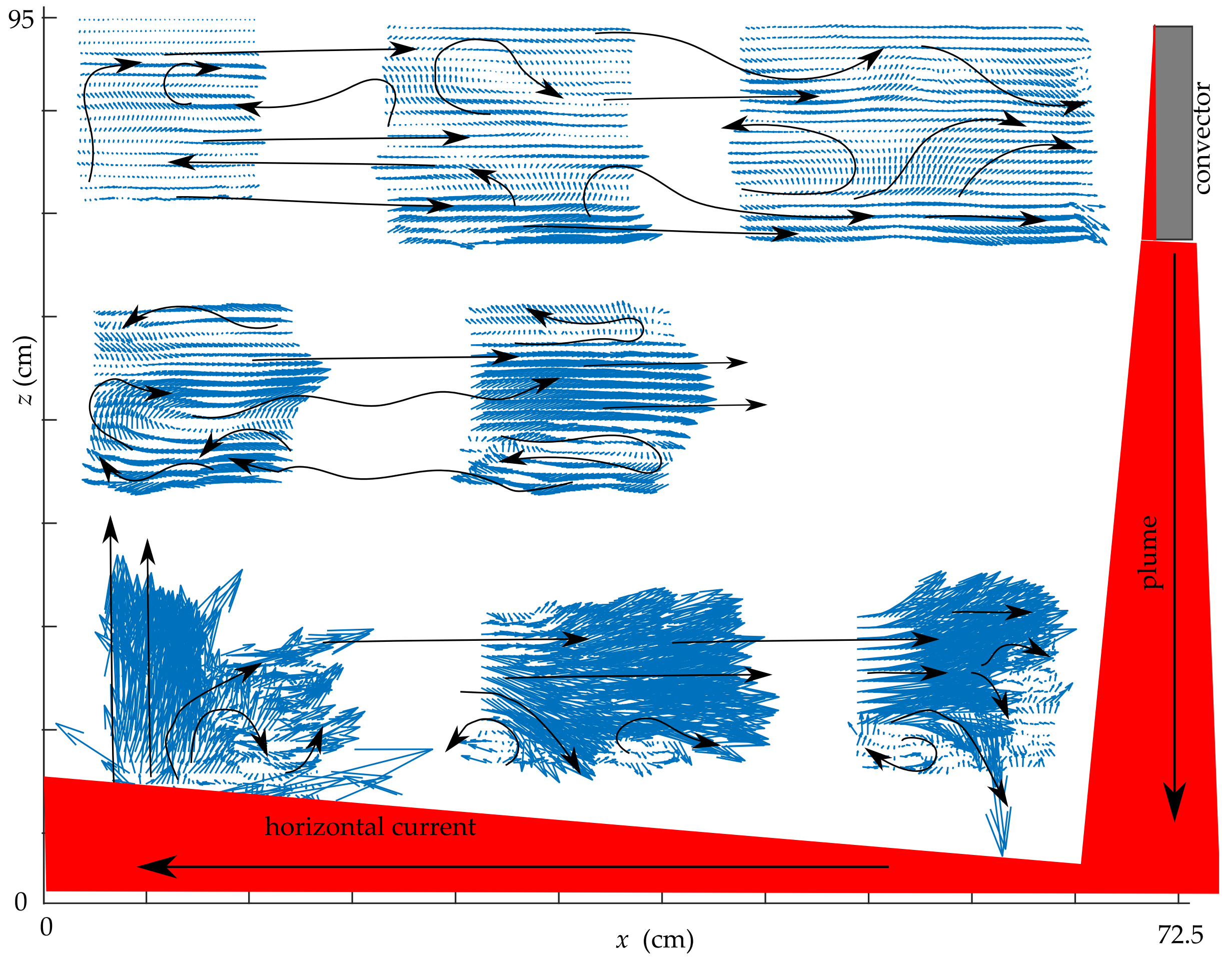

Figure 7.8: Velocity vector field induced by filling in a half of the tank (in elevation) in the early period at $t = 3T_{exp}$. Vector field consist of 8 stitched vector fields captured at 8 FOVs (location of FOVs correspond to location of vector fields). Blue arrows are velocity vectors, relatively scale to provide meaningful representation of the flow in the tank. Black arrows mark trends in the flow direction.

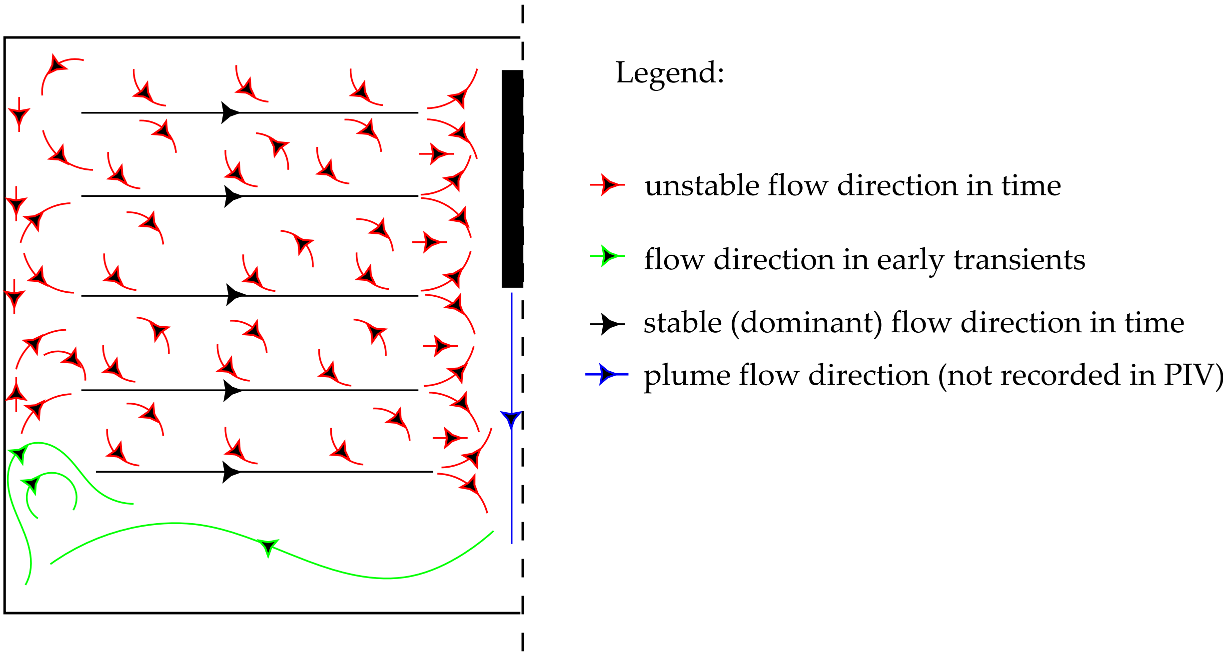

Figure 7.9: Schematic of induced flows in a half of the tank (in elevation) in the early period. Dashed vertical line marks the middle of the tank.

near field velocities closer to the plume are higher. Also close to the plume and the horizontal current, velocities increase as these buoyant flows progress.

0.023 (40%)	0.0435 (75%)	0.0584 (100%)
0.023 (40%)	0.032 (56%)	
0.13 (220%)	0.12 (205%)	0.0632 (110%)

Table 7.1: Values of m (cms^{-1}) for 8 vector fields comprising the stitched velocity vector field in the early period at $t = 3T_{exp}$. Values presented in the order matching distribution in Figure 7.8. Percentage used to compare mean velocities induced in the tank.

Figure 7.9 shows a representation of the flows induced in the tank in the early period, based on the results extracted from eight FOVs, corresponding to the central plane. The dominant direction of the induced flows appears to be towards the convector (plume) in the near field and towards the plume in the far field except close to the tank boundaries, i.e. side walls and base, where transients develop and/or flow reverses. The vector fields in the central plane also appear to have a rotational tendency with the flow moving either in the clockwise or in the anticlockwise direction.

7.3 Late filling period

At the beginning of the late period, the interface reaches the trailing edge of the convector and continues its ascent in the near field (see Chapter 5 for reference). During PIV experiments salinity measurements were taken simultaneously to mark the beginning of the late period (see Section 7.1). Figure 7.10 shows two velocity vector fields in the FOV closest to the convector in the central plane during the late period, captured at 6τ and 18τ, respectively. The figure shows that during the late period, similarly to the early period, the induced flows appear to be primarily towards the convector (plume). The vector field has also a rotational tendency. It is worth discussing the late-period vector field in relation to the interface position, tracked using salinity measurements. Above the interface region, e.g. $0.1H_*$ above the interface in Figure 7.10 a, the direction of the induced flow appears to be mainly horizontal with a slight rotational tendency in clockwise direction. The interface continues ascending during the late period, which may lead to more rapid changes in the flow direction at the interface and below within the stratified layer. Consider the interface region to be approximately in the range $\pm$ $0.05H_*$ above/ below the interface (Figure 7.10), the flow direction appears unsteady and in this region there may be vortical structures. These could be attributed to mixing between the buoyant and ambient layers and the shear stress at the interface. In the interface region, the dominant flow direction, however, still appears to be towards the convector. Below the interface region, the induced flow appears to be also mainly towards the convector (plume). The rotational tendency in the buoyant region below the interface seems to be clearer than in the ambient region above the interface, evidence of the rotational tendency can be seen in Figure 7.10 a and Figure 7.10 b. Decreasing values of m (by 10%) indicate that the velocity magnitude of the induced flows decreases in the near field as the stratification develops.

Figure 7.11 shows the velocity field in one half of the tank (in elevation) in the late period at 28τ. The image consists of eight stitched vector fields which allows a full image of the flowfield to be seen. However, locally in the stratified environment (both fields), there are horizontal intrusions in the direction away from the plume. The horizontal intrusions captured at 28τ coincide with intrusions captured using methylene blue paste during shadowgraph experiments and salinity peaks in salinity profiles (see Section 6.2). PIV data thus confirms that the development of stratification is affected by horizontal motions in the direction away from the plume both in the near and far field. The sources of each intrusion, however, have not been uncovered and a further investigation into these phenomena is needed.

Table 7.2 shows values of m for eight vector fields comprising the stitched velocity vector field in the late period at 28τ. The relative trends between mean velocities in different FOVs have been maintained in the late period. Namely, in the near field velocities closer to the plume are higher. Also, close to the plume and the horizontal current, velocities increase as these buoyant flows progress. Apart from the flows in close proximity to the horizontal current, the flows induced in the environment in the late period are slower than in the early period (by 20%-80%). Figure 7.12 shows a schematic of the flows induced in the tank in the late period,

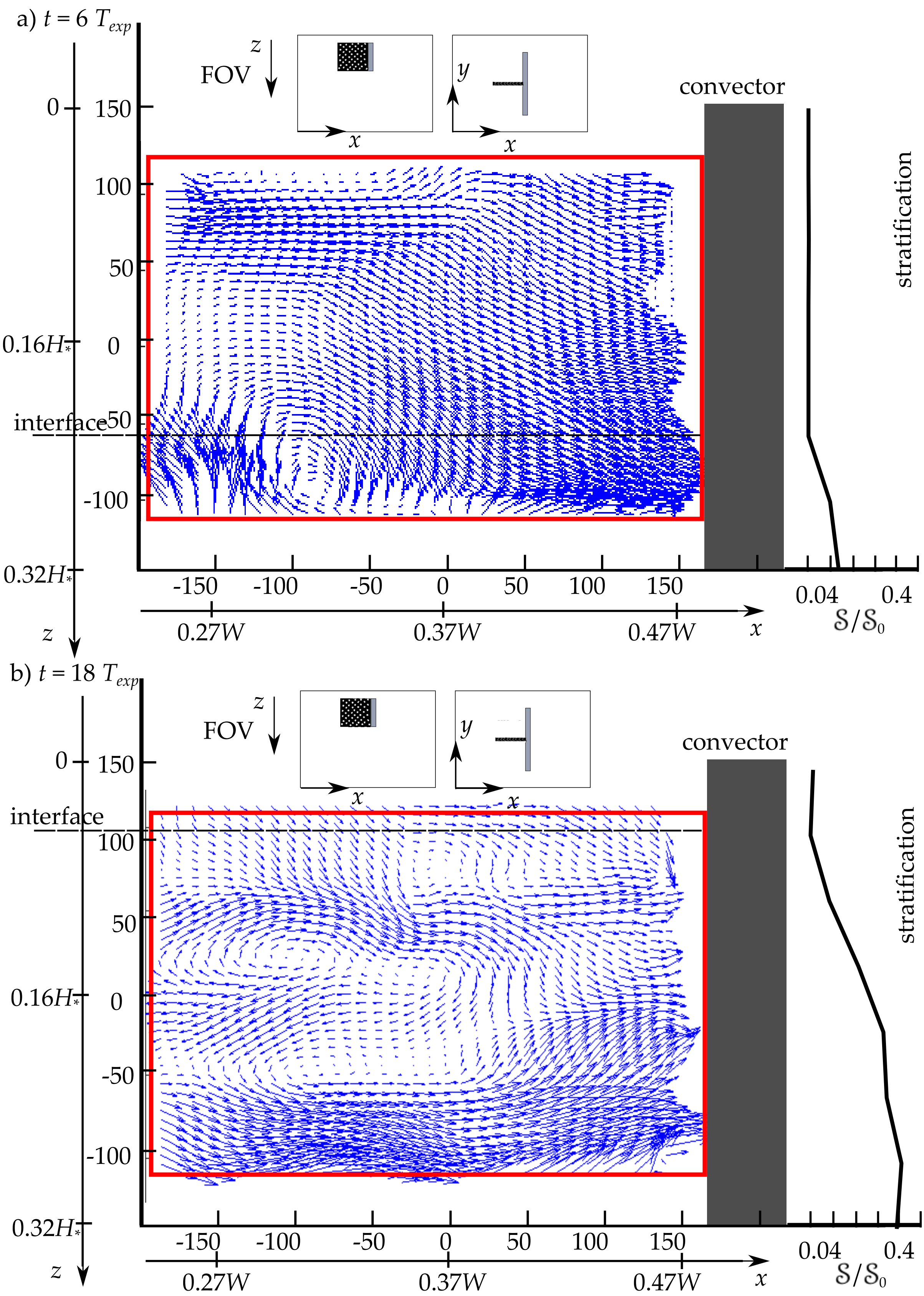

Figure 7.10: Velocity vector fields during the late period in the near field, in the FOV closest to the convector, in the central plane a) at $t = 6T_{exp}$ ($m = m_{*,lp} = 0.0447$ cms^{-1}) and b) at $t = 18T_{exp}$ ($m/m_{*,lp} = 0.91$) and the corresponding instantaneous salinity/density profile.

based on the PIV results in the central plane. The dominant direction of the induced flows seems to remain towards the convector. The flow direction appears more unsteady than during the early period and more vortical structures are expected within the field.

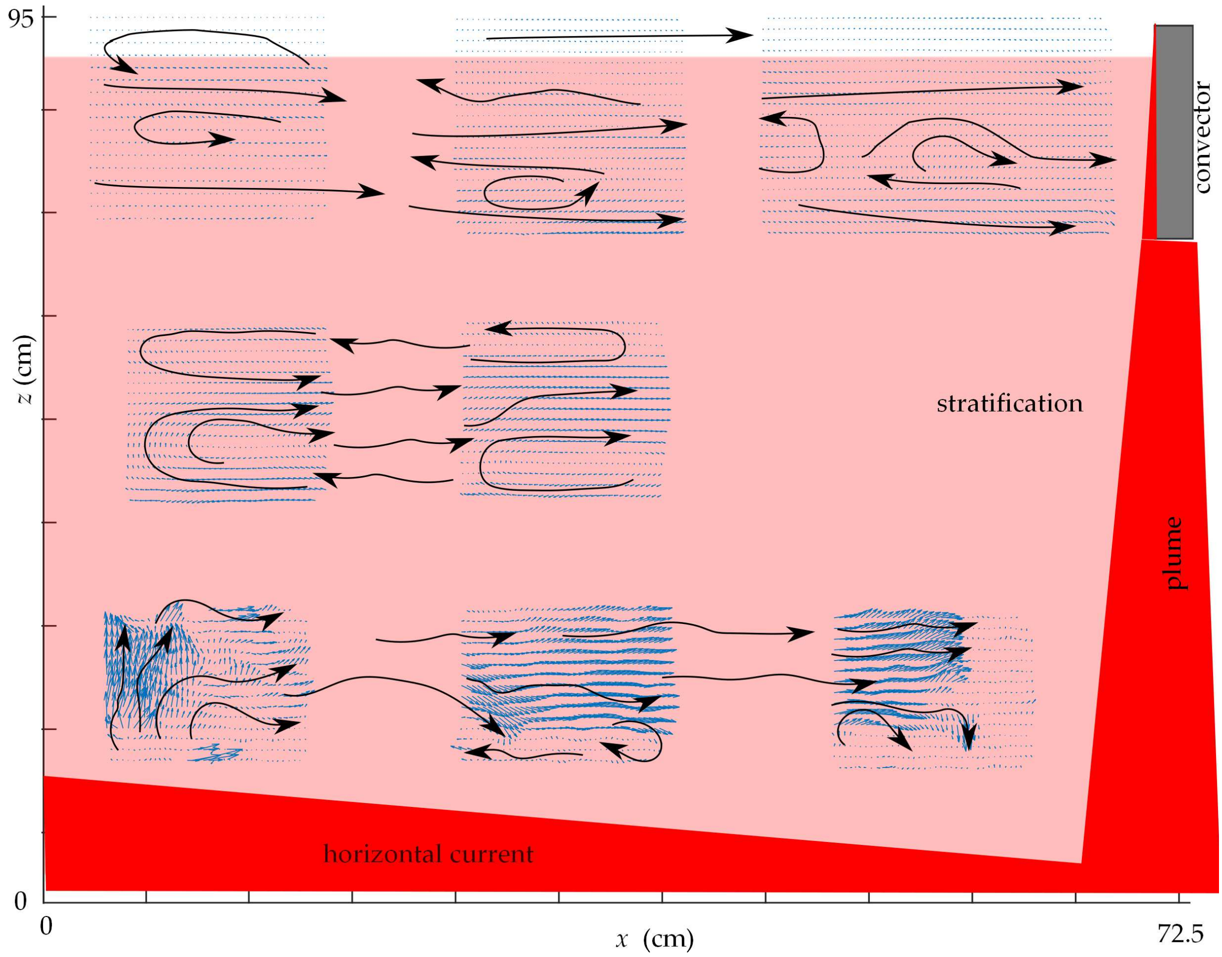

Figure 7.11: Velocity vector field induced by filling in a half of the tank (in elevation) in the late period at $t = 28T_{exp}$. Vector field consist of 8 stitched vector fields captured at 8 FOVs (location of FOVs correspond to location of vector fields). Blue arrows are velocity vectors, relatively scaled to provide meaningful representation of the flow in the tank. Black arrows mark trends in the flow direction.

7.4 Vorticity fields

The velocity fields in Figures 7.3 - 7.12 indicate that structures, which have features resembling vortices, are present in the flowfields. This is illustrated by Figure 7.13 which shows vorticity (see Section 4.5.3.8) close to the region where the plume outflow overturns[1]. In this particular

[1]Overturning was detected close to the tank corner in dye-attenuation technique after the plume outlow (horizontal current) impinged on a side wall, ascended along a side wall and collapsed under gravity.

0.005(11%)	0.0259 (57%)	0.0455(100%)
0.0086 (19%)	0.039 (87%)	
0.23 (505%)	0.34 (746%)	0.23 (505%)

Table 7.2: Values of m (cms^{-1}) for 8 vector fields comprising the stitched velocity vector field in the late period at $t = 28T_{exp}$. Values presented in the order matching distribution in Figure 7.11. Percentage used to compare mean velocities induced in the tank.

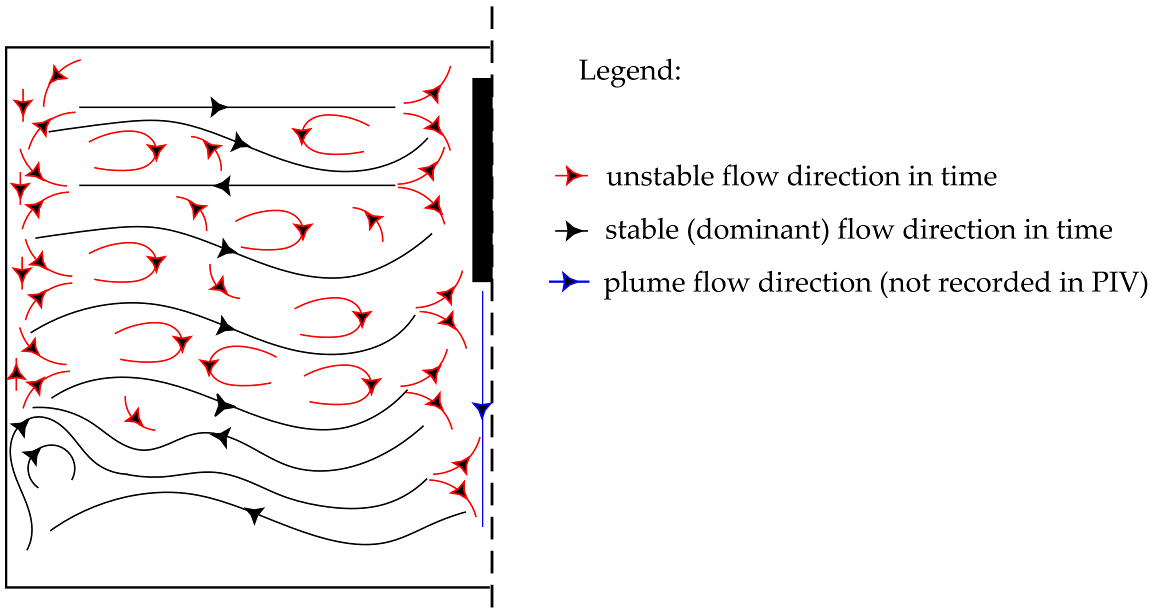

Figure 7.12: Schematic of the induced flows in a half of the tank (in elevation) in the late period. Dashed vertical line marks the middle of the tank.

region, which is close to the corner of the tank, vortical structures seem relatively obvious. Figure 7.14 shows a time series of vorticity in the same FOV as in Figure 7.13. At times we appear to see clear vortical structures (e.g. Figure 7.14 a, f), whereas at other instances at the same system coordinates the vorticity field is just smeared (e.g. Figure 7.14 c-e). The flow thus appears to be quite unsteady with no dominant, persistent vorticies alluding that there is a lot of mixing in the region. In the context of convector-induced filling flow, using PIV to detect vortical structures, is clearly advantageous. It allows the detection of regions where intense mixing occurs due to rotation of the fluid, which promotes faster filling.

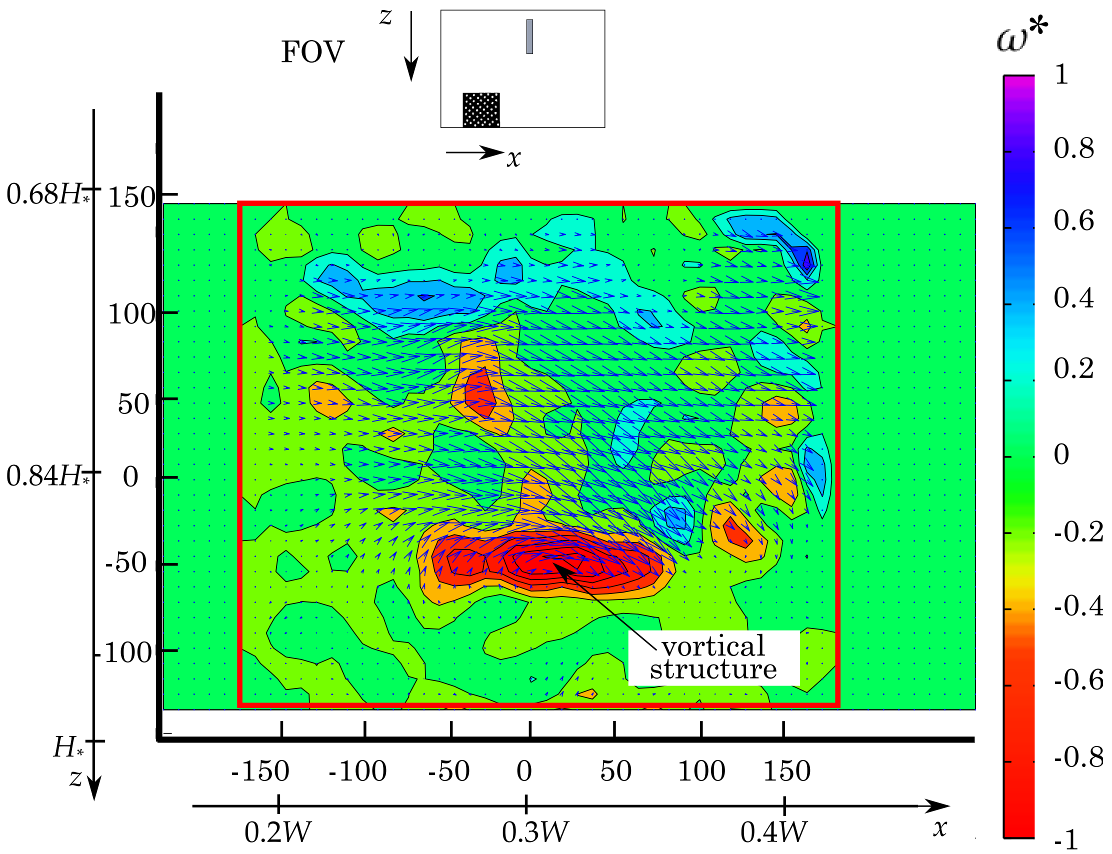

Figure 7.13: Flowfield representation using vorticity as vortex detection technique.

For the flowfield close to the corner, vortical structures were relatively obvious; however, in general this is not the case. In most cases, the computation of vorticity on the PIV data sets yielded a very noisy field. The vortical structures might not be discernible in these regions using vorticity due to strong velocity gradients and noise amplification. It is worth noting here that the noisy vorticity fields could be due to amplification of PIV errors or could be a genuine feature of the turbulent flow field.

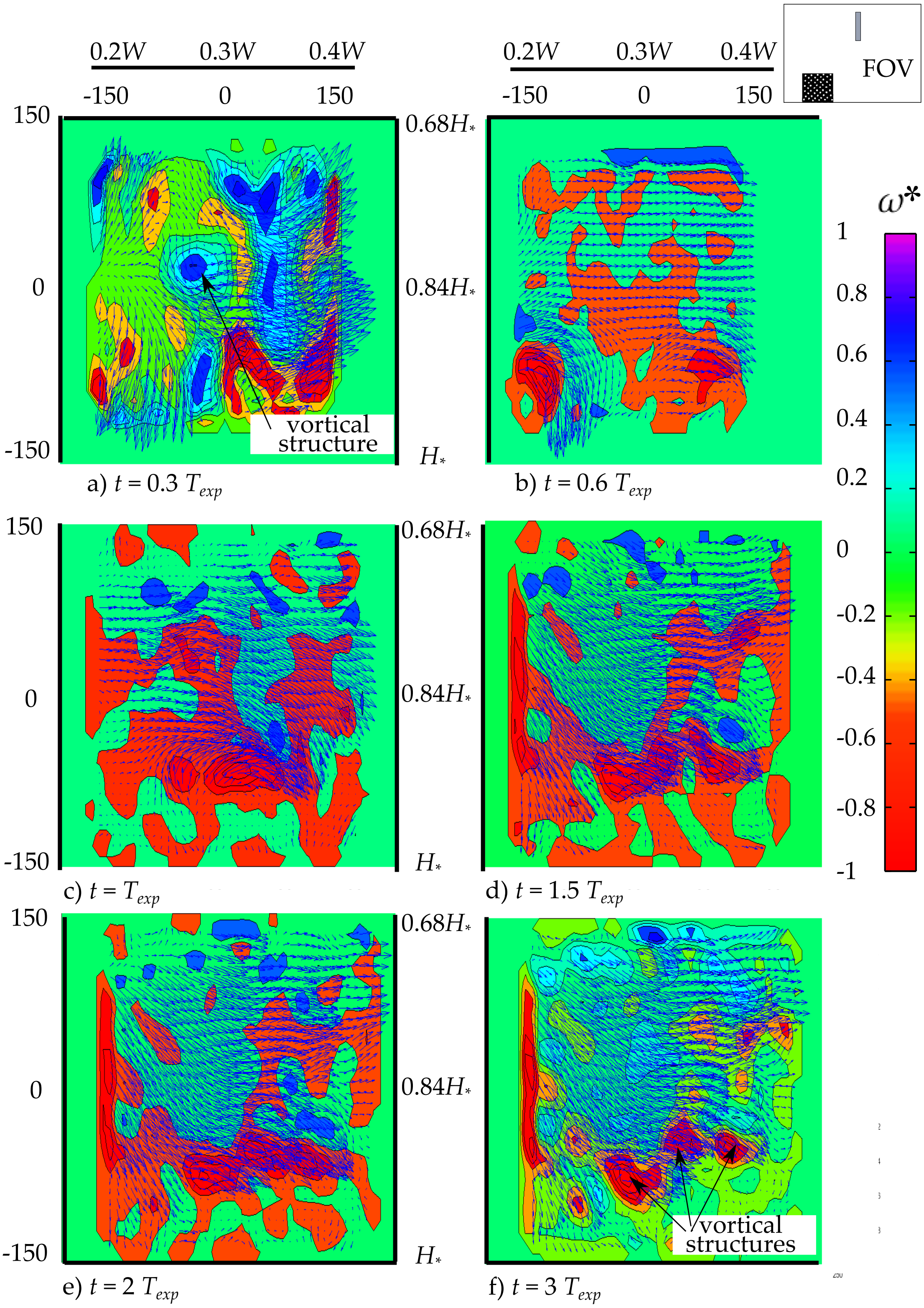

Figure 7.14: Flowfield representations using vorticity as vortex detection technique in time series.

7.5 Summary of Results

PIV vector fields, used for the example case, allow a representation of the motion of the fluid in the environment outside the filling flows. Two stitched velocity vector fields and two corresponding schematics of induced flows in the early and late period, respectively, have been prepared to demonstrate typical induced flows within the entire central plane as opposed to a single FOV. Chapter 5 discussed rate of filling but lacked insight into the contributing mixing mechanisms. The PIV data in this chapter has allowed a representation of the fluid motion outside of the buoyant front. Overall, the flow direction appears to be mainly towards the plume with a dominant horizontal velocity component and with a vortical tendency so that vectors move in a clockwise or anticlockwise direction depending on the region in the tank. The vortical tendency seems stronger in the late period. In the late period horizontal intrusions away from the plume have been detected. The flow in the entire system in both periods tends towards rotation. In addition, PIV shows that induced flows have a non-two-dimensional structure. Occasionally concentrations of vorticity are observed suggesting the presence of vortices. These structures, which resemble vortices, appear to be short-lived and somewhat random. However, in most of the PIV data vortical structures are not immediately obvious and perhaps more sophisticated analysis techniques are needed. In Chapter 6, disturbances in density distribution with height were seen in shadowgraphs both in the near and far fields. PIV data appears to confirm that shearing motions are influential on the disturbances in the buoyancy distribution with height.

The insight gained through PIV data helps to understand the flow induced in the surrounding area outside the buoyant filling flow. The inspection of unsteady and rotational flow provides preliminary insight into mixing mechanisms which contribute to faster filling.

Chapter 8

Conclusions

In the centre of the research presented herein has been a convector, a device ensuring thermal comfort in occupied spaces by inducing bulk flows of warm air. A standard approach to evaluate convector performance is based on the convector strength alone with the implication being that the stronger the convector the better the performance. This work has gone beyond the limits of a stereotypical assessment in pursuit of answers regarding the physics of convector-induced filling and a new objective method to evaluate the efficiency of this transient process. The ultimate motivation has been to investigate what are the dependencies on the efficiency of heat distribution during convector-induced filling.

A comprehensive literature review has revealed a research gap in the field of buoyancy-driven flows, corresponding to a lack of knowledge of the fundamental physics governing convector-induced flows during filling in a heated room. Knowledge of buoyancy-driven flows gained in prior research has not given a full appreciation of the influence that governing parameters, other than the buoyancy source strength (i.e. source geometry and location) have on the buoyancy-driven filling rate and the developing stratification. One objective of this thesis has thus been to verify the influence of these newly-found governing parameters on convector-induced flows and to establish guidelines leading to more efficient convector-induced filling, corresponding to faster filling and more uniform stratification. A review of existing efficiency measures confirmed the need for a new assessment strategy dedicated to the efficiency of convector induced-filling.

Small scale experiments have been conducted. To approximate dynamic similarity between a small-scale set-up and a real-life application, an experimental facility has been designed. Experiments have been performed in water with a saline solution supplied to ensure high Rayleigh numbers. Experimental programmes have been designed to investigate the impact of the convector's position and strength on the filling rate and developing stratification. A combination of a shadowgraph method, a dye-attenuation method, Particle Image Velocimetry (PIV) and direct salinity measurements have been used as indicative tools. A qualitative description of the filling has been based on grayscale images from dye-attenuation and shadowgraph data. Salinity measurements from conductivity probes provided quantitative data on the development of stratification. A quantitative description of the flows induced in the environment has been gained from PIV data. The unique PIV arrangement, which has been proposed in this thesis, involved using a light sheet of white light, formed from a projector lamp source. The set-up has allowed capturing PIV data and salinity measurements simultaneously.

The new experimental results are used to describe mechanisms of convector-induced filling. For instance somewhat counter-intuitively, faster filling occurs in rooms with shorter convectors detached from side walls, due to large-scale mixing flows during the early period of filling. The transient filling has been successfully described using newly-developed, application-specific, statistical methods. As a result, the empirical equations describing both the filling rates in different stages of filling and the development of stratification have been derived, which rank the governing parameters, based on their importance, as either dominant or subordinate.

Finally, two new methods (instantaneous and time-averaged) of evaluating efficiency of convector-induced filling have been developed and successfully applied.

8.1 Rate of filling

Small-scale experiments confirmed the sequence of flows during convector-induced filling, from the starting plume, followed by the horizontal current, the vertical intrusion, horizontal reflections to the interface advection. The filling rate decreased as the process continued. There were a few factors influencing the rate of filling during different stages of filling. For instance, in the early period, prior to establishing the interface, filling flows were characterised by large-scale mixing (engulfment) between the buoyant bulk flow and the ambient environment, caused by the interplay between inertia and buoyancy. These contributed to a faster filling rate. Large-scale mixing died out once an interface was established, which caused a noticeable decrease in the filling rate. From this instance of time, the filling, now limited to the interface advection, was a result of the plume entering the buoyant layer only. From the volume conservation, the larger the volume flow rate entering the buoyant layer was, the faster the filling. The dependency of the filling on the plume development explains further deceleration of filling upon reaching the trailing edge of the convector, due to limited entrainment into the plume in the near field. Based on the following observations, confirmed by the quantitative data, it was established that faster filling may be achieved by reducing the extent of the near field compared to the far field and moving the convector away from the side wall to increase entrainment into the plume.

Key results of studies on each flow type include the following:

- The convector strength B_0 maintains a steady influence on the filling rate for the duration of filling.
- For a given height H, maximising the vertical distance $H - \mathcal{L}$ should be a priority as it leads to the faster filling.
- Moving the convector away from the side wall, increases the entrainment into the plume, thus leading to the faster filling.

- For $a \leq 4d$, the development of the starting plume and plume is at least partially confined by a side wall and there are two characteristic lengths $H - \mathcal{L}$ and a. For $a > 4d$, $H - \mathcal{L}$ is the only characteristic length.
- The development of the horizontal current depends on a and $H - \mathcal{L}$.
- The maximum penetration λ of vertical intrusion depends on H and $\mathcal{L}$.
- Depending on H and $\mathcal{L}$, vertical intrusion collapses into:
  - overturning for $\left(\frac{H}{\mathcal{L}}\right) > 1.3$;
  - slumping for $\left(\frac{H}{\mathcal{L}}\right) < 1.3$.

Two dominant parameters governing filling flows are the non-dimensional accumulation parameter ($\mathcal{B}$, see eq. (4.27)) and the Rayleigh number (ΔRa, see eq. (4.28)). The impact of these two parameters is constant throughout the process. The non-dimensional geometry ($\{\mathcal{G}, \mathcal{G}^*\}$, see eq.(4.30-4.31)) and time parameter ($\mathbf{T}$, see eq. (4.33)) are subordinate parameters. Their impact, visible in the early period, decreases as filling continues.

Preliminary insight into mixing mechanisms which contribute to the rate on filling has been based on the PIV data. PIV vector fields allowed a representation of the motion of the fluid outside the buoyant front, which was invisible in other techniques. As a result, a complete picture of flows induced by a convector are presented in this work. Outside the buoyant flow, the flow direction appeared to be mainly towards the plume with a dominant horizontal velocity component and with a vortical tendency so that vectors were moving in clockwise or anticlockwise direction depending on the region in the tank. The vortical tendency seemed stronger in the stratified region of the late period, where horizontal motions away from the plume were also observed. In addition, PIV showed that induced flows have a non-two-dimensional complex structure, which could affect perpendicular flows towards the convector. Computation of vorticity from PIV data has shown that vortical structures can sometimes be identified. In most of the PIV data vortical structures were not immediately obvious.

8.2 Stratification

Experimental results confirmed that, similarly to the filling rate, the stratification depends not only on the convector strength but also on the convector position and relative room size. The interdependence between the filling rate and the stratification has been confirmed and proved beneficial when searching for the more efficient convector-room systems. Design guidelines, aimed at increasing the filling rate for a given source strength lead to a more uniform distribution of buoyancy with height. Adjusting the convector horizontal position, by detaching the convector from the wall, increases the entrainment into the plume, thus initially promoting the weakening of stratification. For $a > 4d$, when the distance a allowing the free development of plume across the entire vertical distance H is exceeded, the environment tends to stratify more again. A vast difference between the rate of entrainment in the convector near and far fields leads to a significant difference in the stratification development between both fields. In the far field (away from the convector), characterised by a higher rate of entrainment, after initial time lags associated with early period filling, the stratification tends towards a more uniform distribution. In the near field (convector level), the slower rate of entrainment leads to a sharper stratification, which is maintained for the duration of each experiment.

From a comfort perspective, promoting an even distribution of buoyancy is more beneficial. For a given vertical distance H, therefore, extending the far field compared to the near field by using shorter convectors of equivalent strength leads to a more efficient buoyancy distribution. Interestingly, the buoyancy increase caused by increasing the convector strength tends to be evenly distributed with height. The resulting trends of buoyancy accumulation at different zones are steeper but maintain similar relative distribution. This shows that quantitatively the source strength determines the density at different heights but qualitatively it plays a secondary role in shaping the relative buoyancy distribution with height. The latter is determined by the convector position and room size. Empirical equations derived to describe stratification and filling rate support these results. The non-dimensional representation of the convector strength is the accumulation parameter $\mathcal{B}$, which maintains a constant influence on the filling rate for the duration of filling, while being ranked as a subordinate parameter to the developing stratification. The development of stratification at a given height strongly depends on the geometric parameter $\mathcal{G}_{pr}$, which relates the position of a salinity probe and the height H, the time parameter and the Rayleigh number.

A closer inspection of the stratification in the late period revealed a locally unbalanced development of stratification. Disturbances in density distribution with height have been recorded both in the near and far fields. Shadowgraph images revealed that shearing motions, which were induced for instance by the plume detrainments, appeared to cause these disturbances. To gather further evidence experiments have been conducted where both PIV measurements and salinity readings were taken. These appear to confirm the influence of the shearing motions on the disturbances in the buoyancy distribution with height.

8.3 Efficiency of convector-induced filling

Two newly-developed assessment methods have been successfully used to evaluate the efficiency of convector-induced filling. The first, instantaneous method, based on following the trends of both salinity readings and curves of the interface position, resulted in the design recommendations as discussed in the context of the filling rate and stratification. The second, time-averaged method, based on the newly-defined performance indicators, allowed evaluating the convector operation against a benchmark operation. These two methods, based on different approaches, are in agreement, thus leading to the same design recommendations. The latter method, however, has the potential for much wider application due to the scaling applied, which allows meaningful comparisons between different zones within a room, various room sizes and even distinct convective heating systems. By inspecting the history of filling, zones which underperform and overperform can be easily detected and efforts may be undertaken to ensure transport of buoyancy across these zones.

8.4 Relevance to practical applications

A newly-gained understanding of mechanisms driving convector-induced filling and developing stratification has been crucial to establishing guidelines aimed at heating rooms more rapidly and effectively. The key outcome that can be immediately applied is that, for a given convector strength, heat distribution with height can be improved by adjusting the convector position. However, practicality of implementing each proposed design amendment should be considered. While reducing the convector height relative to the room height is rather straightforward, moving convector away from walls could be aesthetically and functionally challenging. Possible design solutions that could overcome these challenges include: portable convectors, convectors posing as architectural features, i.e. sculptures and convectors embedded into other elements of interior design, e.g. table, bench. The pursuit of design solutions that would promote moving convector away from the walls is undoubtedly energy-beneficial and could lead to 20% faster room heating.

8.5 Future work

There are some unanswered questions for future research in the field of convector-induced filling in a heated room. There are two main directions for future work, the first involves further experimental analysis and the second involves further work on the efficiency benchmark for operation of buoyancy-driven devices.

The influence of the room size, the convector position and strength have been investigated in this work. However, the convector thickness d remained unchanged in all the experiments due to limitations of the physical representation of convector. It is expected that the convector thickness may have an effect on the filling in the far field. As a result, a study on the influence of system configuration with varying d could lead to further design guidelines regarding the size of the convector.

The experiments in this thesis have been shown to be affected by the three-dimensionality of filling flows. A further study on the flow structure could help to provide further information on the complexity of filling flows. An example of where vorticity was useful to describe features of the flow was given. A further analysis of the flowfield using PIV could allow further insight into the flow structure and detection of vortical structures which are not immediately obvious. To enable the latter, it is recommended to perform further analysis of PIV data using techniques which eliminate the noise amplification associated with differentiation of a PIV vector field.

A study whereby the experimental configurations examined here are combined with periodical operation of a convector and external disturbances, due to losses through partitions, is needed to examine how stable, conditions established in a heated room are. This study would also be useful to test the performance indicators in the context of dynamic monitoring of the room conditions.

8.6 Final remarks

This thesis provides answers for: how the development of time-dependent convector-induced stratification differs from Cooper & Hunt's (2010) description for a heated wall and how to fill rooms faster and more effectively. A new appreciation of design aspects often overlooked, such as the position of the convector and its relative height, is gained. Also, fundamental mechanisms governing convector-induced filling and developing stratification are now known.

Appendix A

Experiments

Tables A.1 and A.2 contain set-up conditions used during small-scale experiments.

Table A.1: Room's width, effective depth H and aspect ratios $\mathcal{AR}$ for $\mathcal{L} = 30\,\text{cm}$.

Test	H	$a + 2.5$	W	$\mathcal{AR}$	$\left(\frac{H-\mathcal{L}}{W-a-0.5d}\right)$	$\dot{Q}$	ρ	g'_s
	(cm)	(cm)	(cm)	(-)	(-)	(cm^{3}s^{-1})	(g cm^{-3})	(cm s^{-2})
T1	95	75	150	1.26	0.86	25	1.026	26.8
T2	95	75	150	1.26	0.86	50	1.023	22.7
T3	75	75	150	1	0.6	50	1.025	26.2
T4	95	75	150	1.26	0.86	50	1.006	7
T5	95	75	150	1.26	0.86	67	1.021	21.6
T6	95	75	150	1.26	0.86	50	1.011	12.1
T7	95	75	150	1.26	0.86	50	1.023	23.5
T8	95	75	150	1.26	0.86	67	1.022	22.8
T9	95	75	150	1.26	0.86	50	1.029	29.5
T10	35	75	150	0.46	0.07	50	1.01	11.5
T11	35	75	150	0.46	0.07	50	1.015	16.4
T12	90	2.5	80	1.16	0.77	50	1.026	26.5
T13	90	2.5	80	1.16	0.77	50	1.026	26.4
T14	90	2.5	80	1.16	0.77	50	1.026	27.1
T15	90	2.5	80	1.16	0.77	25	1.026	27.1
T16	90	2.5	80	1.16	0.77	12.5	1.026	27.1
T17	90	40	80	2.25	1.5	50	1.028	28.3
T18	90	40	80	2.25	1.5	50	1.028	28.3
T19	90	2.5	45	2.12	1.41	50	1.028	28.4
T20	90	2.5	45	2.12	1.41	50	1.027	28.2
T21	90	2.5	45	2.12	1.41	50	1.027	28.2
T22	95	2.5	80	1.22	0.84	50	1.028	28.3
T23	95	40	80	2.38	1.63	50	1.028	28.3

T24	95	2.5	80	1.22	0.84	50	1.028	28.3
T25	95	2.5	80	1.22	0.84	50	1.018	19.3
T26	95	7.5	150	0.67	0.46	50	1.031	31.5
T27	95	12.5	150	0.69	0.47	50	1.035	35.5
T28	95	22.5	150	0.74	0.51	50	1.035	35.7
T29	95	32.5	150	0.81	0.55	50	1.028	28.8
T30	95	42.5	150	0.88	0.6	50	1.035	35.3
T31	75	7.5	150	0.53	0.31	50	1.032	32.5
T32	75	12.5	150	0.54	0.33	50	1.032	32.5
T33	75	22.5	150	0.59	0.35	50	1.028	28.5
T34	75	32.5	150	0.64	0.38	50	1.027	27.8
T35	50	12.5	150	0.36	0.14	50	1.032	32.9
T36	50	42.5	150	0.46	0.19	50	1.027	28.2
T37	50	32.5	150	0.42	0.39	50	1.032	32.2
T38	50	22.5	150	0.39	0.35	50	1.032	32.9
T39	95	2.5	150	0.64	0.44	50	1.03	31.1
T40	95	2.5	150	0.64	0.44	50	1.03	30.7
T41	75	2.5	150	0.51	0.3	50	1.032	32.6
T42	50	2.5	150	0.34	0.13	50	1.036	36.2
T43	31	2.5	150	0.21	0.007	50	1.023	24.3
T44	31	2.5	150	0.21	0.007	50	1.025	26.1
T45	95	75	150	1.26	0.86	50	1.013	14.6
T46	95	75	150	1.26	0.86	50	1.019	19.8
T47	50	75	150	0.67	0.26	50	1.011	12.1
T48	95	75	150	1.26	0.86	50	1.023	23.4
T49	95	75	150	1.26	0.86	50	1.02	20.7

Table A.2: Room's width, effective depth H and aspect ratios $\AE$ for $\mathcal{L} = 60\,\text{cm}$.

Test	H	$a + 2.5$	W	$\AE$	$\left(\frac{H-\mathcal{L}}{W-a-0.5d}\right)$	$\dot{Q}$	ρ	g'_s
	(cm)	(cm)	(cm)	(-)	(-)	(cm^{3}s^{-1})	(g cm^{-3})	(cm s^{-2})
T1	90	75	150	1.2	0.4	50	1.018	19.3
T2	90	75	150	1.2	0.4	50	1.018	19.3
T3	90	75	150	1.2	0.4	50	1.019	19.8
T4	90	75	150	1.2	0.4	50	1.013	14.6
T5	90	75	150	1.2	0.4	50	1.011	11.9
T6	90	2.5	150	0.61	0.2	50	1.01	11.3
T7	90	2.5	150	0.61	0.2	50	1.013	13.9
T8	90	2.5	150	0.61	0.2	50	1.013	14.3
T9	75	2.5	150	0.51	0.1	50	1.013	14.3
T10	75	75	150	1	0.2	50	1.024	25.1
T11	65	75	150	0.86	0.06	50	1.025	25.4

T12	65	2.5	150	0.44	0.03	50	1.025	25.6
T13	65	2.5	150	0.44	0.03	50	1.028	28.2
T14	65	2.5	150	0.44	0.03	50	1.022	22.9
T15	61	2.5	150	0.41	0.007	25	1.021	22.2
T16	61	2.5	150	0.41	0.007	12.5	1.013	13.8
T17	65	2.5	150	0.44	0.03	50	1.021	22.3
T18	90	2.5	150	0.61	0.2	50	1.023	23.6
T19	90	7.5	150	0.63	0.21	50	1.023	23.8
T20	90	12.5	150	0.65	0.22	50	1.023	23.4
T21	90	22.5	150	0.71	0.23	50	1.023	23.4
T22	90	2.5	150	0.61	0.2	50	1.03	30.5
T23	90	2.5	80	1.16	0.39	50	1.018	19.1
T24	90	2.5	45	2.12	0.71	50	1.018	19.1
T25	90	40	80	2.25	0.75	50	1.026	27.3
T26	90	40	80	2.25	0.75	50	1.027	28
T27	90	2.5	45	2.12	0.71	50	1.027	28.3
T28	90	2.5	80	1.16	0.39	50	1.027	28.3
T29	90	75	150	1.2	0.4	50	1.027	28.2

Appendix B

Set-up

This appendix outlines details of the experimental set-up. Figure B.1 shows a plan view of the laboratory area used during small-scale experiments. The experimental set-up was divided into three zones: experimental zone, saline supply zone and water supply zone. Experiments were conducted, recorded and adjusted in the experimental zone. The saline supply and water supply zones were used to deliver fluids to the experimental zone. The critical temperature difference between the saline solution and water was set at $\pm 1K$(see Section 4.5.4.5). To meet this critical temperature condition both water and saline solutions were prepared at least 24 hours prior to the experiment.

B.1 Saline supply

The source of the saline solution consisted of 3 reservoirs:

- the direct source - 100l cylindrical tank (SS3);
- the two indirect sources - 900l fibreglass tanks (open SS1 - for preparation of the saline solution and closed SS2 - for storing saline solution and feeding the direct source).

These three reservoirs were connected with each other in the following way:

- a one-way draining cycle between SS1 and SS2 (a submersible pump + 1.5 m reinforced hose);
- a recirculation cycle between SS2 and SS3 (a submersible pump + a rotary volume flow rate meter 2 lengths of reinforced hose; an overflow pipe connecting SS3 and SS2).

SS1 was used only for the preparation of the saline solution. From SS1 saline solution was pumped to SS2 which supplied SS3. During the experiment, the saline solution was pumped directly from SS3 via a LowFlo flow rate meter with totaliser VFR1 and a rotary volume flow rate meter VFR2 to the model convector M. Recirculation between SS2 and SS3 was established

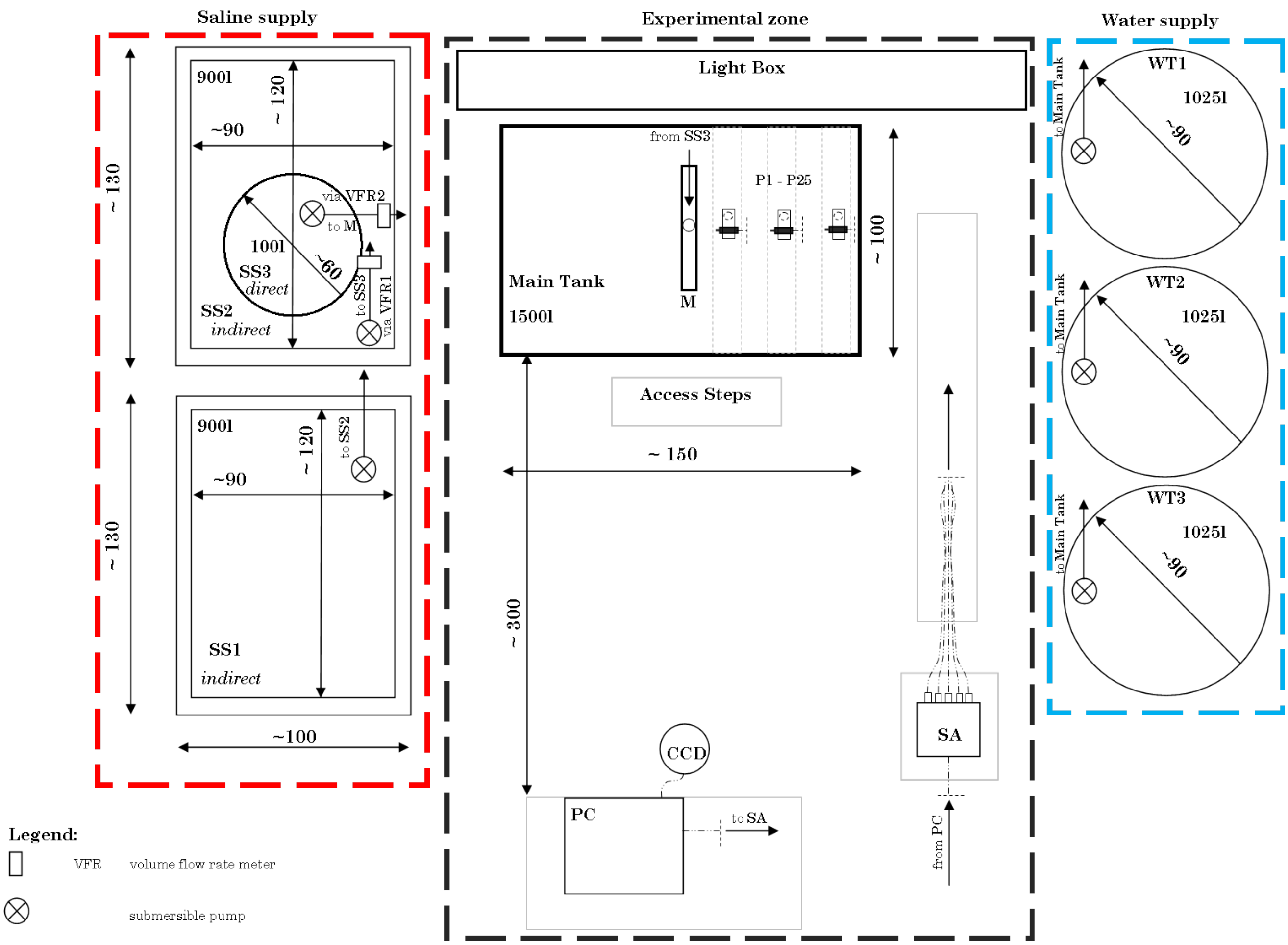

Figure B.1: Schematic of experimental set-up prepared for dye attenuation and conductivity measurements.

to maintain a constant level of solution (constant pressure head) in SS3 and to prevent any changes in volume flow rate throughout the experiment.

B.2 Water supply

Average experiment required 1500 l of freshwater. To ensure that the water temperature was approximately equal to room temperature, three tanks (WT1-WT3) of volume 1025 l each were filled with water at least 24 hours prior to the experiment. Approximately an hour before the experiment, the water was supplied to the Main Tank via submersible pumps. The volume of water stored in tanks WT1-WT3 allowed two experiments to be performed.

B.3 Experimental zone

The fluid exchange during the experiment was enabled by two cycles: the supply cycle and the discharge cycle. In the supply cycle, which connects the direct source SS3 with the model M, the submersible pump was immersed in SS3. The discharge cycle consisted of the vertical, overflow pipe that was connected to the drains. The equivalent volume flow rates were supplied and drained from the tank. Figure 4.8 shows a schematic of the experimental zone.

Appendix C

Conversion from small scale to full scale

Table C.1 summaries the dimensionless quantities resulting from the scaling relations between small-scale and full-scale variables characterising filling flows. Each variable is represented as a power function of a characteristic length and buoyancy. These dimensionless quantities, also presented as power functions of two basic dimensionless quantities: LS and BS, enable conversion of filling time, the rate of filling, expressed in terms of the velocity and fluxes of volume, momentum and buoyancy, and the stratification, based on the density (temperature) profiles.

Variable	Small scale	Full scale	Scaling	f(LS, BS)
Time	$l_m^{1/2} {g'}_m^{-1/2}$	$l_f^{1/2} {g'}_f^{-1/2}$	$TS = \frac{t_m}{t_f}$	$TS = LS^{1/2} BS^{-1/2}$
Velocity	$l_m^{1/2} {g'}_m^{1/2}$	$l_f^{1/2} {g'}_f^{1/2}$	$VS = \frac{u_m}{u_f}$	$VS = LS^{1/2} BS^{1/2}$
Volume Flux	$l_m^{5/2} {g'}_m^{1/2}$	$l_f^{5/2} {g'}_f^{1/2}$	$VFS = \frac{Q_m}{Q_f}$	$VFS = LS^{5/2} BS^{1/2}$
Momentum Flux	$l_m^3 {g'}_m$	$l_f^3 {g'}_f$	$MFS = \frac{M_m}{M_f}$	$MFS = LS^3 BS$
Buoyancy Flux	$l_m^{5/2} {g'}_m^{3/2}$	$l_f^{5/2} {g'}_f^{3/2}$	$BFS = \frac{B_m}{B_f}$	$BFS = LS^{5/2} BS^{3/2}$

Table C.1: The scaling relations between small scale and full scale for buoyancy-driven filling flows.

The full-scale filling time may be estimated from the relationship: $t_f = (TS)^{-1} t_m$. For TS greater than 1, the full-scale filling time is less than the corresponding small-scale filling time, thus full-scale filling is faster than in the experiments. The reverse applied to TS smaller than 1. TS is a power function of LS and BS and, as a result, these non-dimensional quantities influence the filling time. Figure C.1 contains two nomographs for a rapid estimation of TS and VS for a number of *BS* and *LS*. There are two possible applications of the nomograph. Firstly, for known *BS* and *LS*, it allows quick estimation of each dimensionless quantity. Secondly, for known dimensionless quantities and *BS* (*LS*), it allows estimation of *LS* (*BS*) necessary to fulfil the design conditions. Each nomograph is colour-coded to distinguish between values of each dimensionless quantity that are greater than 1 and less than 1.

TS

BS \ *LS*	1 : 1	1 : 2	1 : 3	1 : 4	1 : 5	1 : 6	1 : 7	1 : 8	1 : 9	1 : 10
1 : 1	1.00	0.71	0.58	0.50	0.45	0.41	0.38	0.35	0.33	0.32
1 : 2	1.41	1.00	0.82	0.71	0.63	0.58	0.53	0.50	0.47	0.45
1 : 3	1.73	1.22	1.00	0.87	0.77	0.71	0.65	0.61	0.58	0.55
1 : 4	2.00	1.41	1.15	1.00	0.89	0.82	0.76	0.71	0.67	0.63
1 : 5	2.24	1.58	1.29	1.12	1.00	0.91	0.85	0.79	0.75	0.71
1 : 6	2.45	1.73	1.41	1.22	1.10	1.00	0.93	0.87	0.82	0.77
1 : 7	2.65	1.87	1.53	1.32	1.18	1.08	1.00	0.94	0.88	0.84
1 : 8	2.83	2.00	1.63	1.41	1.26	1.15	1.07	1.00	0.94	0.89
1 : 9	3.00	2.12	1.73	1.50	1.34	1.22	1.13	1.06	1.00	0.95
1 : 10	3.16	2.24	1.83	1.58	1.41	1.29	1.20	1.12	1.05	1.00

VS

LS \ *BS*	1 : 1	1 : 2	1 : 3	1 : 4	1 : 5	1 : 6	1 : 7	1 : 8	1 : 9	1 : 10
1 : 1	1.00	0.71	0.58	0.50	0.45	0.41	0.38	0.35	0.33	0.32
1 : 2	0.71	0.50	0.41	0.35	0.32	0.29	0.27	0.25	0.24	0.22
1 : 3	0.58	0.41	0.33	0.29	0.26	0.24	0.22	0.20	0.19	0.18
1 : 4	0.50	0.35	0.29	0.25	0.22	0.20	0.19	0.18	0.17	0.16
1 : 5	0.45	0.32	0.26	0.22	0.20	0.18	0.17	0.16	0.15	0.14
1 : 6	0.41	0.29	0.24	0.20	0.18	0.17	0.15	0.14	0.14	0.13
1 : 7	0.38	0.27	0.22	0.19	0.17	0.15	0.14	0.13	0.13	0.12
1 : 8	0.35	0.25	0.20	0.18	0.16	0.14	0.13	0.13	0.12	0.11
1 : 9	0.33	0.24	0.19	0.17	0.15	0.14	0.13	0.12	0.11	0.11
1 : 10	0.32	0.22	0.18	0.16	0.14	0.13	0.12	0.11	0.11	0.10

- (blue) $TS < 1$
- (red) $TS \geq 1$
- (yellow) $VS < 1$
- (purple) $VS \geq 1$

Figure C.1: Nomographs to estimate *TS* and *VS*: *BS* - abscissa and *LS* - ordinate. Note: The nomograph consists of selected values of *BS* and *LS* and may be interpolated or extrapolated as required.

References

[1] Directive 2010/31/EU of the European Parliament and of the Council of 19 May 2010 on the energy performance of buildings (recast). *Official Journal of the European Union*, **18**(06), 2010.

[2] La Vision GmbH. La vision., 2010.

[3] BS EN 442. Radiators and Convectors.

[4] BS EN ISO 7730. *Ergonimics of the thermal environment- Analytical determination and interpretation of thermal comfort using calculation of the PMV and PPD indices and local thermal comfort criteria.*

[5] R. J. Adrian and J. Westerweel. *Particle image velocimetry*. Cambridge University Press, 2011.

[6] D. M. Allgayer and G. R. Hunt. On the application of the light-attenuation technique as a tool for non-intrusive buoyancy measurements. *Experimental Thermal and Fluid Science*, **38**:257–261, 2012.

[7] ANSI/ASHRAE. *Standard 55: Thermal Environmental Conditions for Human Occupancy.*

[8] ASHRAE. *Handbook: Heating, Ventilating, and Air-conditioning Applications*. 2015.

[9] W. D. Baines. Entrainment by a plume or jet at a density interface. *Journal of Fluid Mechanics*, **68**:309–320, 1975.

[10] W. D. Baines and J. S. Turner. Turbulent buoyant convection from a source in a confined region. *Journal of Fluid Mechanics*, **37**:51–80, 1969.

[11] J. S. Barnett. *The dynamics of buoyant releases in confined spaces.* PhD Thesis. University of Cambridge, 1991.

[12] G. K. Batchelor. Heat convection and buoyancy effects in fluids. *Quarterly Journal of the Royal Meteorological Society*, **80**(345):339–358, 1954.

[13] G. K. Batchelor. An introduction to fluid dynamics. Cambridge University Press, 2010.

[14] J. Boussinesq. *Théorie de l'écoulement tourbillonnant et tumultueux des liquides dans les lits rectilignes a grande section*. 1897.

[15] P. Bradshaw. *Experimental fluid mechanics.* Pergamon Press, 1970.

[16] C. Brossard, J.-C. Monnier, P. Barricau, F.-X. Vandernoot, Y. Le Sant, F. Champagnat, and G. Le Besnerais. Principles and applications of particle image velocimetry. *Aerospace Lab Journal*, **AL01-03**:1–11, 2009.

[17] T. J. Bruno and P. D. N. Svoronos. *CRC handbook of fundamental spectroscopic correlation charts*. CRC Press, 2005.

[18] G. Carazzo, E. Kaminski, and S. Tait. The route to self-similarity in turbulent jets and plumes. *Journal of Fluid Mechanics*, **547**:137–148, 2006.

[19] S. S. S. Cardoso and A. W. Woods. Mixing by a turbulent plume in a confined stratified region. *Journal of Fluid Mechanics*, **250**:277–305, 1993.

[20] T. Caudwell, J. B. Flór, and M. E. Negretti. Convection at an isothermal wall in an enclosure and establishment of stratification. *Journal of Fluid Mechanics*, **799**:448–475, 2016.

[21] C. Cenedese and S. B. Dalziel. Concentration and depth field determined by the light transmitted through a dyed solution. *8th International Symposium of Flow Visualization*, 1998.

[22] R. Cheesewright. Turbulent natural convection from a vertical plane surface. *Journal of Heat Transfer*, **90**(1):1–6, 1968.

[23] R. Clift, J. R. Grace, and M. E. Weber. *Bubbles, Drops and Particles*. Academic Press, Inc., 1978.

[24] C. J. Coffey and G. R. Hunt. Ventilation effectiveness measures based on heat removal: Part 1. definitions. *Building and Environment*, **42**:2241–2248, 2007.

[25] C. J. Coffey and G. R. Hunt. Ventilation effectiveness measures based on heat removal: Part 2. application to natural ventilation flows. *Building and Environment*, **42**:2249–2262, 2007.

[26] J. Colomer, B. M. Boubnov, and H. J. S. Fernando. Turbulent convection from isolated sources. *Dynamics of atmospheres and oceans*, **30**(2):125–148, 1999.

[27] P. Cooper and G. R. Hunt. The ventilated filling box containing a vertically distributed source of buoyancy. *Journal of Fluid Mechanics*, **646**:39–58, 2010.

[28] F. R. d'Ambrosio Alfano, B. W. Olesen, B. I. Palella, and G. Riccio. Thermal comfort: Design and assessment for energy saving. *Energy and Buildings*, **81**:326–336, 2014.

[29] E. R. G. Eckert and T. W. Jackson. Analysis of turbulent free-convection boundary layer on flat plate. *Technical Note 2207 (National Advisory Committee for Aeronautics)*, 1950.

[30] T. H. Ellison and J. S. Turner. Turbulent entrainment in stratified flows. *Journal of Fluid Mechanics*, **6**(3):423–448, 1959.

[31] M. Epstein and J. P. Burelbach. Vertical mixing above a steady circular source of buoyancy. *International Journal of Heat and Mass Transfer*, **44**(3):525–536, 2001.

[32] A. Ezzamel, P. Salizzoni, and G. R. Hunt. Dynamical variability of axisymmetric buoyant plumes. *Journal of Fluid Mechanics*, **765**:576–611, 2015.

[33] J. Fall and P. Holland. *Personal Communication.* 2011–2015.

[34] P.O. Fanger. *Thermal comfort*. New York: McGraw-Hill, 1972.

[35] P.O. Fanger. Thermal discomfort caused by radiant asymmetry, local air velocities, warm and cold floors, and vertical air temperature gradients. In *Confort Termique: Aspects physiologiques et psychologiques*, pages 203–210. INSERM, 1977.

[36] A. M. Fincham and G. R. Spedding. Low cost, high resolution DPIV for measurement of turbulent fluid flow. *Experiments in Fluids*, **23**(6):449–462, 1997.

[37] H. B. Fischer, E. J. List, R. C. Y. Koh, J. Imberger, and N. H. Brooks. *Mixing in Inland and Costal Waters*. Academic Press, Inc., 1979.

[38] M. J. Friedl, C. Härtel, and T. K. Fanneløp. An experimental study of starting plumes over area sources. *Nuovo cimento della Società italiana di fisica. C*, **22**.

[39] W. K. George and S. P. Capp. A theory for natural convection turbulent boundary layers next to heated vertical surfaces. *International Journal of Heat Mass Transfer*, **22**:813–826, 1979.

[40] A. E. Germeles. Forced plumes and mixing of liquids in tanks. *Journal of Fluid Mechanics*, **71**(03):601 – 623, 1975.

[41] A. Giambattista, R. C. Richardson, and B. M. Richardson. *College physics*. 2007.

[42] B. A. Giannakopoulos, N. B. Kaye, and G. R. Hunt. The influence of room geometry on the overturning of smoke owing to a floor fire. *Proceedings of the Institution of Civil Engineers-Engineering and Computational Mechanics*, **166**(2):69–87, 2013.

[43] C. Gladstone and A. W. Woods. Detrainment from a turbulent plume produced by a vertical line source of buoyancy in a confined, ventilated space. *Journal of Fluid Mechanics*, **742**:35–49, 2014.

[44] J. H. Gladstone and T. P. Dale. Researches on the refraction, dispersion, and sensitiveness of liquids. *Philosophical Transactions of the Royal Society of London*, **153**:317–343, 1863.

[45] J. J. Grella and G. M. Faeth. Measurements in a two-dimensional thermal plume along a vertical adiabatic wall. *Journal of Fluid Mechanics*, **71**(04):701 – 710, 1975.

[46] M. F. Hibberd and B. L. Sawford. Design criteria for water tank models of dispersion in the planetary convective layer. *Boundary-Layer Meteorology*, **67**:97–118, 1994.

[47] J. S. Hübner. *Buoyant plumes in a turbulent environment.* PhD thesis, University of Cambridge, 2004.

[48] G. R. Hunt and N. B. Kaye. Lazy plumes. *Journal of Fluid Mechanics*, **533**:329–338, 2005.

[49] Y. Jaluria. Natural convection. In *Heat transfer handbook, Volume 1*, pages 525–572. John Wiley & Sons, Inc., 2003.

[50] Y. Jaluria and B. Gebhart. On transition mechanisms in vertical natural convection flow. *Journal of Fluid Mechanics*, **66**(2):309–337, 1974.

[51] A. Jones. *Unsteady Low Reynolds Number Aerodynamics of a Waving Wing.* PhD thesis, University of Cambridge, 2010.

[52] B. W. Jones. Capabilities and limitations of thermal models for use in thermal comfort standards. *Energy and Buildings*, **34**(6):653–659, 2002.

[53] N. B. Kaye and G. R. Hunt. Overturning in a filling box. *Journal of Fluid Mechanics*, **576**:297–323, 2007.

[54] N. B. Kaye and G. R. Hunt. Smoke filling time for a room due to a small fire: The effect of ceiling height to floor width aspect ratio. *Fire Safety Journal*, **42**(5):329–339, 2007.

[55] R. C. Kerr and C. D. McConnochie. Dissolution of a vertical solid surface by turbulent compositional convection. *Journal of Fluid Mechanics*, **765**:211–228, 2015.

[56] P. D. Killworth and J. S. Turner. Plumes with time-varying buoyancy in a confined region. *Geophysical & Astrophysical Fluid Dynamics*, **20**(3-4):265–291, 1982.

[57] G. Laufer. *Introduction to optics and lasers in Engineering.* Cambridge University Press, 1996.

[58] S. L. Lee and H. W. Emmons. A study of natural convection above a line fire. *Journal of Fluid Mechanics*, **2**(03):353 – 368, 1961.

[59] P. F. Linden. Convection in the Environment. In *Perspective in Fluid Dynamics: A collective introduction to current research.*, pages 289 – 345. 2000.

[60] P. F. Linden, G. F. Lane-Serff, and D. A. Smeed. Emptying filling boxes: the fluid mechanics of natural ventilation. *Journal of Fluid Mechanics*, **212**:309–335, 1990.

[61] D. V. Lindley and W. F. Scott. *New Cambridge Statistical Tables.* Cambridge University Press, 2nd edition, 1984.

[62] P. Lynch. *Aspects of the fluid mechanics of night-purging multi-storey buildings.* PhD thesis, Imperial College London, 2012.

[63] R. L. Mahajan and B. Gebhart. An experimental determination of transition limits in a vertical natural convection flow adjacent to a surface. *Journal of Fluid Mechanics*, **91**:131–154, 1979.

[64] M. Maivel and J. Kurnitski. Low temperature radiator heating distribution and emission efficiency in residential buildings. *Energy and Buildings*, **69**:224–236, 2014.

[65] P. C. Manins. Turbulent buoyant convection from a source in a confined region. *Journal of Fluid Mechanics*, **91**(4):767–781, 1979.

[66] C. D. McConnochie and R. C. Kerr. The turbulent wall plume from a vertically distributed source of buoyancy. *Journal of Fluid Mechanics*, **787**:237–253, 2016.

[67] D. C. Montgomery and G. C. Runger. *Applied Statistics and Pobability for Engineers*. John Wiley & Sons, Inc., 6th edition, 2011.

[68] B. R. Morton, G. Taylor, and J. S. Turner. Turbulent gravitational convection from maintained and instantaneous sources. *Proc. R. Soc. Lond. A*, **234**:1–23, 1956.

[69] B. R. Munson, D. F. Young, and T. H. Okiishi. *Fundamentals of Fluid Mechanics*. John Wiley & Sons, Inc., 1990.

[70] J. J. Niemela, L. Skrbek, K. R. Sreenivasan, and R. J. Donnelly. Turbulent convection at very high rayleigh numbers. *Nature*, **404**(6780):837–840, 2000.

[71] W. Nusselt. The rate of ignition of combustible gas mixtures. *Z. Ver. Dtsch. Ing*, **59**:872–878, 1915.

[72] B.W. Olesen, M. Scholer, and P.O. Fanger. Discomfort caused by vertical air temperature differences. *Indoor climate*, **36**, 1979.

[73] M. G. Patterson. What is energy efficiency? Concepts, indicators and methodological issues. *Energy Policy*, **24**(5):377–390, 1996.

[74] C. A. Peters. Statistics for Analysis of Experimental Data. In *Environmental Engineering Process Laboratory Manual*. AEEP, Champaign IL, 2001.

[75] C. W. Pitt Ford. *Unsteady Aerodynamic Forces on Accelerating Wings at Low Reynolds Numbers*. PhD thesis, University of Cambridge, 2013.

[76] S. Prahl. Absorption spectrum of methylene blue. `http://omlc.org/spectra/mb/`. (Accessed on 18/09/2017).

[77] L. Prandtl. *Führer durch die Strömungslehre.* Vieweg und Sohn, 3rd edition, 1949.

[78] E. Przydróżny. *Wymiana ciepła i masy w zraszanych jednorzędowych wymiennikach ciepła z rur gładkich.* PhD thesis, Wrocław University of Technology, 1983.

[79] M. Raffel, C. Willert, S. Wereley, and J. Kompenhans. Particle Image Velocimetry: A practical Guide. Experimental Fluid Mechanics, pages 15–77. Springer Berlin Heidelberg, 2007.

[80] G. Rogers and Y. Mayhew. Convection. In *Engineering thermodynamics work and heat transfer*, pages 580–585. Prentice Hall, 1994.

[81] J. Rosenow and A. Misra. Energy Efficiency Trends and Policies in the UK, 2012.

[82] H. Rouse, C. S. Yih, and H. W. Humphreys. Gravitational Convection from a Boundary Source. *Tellus 4.3*, pages 201–210, 1952.

[83] H. Schlichting. *Boundary-Layer Theory*. McGraw-Hill Book Company, 7th edition, 1979.

[84] G. S. Settles. *Schlieren and shadowgraph techniques: visualizing phenomena in transparent media.* Springer Science & Business Media, 2012.

[85] M. R. Spiegel and L. J. Stephens. *Schaum's outlines Statistics*. 4th edition.

[86] P. R. R. J. Stevens. *Unsteady Low Reynolds Number Aerodynamic Forces*. PhD thesis, University of Cambridge, 2015.

[87] E. Szűcs. *Similitude and modelling*. Elsevier Scientific Publishing Company, 1980.

[88] K. Tanaka. Assessment of energy efficiency performance measures in industry and their application for policy. *Energy Policy*, **36**(8):2887–2902, 2008.

[89] G. I. Taylor. *Dynamics of a mass of hot gas rising in air.* Technical Information Division, Oak Ridge Operations, 1945.

[90] J. R. Taylor. *An introduction to error analysis. The study of uncertainties in physical measurements.* University Science Books, Sausalito CA, 2nd edition, 1997.

[91] T. Tsuji and Y. Nagano. Characteristics of a turbulent natural convection boundary layer along a vertical flat plate. *International Journal of Heat and Mass Transfer*, **31**(8):1723–1734, 1988.

[92] J. S. Turner. *Buoyancy effects in fluids*. Cambridge University Press, 1973.

[93] J. S. Turner. Turbulent entrainment: the development of the entrainment assumption, and its application to geophysical flows. *Journal of Fluid Mechanics*, **173**:431–471, 1986.

[94] D. Ürge-Vorsatz. Energy End-Use: Buildings. In *Global Energy Assessment - Toward a Sustainable Future*, pages 649–760. Cambridge University Press, 2012.

[95] T. S. Van Den Bremer and G. R. Hunt. Universal solutions for Boussinesq and non-Boussinesq plumes. *Journal of Fluid Mechanics*, **644**:165 – 191, 2010.

[96] T. S. Van Den Bremer and G. R. Hunt. Two-dimensional planar plumes: non-Boussinesq effects. *Journal of Fluid Mechanics*, **750**:245–258, 2014.

[97] C. van Treeck. Indoor thermal quality performance prediction. In J. L. M. Hensen and R. Lamberts, editors, *Building Performance Simulation for Design and Operation*, pages 180–217. Spon Press, 2011.

[98] G. C. Vliet and C. K. Liu. An experimental study of turbulent natural convection boundary layers. *Journal of Heat Transfer*, **91**(4):517–531, 1969.

[99] Ch. Y. Warner and V. Arpaci. An experimetal investigation of turbulent natural convection in air at low pressure along a vertical heated flat plate. *International Journal of Heat Mass Transfer*, **11**:397–406, 1968.

[100] E. R. Weiner. *Applications of Environmental Aquatic Chemistry: A Practical Guide.* CRC Press, Taylor & Francis Group, 3rd edition, 2013.

[101] A. J. Wells and M. G. Worster. A geophysical-scale model of vertical natural convection boundary layers. *Journal of Fluid Mechanics*, **609**:111–137, 2008.

[102] J. Westerweel. Fundamentals of digital particle image velocimetry. *Measurement Science and Technology*, **8**(12):1379, 1997.

[103] B. Wieneke. Stereo-PIV using self-calibration on particle images. *Experiments in Fluids*, **39**:267–280, 2005.

[104] C. Willert, B. Stasicki, J. Klinner, and S. Moessner. Pulsed operation of high-power light emitting diodes for imaging flow velocimetry. *Measurement Science and Technology*, **21**(7):075402, 2010.

[105] A. B. D. Wong and R. W. Griffiths. Stratification and convection produced by multiple turbulent plumes. *Dynamics of Atmospheres and Oceans*, **30**:101–123, 1999.

[106] A. B. D. Wong, R. W. Griffiths, and G. O. Hughes. Shear layers driven by turbulent plumes. *Journal of Fluid Mechanics*, **434**:209–241, 2001.

[107] M. G. Worster and H. E. Huppert. Time-dependent density profiles in a filling box. **132**:457 – 466, 1983.

[108] L.-M. Yuana and G. Cox. An experimental study of some line fires. *Fire Safety Journal*, **27**(2):123–139, 1996.

[109] J. Zierep. *Ähnlichkeitsgesetze und Modellregeln der Strömungslehre.* G. Braun, 1972.

[110] C. Zoski. *Handbook of Electrochemistry.* Elsevier Science, 2007.